Scanning Single-Electron Transistor Array Microscope to Probe a Two-Dimensional Electron System under Quantum Hall Conditions below 40 milli-Kelvin

Von der Fakultät Mathematik und Physik der Universität Stuttgart
zur Erlangung der Würde eines Doktors der
Naturwissenschaften (Dr. rer. nat.) genehmigte Abhandlung

vorgelegt von

Marcel D. Mausser

aus Bad Cannstatt

Hauptberichter:	**Prof. Dr. Klaus von Klitzing**
Mitberichter:	**Prof. Dr. Peter Michler**
Tag der mündl. Prüfung:	27.01.2017

Max-Planck-Institut für Festkörperforschung

Stuttgart, 2017

Contents

List of Symbols and Abbreviations **vi**

1 Introduction **1**

2 Theoretical Basics **5**

I The Single-Electron Transistor (SET) **6**
2.1 Electrostatics and Energy Scheme of an SET 8
2.2 Electric Current versus Source-Drain Voltage Characteristic of an SET 11
2.3 Electric Current versus Gate Voltage Characteristic of an SET 13
2.4 Charge Stability Diagram 14

II Two-Dimensional Electron System (2DES) in High Magnetic Fields **16**
2.5 2DES Embedded in an (Al,Ga)As Heterostructure 18
2.6 Magneto Transport 20
2.7 Hall Potential Profiles 23
2.8 Microscopic Picture of the QHE 27

3 Microscope Setup and Probing Tips **29**
3.1 Probing Tips: Fabrication and Characterization 31
3.2 Microscope Setup 35
3.3 Laboratory Premises 39
3.4 Summary and Outlook 47

4 Measurement Concepts **49**
4.1 The Single-Electron Transistor as an Electrometer 50
4.2 The Coulomb Blockade Oscillation Measurement Method 55
4.3 The Feedback Loop Measurement Method 61
4.4 AC-Feedback Loop Measurement Method 68
4.5 Summary and Method Comparison 72

5 Navigation and Sample Design **75**
5.1 Navigation of the Probing Tip over the Sample Structure 76
5.2 Sample Design 80

5.3 Summary 84

6 Characterization **85**
6.1 Adjustment and Test of the Scanning System 86
6.2 Lateral Scan Range Calibration 89
6.3 Vertical Scan Range Calibration 91
6.4 Mechanical Stability 93
6.5 Spatial Resolution 97
6.6 Compensation of Magnetic-Field-Induced Mechanical Shifts 100
6.7 Remarks on the Electrical Characterization 104
6.8 Electrical Signal Stability 105
6.9 Electrical Signal Sensitivity 109
6.10 Working Temperature 113
6.11 Summary and Judgment on Use for the Fractional Quantum Hall Effect 116

7 Tip-Sample Compensation Voltage **119**
7.1 Distance Dependence of the Compensation Voltage 120
7.2 Compensation Voltage Shifts over Different Sample Surface Configurations 122
7.3 Simulation of Distance Dependent Compensation Voltage Shifts . . 126
7.4 Simulation of Correlated SET Current Jumps 128
7.5 Summary 130

8 Potential Probing of a Buried Electrode Structure **131**
8.1 Complications Probing a Two-Dimensional Electron System in a (Al,Ga)As Heterostructure 133
8.2 Capacitive Coupling between SET Island and a Buried Electrode Structure 135
8.3 z-Calibration over a Buried 2DES 138
8.4 Potential Distribution over a Buried Periodic Electrode Structure . . 140
8.5 Distortion of the 2DES by the Probing Tip 143
8.6 Probing Technique for Current Induced Electrostatic Potential Distributions 144
8.7 Summary 149

9 Hall Potential Profiles **151**
9.1 Hall Bar Characterization 152
9.2 Surface Homogeneity of the Investigated Sample Area 154
9.3 Tip-Sample Compensation 156
9.4 Line Scans - Raw Data and Resulting Calibrated Potential 157
9.5 Hall Potential Profiles at $\nu = 4$ 159

9.6 Summary 164

10 Summary and Outlook **167**

11 Zusammenfassung **175**

Appendix **183**

A Used and Developed Software **183**
A.1 Simulation of Electrostatic Potentials and SET Current 183
A.2 Developed Measurement Software 186

B New Head for Microscope Rod **189**

C Further Measurements and Simulation **193**
C.1 Strange SET Current Modulation Behavior 193
C.2 High Resolution Area Scans 195
C.3 Different Excitation Amplitudes for the Temperature Measurement 197
C.4 Resolution Comparison Between CBO and FBL Method 198
C.5 Electrostatic Potential Area Scan for Different Sample Potential with the CBO Method 199
C.6 Mechanical Induced Alteration of a Metal Electrode 200
C.7 Tip-Sample Compensation by FBL Method 202
C.8 Decay of Potential Modulation 203
C.9 α- and β-Trace of Potential Profile Measurements 204
C.10 Signal-to-Noise Ratio 205

D Laboratory Premises **207**
D.1 Image of the Electrical Setup used for the SPM 207
D.2 Image of Investigated Sample 209
D.3 Image of Ultra High Vacuum System for SET Fabrication 210

Bibliography **212**

List of Symbols and Abbreviations

Abbreviations

2DES	two-dimensional electron system
AC-FBL	feedback loop with direct and alternating current
AFM	atomic force microscope
α-trace , β-trace	measurement traces with (α) and without (β) current driven through the sample, necessary to get a calibrated Hall potential
AP	positioners from Attocube
CBO	Coulomb blockade oscillation
COM	common voltage changing the potential of source and drain contact on an SET
const	arbitrary constant value
D	drain electrode
DAC	digital-analog converter
Env	environment
FBL	feedback loop
FIB	focused ion beam
G	gate electrode
GPIB	general purpose interface bus
HF	high frequency
MBE	molecular beam epitaxy
measkern	C++ and Python based measurement software
measpy	Python based extension of measkern
PID	proportional integral differential
RC	element consisting of a capacitor and a ohmic resistor
RIE	reactive ion etching
S	source electrode
SEM	scanning electron microscopy
SET	single-electron transistor
STM	scanning tunneling microscope
SNR	signal-to-noise ratio
TBUI	text-based user interface

(N,N+1)	transition between the charge states with N and N+1 additional electrons on the SET island

Physical / Mathematical Constants

e	elementary charge
ϵ_0	vacuum permittivity
Φ_0	magnetic flux quantum
h	Planck's constant
π	ratio of a circle's circumference to its diameter
$\hbar$	reduced Planck's constant $\hbar = h/2\pi$
k_B	Boltzmann constant
μ_0	vacuum permeability
m_e	electron mass in vacuum

Chemical Elements

Al	aluminum
As	arsenide
Au	gold
Ga	gallium
He	helium
^{3}He	helium isotope with three nuclei
^{4}He	helium isotope with four nuclei
$\mathrm{Al}_\gamma\mathrm{Ga}_{1\text{-}\gamma}\mathrm{As}$	aluminum gallium arsenide with a percentage of $\gamma \cdot 100\%$ gallium atoms being replaced by aluminum
(Al,Ga)As	atomic layer sequence of $\mathrm{Al}_\gamma\mathrm{Ga}_{1\text{-}\gamma}\mathrm{As}$ and GaAs

Symbols

a	acceleration, area element
A	area of a plate-type capacitor
$A_\mathrm{a}, A_\mathrm{v}, A_\mathrm{e}$	acceleration, velocity and elongation amplitude in a harmonic oscillation
$B, \vec{B}$	magnetic field, magnetic field vector
B_ν	magnetic field for specific, certain integer filling factors ν
B_i, B_f	initial magnetic field, final magnetic field
C_i	partial capacitance between SET island and surrounding electrodes i
C_S	partial capacitance between SET island and SET source electrode
C_D	partial capacitance between SET island and SET drain electrode
C_sample	partial capacitance between SET island and sample electrode
C_Env	partial capacitance between SET island and environment
C_Σ	total capacitance of the SET island
$D(\varepsilon)$	density of states
d	distance between the plates of a plate-type capacitor
d_1, d_2	distance between SET island and surface electrode, distance between SET island and buried electrode
E	vibration energy
E_barrier	electrostatical energy barriers to charge or discharge the SET island
$\Delta E(N, V_i)$	charging energy for changing from (N-1) to N electrons on an SET island
E_C	single-electron charging energy
$E_\mathrm{el\text{-}stat.}(N, \{V_i\})$	total electrostatic energy of N electrons on the SET island for given electrode potentials
$\vec{E}$	electric field vector
ε	energy of an electron
ε_F	Fermi energy
ε_i^z	energy level of the i-th subband in the 2DES confinement potential
ε_n^Σ	energy level including subband energy, cyclotron energy, Zeeman energy
ϵ_r	dielectric constant
F	force
f	frequency
f_a, f_b, f_c	fit parameters

$G, G_{\max}$	conductance, conductance peak height
g^*	effective Landé factor
i, j	integer count variables
$\vec{j}, j_i$	current density vector and current density vector components i
I_{SET}	electric current through the SET
$I_{\mathrm{D}}, I_{\mathrm{S}}$	electric drain current, electric source current
$I_{\mathrm{d}}^{DC}, I_{\mathrm{d}}^{AC}$	direct, alternating current drain current
$I_{x,\mathrm{net}}$	net current, additional current beside the diamagnetic currents in the incompressible stripe
$\vec{k}, k_j$	momentum vector and momentum vector components j
k	integer count variable for the incompressible stripes in a 2DES
κ	compressibility of the 2DES
l	distance between the side contact pairs along the 2DES
M	arbitrary N, representing the number of electrons on a SET island
m^*	effective electron mass
m	mass
N	number of electrons added to an electric neutral SET island
n	integer counting variable for the harmonic oscillator eigenstates
$\vec{n}$	normal unit vector
n_s	electron density in 2DES
N_s	number of electrons in a certain 2DES area
n_L	degeneracy of the different Landau levels
ϕ	electrostatic potential
$\phi_{\mathrm{island}}, \phi_{\mathrm{i}}$	electrostatic potential of the SET island
$\phi_s(r)$	electrostatic sample potential over position $\vec{r}$
$\Delta\phi_{\mathrm{i}}$	shift of electrostatic SET island potential
$\phi_{\mathrm{i}}^{\mathrm{isol}}$	electrostatic potential of an isolated SET island
Φ	number of magnetic flux quanta in a certain 2DES area
Q_{island}	charge located on the SET island
$Q^{ind}, Q_{\mathrm{island}}^{ind}$	induced charge on the SET island
$Q_{\mathrm{island}}^{ind,vir}$	virtually induced charge on the SET island
$Q_{\mathrm{island}}^{surplus}$	surplus charge, charge following ϕ_{i}
Q_{q}	charge on the sample surface
$Q_{\mathrm{i,\,q}}^{ind,vir}$	virtually induced charge on SET island by Q_{q}
Q_0	initial charge on SET island
Q_{Env}^{ind}	charge induced on SET island by the environment
q	electric charge
$\vec{r}$	position vector
R	absolute value of the lock-in amplifier signal

R_{Hall}	Hall resistance, transversal voltage over current
R_{long}	longitudinal resistance
$\vec{\rho}, \rho_{xx}, \rho_{xy}$	resistivity tensor of second order, diagonal component of the resistivity tensor, non-diagonal component of the resistivity tensor
S	border of an area element
s	spin
T	temperature
τ	mean scattering time
t	time
Θ	phase of the lock-in amplifier signal
μ	electron mobility
μ_B	Bohr magneton
μ_{ch}	chemical potential
μ_{elch}	electrochemical potential
V_i	electrostatic potential of electrode i
V_{S}	source potential
V_{D}	drain potential
V_{long}	longitudinal voltage drop
V_{Hall}	Hall voltage
V_{SD}	source-drain voltage
V_{sample}	sample voltage
V_{Env}	electrostatic potential of the environment
$V_{\text{AC}}(t), \hat{V}_{\text{AC}}$	alternating voltage signal, voltage amplitude
$V_{\text{AC,COM}}$	voltage amplitude in β-trace measurement
V_{ref}	reference voltage
$V_{\text{DC,Offset}}$	constant offset voltage
V_{G}	gate voltage
v	velocity
V_{com}	common voltage applied to source and drain electrode
$V_{\text{sam-i}}$	voltage applied to the i-th sample electrode
V_{period}	voltage change on the sample electrode needed to add one additional electron onto the SET island and obtaining the same resonance condition for electrical transport
ν	Landau level filling factor
w	Hall bar width in the area between the side contact pairs
ω_c	cyclotron frequency
x_i, x_f	initial x-position, final x-position
z_i, z_f	initial z-position, final z-position
x, y, z	general Cartesian spatial coordinates
$(\vec{x}_{\text{s}}, \vec{y}_{\text{s}}, \vec{z}_{\text{s}})$	Cartesian coordinate system of the sample
$(\vec{x}_{\text{i}}, \vec{y}_{\text{i}}, \vec{z}_{\text{i}})$	Cartesian coordinate system of the SET island
$(\vec{x}_{\text{t}}, \vec{y}_{\text{t}}, \vec{z}_{\text{t}})$	Cartesian coordinate system of the piezo scanning tube

1 Introduction

In 1879 the American physicist E. H. Hall [1] discovered that an electric current through a metal sheet in a magnetic field produces a voltage perpendicular to the electric current direction. Dividing this voltage by the applied current gives the Hall resistance. This resistance shows a linear dependence versus the applied magnetic field.

In 1980 Klaus von Klitzing (Nobel Prize awarded 1985) observed a non-linear behavior of the Hall resistance in a two-dimensional electron system in silicon field effect transistor samples at very low temperature and high magnetic field and recognized the significance of this observation [2]. This effect is called the quantum Hall effect (QHE) due to the fact that it shows quantized resistance plateaus at values described by an integer division of the von-Klitzing constant defined by

$$R_{\mathrm{K}} = \frac{h}{e^2} \tag{1.1}$$

where h is the Planck constant and e the electron charge.

Just two years after the discovery of the integer quantum Hall effect, further resistance plateaus were recorded by D. C. Tsui and H. L. Störmer [3] at even lower temperatures with samples showing much higher charge carrier mobilities. Together with R.B. Laughlin [4] they received the Nobel Prize in 1998. The effect exhibiting those additional resistance plateaus is called the fractional quantum Hall effect due to its fractional division of the von-Klitzing constant for its resistance values.

The quantization is independent of the sample material and geometry and therefore is used as the resistance standard in metrology. As a consequence the value of the von-Klitzing constant was defined to $R_{\text{K-90}} = 25\,812.807\,\Omega$ in 1990. The quantum Hall effect nowadays enables the conversion of the base of the international system of units to natural constants [5]. Together with the Josephson effect

it links the definition of the kilogram to the Planck constant h by the use of a Watt balance [6–10].

For a fundamental understanding of the accuracy of the QHE a microscopic understanding of the effect is essential. Scanning probe experiments [11–20] have been performed to determine the Hall potential profile and therefore the current distribution for a 2DES in the quantum Hall regime. Most experiments were limited to temperatures above 1 K and thereby investigated only the integer quantum Hall effect.

Further experiments were done with metallic single-electron transistors (SET) as a highly sensitive electrometer implemented directly on the surface of the sample [21–26]. Nevertheless, this approach distorts the electron system underneath the SET structure due to contact voltages and mechanical strain. Other groups have built scanning SET microscopes but are either working at temperatures around 0.8 K [27, 28] or have to apply large voltages to form their SET in a single-walled carbon nanotube [29].

Also scanning gate microscopes were set up [30–32] to affect the electrical transport through a quantum point contact in the integer and fractional quantum Hall regime. Those microscopes are strongly invasive on the electron system because they intentionally disturb the electrostatic potential of the sample at different spots and conclude results from the integral conductance of the sample.

The task of this PhD thesis was to set up a scanning probe microscope able to measure Hall potential profiles on a two-dimensional electron system in the fractional quantum Hall regime. The microscope should work reliably at temperatures below 0.1 K and in high magnetic fields up to 18 T, and have a probing tip sensitive to potential variations in the range of few 100 µV. Furthermore, the probing tip should almost not disturb the two-dimensional electron system due to its presence. Therefore, a dilution refrigerator was installed in a new highly vibration damped laboratory. A unique characteristic of the microscope is the one-dimensional array of eight tip-like single-electron transistors used as highly sensitive electrometers. An extensive experimental characterization of the microscope and electrostatic simulations of the SET-sample configuration were required to understand the interaction and the conditions for a non-invasive behavior. To demonstrate the capabilities of the microscope a high mobility (Al,Ga)As heterostructure was used to probe the Hall potential profiles of an integer quantum Hall state.

Due to the large scope of the project, the thesis is structured into ten parts:
Chapter 2 presents the essentials of a metallic single-electron transistor and describes the present microscopic picture of the integer quantum Hall effect.

In **chapter 3** the microscope setup and its probing tips will be presented briefly even though the construction and fabrication presented a major part of this PhD work.

Methods of measuring electrostatic potential distributions on the sample by a scanning SET tip will be explained in **chapter 4**, and important aspects of the SET-sample interaction will be discussed.

In **chapter 5** the sample design will be introduced allowing to navigate the probing tips to the spot of interest, in our case a certain cross section of a Hall bar.

An extensive characterization of the microscope concerning mechanical properties and electrical probing sensitivity will be presented in **chapter 6**.

In **chapter 7** the investigation of a simple gold electrode will show the complexity one faces in finding the right bias voltage to compensate for a possible work function difference between sample and SET tip.

In **chapter 8** aspects of probing the electrostatic potential distribution of an electrode structure buried under dielectric layers like our 2DES embedded in an (Al,Ga)As heterostructure, will be simulated and discussed in comparison with the simpler arrangement of an electrode structure on the surface.

First, Hall potential profiles measured around an integer Landau level filling factor with this microscope will be presented in **chapter 9**, verifying the functionality of the microscope and showing the Hall potential distribution with significantly improved electrical sensitivity compared to previous measurements [16].

Chapter 10 will give a summary and outlook on the measurements done with this microscope and future measurement opportunities enabled by the microscope.

In the **Appendices**, supplementary information will be provided.

2
Theoretical Basics

This chapter serves to give an overview about the theoretical background for the two main topics, the probing device - a single-electron transistor (SET), and the evolution of the Hall potential profile in a two-dimensional electron system (2DES) over a quantum Hall plateau. Therefore, the chapter is split into two parts, firstly, introducing the metallic single-electron transistor, secondly, explaining the relevant aspects about the quantum Hall effect.

I The Single-Electron Transistor (SET)

The single-electron transistor (SET) is like the field effect transistor a device in which the electrostatic potential of a gate electrode influences the conductance from source to drain electrode through the device. Although in both devices an energetic barrier is controlled by the gate, there is a significant difference in the working concept and the resulting electrical characteristic between the two. The gate electrode in the field effect transistor changes the conductance by continuously increasing the charge carrier density in the channel between source and drain. In contrast the working mechanism of a single-electron transistor is based on the quantization of charge by electrons. Due to the necessary Coulomb energy for charging a tiny quasi-isolated island between source and drain, an electrostatic energy barrier is present which may block the electric transport through the device. Thus, for small source-drain voltages and low temperature just certain gate potential values allow single-electron tunneling from one side of the device towards the other. This single-electron transport was theoretically described in 1986 by D. V. Averin and K. K. Likharev [33] and first experimentally realized just a year later by T. A. Fulton and G. J. Dolan [34].

In this thesis the single-electron transistor is used as a local probing device to sense electrostatic potential variations (electrometer [21,25,27,28,35,36]) of a 2DES under quantum Hall condition. This will be done by using the 2DES as a gate electrode for the SET and record variations in the 2DES potential by observing a change in the electric current flow through the SET. In the following sections the basic physical properties and characteristics of a metal single-electron transistor are explained. This is the base to understand in the following chapters how the SET is used as probing sensor.

For further interest the reading of [37,38] is recommended.

2.1 Electrostatics and Energy Scheme of an SET

In this part we will do a purely electrostatic consideration of a metallic single-electron transistor. It consists of a metallic island, which is quasi-isolated by tunnel barriers towards the source and towards the drain electrode. The schematic structure of an SET is shown in Figure 2.1 (a) and the equivalent electric circuit is schematically shown in (b). Further, a gate electrode and electrodes in the near environment can couple capacitively to the island.

The total capacitance C_Σ of the SET island is given by a summation over all partial capacitances C_i between SET island and the surrounding electrodes denoted by

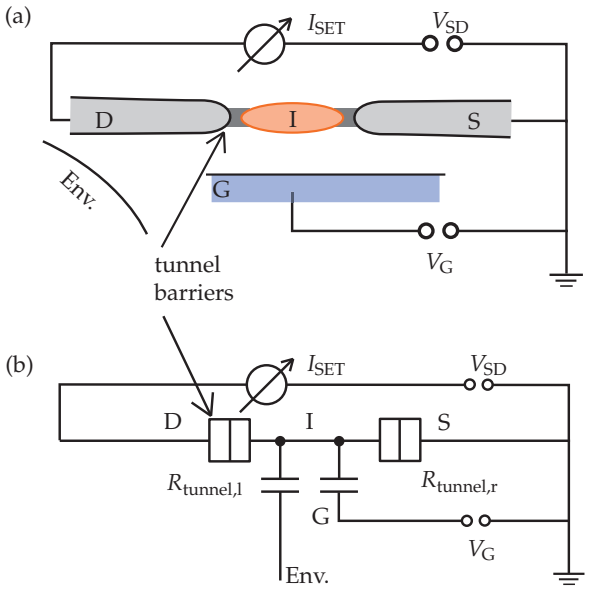

Figure 2.1:
(a) Schematic arrangement of a single-electron transistor (SET), consisting of a quasi-isolated island connected via tunnel barriers to the source and drain electrode. A source-drain voltage V_{SD} is applied to the SET structure and the electric current through the device I_{SET} is measured. An electrode on the surface of the sample can be used as a gate electrode influencing the electrostatic potential of the SET island by its applied gate voltage V_G. Further electrodes in the near environment (Env.) of the SET island can also influence the electrostatic potential of the SET island. (b) Equivalent electrical circuit for an SET applying a source-drain and a gate voltage while measuring the electric current through the SET.

i. The electrostatic potential of the island depends on two terms, the number of electrons N added to the electrically neutral island and the electrostatic influence by the electrodes' potentials V_i and is expressed by

$$\phi_{\text{island}} = -\frac{N \cdot e}{C_\Sigma} + \sum_{i \in \text{electrodes}} \frac{C_i}{C_\Sigma} V_i. \tag{2.1}$$

The total electrostatic energy for charging an electrical neutral island with N electrons is calculated by an integration of the work $\phi_{\text{island}}(q) \cdot \mathrm{d}q$ needed to add a tiny fraction of charge $\mathrm{d}q$ to the island while the charge q is already present on the island

$$\begin{aligned} E(N, \{V_i\}) &= \int_0^{-e \cdot N} \phi_{\text{island}}(q) \mathrm{d}q \\ &= \frac{(N \cdot e)^2}{2C_\Sigma} - N \cdot e \sum_{i \in \text{electrodes}} \frac{C_i}{C_\Sigma} \cdot V_i. \end{aligned} \tag{2.2}$$

Note, this relation is valid for electrons taken from an electrode with an electrostatic potential equal to zero. To charge the SET island from this state of N electrons with one further electron costs the charging energy

$$\begin{aligned} \Delta E(N+1, \{V_i\}) &= E(N+1, \{V_i\}) - E(N, \{V_i\}) \\ &= (2N+1) \frac{e^2}{2C_\Sigma} - e \cdot \sum_{i \in \text{electrodes}} \frac{C_i}{C_\Sigma} \cdot V_i. \end{aligned} \tag{2.3}$$

The energy difference between two sequential charging energies, for instance $\Delta E(N, \{V_i\})$ and $\Delta E(N+1, \{V_i\})$, is given by $E = e^2/C_\Sigma$. In Figure 2.2 the energy scheme for a source, drain, island configuration with zero source-drain voltage is shown. On the island, charged with N electrons, the last filled charging energy level $\Delta E(N, \{V_i\})$ and the first empty charging energy level $\Delta E(N+1, \{V_i\})$ both with equal distance to the Fermi level of the source and drain electrode are plotted. In this case the energy barriers for charging {1} or discharging {2} the SET island by a single electron from the source and to the drain electrode equals

$$E_C = \frac{e^2}{2C_\Sigma}. \tag{2.4}$$

This energy is called the single-electron charging energy[1] and is a property of the SET, depending on the island size, shape and the capacitive arrangement around it.

[1] Sometimes e^2/C_Σ is called the single-electron charging energy.

The energy barriers can be overcome either by a change in the drain potential (source fixed to ground level) or by thermal excitation. If a charging energy $\Delta E(N+1, \{V_i\})$ is energetically accessible by one of those options and a source-drain voltage is applied, electrical transport through the SET becomes possible. Knowing the tunnel barrier resistance values, the dynamics and therefore the current-voltage characteristic can be calculated by a master equation approach [37].

To obtain a well expressed current-voltage characteristic for the SET with a well defined Coulomb blockade regime, the conditions

$$k_B T \ll E_C \qquad \text{and} \qquad \{R_T^{(S)}, R_T^{(D)}\} \gg \frac{h}{e^2} \tag{2.5}$$

have to be fulfilled. In this thesis the single-electron charging energy of the different SETs, used to execute the measurements, was at best to about 0.27 meV. Therefore, a dilution refrigerator [39] with a base temperature in the mK-range ($k_B T < 9\,\mu eV$) has to be used.

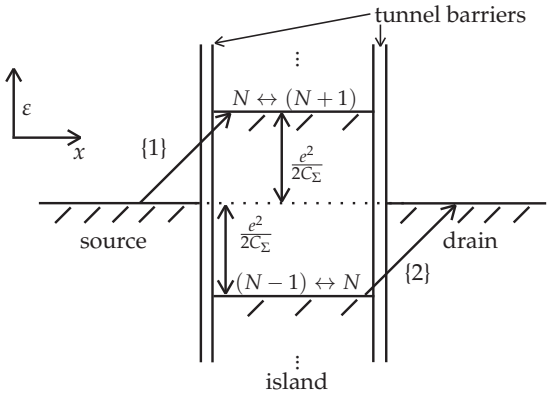

Figure 2.2:
Energy level scheme of an SET. The Fermi level of the source and drain contact as well as the different charging threshold levels of the SET island are marked. In this case the two charging energies $\Delta E(N, \{V_i\})$ and $\Delta E(N+1, \{V_i\})$ are symmetrically arranged around the Fermi levels of source and drain. Therefore, the energy barrier to charge {1} or discharge {2} the SET island by a single electron is the same, the so-called single-electron charging energy $E_C = e^2/2C_\Sigma$.

2.2 Electric Current versus Source-Drain Voltage Characteristic of an SET

The charging and discharging of the island is blocked if the electrons are not respectively excited. Thereby we obtain the so-called Coulomb blockade for very low temperature. An electric current flow through the SET is only possible if the condition

$$-eV_S \geq \Delta E(V_i) \geq -eV_D \tag{2.6}$$

is fulfilled with the source potential fixed to ground in our case. In this relation we have to be aware that the charging energy ΔE also depends on the drain potential V_D and is thereby shifted if the drain potential changes.

An electric current versus applied source-drain voltage characteristic of an SET and the different corresponding energy level schemes are shown in Figure 2.3 for $T = 0\,\mathrm{K}$. Further, equal capacitive coupling from the SET island to the source and to the drain electrode and a negligible partial capacitance to the gate are assumed. In the first configuration (Figure 2.3 (a)) the relation (2.6) is not fulfilled. Therefore, no electric current can flow through the SET and we are in the Coulomb blockade regime.

In configuration (b), (2.6) is just fulfilled because $\Delta E(N, V_i) = -eV_D$. The transport happens by single electrons tunneling onto the SET island from the source electrode and leaving the SET island towards the drain electrode. The tunneling process is an elastic process, meaning there is no energy loss during the tunneling resulting in a horizontal transition in the energy level schemes. Though there can be relaxation processes available on the electrodes and on the SET island. For $T > 0\,\mathrm{K}$ the thermal fluctuations already enable a finite electric current flow through the device before configuration (b) is reached with the applied source-drain voltage.

Increasing the source-drain voltage further we end up in the last configuration (c) with (2.6) fulfilled. Therefore, an electric current flow through the device caused by single electrons passing at a time is possible. Further increasing the source-drain voltage raises the number of available electron states to tunnel through the barriers, therefore, the electric current through the device increases.

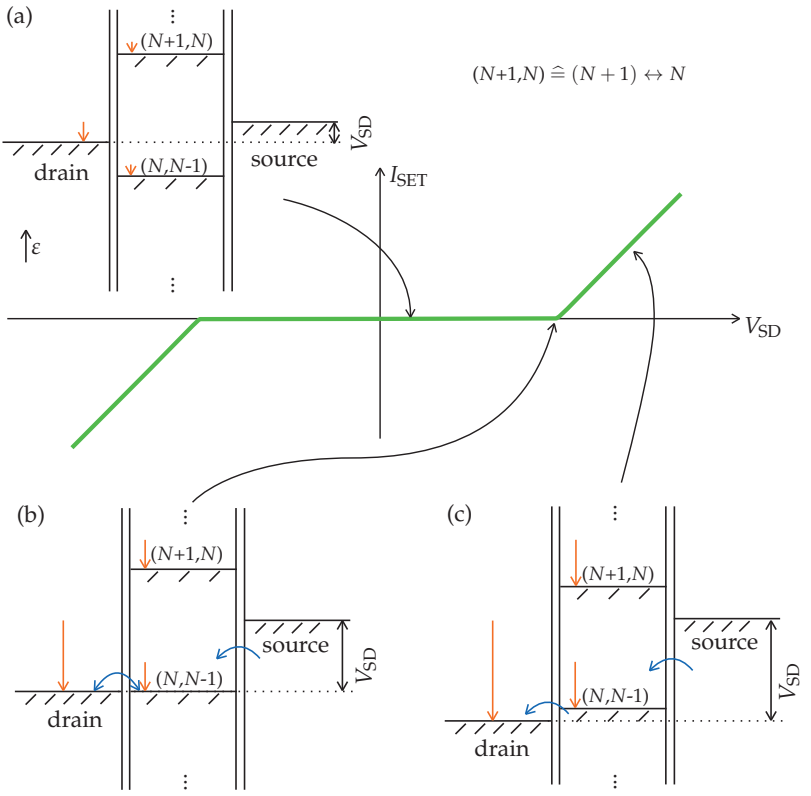

Figure 2.3:
Electric current versus applied source-drain voltage characteristic of an SET with corresponding energy level schemes. The red arrows indicate the shift of the different Fermi levels due to an applied source-drain voltage. (a) The applied source-drain voltage is not sufficient to allow the island to change between different charge states. Therefore, the electric current through the SET is equal to zero. This condition is called the Coulomb blockade regime. (b) The Fermi level of the drain contact lies on the same energy level as the charging energy $\Delta E(N, V_i)$. In this case the transport through the SET just starts for $T = 0\,\mathrm{K}$. Thermal fluctuation would, however, enable an electric current already for smaller source-drain voltages. (c) One charging energy threshold level lies between the source and drain Fermi levels, therefore, the island can change its charge state. This allows an electric current through the SET by charging from from the source side and discharging to the drain side.

2.3 Electric Current versus Gate Voltage Characteristic of an SET

Besides the source-drain voltage also an applied gate voltage can shift the charging energy levels $\Delta E(V_i)$ on the energy scale. With a small source-drain voltage applied to the SET we can change between Coulomb blockade and single-electron tunneling regime for a changing gate potential. Again transport is only possible if the condition (2.6) is fulfilled. The electric current versus gate voltage characteristic of an SET is shown in Figure 2.4 for zero temperature. The Coulomb blockade regime in which no current is flowing through the SET is shown by (a) and (c). Single-electron tunneling and therefore a current peak is possible in configuration (b). The periodicity for the current peaks versus gate potential can be derived by assuming the same resonance condition for two different charge states of the SET island caused by the gate voltage change ΔV_G i.e. $\Delta E(N+1, V_G) = -eV_S$ and $\Delta E(N, V_G + \Delta V_G^p) = -eV_S$ resulting in $|\Delta V_G^p| = e/C_G$.

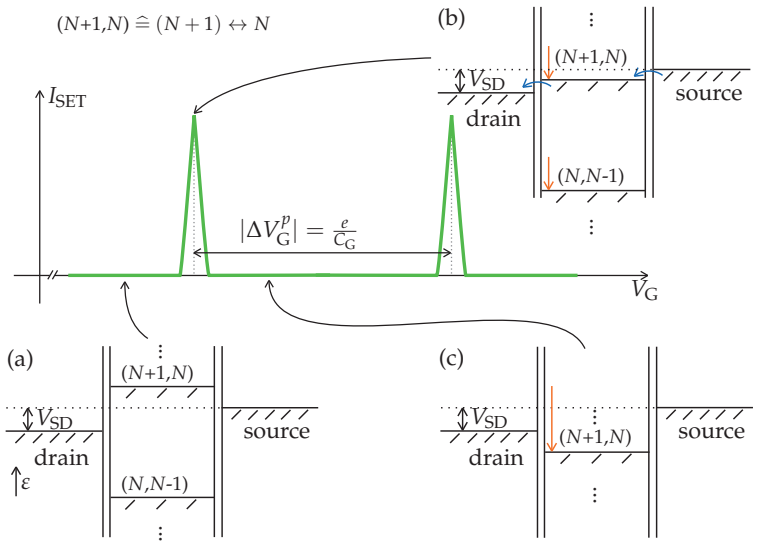

Figure 2.4:
Electric current versus gate voltage characteristic of an SET. The gate voltage shifts the energetic position of the charging energy threshold levels $\Delta E(\{V_i\})$ on the SET island. (a), (c) Coulomb blockade regime in which no charging energy level lies between source and drain potential. Thus, no current flows through the SET. (b) Due to a specific gate potential one charging energy level is shifted between source and drain Fermi level allowing single-electron transport.

2.4 Charge Stability Diagram

Figure 2.5 shows the charge stability diagram i.e. the charge states of the SET island that are energetically accessible for certain combinations of V_{SD} and V_G. In the Coulomb blockade regime, marked in white, all electrical transport through the SET is blocked and the inequation

$$\Delta E(M+1, V_i) > 0 = -eV_S > -eV_D > \Delta E(M, V_i), \tag{2.7}$$

is valid with M representing an arbitrary N. The light gray areas represent the single-electron tunneling regime for which the relation

$$0 = -eV_S \geq \Delta E(M, V_i) \geq -eV_D, \tag{2.8}$$

is fulfilled. If the source-drain voltage is further increased multi-electron tunneling becomes possible (dark gray), fulfilling the relation

$$0 = -eV_S \geq \{\Delta E(M+1, V_i); \Delta E(M, V_i); ...\} \geq -eV_D. \tag{2.9}$$

The borderlines between the different configurations of energetically accessible charge states are derived in [37] and the slopes are expressed by

$$\frac{\partial V_G}{\partial V_{SD}} = -\frac{C_D}{C_G} \tag{2.10}$$

$$\frac{\partial V_G}{\partial V_{SD}} = \frac{C_\Sigma - C_D}{C_G}. \tag{2.11}$$

With those relations the partial capacitances between SET island and source, drain electrode can be experimentally determined. Figure 2.5 shows the case of symmetric, dominating partial capacitances toward the source and drain electrodes. If this would not be the case the descending and ascending lines would have different absolute values for their slopes.

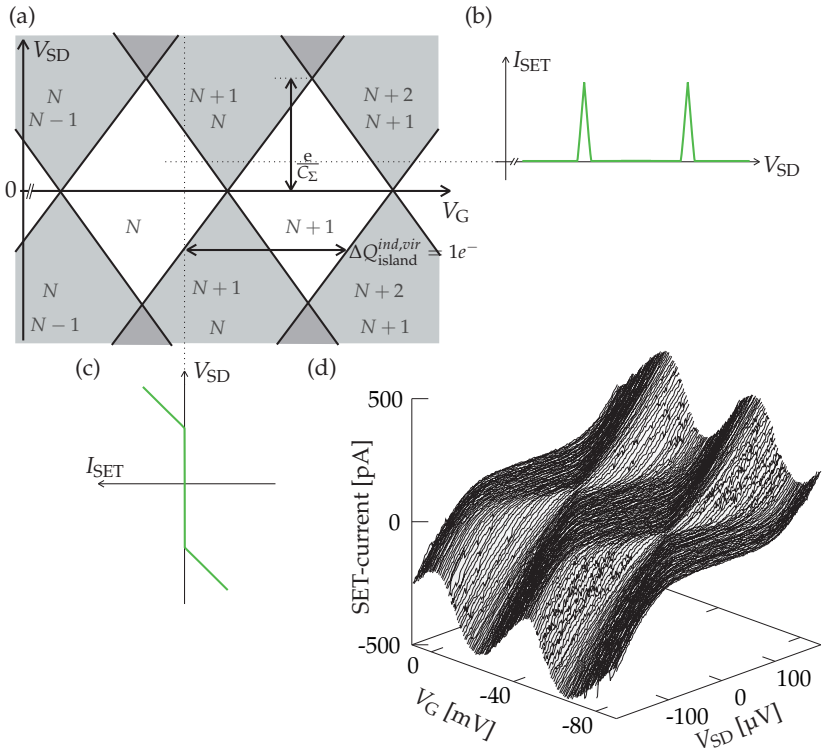

Figure 2.5:
(a) Charge stability diagram showing the different allowed charge states for the island over source-drain and gate voltage ranges. The white areas represent the Coulomb blockade regime in which the current through the SET is blocked. The light gray areas mark the voltage range for which a current carried by single-electron tunneling is present. The dark gray areas stand for the multi(=2)-electron tunneling regime. (b) Expected current modulation along the gate voltage axis for fixed V_{SD}. (c) Expected current characteristic along the source-drain voltage axis for fixed V_G. (d) Pseudo three-dimensional plot of the measured current through an SET versus applied source-drain and gate voltage.

II Two-Dimensional Electron System (2DES) in High Magnetic Fields

If the Hall effect is probed in two-dimensional, high mobility electron systems at low temperatures just some Kelvin above absolute zero, the Hall resistance curve shows quantized plateaus. This deviation from the linear Hall resistance curve is called the quantum Hall effect. The high electron mobilities can be found in semiconductor heterostructure interfaces.

In this part we will start with the sample structure that is used in this thesis to obtain the quantum Hall effect. Afterwards we will compare the classical magneto transport with the magneto transport in the quantum Hall regime. Then previously measured Hall potential profiles and the resulting microscopic picture of the quantum Hall effect will be presented.

The aim of this part is to come to the point that the reader understands the characteristics of the quantum Hall effect, the Hall potential profiles and the thereby linked electric current distribution. For further reading, the references [40,41] are recommended.

2.5 2DES Embedded in an (Al,Ga)As Heterostructure

To obtain a two-dimensional electron system with a very high mobility $\mu = e\tau/m^*$ we can use a material with a low effective electron mass m^*. Further, we need a structure with a low concentration of imperfections to avoid scattering centers and to raise the mean scattering time τ.

A heterostructure made of $Al_\gamma Ga_{1-\gamma}As$ and GaAs layers can provide both [42, 43]. The effective mass of GaAs is $m^* = 0.067 m_e$ [44] while m_e is the free electron mass. By molecular beam epitaxy, very homogeneous layers of predetermined thickness of (Al,Ga)As can be grown. The heterostructure used in this thesis is shown in Figure 2.6 [2].

On a GaAs substrate a layer lattice consisting of GaAs and $Al_\gamma Ga_{1-\gamma}As$ was grown to smoothen the surface. On top, an undoped GaAs layer of 1 µm follows that includes the two-dimensional electron system (2DES) at the interface to the next layer made of $Al_\gamma Ga_{1-\gamma}As$. The electrons are trapped in the triangular

[2] The wafer material was grown by Dr. C. Reichl in the group of Prof. Dr. W. Wegscheider and organized by Dr. W. Dietsche. The values for the used heterostructure are $\mu \approx 8.9 \times 10^6\,\mathrm{cm}^2/\mathrm{Vs}$, $n_s \approx 2.0 \times 10^{11}\,/\mathrm{cm}^2$.

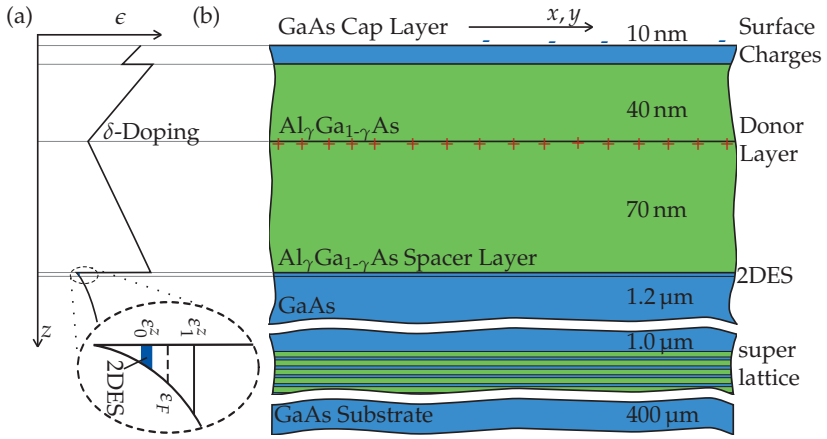

Figure 2.6:
Modulation doped (Al,Ga)As heterostructure with corresponding band bending scheme. (a) Profile of the conduction band minimum through the layers with 2DES present in the triangular shaped confinement at the GaAs to $Al_\gamma Ga_{1-\gamma}As$ interface. (b) Layer scheme with thickness and material information.

shaped confinement potential resulting from the band bending at the interface [45]. Nevertheless they are only confined in z-direction and can move freely in the (x, y)-plane. The $Al_\gamma Ga_{1-\gamma}As$ layer above this heterostructure interface separates the silicon donor layer, providing the electrons for the 2DES, from the 2DES. Therefore it is called "spacer" layer [42]. On top of the doping layer another layer of $Al_\gamma Ga_{1-\gamma}As$ was grown to separate the donor layer from the surface of the sample. To avoid oxidation of this last layer a thin but sufficient cap layer of GaAs (10 nm) was deposited.

Reducing the $Al_\gamma Ga_{1-\gamma}As$ layer above the donor atoms will allow more electrons to go to the surface states and less to the 2DES which has to be compensated with more donor atoms acting ionized as scattering centers [46]. Increasing the thickness of the spacer layer is reducing the strength of the scattering centers but has again to be compensated by an increase in the number of donor atoms to achieve the same charge carrier density. With the microscope we had to compromise between the charge carrier mobility in the 2DES and the surface-2DES distance. The distance is mainly caused by the two $Al_\gamma Ga_{1-\gamma}As$ layers around the doping layer and can reduce the lateral scan resolution.

The energy of the electrons in the two-dimensional electron system and higher subbands can be described in k-space by

$$\varepsilon(i, k_x, k_y) = \varepsilon_i^z + \sum_{j \in x,y} \frac{\hbar^2 k_j^2}{2m^*}, \tag{2.12}$$

where ε_i^z describes the energy of the different subband minima i due to the spatial confinement in z [47]. Further, the electrons can be described by plane waves propagating in the (x, y)-plane and k_j are the Cartesian components of the wave vector $\vec{k}$.

A specificity of the 2DES is its constant density of states only depending on the effective electron mass [44] as the relation

$$D(\varepsilon) = \frac{m^*}{\pi\hbar^2} \tag{2.13}$$

shows. Therefore, the Fermi energy ε_F of the 2DES is proportional to the charge carrier density n_s and is described by

$$\varepsilon_F = \frac{\pi\hbar^2}{m^*} \cdot n_s. \tag{2.14}$$

2.6 Magneto Transport

If an electric current is driven through a 2DES and a magnetic field perpendicular to the 2DES is applied, a voltage drop V_{Hall} perpendicular to the electric current I and magnetic field $\vec{B}$ can be recorded. The resistance calculated by $R_{\text{Hall}} = {}^{V_{\text{Hall}}}/_{I}$ with V_{Hall} measured perpendicular to I at the sample structure is called the Hall resistance. The Hall resistance increases linearly with the magnetic field as the black curve in Figure 2.7 shows. This linear dependence can be derived classically from the Drude equation of motion [48, 49] and results in the relations

$$\rho_{xy} = \frac{E_y}{j_x} = \frac{1}{en_s} \cdot B \tag{2.15}$$

$$\rho_{xx} = \frac{E_x}{j_x} = \frac{1}{en_s\mu}. \tag{2.16}$$

In those equations E_i is the electric field component in x or y direction and j_x the electric current density in x-direction. For a homogeneous system the relations

$$R_{\text{Hall}} = \rho_{xy} = \frac{1}{en_s} \cdot B \tag{2.17}$$

$$\frac{w}{l} R_{\text{long}} = \rho_{xx} = \frac{1}{en_s\mu}. \tag{2.18}$$

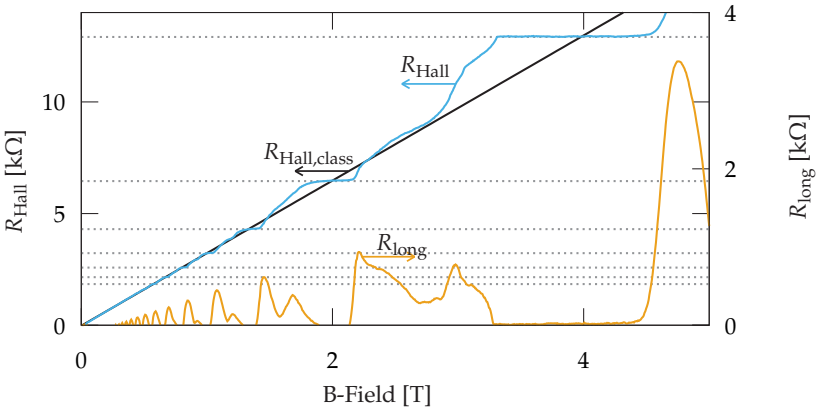

Figure 2.7:
Classical Hall resistance (black), quantized Hall resistance (blue) with according longitudinal resistance (orange). The longitudinal resistance goes towards zero while a Hall resistance plateau is present.

between the integral and local quantities are valid. Thereby the charge carrier density n_s of the 2DES determines the Hall resistance R_{Hall} slope versus magnetic field. For $B = 0$, the second equation links the charge carrier mobility μ with the longitudinal resistance R_{long} over a sample length l and a sample width w.

From the Hall resistance measurement at low temperatures (blue curve) in Figure 2.7 it is obvious that there are strong deviations from the classical Hall resistance curve. For certain magnetic field ranges the Hall resistance stays constant at quantized values and shows a plateau-like feature. During those Hall plateaus the longitudinal resistance (orange curve) goes to zero.

The quantum mechanical treatment of a single electron in a 2D plane with an perpendicularly applied magnetic field leads to eigen-energies [3], called Landau levels [50], given by

$$\varepsilon_n = \hbar\omega_c(n + \frac{1}{2}), \qquad n = \{0, 1, 2, \cdots\}, \tag{2.19}$$

where n is the Landau quantum number.

Also considering the lowest subband level energy ε_0^z of the 2DES and the Zeeman splitting the energy is given by

$$\varepsilon_{n,s}^{\Sigma}(B) = \varepsilon_0^z + \hbar\omega_c(n + \frac{1}{2}) + sg^*\mu_B B, \qquad s = \{+\frac{1}{2}; -\frac{1}{2}\}. \tag{2.20}$$

In this equation s stands for the spin, g^* for the effective Landé factor[4] and $\mu_B = {}^{e\hbar}/_{2m_e}$ for the Bohr magneton. As (2.20) shows we have for each magnetic field discrete energy levels to be filled up with electrons. Hence, the density of states is not a constant anymore, it has become a sum of δ-peaks described by

$$D(\varepsilon) = n_L \sum_{n=0}^{\infty} \sum_{s=-1/2}^{+1/2} \delta(\varepsilon - \varepsilon_{n,s}^{\Sigma}) \tag{2.21}$$

while n_L is the degeneracy of the different Landau levels. The value of the degeneracy is determined by $n_L = \frac{e}{h}B$ [47].

The Landau level filling factor ν for a homogeneous 2DES can be described by two ways. Either by the proportion between charge carrier density n_s and degeneracy n_L or by the proportion between number of electrons N_s and number of flux

[3] The cyclotron energy $\hbar\omega_c$ for GaAs is approximately 1.75 meV T^{-1} and the magnetic length l_B, a measure for the wave function extension, is approximately 26 nm at 1 T.

[4] The Landé factor is affected by electron-electron interactions and is depending on the magnetic field and the Landau level filling factor. It can vary from -0.44 to -6 [51–53].

quanta Φ/Φ_0 of the magnetic field in the same sample area

$$\nu \equiv \frac{n_s}{n_L} = \frac{h}{e} \cdot \frac{n_s}{B}, \qquad \nu = \frac{N_s}{\Phi/\Phi_0}. \tag{2.22}$$

To describe now the value of the quantized Hall resistance around certain magnetic fields we take the classical equation (2.17) for R_{Hall} and apply the equation (2.22) for the electron density to get

$$R_{\text{Hall}} = \frac{h}{e^2\nu} \qquad \text{for} \qquad B_\nu = \frac{h}{e} \cdot \frac{n_s}{\nu}. \tag{2.23}$$

This equation corresponds to the quantized values of the Hall plateau measured, but presents in this consideration only single points on the classical Hall resistance curve.

The equation 2.23 is only valid for a homogeneous 2DES but we will see that this assumption of a homogeneous system is not valid. The extension of those resistance values to a resistance plateau versus magnetic field and the vanishing longitudinal resistance will be explained in the following sections with the microscopic picture of the quantum Hall effect.

2.7 Hall Potential Profiles

Due to the interest to find out the electric current distribution in a 2DES in the quantum Hall regime and thereby get a microscopic picture of the effect, measurements with scanning force microscopes were executed by K.L. McCormick et al. 1999 [11] and in the following years by Peter Weitz and Erik Ahlswede [13–15, 54]. The results for filling factor $\nu = 4$ are shown in Figure 2.8. In those measurement results we can see that the potential drop across the 2DES is non-linear. The

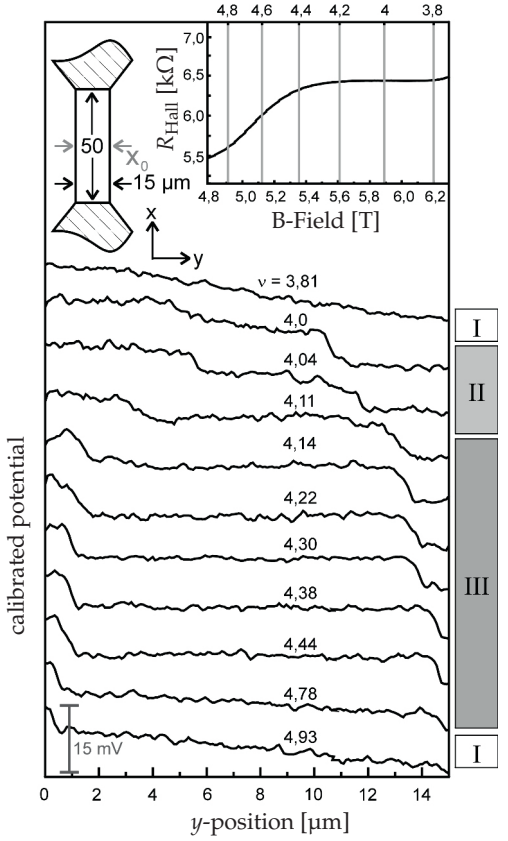

Figure 2.8:
Evolution of the calibrated Hall potential profile for filling factors around $\nu = 4$, adapted from [16].

position of the potential-drop depends on the magnetic field and shifts obviously from the edge towards the center of the sample, the so-called bulk, for an increase in the magnetic field until the Hall potential drop is broadly, linearly distributed over the whole Hall bar width.

To understand this behavior of the Hall potential drop we can first look at an equilibrium situation. Chklovskii et al. [55] and separately Kane [56] calculated analytically a gate induced depletion region of a 2DES in high magnetic field with a self-consistent treatment of the electrostatic potential. Lier and Gerhardts [57] calculated the same configuration numerically considering a constant electrochemical potential, this results in great accordance to Chklovskii et al.. The resulting profile of the Landau level bending and of the charge carrier density starting from the border of the depletion region into the bulk of the 2DES are shown in Figure 2.9. From the edge towards the bulk of the 2DES different stripes can be distinguished. The first stripe is completely depleted and the lowest Landau level approaches the electrochemical potential from above. If the first Landau level reaches the energy level of the electrochemical potential it stays constant and the charge carrier density increases. The stripes in which the charge carrier density changes will further on be called "compressible" stripes. This naming indicates the possibility to change the charge carrier density with only small energetic effort, therefore, further electrons can be added to the 2DES and it behaves compressible. If the first Landau level is completely filled up the charge carrier density stays

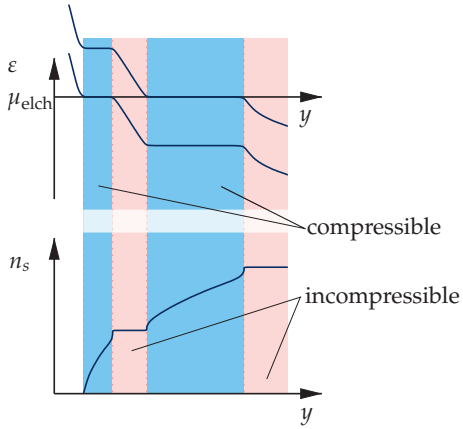

Figure 2.9:
Landau level position in correlation to the electrochemical potential and electron density n_s versus distance to the 2DES edge adapted from [58].

constant until the second Landau level is touching the electrochemical potential energetically and so on. To put an additional electron into a stripe with constant charge carrier density a lot of energy is required to reach the next higher Landau level. Therefore, those stripes are called "incompressible". The compressibility κ in general is defined by [59, 60]

$$\frac{1}{\kappa} = n_s^2 \cdot \left(\frac{\partial \mu_{\mathrm{ch}}}{\partial n_s} \right). \tag{2.24}$$

In incompressible stripes with a constant charge carrier density due to the fully filled Landau level, the Landau filling factor is fixed to an integer value. For increasing magnetic field the width of the incompressible stripes increases and they are shifted towards the bulk of the sample [55, 57].

In Figure 2.10 the assumed evolution of the in-/compressible landscape versus the magnetic field is schematically shown for the most inner incompressible stripe. The other incompressible stripes are negligibly thin near the border of the sample and are thereby not illustrated. In this evolution we can distinguish between three regimes marked in Figure 2.8 by the roman numbers [40]:

I In the **out-of-plateau** regime, the whole sample is compressible (a) and the Hall potential drop happens along the sample with homogeneous electric current distribution across the sample,

II In the **bulk-dominated** regime on the high magnetic field side of the plateau, the bulk of the sample is mostly incompressible (c) and carries the electric current,

III In the **edge-dominated** regime on the low magnetic field side of the plateau in which an incompressible (b) stripe near the sample edges is present (b), carrying the electric current.

The measurements by scanning force microscopy [16] show in great accordance to the calculated position of the most inner incompressible stripe a confined Hall potential drop.

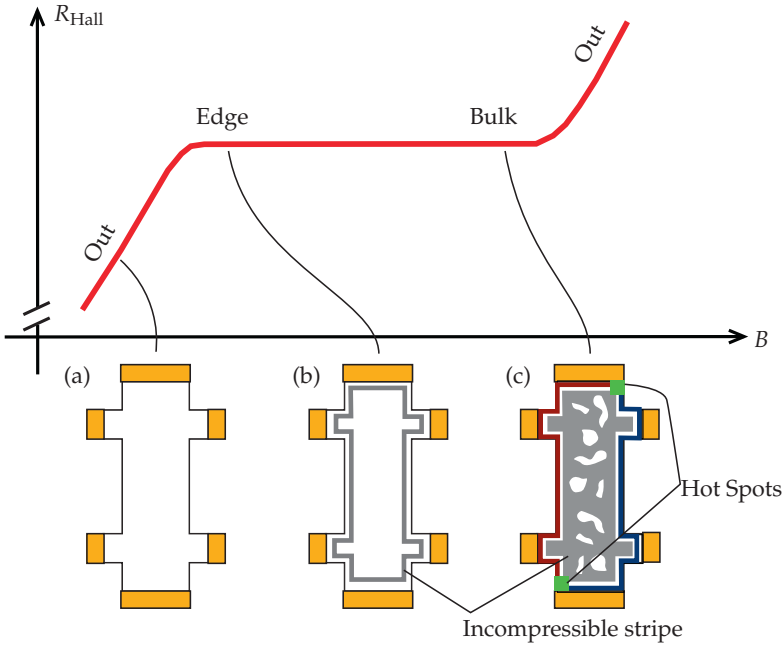

Figure 2.10:
Three different regimes can be distinguished in the quantum Hall effect correlating to the roman numbers in Figure 2.8: (a) Out of the resistance plateau (I), the whole sample is compressible and the Hall potential drop happens across the whole sample. (b) Edge-dominated regime on the low magnetic field side of the resistance plateau (III), one incompressible stripe is running along each edge of the sample and they carry the electric current. (c) Bulk-dominated regime on the low magnetic field side of the resistance plateau (II), the whole bulk of the sample is incompressible and the potential drop happens across the inner part of the sample. The red and blue line show how the potentials applied to source and drain propagate along the edges of the sample, coming together at the "hot spots" (green) where the dissipation in the sample takes place.

2.8 Microscopic Picture of the QHE

The Landau level bending and the level of the electrochemical potential for filling factor $\nu = 4$ across a sample in equilibrium is shown in Figure 2.11 (a). In all regions where the Landau levels are bended a diamagnetic current is flowing already in equilibrium. Those electric currents compensate in the cross section so that there is no net current flowing through the cross section. In the following if we speak of net currents we mean the electric currents that are additional to the diamagnetic currents and result from an externally imprinted sample current.

If we drive now an electric current through the sample by applying a voltage the Hall potential drop just happens across the most inner incompressible stripe which has an integer filling factor of $\nu = 4$ (four fully filled Landau levels) as the measurements in Figure 2.8 from [16] show. The outer incompressible stripes seem to be too thin to isolate the neighboring compressible stripes. Due to MacDonald [61] we get an electric current density perpendicular to the measured electrostatic potential drop expressed by

$$j_x = \nu \frac{e^2}{h} E_y. \tag{2.25}$$

The non-equilibrium situation and the areas where the net current is flowing are illustrated in Figure 2.11 (b). The net current flow hereby results from a change of the group velocity of all occupied electron states in the most inner incompressible stripe induced by the Hall voltage drop across the stripe. The net current and the voltage drop are perpendicular to each other, therefore, we get a dissipationless net current in the 2DES. If the non-equilibrium current is carried along the whole sample only by incompressible regions of the same filling factor the condition of a homogeneous system for (2.23) is fulfilled and a quantized value for the Hall resistance can be measured.

As long as the voltage drop happens across an incompressible stripe, the most outer compressible stripe is able to equilibrate the contact potentials on both sides of the sample separately, see Figure 2.10 red and blue line. Therefore, the longitudinal voltage drop and following the longitudinal resistance goes to zero. Both sides of the sample are potentially separated by hot spots (green area in Figure 2.10) [16] at the source and drain contact. Those hot spots are the area where the dissipation in the sample happens [62, 63].

All this is valid as long as the quantum Hall effect is well developed between the side contacts. If there is no incompressible stripe well enough developed to carry

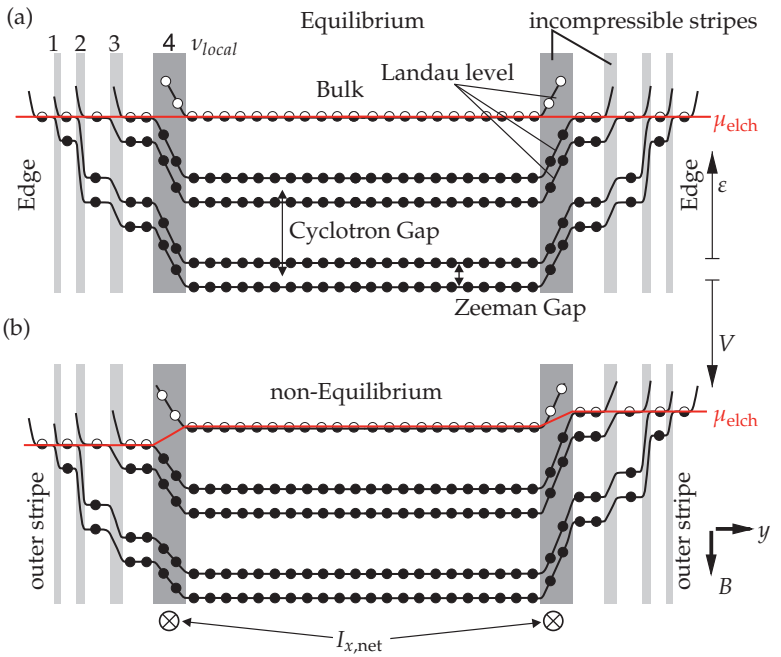

Figure 2.11:
Landau level (black lines) bending for (a) equilibrium and (b) non-equilibrium (externally imprinted electric current) situation for a bulk filling factor $\nu_{\text{bulk}} > 4$. The electron states in the incompressible stripes are either fully filled (filled dots) or completely empty (empty dots). In the compressible stripes the highest Landau level is partly filled (half filled dots). In the equilibrium situation the electrochemical potential μ_{elch} is constant. For the non-equilibrium case for the most inner incompressible stripes a drop of the electrochemical potential happens which is measurable as electrostatic potential drop. Hence, a net current in x-direction (into the drawing plane), divided between both incompressible stripes of same Landau level filling factor, is present. The outer incompressible stripes are expected to be too thin to isolate the neighboring compressible stripes from each other, therefore, the electrochemical potential is constant across them.

the externally imprinted electric current, the potential drop happens also across and along the compressible area and the net current is distributed across the whole sample width. In this configuration neither the longitudinal resistance is zero nor the Hall resistance is quantized and the quantum Hall effect is not measurable.

3
Microscope Setup and Probing Tips

Due to the relocation of the experimental setup into the newly built high precision laboratory of MPI-FKF [64], all parts of the setup had to be reinstalled and modified to improve the microscopes functionality. Figure 3.1 gives an overview over the setup consisting of the probing tips, a microscope rod for a top-loading ^{3}He-^{4}He dilution refrigerator, the necessary pumping lines, electrical and laboratory supply as well as the measurement management. To keep this chapter short but the experimental settings for the following chapters understandable, we want to concentrate in the following sections only on three parts of the setup.

The first section will elaborate on the center piece of this microscope, the one-dimensional array of single-electron transistors (SETs). Those probing tips are used

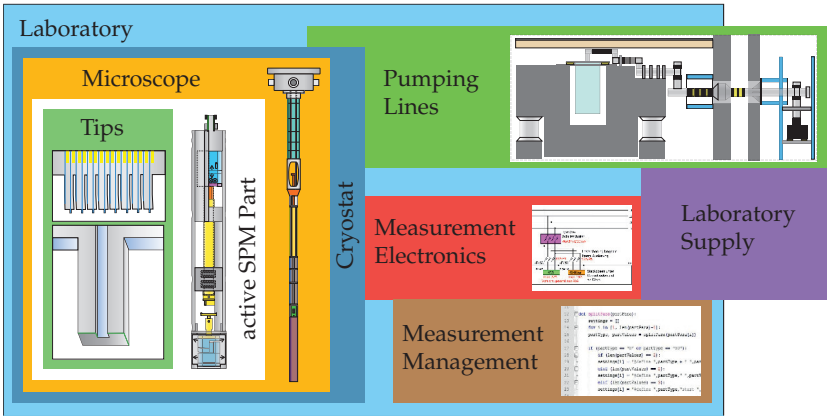

Figure 3.1:
Overview of the scanning probe microscope setup. Most displayed parts will be discussed in more detail within this chapter or the appendix.

as highly sensitive electrometer. The fabrication of those nano-scaled electronic devices will be outlined and the characteristic figures of the SETs, are discussed.

In the second part, the functionality of the scanning SET microscope rod for the top-loading cryostat, which was mainly built during the preceding diploma thesis, will be briefly explained. As the diploma thesis was written in German, it seems reasonable to give this short outline of the microscope to make the information available to a broader English-speaking scientist community.

As a last part, the laboratory premises will be presented. The concept for a vibration damping and isolation for the pumping lines as well as the results of vibration measurements on the setup, will be presented.

More information about the used electronic equipment, the electrical setup of the laboratory and the self-developed measurement software and a picture of the instrument setup can be found in Appendix A.2 and D.1.

3.1 Probing Tips: Fabrication and Characterization

One of the unique features of this microscope is the probing device that consists of eight tip-like structures with an SET located at each tip end. Those SET tips are arranged in an one-dimensional array.

Fabrication Process
The fabrication of the tip array is a complex and time-consuming process and uses up to five steps of electron beam lithography (including cleaning, high vacuum evaporation, reactive ion etching and further steps) to achieve the desired tip structures shown in Figure 3.2 (a).[1] To fabricate a larger number of SET tips is just a minor additional effort. After finishing those five electron beam lithography steps the chip possesses tips, gold electrodes for wire bonding (yellow) and 80 nm wide trenches (blue). Further, the shown tip and SET structures are obtained. The length of the tip structures measures 20 µm which is necessary to gain some distance between chip edge and SET structure. Later the chip is scratched orthogonally to the under-etched tip structures and broken on the height of the tip structures to get free standing tips. If the length would be raised, the structures would become instable and bend out of the drawing plane of Figure 3.2 (a). For shorter lengths a slighter tilt of the chip placed in the scanning SET microscope would lead to a contact between the SET chip edge further aside of the SET structure and the sample surface.

After the electron beam lithography steps a focused ion beam (FIB) in combination with a scanning electron microscope (SEM) is used to downsize the SET structure width, see Figure 3.2 (b). By reducing the width of the SET structure, the area for the later SET island is reduced which raises the charging energy and enhances the lateral resolution of the probing tip due to the smaller tip size. Using this procedure, the achievable size for the SET island lies in the range of 180 nm to 230 nm, usually 200 nm. On the other hand the smaller the remaining width, the higher the risk of losing the SET due to damaging the tip structure with the FIB, so that later no electrical contact is possible.

The shape of the tip structure and the trenches are required for the final aluminum evaporation steps to achieve the electronic structure necessary for a single-electron transistor. First, aluminum is evaporated to create the contacts of the SET that are separated by the trenches. Afterwards in another chamber the aluminum is oxidized to achieve the tunnel barriers in the electronic structure of the SET. In the last step the aluminum for the island of the SET is evaporated under a slight angle

[1] More information about the fabrication process can be found in [65, 66].

to the chip surface and under a slight angle to the trenches. Thereby, the shown tip structure covers the trenches and prevents shortcuts between neighboring SETs. All those evaporation steps are carried out under ultra high vacuum conditions to enhance the quality of the aluminum. Additionally the SET chip is cooled down to less than $-20\,^{\circ}\mathrm{C}$ to reduce the grain size of the aluminum film resulting in a smoother layer.

The SETs fabricated with this process usually show electric resistance values of more than $1\,\mathrm{M}\Omega$. If the SETs of a chip are not working the FIB can be used a

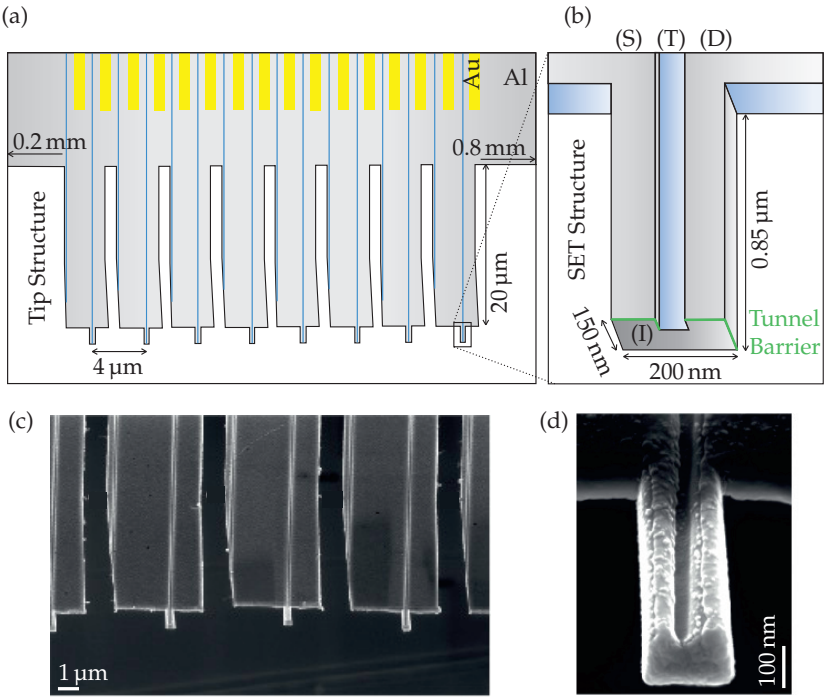

Figure 3.2:
Schematic view and scanning electron microscope (SEM) pictures of the probing tips. (a) Sketch of the one-dimensional tip array with trenches (blue) and gold leads (yellow). The whole array is covered by a thin layer of aluminum except for the trenches. (b) Sketch of one SET structure with source (S), drain (D) leads and trench (T) as well as SET island (I). The tunnel barriers are indicated in green. (c) SEM picture of the one-dimensional tip array, matching the schematic drawing in (a). (d) SEM picture of a single SET structure displayed in the schematic drawing in (b), showing the slightly grainy aluminum layer.

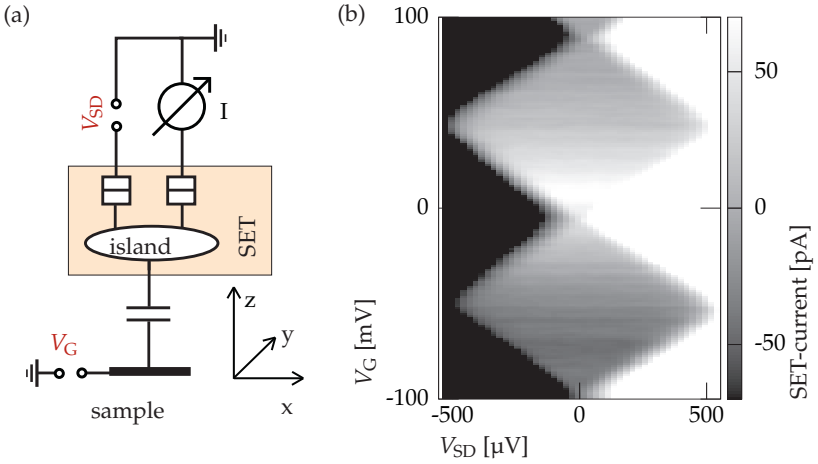

Figure 3.3:
Electrical characterization of a fabricated SET by a charge stability measurement versus gate and source-drain voltage. This SET was mainly used to execute the characterization of the microscope in the later chapters. (a) Sketch of the electrical setup for measuring the charge stability diagram. (b) Current plotted versus source-drain and gate voltage.

second time to fix shortcuts by cutting material out or to repair missing electronic connections by depositing some platinum particles where the connection is broken.

The final tip and SET structures resulting from the fabrication process are shown in Figure 3.2 (c) and (d). In the latter one, the trench, the aluminum coating for the contacts and the aluminum island at the end of the structure are visible.

SET Characterization

The physical properties of the fabricated SETs can be characterized by a charge stability diagram which can be measured by changing the source-drain and gate voltage, see Figure 3.3. The characterization in our case can only be done after cooling down the probing tips typically down to below 0.1 K.

From the maximum width of the Coulomb blockade region in one direction of the source-drain voltage $e/C_\Sigma = 0.53\,\mathrm{mV}$ we get a value for the total capacitance of the SET island $C_\Sigma = 3.01 \times 10^{-16}\,\mathrm{F}$. Furthermore, the charging energy of the SET can be calculated to $e^2/2{\cdot}C_\Sigma = 265\,\mu\mathrm{eV}$. The charging energy of this SET is large enough, that we are able to measure the shape of the Coulomb blockade region just below 0.9 K ($k_B T = 86\,\mu\mathrm{eV}$). Additionally, the gate capacitance C_G can be determined to $C_G = 1.72 \times 10^{-18}\,\mathrm{F}$ from the periodicity of the diagram

in gate-direction $e/C_G = 93\,\mathrm{mV}$. From the slope of the descending borderlines between different charge states the drain capacitance C_D can be calculated to $C_D = 1.48 \times 10^{-16}\,\mathrm{F}$. The source and drain capacitance towards the island are by two orders of magnitude the strongest capacitances. Therefore, we can estimate the source capacitance C_S to $C_S = 1.5 \times 10^{-16}\,\mathrm{F}$. Comparing the source and drain capacitance, a symmetric capacitive situation for this SET is present.

3.2 Microscope Setup

In the following the structure of the microscope and its mechanical functionality is briefly explained. For a more detailed description, I refer to [67].

The primary purpose of this scanning probe microscope is to navigate an array of single-electron transistors over a Hall bar structure on a sample and scan an area of interest while recording the electrostatic potential distribution created by the 2DES in the (fractional) quantum Hall regime. To be able to carry out such measurements the following conditions have to be fulfilled:

1. **Milli-Kelvin temperatures** have to be achieved to get a detailed SET current characteristic used as probing signal and a clear formation of quantum Hall states resulting in a detailed measurement signal.
2. **High magnetic fields** are required for stable fractional quantum Hall states below filling factor one due to the used sample structures.
3. A **positioning system** has to be installed to navigate the probing tips to the sample spot of interest.
4. A **tilting** option for either the sample or the tip array is needed to position all the probing SET tips at the same distance to the sample.
5. A **scanning unit** is required to be able to continuously scan an area with high resolution.
6. **Crosstalk** between high- and low-voltage electric lines and an electrostatic influence on the tips have to be avoided by an electric shielding along the whole length of the microscope rod.
7. A **flexible design** of the wiring for the probing tips and sample and **sufficient space** to exchange both is needed to simplify the handling and reduce the chance of damaging the sample or probing tips.

The required milli-Kelvin temperatures for operating an SET can either be achieved by a ^{3}He-cryostat or by a ^{3}He-^{4}He dilution refrigerator [68]. During this PhD work a top loading Kelvinox 400 ^{3}He-^{4}He-cryostat from Oxford Instruments was installed to setup the microscope. Thereby a base temperature of 16 mK can be achieved. This top-loading cryostat system requires a microscope rod that is 2.3 m long and less than 50 mm in diameter above the 1K pot.

To reach the high magnetic fields necessary for the fractional quantum Hall effect a superconducting magnet going up to 18 T is installed in the cryostat. This constrains the space available for the microscope rod below the 1K-pot to less than 24 mm in diameter.

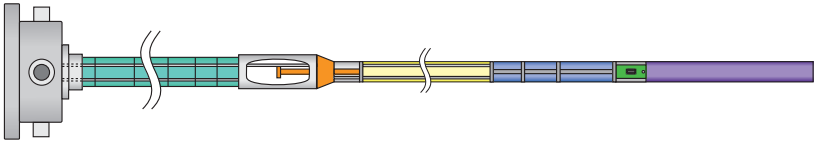

Figure 3.4:
Sketch of the microscope rod for the available top-loading ^{3}He-^{4}He dilution cryostat [67]. Rod head (gray) for electrical connections, thermal isolation (turquoise), 1K-pot connector (orange), displacer for sealing and thermally isolating the mixing chamber part (yellow), free space for thermal and low-pass filters (blue), and active microscope part (violet). The small green part stands for mechanical and electrical intersection between passive and active microscope part. At this point the parts can be separated and exchanged.

The whole microscope rod is shown in Figure 3.4. It consists of six different parts:

- head (gray) for the connection towards the measurement equipment,
- thermal isolation (turquoise, displayed truncated) to reduce convection and radiation between room temperature and 1K pot region,
- 1K-pot-heat-exchange connection (orange) consisting of copper to couple all leads thermally to the 1K-pot of the cryostat,
- the displacer (yellow, displayed truncated) to thermally seal the mixing-chamber from the 1K-pot,
- the filter and thermal equilibration part (blue) offers space for thermally anchored electrical filters,
- the active microscopy part (violet) containing the scanning and positioning units as well as the sample and probing tip space.

In the small diameter of the active microscope part (violet) that extends over the last 0.3 m, conceptually planed by Stefan Falk, a positioning system consisting of a set of customized positioners from the company Attocube is installed, see Figure 3.5 (a). There are an x- and z-positioner (light blue) moving the probing tips ± 1.6 mm horizontally and 2.5 mm vertically. Further, a y-positioner and a goniometer are moving the sample ± 1.6 mm horizontally and tilting it $\pm 3.5°$ (light blue). x-, y- and z-positioner possess a navigation system working with an uncertainty of around 30 µm below 1 K.

A goniometer is necessary to be able to tilt the sample in a way that the SETs can be aligned that all have the same distance to the sample surface. The y positioner is installed below the goniometer to correct shifts caused by the tilting.

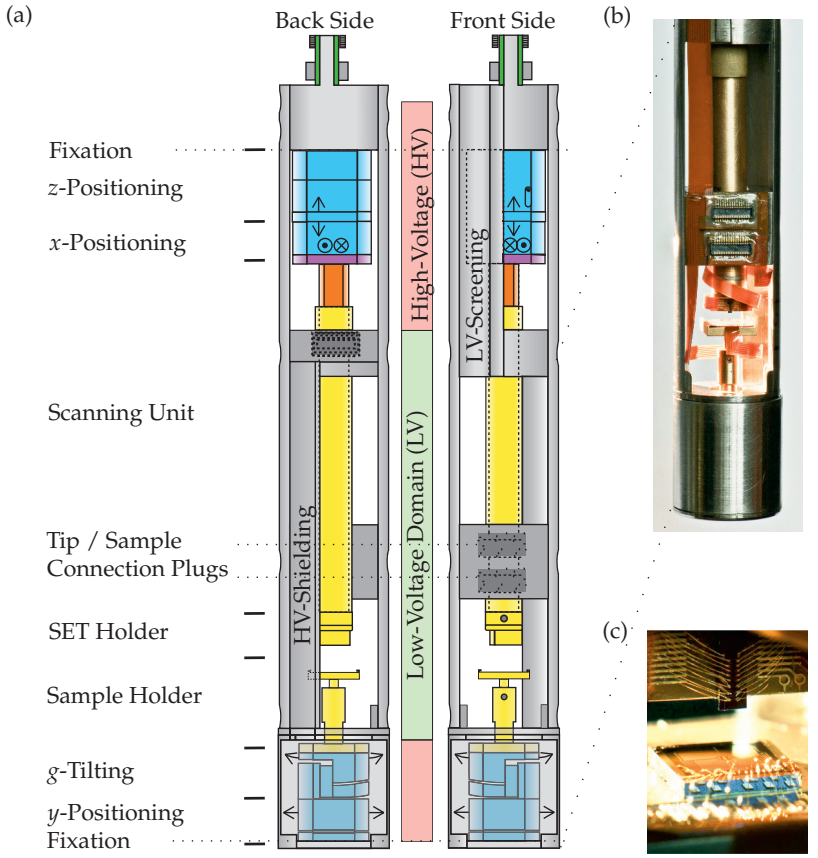

Figure 3.5:
Construction drawings and pictures of the active microscope part reaching into the helium mixture of the cryostat. (a) Front- and back side view of the frame holding the positioning units and scanning unit and electrically shielding the high-voltage area from the low-voltage area. (b) Photograph of the lower part of the active microscope showing the flexible circuit boards (red) used for all electric connections. (c) Photograph of the SET chip positioned over the sample chip. Both are wire bonded to flexible circuit boards.

Below the upper positioning unit, the scanning unit is installed. It is holding the chip with the probing tips and consists of a 75 mm long piezo tube (orange). The piezo ceramic is connected by five sintered silver electrodes to achieve elongations into all spatial directions. Around the piezo tube a metal tube made of brass (yellow) is installed to shield the applied voltage differences of up to 430 V from

the sample and probing tips space. The lengthy scan piezo tube should be capable of scanning an area of more than 20 µm squared at milli-Kelvin temperatures.

To achieve an effective cooling the best thermal coupling between the ^{3}He-^{4}He mixture and the probing tips, sample is needed. This was achieved by putting the microscope with all its functional parts directly into the helium mixture without using a vacuum chamber and cold finger. This decision has the minor disadvantage that dirt present in the mixture can stick to the sample or tips surface.

On the small diameters of the microscope rod, 96 leads are installed to electrically connect sample, tips, scanning and positioning units. We apply voltage in the range from 1 µV to 215 V and electric currents between 10 pA and 0.1 A to the electrical contacts. The higher values and pulsed voltages are necessary for the positioning and scanning units, whereas the lower values are needed for the sample and probing tips. For each scanning unit, sample and tips, 12 twisted pairs of woven constantan LOOM from CMR-Direct are installed between the upper mixing chamber volume and the active part of the microscope. For the positioning unit a combination of copper and superconducting leads made in the same woven way are used. This combination reduces the ohmic resistance of the electrical contacts and the low-pass filter-like behavior of the leads for the necessary steep voltage pulses due to the slip-stick technique. Due to the restriction in space and temperature it was not possible to use coaxial cables. Thus, the leads for the different units of the microscope are well separated and shielded to each other over the whole length of the sample rod.

The electrical connections in the active microscope part are implemented by flexible circuit boards made of a layer of kapton, copper leads and a cap layer of a flexible polymer. Figure 3.5 (b) and (c) display the flexible circuit boards to which the probing tips and sample are wire bonded. The circuit boards leading to the sample and tips are connected with a Molex plug to the next circuit board. Due to this design decision, the sample and probing tips can be exchanged without soldering any connection a second time. Furthermore, there is enough flexibility to move those parts even out of the microscope rod before they have to be disconnected. To electrically ground the electrostatically fragile devices, the connector is double-sided, allowing to plug a short-cut before taking out or putting in the devices.

The frame of the microscope (gray) to which all parts are fixed, consists of non-magnetic stainless steel. The sophisticated design offers an electrical shielding between low-voltage sample, probing tips space and the surrounding high-voltage positioning and scanning units as shown in the middle section of Figure 3.5 (a).

3.3 Laboratory Premises

A scanning probe microscope, further denoted as SPM, in low temperature condition has specific requirements to its surroundings which have to be met by the laboratory premises. These are

1. long-term reliability in terms of power supply to run long-term measurements ranging over several months,
2. prevention of external electrical noise, caused by ground loops and broadcast signals coupling onto the signal wires,
3. vibration isolation and damping to achieve a low mechanical noise level, reducing the noise level of the measurement signal due to a more stable tip-sample position.

The environment in which the setup is installed, is one of the world leading precision laboratories in terms of vibration level [64]. However, other aspects are also satisfied by its thoughtful building design, such as acoustic damping, electromagnetic shielding, etc..

Long-Term Reliability
To reach stable long-term conditions for the installed setups the building is equipped with an uninterrupted power supply unit for each laboratory and a dedicated local computer server. The installation of such redundant systems guarantees the avoidance of blackouts and data loss during measurements. Furthermore, it protects the electrically fragile single-electron transistor tips.

Prevention of External Electronic Noise
For the use of our single-electron transistors, applied voltages of more than 2 mV have to be avoided to prevent the electronic relevant structure from damage and reduce the noise in the measurement. Hence, two aspects have to be considered. Firstly, high frequency noise from broadcasting signals (TV, Radio, Wifi, mobile phones,...) coupling onto the signal wires. Secondly, grounding loops going through the sample applying unwanted voltages caused for example by different ground potentials.

To damp the external electrical noise. The housing of the laboratory box is covered with a metal cover layer on the outside. It has a damping of up to -60 dB. Further, all the tube connections for the gas exchange between inside and outside of the laboratory box contain a metal grid and all electrical wires running through the shielding are led through a low pass filter.

To cut grounding loops, numerous isolating transformers[2] for the power lines and optical fibers for the data communication were installed. In addition, a star-like structure for the grounding of the different electrical measurement components was implemented. The anchor point for the grounding is the power supply of the superconducting magnet of the cryogenic system. This point was chosen due to the necessary low ohmic safety connection between the housing of the cryostat and the power supply.

Vibration Isolation and Damping

The most time-consuming part of setting up the laboratory and cooling system was to design and implement a proper concept for vibration damping. This vibration damping and isolation has to be installed between the dilution refrigerator and the pumps. The pumps are necessary to cool down different parts of the cryostat. One of them evacuates the 1K-pot to evaporate ^{4}He from the bath and thereby cool a certain part of the cryostat to roughly 1.3 K. Other two pumps circulate the ^{3}He from the still into the mixing chamber to cool down the scanning probe microscope to the base temperature of 16 mK. A further pumping line is used as an auxiliary line to generate a vacuum, e.g. at the thermal insulations of the cryostat, if required. In total there are four permanently running pumps. All are producing vibrations which are guided towards the cryostat by metal[3] vacuum tubes, support constructions, the surrounding air, as well as the helium inside the tubes.

In Figure 3.6, a sketch of the vibration damping and isolation concept along the pumping lines is shown. The colored areas marked with the letters (a) to (f) illustrate the six different levels of mechanical noise separated by different vibration damping solutions. In the Figure, position (a) marks the highest noise level including the pumps that are put on soft rubber in a solid suspension frame. On top of the pumps a very elastic corrugated tube is installed[4]. The extension of this corrugated tube is fixed by the weight of the pumps (usually 60 kg to 120 kg) and by the fixation of the solid tube above. Usually the vacuum will pull the variable parts together and eliminate any vibration isolation. In this case the vacuum inside plays no role for the properties of this vibration isolating part due to its fixed extension. The same isolation concept is also used between (c) and (d), (e) and (f).

[2]The isolating transformers are installed below the floor around four meters away from all the electrical measurement setup to reduce the influence of their electro-magnetic fields.

[3]The metal of the tubes was the largest challenge due to its good transmittance of vibrations. However the usage of other materials like teflon or rubber for tubes was not possible due to the necessary vacuum and possible losses of the costly helium-3.

[4]This part is also used to compensate height differences of the exchange pumps.

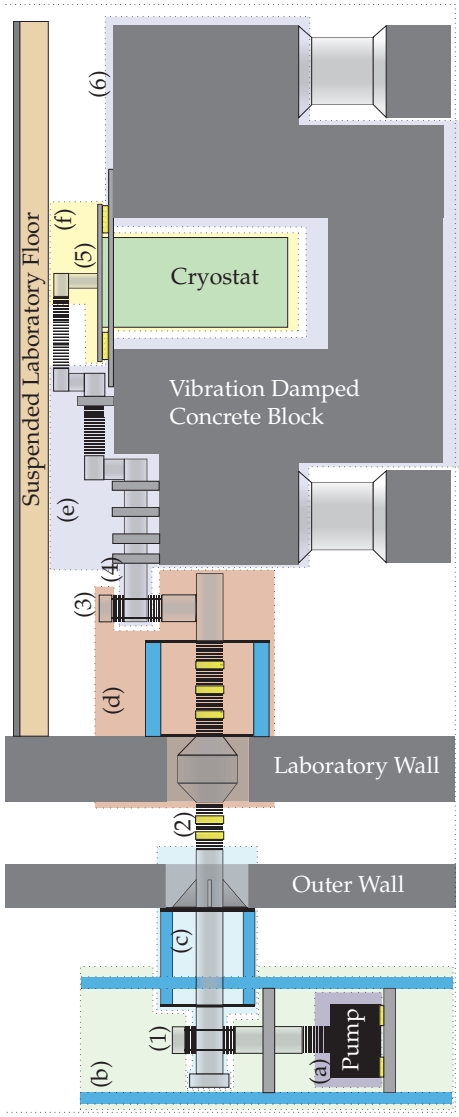

Figure 3.6:
Vibration damping along the pumping lines through six different vibration noise levels starting at the pump position (a) to the cryostat position (f). The different sections are highlighted by multi colored areas. Due to space limitations, page needs to be turned 90° to match drawing with actual laboratory setup.

The solid tube is fixed to the suspension frame mentioned before representing the second mechanical noise level at position (b) consisting of an aluminum frame fixed to the floor and ceiling of the pumping room. Position (c) marks the vibration level fixed to the outer wall using a different basement than the pumping room floor and ceiling. Vibration isolation between (b) and (c) is done by a balk transducer, a construction keeping its inner volume constant under pressure variations. Thereby, it is unaffected in its vibration isolation properties under vacuum. This type of vibration isolation is used as well between (d) and (e).

In (c) a sand box for further vibration reduction can be installed. However, there are a few disadvantages of such a sand box for example a required loosening up of the sand every quarter of a year and the produced dust. Therefore, the sand box is not yet installed. The vibration level at position (d) is fixed to the noise level of the laboratory wall. The tubes within the laboratory wall include a metal mesh to reach the $-60\,\mathrm{dB}$ shielding of electro-magnetic fields. Between position (c) and (d) and in the noise level of position (d) foamed material[5] (yellow) is installed around the corrugated tube to damp down surface acoustic waves running along the tubes. Furthermore, a Teflon sealing between two metal tubes and electrically isolating clamps are installed in the vertical part of the tube configuration. The Teflon sealing fulfills the function of a galvanic isolation of the cryostat, this is necessary to separate the electric ground level of the pumping room from the one of the cryostat in the laboratory.

At the right end of the horizontal tube line reaching from (c) to (d) a dead-end is installed to reflect acoustic waves transmitted over the helium gas in the tubes. On the left end of this horizontal tube line a valve is installed to preserve the possibility to add another dead-end to the tube line that has vibration damping materials inside.

The tubes at position (e) are fixed several times with solid connections to the vibration damped concrete block. Over an elastic corrugated tube the cryostat is connected with the tubes in (e). The cryostat, as the last part of the tube line, is held by a 40 mm thick aluminum suspension plate while it is reaching about 2 m downwards into a ditch of the concrete block. The cryostat plate is mounted on the same foamed material used to damp the surface acoustic waves along the metallic vacuum tubes. A fixation of the cryostat directly to the concrete block was avoided due to the expected crosstalk between the different cryogenic systems installed on the same concrete block. As a last step all the walls of the ditch in the

[5]Sylomer from proctor Group Ltd. is a foamed material usually used in construction sites.

concrete block in which the cryostat is installed are covered with 100 mm thick sound absorbing material.

An intrinsic weakness in concerns of the vibration damping is the suspended laboratory floor acting like a membrane if a person is walking on it. The produced oscillation can be transmitted to the damped concrete block and results in measurable vibrations.

Result of the Pumping Line Concept

Vibration measurements along the largest pumping line were done to visualize the impact of the different vibration isolation steps. The results of a standardized measurement procedure carried out with a Bartington Instruments equipment are shown in Figure 3.7. (1) to (6) refer to the accordingly numbered positions in Figure 3.6. Comparing the different spectra, we have to pay attention to the changing range of the ordinate axis. The measured acceleration a of the vibration sensor is plotted linearly (blue). This measurement type can be used to figure out the force F acting on an object with mass m by $F = m \cdot a$. The derivated velocity v of the system is shown in violet and correlates to the vibration energy by $E = \frac{m \cdot v^2}{2}$. The derivated elongation is represented by the light-brown curve.[6]

The spectra of position (1) show very strong intensity peaks situated at frequencies of integer multiples of around 50 Hz[7]. Measurement position (2) displays a spectra reduced by a factor of 30 showing only two remaining major peaks at 50 Hz and 300 Hz. The reduction is a result of the separating wall, the fixation of the the vibration levels to different bases, and the balk transducer as a vibration isolation in between. A further reduction of a factor nine happens at (3) due to the second separating wall and the described surface wave damping. At this point the vibration more or less consists solely of low frequency oscillations with by far the strongest peak at around 50 Hz.

The second balk transducer and the strong fixation of the pumping line to the vibration damped concrete block reduce the strongest peak levels by a factor of 10. Now at position (4) the lower frequency spectra (7 Hz to 200 Hz) is gone and only peaks above and equal to 200 Hz are present. This is the result of the damping system of the concrete block and its large mass.

Nevertheless, low frequency peaks around 18 Hz and 36 Hz appear on the top plate of the cryostat (5). However once more, the scale is reduced by a factor of

[6] To calculate the velocity A_v and elongation A_e amplitudes from the acceleration amplitude A_a one can use the simple relations $A_v = A_a/(2\pi f)$, $A_e = A_a/(2\pi f)^2$ with the frequency f.

[7] The 50 Hz peak is not caused by any power supply because both the sensor and the notebook PC were running on battery to avoid measurement artifacts. Further, the peak would not be reduced in the spectra if it would have an electric origin.

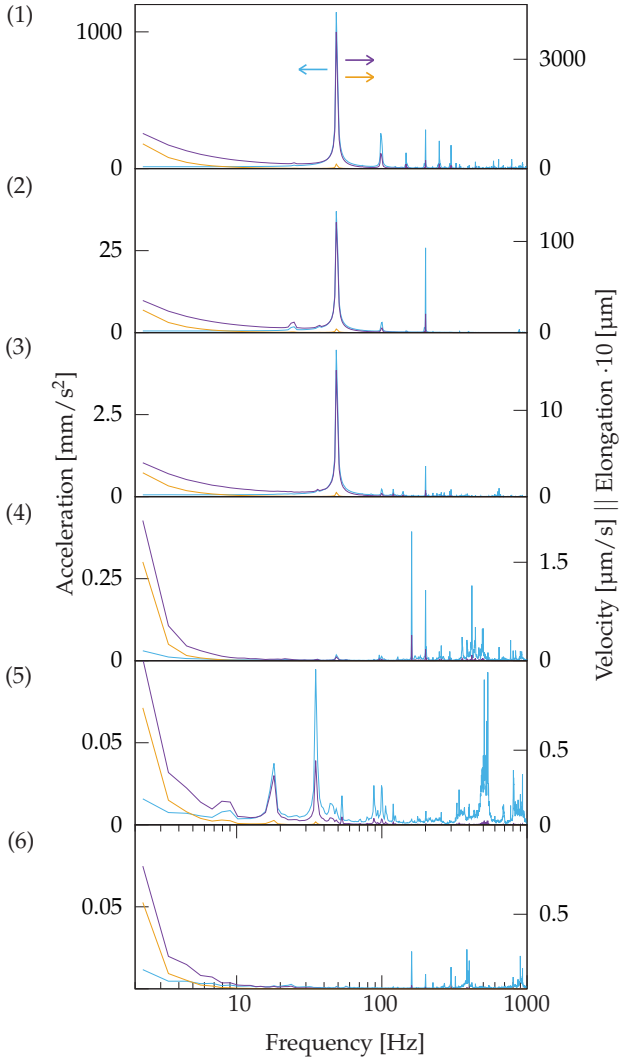

Figure 3.7:
Measurements of the vibration noise level along the largest pumping line at six different positions. Diagram (1) to (6) correlate to the positions accordingly numbered in Figure 3.6. The blue lines correspond to the measured acceleration amplitude (left ordinate axis), the violet lines to the velocity amplitude (right ordinate axis), and the orange lines to the elongation amplitude (right ordinate axis).

three compared to the previous spectra. Signals at these frequencies can either result from acoustic noise produced in the room or from a resonance frequency of the cryostat dewar. At this level we are talking about an acceleration of less than $0.1\,\mathrm{mm/s^2}$ for the measured peak at 36 Hz. From the acceleration amplitude we can calculate a velocity amplitude of less than $0.45\,\mu\mathrm{m\,s^{-1}}$ and an elongation amplitude of less than 2 nm. A bit less than those values is calculated for the peak at 18 Hz. The velocity and elongation calculated around 3 Hz exceed those values ($0.5\,\mu\mathrm{m\,s^{-1}}$ and $0.03\,\mu\mathrm{m}$). As well as for atomic force and scanning tunneling microscopes the stiffness between probing tip and investigated sample is of major importance for our scanning SET microscope. If resonance frequencies are avoided with the peaks around 18 Hz and 36 Hz and below 4 Hz, the absolute vibration amplitude is reduced to a much smaller relative vibration amplitude between probing tip and sample.

Comparing the actual vibration level of the cryostat (5) with the one of the vibration damped concrete block (6) we could only significantly improve the vibration level in the frequency spectra above 15 Hz by reducing all the spectra peaks. The lower end differs only about 20 % in comparison.

A comparison of the vibration spectra for the old and new laboratory is shown in Figure 3.8, this time in double logarithmic scales. The vibration damping for the old setup consisted of a separated pump room, a sand box installed around the largest pumping line, and passive air dampers for the cryostat plate. The vibration noise level for the new laboratory is a factor of 90 lower than the noise level for the old laboratory measured both times on the top plate of the cryostat. For a frequency range from 3.5 Hz to 1200 Hz, the value for the old setup lies between the noise level of the positions (2) and (3). A reduction of the maximal measured elongation amplitude at 3.5 Hz from 1380 nm on the cryostat in the old setup to 15.4 nm on the cryostat in the new setup was achieved. The arrangement for vibration damping enhances the measurement capabilities of the microscope in respect to its resolution and stability.

Nevertheless the cryostat has to be refilled with helium at least every four days. During this filling procedure the tips have to be withdrawn. The first hour after filling the cryostat with helium, an oscillation on the measurement signal in the range from 110 Hz to 130 Hz can appear resulting from boiling helium in the cryostat bath. Therefore, the tips should stay withdrawn for another hour and afterwards they can be approached towards the sample.

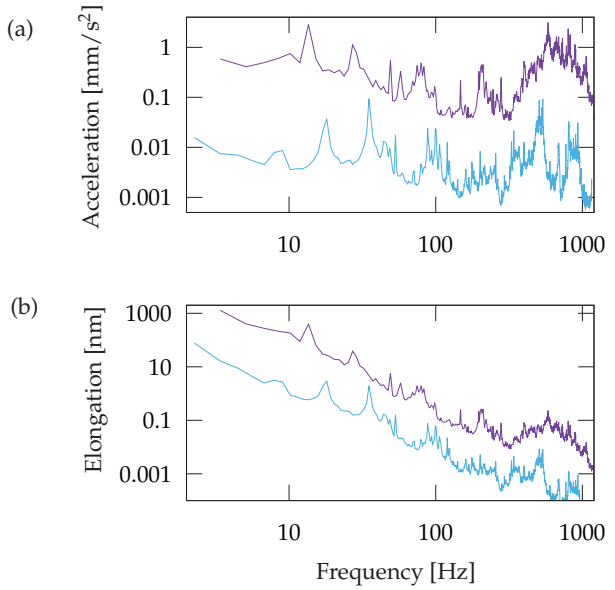

Figure 3.8:
Comparison of the vibration level between the old laboratory (violet) and the new one (blue). The vibration damping in the old laboratory consisted of a separated pumping room, a sand box around the corrugated metal tubes and a passive air damping system for the cryostat. (a) Acceleration spectra in double logarithmic scales. (b) Elongation spectra in double logarithmic scales.

3.4 Summary and Outlook

In this chapter the SET fabrication process, the construction scheme of the microscope rod and the vibration damping concept were explained and key features were determined.

Firstly, a short overview of the SET fabrication process was presented, highlighting the fact that the probing tip array consists of eight SETs in a row with a distance of 4 µm between neighboring SETs. The island size for those electronic nanoscale devices usually measures around 150 nm by 200 nm. By a charge stability measurement the charging energy was determined to 265 µeV displaying a well defined current-voltage characteristic of the SET already for temperatures from 0.9 K downwards. If the charging energy could be enhanced only by a factor of two, it would be possible to characterize each SET array in an available helium-4 pumped system at 1.3 K before installing them into the microscope. This would simplify the SET tip characterization and would accelerate the development of the SET sensor combined with new sensor types like SQUIDs, Hall sensors and others. To achieve such a charging energy enhancement the total capacitance has to be lowered either by reducing the overlap with source and drain contact, for example, by reducing the island size or by thickening the tunnel barriers. The first suggestion is more difficult to be put into practice, but would even enhance the lateral resolution. The latter would lower the SET current and would therefore require an enhancement of the IV-converter resolution. Nevertheless, there was already a project to add Hall sensors to the tip array [69].

We also showed the construction drawings of the microscope rod, that was built for a ^{3}He-^{4}He dilution fridge to reach temperatures below 100 mK and magnetic flux densities of up to 18 T. Therefore, the diameter of the microscope rod was strongly restricted to 24 mm on the height of the mixing chamber and below. In a tube of around 0.3 m length, a positioning and scanning system are placed allowing the SET tips and sample to be shifted 3.2 mm horizontally and 2.5 mm vertically. Additionally, the sample can be tilted $\pm 3.5^\circ$ to match the plane through the SET islands. Due to previous experiments, a scan area of more than 20 µm in square at milli-Klevin temperatures can be expected with the used scanning piezo tube. To supply all of those units with electrical connections, 96 leads in bundles of 24 are installed. The bundles are electrically shielded from each other. The exchange of the probing tips and sample is simplified by using flexible circuit boards and thin "molex" connectors, as used in older generations of mobile phones. The frame of the microscope rod was made of a few non-magnetic stainless steel parts. Still with high magnetic fields the microscope is expected to slightly deform and shift

the tip-sample position. Further, the navigation measurement of the positioning system has an uncertainty of around $\pm 15\,\mu m$ for milli-Kelvin temperatures.

To overcome some withdraws of the present design, a new active part of the sample holder with an enhanced positioning and simplified scanning system was planned at the end of this thesis. The new active microscope part is not affected by strong magnetic fields due to the used titanium alloy. This reduces the effort of correcting the tip sample position for different magnetic fields. The applied print technique is further allowing to fabricate the whole frame part as one piece enhancing the stiffness of the microscope to make it more stable against vibrations for example of boiling helium. Drawings of the new microscope part and a short explanation can be found in Appendix B on page 189.

The laboratory was relocated into a precision laboratory with a vibration damping system at the beginning of this PhD thesis. Therefore, an extensive vibration damping and vibration isolation concept with six stages for the pumping lines was installed. Compared to the old laboratory the vibration noise level was reduced to around 1 % of the previous mechanical noise level. In the actual state the elongation amplitude on top of the cryostat lies around 15 nm at a frequency of 3.5 Hz and well below in the frequency range from 4 Hz to 1200 Hz. This value might reduce further for the tip-sample vibration elongation if no resonance frequencies of the microscope are matched. Only two remarkable vibration elongation peaks remained in the spectrum: one at 18 Hz and the other one at 36 Hz. Those two peaks, resulting from natural resonances of the cryostat, are of minor interest compared to the rising noise level at lower frequencies. The noise level between the vibration damped concrete block and the cryostat top plate differs only around 20 %. Therefore further optionally planned vibration damping parts like a sand box or a sound damping system within the tube are not necessary. Besides the vibration reduction the new laboratory features a reduction of the sound level and very stable electrical conditions to run this long term experiment over several months.

4
Measurement Concepts

The purpose of the microscope is to measure the electrostatic potential distribution within an integer and fractional quantum Hall sample. Therefore, we use the single-electron transistor (SET) as a highly sensitive electrometer [21, 27]. It consists of a source, drain electrode and a quasi-isolated island that is scanned in close proximity over the sample surface. The sample made of an (Al,Ga)As heterostructure possesses a two-dimensional electron system (2DES) coupling capacitively as a gate electrode to the SET island. For the quantum Hall effect (QHE) regime, the 2DES exhibits a variation of the electrostatic potential at different scan positions that we want to measure. However, trapped charges in the donor layer or leftover resist particles or charges on the sample surface will disturb this measurement. In addition a variation in the probe-sample distance or the lateral limited 2DES, over which will be scanned, also influence the signal of our electrometer due to changes in the partial capacitances. Taking all this and additional electrodes in the near environment of the SET into account we have to handle a rather complex measurement situation. Therefore, in the first part of this chapter we explain the electrostatic situation in different simplified scenarios and will clarify the physical terms used in the following chapters. In the second part different measurement principles are introduced, explaining which information we obtain from the electrostatics on a sample surface and which is not accessible.

4.1 The Single-Electron Transistor as an Electrometer

To understand the SET as an electrometer the electrostatic influence on its island for different situations, as shown in Figure 4.1 has to be taken into account. Therefore, the source (S), drain (D), gate (G) and all other electrodes in the near environment (Env) are treated as partial capacitances C_S, C_D, C_G and C_{Env} towards the SET island. First we look at the simplest case for which all electrostatic potentials except the one of the gate are fixed to 0 V, see Figure 4.1 (a). With a gate potential of V_G, we get a real induced charge of

$$Q^{ind}_{island} = C_G \cdot V_G \,, \tag{4.1}$$

on the island. This can be proven by Gauss's law [70]

$$Q^{ind} = \oint_S \epsilon_0 \cdot \vec{E} \cdot \vec{n} \, \mathrm{d}a. \tag{4.2}$$

The charge on the island is obtained by integrating over the normal component of the dielectric displacement field $\epsilon_0 \cdot \vec{E} \cdot \vec{n}$, at an area element d$a$ of the surface S, that is completely enclosing the island of the SET.

As a next step we want to assume a completely isolated SET island without fixing the electrostatic potential but the charge on it, this is illustrated in Figure 4.1 (b). If

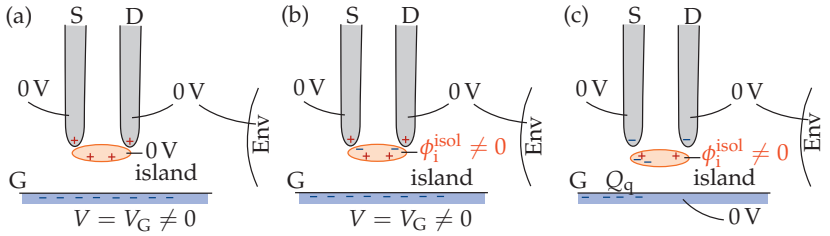

Figure 4.1:
Different electrostatic configurations for an SET tip over a sample surface. (a) Simplest arrangement of the electrostatic situation for an SET island. It is including the source S, drain D, gate G electrodes and further electrodes denoted as environment (Env). Except the gate potential, all others are fixed to ground potential and charges can be induced on each electrode. (b) An isolated island with unfixed electrostatic potential ϕ_i^{isol}. In reality we have a quasi-isolated island on which the charge can just be changed in integer steps of the elementary charge. (c) Charge located on the gate electrode that is fixed to ground potential. The presence of the charge polarizes the island and therefore the island's electrostatic potential is changed.

we change the electrostatic potential of the gate electrode an electrostatic potential difference between gate and island is present, leading to an induced charge of $C_G \cdot (V_G - \phi_i^{isol})$ on the island. An electrostatic potential difference is also present between the island and the source, drain contacts, and the environment leading to induced charges of $C_S \cdot \phi_i^{isol}$, $C_D \cdot \phi_i^{isol}$ and $C_{Env} \cdot \phi_i^{isol}$. Summing up over all those induced charges on the SET island we have to get a constant total charge for the isolated island that is the initially fixed charge Q_0. This leads us to the relation

$$\begin{aligned} Q_0 &= C_G \cdot (V_G - \phi_i^{isol}) - C_S \cdot \phi_i^{isol} - C_D \cdot \phi_i^{isol} - C_{Env} \cdot \phi_i^{isol} \\ &= C_G \cdot V_G - C_\Sigma \cdot \phi_i^{isol} \,. \end{aligned} \tag{4.3}$$

Rearranging the equation determines the electrostatic potential of the isolated island ϕ_i^{isol} to

$$\phi_i^{isol} = \frac{C_G \cdot V_G}{C_\Sigma} - \frac{Q_0}{C_\Sigma} = \frac{Q_{island}^{ind,vir}}{C_\Sigma} - \frac{Q_0}{C_\Sigma} \,, \tag{4.4}$$

connecting the electrostatic potential variation on the isolated SET island with a potential change on the gate electrode. In the last step we used (4.1), substituting $C_G \cdot V_G$ by a virtual induced charge $Q_{island}^{ind,vir}$ because it can no longer be determined by simply applying Gauss' law (4.2). The resulting $\Delta\phi_i^{isol}$ shifts the charging energy levels on the island, illustrated in Figure 4.2 (a).

Since the island is only quasi-isolated from the source and drain electrode, every time the positive going electrostatic potential of the island exceeds a threshold an electron can charge the island via the tunnel barriers. This happens every $\Delta\phi_i^{isol} = e/C_G$ as shown in Figure 4.2 (b). Therefore, the fixed charge Q_0 in (4.4) has to be replaced by $N \cdot e$ with $N \in \mathbb{N}$ and the isolated electrostatic potential ϕ_i^{isol} by ϕ_i. If the electrostatic gate potential is raised continuously, ϕ_i follows in the same direction but jumps back every time an additional electron charges the island. This behavior of ϕ_i is shown in Figure 4.2 (c). There is also a discrepancy between the virtual induced charge $Q_{island}^{ind,vir}$ from (4.4) and the real induced charge Q_{island}^{ind} on the island, which is denoted as surplus charge $Q_{island}^{surplus}$ from now on. $Q_{island}^{surplus}$ is following the behavior of ϕ_i and the characteristics is shown in Figure 4.2 (d).

We have just discussed the situation of fixed electrode positions and a change in the gate potential. As a second case we want to have a look at a fixed-to-zero gate potential but a charge Q_q located on the gate electrode near the SET. The configuration is shown in Figure 4.1 (c). The charge Q_q will induce mirror charges on all the surrounding electrodes with fixed potential. Again assuming an isolated island the charge Q_q will polarize the island and therefore change the electrostatic

potential of it. Hence, we can use the previously given relation (4.4) for ϕ_i^{isol} except that $Q_{island}^{ind,vir}$ is induced by Q_q at this point and therefore will be called $Q_{i,q}^{ind,vir}$. Taking the next step and change to an quasi-isolated island we directly get

$$\phi_i = \frac{Q_{island}^{ind,vir}}{C_\Sigma} - \frac{N \cdot e}{C_\Sigma} = \frac{Q_{i,q}^{ind,vir}}{C_\Sigma} - \frac{N \cdot e}{C_\Sigma}. \tag{4.5}$$

Previously the SET tip was positioned over a gate electrode in a fixed geometric situation. When we assume a horizontally moving SET with a fixed distance d between sample and island we can already describe the two cases shown in Figure 4.3 (a) and (b). Just the gate capacitance C_G and its potential V_G have to be substituted by a sample capacitance C_{sample} and its potential V_{sample}, which both can vary over lateral position x, y. The two depicted cases represent an usual sample with charged particles on the surface or in the donor layer and an electrostatic potential distribution on the sample, in example due to the quantum Hall effect. For both, the electrostatic potential ϕ_i of the island will change while scanning.

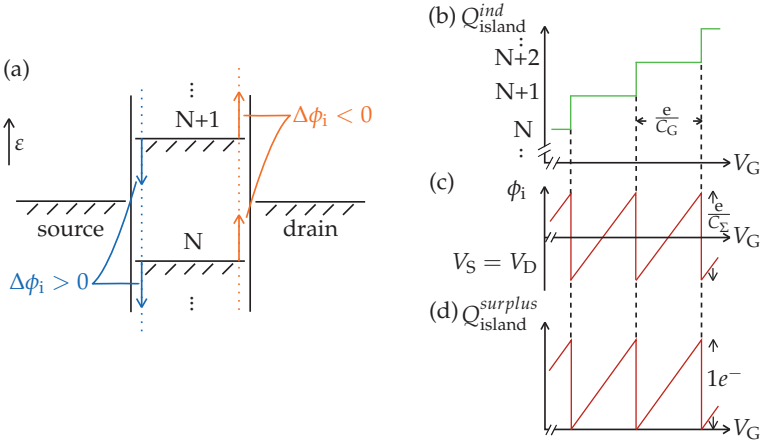

Figure 4.2:
Energy level scheme, real charging, behavior of the electrostatic potential and virtual charging of an SET island versus changing gate voltage. (a) The electrostatic potential change $\Delta\phi_i$ of the SET island shifts the threshold level (charging energy levels) for charging the island with $N, N+1, ...$ electrons. (b) Real charging of the SET with integer values of the elementary charge due to an increase of V_G. (c) Behavior of the electrostatic potential of the quasi-isolated island ϕ_i versus the gate potential. (d) Surplus charge versus gate voltage V_G. Each time an electron jumps onto the island, $Q_{island}^{surplus}$ is reset to zero.

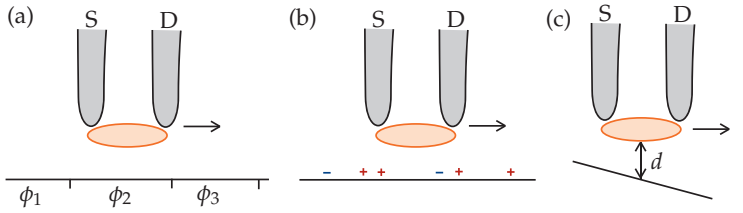

Figure 4.3:
Three different possibilities to vary the electrostatic potential ϕ_i of the SET island while scanning over the sample surface. (a) SET moves over a surface with different electrostatic potentials. (b) SET scanning over a sample with charges located on the surface. (c) A change in the distance between sample and SET island equals a variation in C_{sample} with influence on the electrostatic potential of the SET island.

As a third case we consider the change of the partial capacitance between sample and island. It can be a result of a non-parallel lateral scan direction with respect to the sample surface or from sample roughness. With a sample-tip distance of d, this case is illustrated in Figure 4.3 (c). In this situation C_{sample} and also in general C_Σ will change. Thus, we can calculate the distance d derivative of (4.5) resulting in

$$\partial_d \phi_i = \partial_d \left(\frac{Q_{island}^{ind,vir}}{C_\Sigma} - \frac{N \cdot e}{C_\Sigma} \right) = \partial_d \left(\frac{C_G V_G - N \cdot e}{C_\Sigma} \right) \tag{4.6}$$

$$= (\partial_d C_G) \cdot \frac{V_G}{C_\Sigma} - \frac{C_G \cdot V_G - N \cdot e}{C_\Sigma} \cdot \frac{\partial_d C_G}{C_\Sigma} \tag{4.7}$$

$$= \frac{\partial_d C_G}{C_\Sigma} \cdot \left(V_G - \frac{C_G V_G - N \cdot e}{C_\Sigma} \right) , \tag{4.8}$$

where $\partial_d C_\Sigma \approx \partial_d C_{sample}$ because of the fixed partial capacitances towards drain and source and a neglected C_{Env}. The change in the partial capacitance between SET island and gate electrode has an influence on the electrostatic potential of the SET island.

In summary, in this section we have depicted the three possible ways to change the electrostatic potential of the SET island. Those are an alternation of the nearby electrostatic sample potential, fixed charges at the sample surface and a variation of the partial capacitance between sample and island with a non-zero potential difference. The latter can result from a dielectric particle on the surface, surface roughness or an uncorrected slope while scanning. In the experiment while scanning along a line or over an area, the SET may see a mixture of all three cases as shown in Figure 4.4. Thus, all three types change the electrostatic potential of the SET island by affecting the virtual induced charge on the island, $\Delta\phi_i \approx$

$\Delta Q^{ind,vir}_{island} / C_\Sigma$ ($C_\Sigma \approx$ const as dominated by C_S and C_D). In the measured data the changes of different origin are indistinguishable. Without an exact knowledge of the surface structure, specific measurement procedures and calibration techniques are required to extract the signal part resulting solely from a change in sample potential.

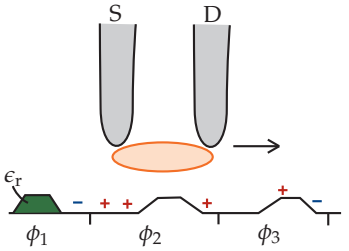

Figure 4.4:
The real electrostatic configuration of an SET scanning over a sample surface. The electrostatic potential of the island is influenced by a mixture of local sample potentials, surface charges, dielectric particles and surface roughness.

4.2 The Coulomb Blockade Oscillation Measurement Method

To use the SET as an electrometer, changes in ϕ_i, respectively $Q^{ind,vir}_{island}$ have to be measured. Because the SET is a device changing its conductance for different $Q^{ind,vir}_{island}$, the simplest way to make an electrostatic potential change on the sample visible is to measure the current through the SET. The charge stability diagram in Figure 4.5 depicts the possible kinds of electron transport for different $Q^{ind,vir}_{island}$ and V_{SD}. Thereby, the conductance of the SET can be approximated. Following, we can conclude on the electric current characteristics at different applied source-drain voltages V_{SD}. Looking for a suitable V_{SD} we have to think about stability and sensitivity of the DC current measurement. Therefore, we should choose a source-drain voltage that offers a large variation in electric current and no ranges in which the electric current through the SET stays constant by changing $Q^{ind,vir}_{island}$. For too small applied source-drain voltages the current-gate-voltage characteristic still covers the Coulomb blockade regime. Hence, we get a range of zero electric current for changing $Q^{ind,vir}_{island}$ (orange,red). Following, we have to look outside the Coulomb blockade regime for an suitable V_{SD}. The electric current modulation amplitude will also flatten for source-drain voltages allowing multiple-electron transport through the SET (green). Therefore, in experiments a source-drain

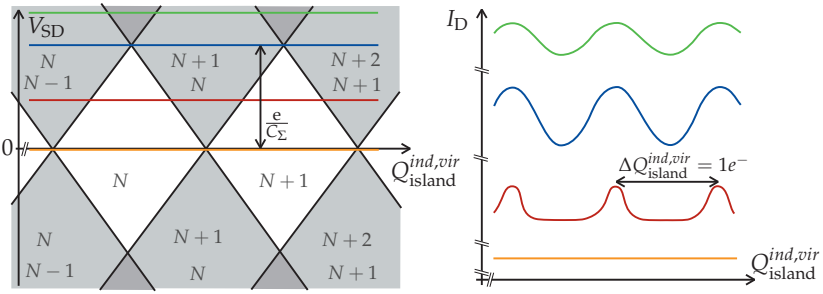

Figure 4.5:
Left side, charge stability diagram versus source-drain voltage and virtual charge on the SET island. The Coulomb blockade regime is illustrated in white and the single-electron tunneling regime in light gray. Along the four line-cuts in the diagram we expect electric current modulations as sketched on the right side. Right side evolution of the SET current modulation over different source-drain voltage values [71]. The amplitude of the modulation increases until $V_{SD} \approx e/C_\Sigma$.

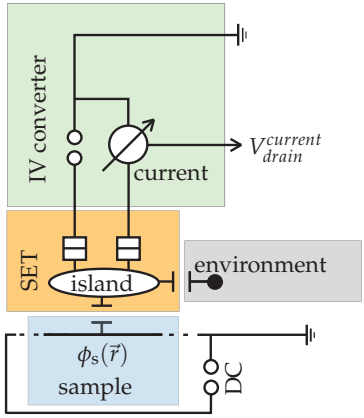

Figure 4.6:
Sketch of electrical measurement setup needed for the Coulomb blockade oscillation method. The IV converter (green) is applying a voltage to the source contact of the SET (orange). On the drain side the electric current through the probing tip is measured and converted to an output voltage. The island of the SET is influenced by two partial capacitances (except for source and drain) one towards the sample (blue) and one to the environment (gray). The environment consists of electrodes from the neighboring SET, other nearby sample electrodes and screening parts of the setup. A voltage is applied to the sample to obtain a potential distribution $\phi_s(\vec{r})$ while scanning the surface.

voltage of around

$$V_{SD} \approx \frac{e}{C_\Sigma} \tag{4.9}$$

turned out to fit best to our purpose (blue). Hence, we can measure changes in $Q_{island}^{ind,vir}$ by monitoring the alternating drain current of the SET. We will call the direct measurement of the SET current versus another changing parameter like tip-sample position or sample potential the Coulomb blockade oscillation method, short CBO method.

Nonetheless we have to be aware that the measurement signal has a periodicity in terms of virtual charging by elementary charges

$$I_D(Q_{island}^{ind,vir}) = I_D(Q_{island}^{ind,vir} \pm N \cdot e) \tag{4.10}$$

and reaches its highest sensitivity on the flanks of each electric current peak.

In Figure 4.6 the electrical measurement setup is shown. The IV-converter (green)

applies a voltage to the source lead of the SET. The electric current is measured on the drain side and converted to an output voltage[1]. In the orange colored area, the typical SET structure is illustrated with its island, two tunnel junctions and the partial capacitances towards the sample (blue) and the environment (gray). The environment in this context stands for other electrodes on the sample, the leads of the neighboring SET or grounded screening parts of the setup. If the SET island is put in close proximity to the sample surface, the partial capacitance between them becomes dominant compared to the environment.

To simplify further considerations we assume different electrostatic potential distributions on the sample for line scans of the SET. In such cases, C_{sample} is assumed to be constant, and changes by surface charges as well as by the capacitive coupling to the environment are neglected.

Although the electrical setup for the CBO method looks rather simple the interpretation of the measured signal is challenging. Figure 4.7 (a) shows how an electrostatic potential increase (blue) is mapped to the measured electric current (red), both versus the same range of position. Firstly, the electrostatic sample potential $\phi_{\text{s}}(\vec{r})$ over the position $\vec{r}$ (point 1) has to be assigned via the SET current characteristics (green) to the I_{D} value (point 2). Following the mapping over the bisectrix the I_{D} value is assigned to $\vec{r}$ (point 3). Doing this for all positions $\vec{r}$ we obtain the complete I_{D} versus $\vec{r}$ diagram.

In Figure 4.7 (a) this procedure is done for a monotonic non-linear rising sample potential profile. The green colored areas illustrate the same electrostatic sample potential difference present over different position distances. While the electric current change (dashed lines) for the potential ranges stays the same, the measured signal is changing with the potential gradient. A steeper slope of the electrostatic potential variation over position results in a faster virtual charging of the island per scanned length. Due to a quicker virtual charging the measured electric current value oscillates faster. Therefore, the Coulomb blockade oscillation (CBO) method can tell us how fast the electrostatic potential $\phi_{\text{s}}(\vec{r})$ of the sample and the related virtual charging $Q^{ind,vir}_{\text{island}}$ of the SET changes over position.

In Figure 4.7 (b) the case for a triangular shaped potential profile is shown. This example has two peculiarites, firstly, it has a sign change and, secondly, this change happens at a turning point of the electric current modulation. Hence, constructing the electric current devolution as before gives the same measured electric current signal as for a linearly rising potential profile. This shows that the CBO method

[1] The voltage we apply is in the range of around 0.5 mV to 0.6 mV and the resulting drain current modulation amplitude is around 100 pA to 400 pA.

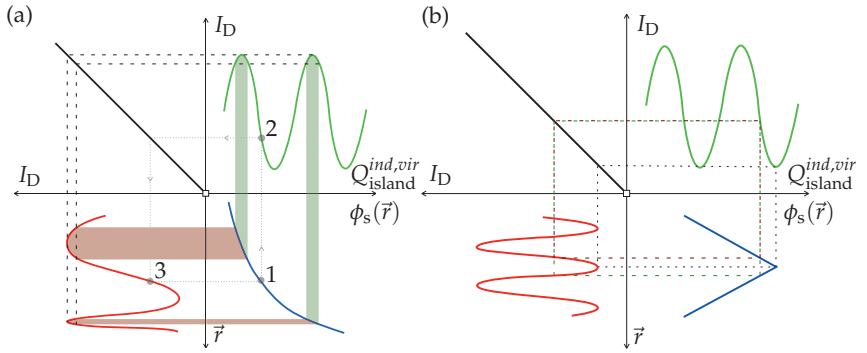

Figure 4.7:
Reconstruction of measurement signal for two exemplary potential profiles. (a) Current signal over position $\vec{r}$ (red line) for different electrostatic potential slopes of a non-linear monotonic potential profile (blue line). The green and red areas show that for the same potential variation a different position range is needed in this non-linear potential profile. Thereby the electric current signal oscillates faster for steeper slopes $\delta\phi_s(\vec{r})/\delta\vec{r}$. (b) Pronounced case in which the electric current signal is equivocal. Due to the reversing slope of the triangular shaped electrostatic potential profile at a current maximum or minimum the electric current signal looks the same as of a linear rising potential profile.

provides information about how much $Q^{ind,vir}_{island}$ and therefore $\phi_s(\vec{r})$ changes but not whether it raises or lowers down. The reconstruction of $\phi_s(\vec{r})$ from the recorded electric SET current is therefore equivocal.

After discussing the CBO measurement method we want to have a look at a real measurement at the edge of a gold surface on top of the GaAs cap layer of the sample. Usually the sample structure in the scanned area is not obvious by itself and needs information from previous capacitance measurements mapped to the sample design. In Figure 4.8 (a) the SET current modulation versus a change of the sample potential and in (b) an (x, y)-scan for fixed sample potential is shown, both recorded with the SET microscope. The drain current of the SET is plotted as a color-coded map over the (x, y)-plane. Two kinds of shapes are apparent in the graph, one following a straight line going from the left to the right bottom and four dot-like structures distributed over the measured area. Due to the unknown exact local consistency of the sample surface, surface charges and a capacitance change between island and sample have to be considered. It is very likely that the roundish shaped features result from charged particles located on the sample surface or from particles with a different dielectric constant. Those particles can be remains of photo resist from the sample fabrication for example. Further, from

the sample design it is known that there is a horizontal borderline between a gold surface and a GaAs surface in this scanned area. So we can identify the straight shaped area as a change in the capacitance C_{sample} combined with a potential gradient of the sample due to contact voltages. A guess of the sample structure is shown in Figure 4.8 (c). As the example shows, the CBO method can give us a first impression of the electrostatic landscape in a scanned area and help to find the area of interest.

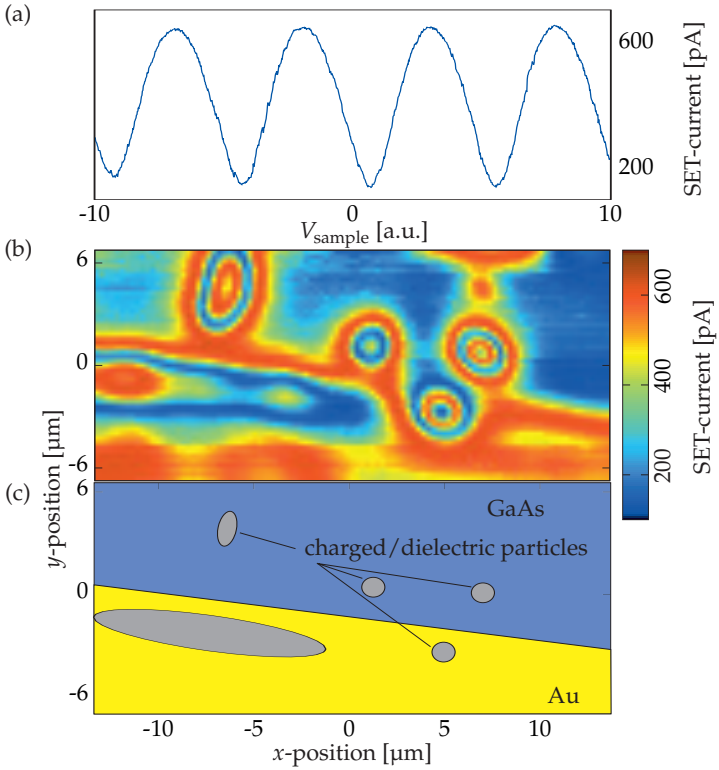

Figure 4.8:
Surface area scan with assumed surface reconstruction. (a) SET current modulation versus changed sample potential. (b) CBO method measurement showing an (x, y)-scan with four dot-like and one elongate structure from the left middle to the right bottom. Connected areas of the same color represent the same virtual charge $Q_{\text{island}}^{ind,vir}$ on the SET. (c) Sketch of the expected sample surface structure due to the measurement. In yellow a gold electrode on top of the GaAs surface (blue), with charged particles (gray) distributed over the area, is shown.

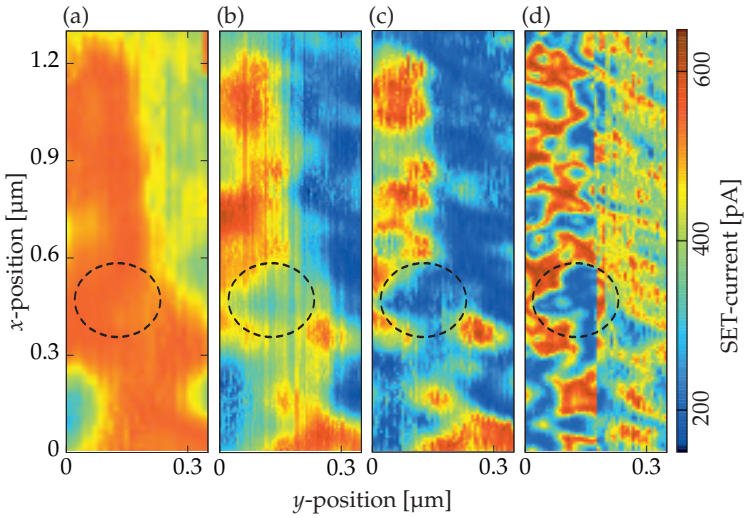

Figure 4.9:
Dependence of measurement details on the island-sample distance. (a)-(d) (x, y)-surface scan over the same sample position. The SET-island-to-sample distance measures around (a) 60 nm, (b) 32 nm, (c) 26 nm and (d) 22 nm (with an electric current modulation period versus sample potential of 30 mV, 16 mV, 13 mV and 11 mV), respectively.

Reducing the distance between sample and tip will enhance the details of the structure due to a stronger capacitive coupling between the SET island and the local sample surface. This is shown in Figure 4.9 where the same area is scanned four times. The distance between the SET island and sample measures about (a) 60 nm, (b) 32 nm, (c) 26 nm and (d) about 22 nm with an uncertainty of 2 nm. Features like the highlighted shape (dashed ellipse) evolve and get a detailed shape with decreased distance. In Figure 4.9 (d) the distance between sample and island becomes too small for the right half of the graph, therefore, we believe the SET tip has caught some particle from the surface that influences the measurement.

4.3 The Feedback Loop Measurement Method

During a scan over a sample surface the electrostatic potential of the island changes. Therefore, also the resonance condition for the electric current through the SET varies. In the previous section the CBO method was introduced which allowed to track the changes in the electric current of the SET, shown in Figure 4.10 (a) (blue).

For the measurement method presented in this section we want to keep the resonance condition for the electric current through the SET constant (black). The motivation for this course of action is to use the highest achievable potential sensitivity around the steepest slope $\delta I_{\mathrm{SET}}/\delta\phi_{\mathrm{i}}$ of the electric current characteristic for all sample potential values. Further, we will get a direct mapping of the sample potential variation without reconstructing it over the electric current characteristic as before. Therefore, the electrostatic potential of the source and drain contact together, denoted as COM potential, has to be adjusted, see Figure 4.10 (b). This can be done by measuring the change of electric current through the SET and comparing its value to a reference value. Further, the difference is used to apply a voltage to the COM potential. A feedback loop can take over this task and fixes the COM potential relative to the island potential to get the same resonance condition, as before. The result is a constant electric current as shown in Figure 4.10 (a) (black).

To see the relation between the sample, COM and island potential we start again with the virtual charge induced by the different electrodes on an isolated island and write down the relation

$$\begin{aligned} Q_0 = {} & C_{\mathrm{sample}}(V_{\mathrm{sample}} - \phi_{\mathrm{i}}^{\mathrm{isol}}) + C_{\mathrm{S}}(V_{\mathrm{S}} + V_{\mathrm{com}} - \phi_{\mathrm{i}}^{\mathrm{isol}}) \\ & + C_{\mathrm{D}}(V_{\mathrm{D}} + V_{\mathrm{com}} - \phi_{\mathrm{i}}^{\mathrm{isol}}) + C_{\mathrm{Env}}(V_{\mathrm{Env}} - \phi_{\mathrm{i}}^{\mathrm{isol}}), \end{aligned} \tag{4.11}$$

as an extension to (4.3). In the next step the environment is neglected by assuming a large capacitive coupling of the island with the sample electrode. Resolving the relation for $\phi_{\mathrm{i}}^{\mathrm{isol}}$ we get

$$\phi_{\mathrm{i}}^{\mathrm{isol}} \approx V_{\mathrm{sample}} + \frac{(C_{\mathrm{S}} + C_{\mathrm{D}})(V_{\mathrm{com}} - \phi_{\mathrm{i}}^{\mathrm{isol}}) + C_{\mathrm{S}}V_{\mathrm{S}} + C_{\mathrm{D}}V_{\mathrm{D}} - Q_0}{C_{\mathrm{sample}}}. \tag{4.12}$$

With a working feedback loop, $V_{\mathrm{com}} - \phi_{\mathrm{i}}^{\mathrm{isol}}$ is kept constant. Also the partial capacitances $C_{\mathrm{S}}, C_{\mathrm{D}}$ and their potentials $V_{\mathrm{S}}, V_{\mathrm{D}}$ are constant as well as Q_0, therefore,

we get

$$V_{\mathrm{com}} \propto \phi_{\mathrm{i}}^{\mathrm{isol}} \approx V_{\mathrm{sample}} + \frac{const}{C_{\mathrm{sample}}} \tag{4.13}$$

showing that for regulated V_{com} and constant C_{sample} the electrostatic potential of the island and thereby V_{com} is directly following all changes of the sample potential.

This direct measurement of electrostatic potential variations with the use of a feedback loop will be denoted as feedback loop method, short FBL method. In equation (4.13) we see that for measuring the sample potential with the feedback loop a constant partial capacitance between sample and island is necessary. If C_{sample} changes it will change the electrostatic potential of the island and therefore the feedback signal.

The electrical setup for the feedback loop method is shown in Figure 4.11. As in the CBO method we use an IV converter. For the same reasons of stability and sensitivity a source-drain voltage of $V_{\mathrm{SD}} \approx e/C_{\Sigma}$ is chosen, to get a large electric current modulation amplitude and no ranges of constant electric current while virtually charging the island. After measuring the electric current through the SET

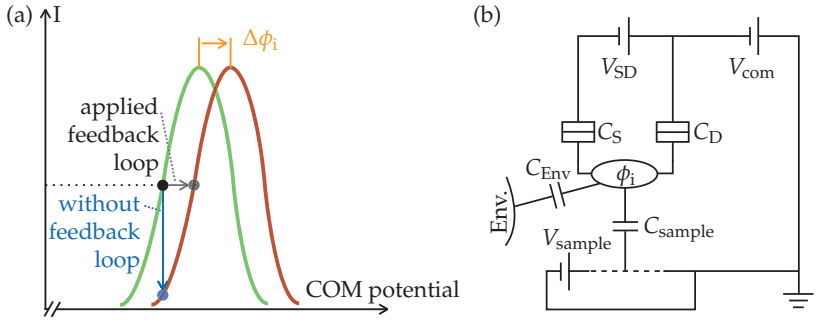

Figure 4.10:
Sketch of measurement concept and electrical circuit for the FBL method. (a) A shift of the Coulomb blockade oscillations by a change in the electrostatic island potential on the COM potential axis is shown. The green and red curve represent the electric current characteristic for different ϕ_{i} induced by the sample. Without feedback loop (blue) the measured electric current changes and we get the CBO method. The case with feedback loop is illustrated in black. The loop keeps the electric current constant by applying a compensation voltage to source and drain (COM) of the SET. (b) Sketch of the substituting electrical circuit for an SET over the sample surface.

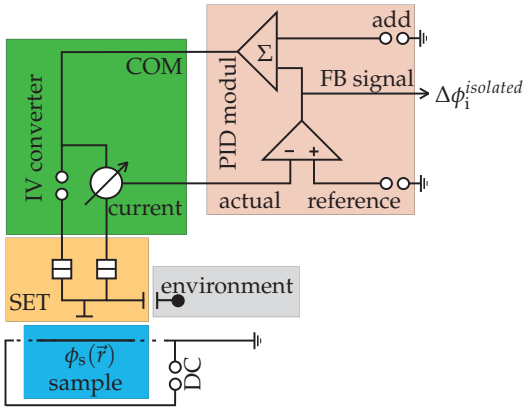

Figure 4.11:
Schematic of the electrical measurement setup needed for the feedback loop method. Compared to the electrical setup scheme of the CBO method a PID module (red) is added. This additional module compares the present electric current to a reference value and applies the difference as a voltage through an adder to the IV-converter. There the voltage is added to the source and drain potential (COM) of the SET. The PID module further features an output for the FBL signal representing the electrostatic potential change of the SET island.

and converting it to a voltage signal, the electrical setup differs from the one of the CBO method. An additional proportional-integral-differential (PID) module is used to compare the measured electric current signal to an applied external voltage.[2] After comparing both signals the difference is split to be measured by a voltmeter and fed back into the IV converter, where it is added to the source and drain potential of the SET as a COM voltage.

We have to think about which electric current through the SET and therefore which fixed $Q_{\text{island}}^{surplus}$ would fit best to get a stable and sensitive feedback loop. For a fixed V_{SD}, an electric current through the SET on the steepest slope of an electric current peak, as shown by the black dot in Figure 4.10 (a), is satisfying both requirements. This gives us two advantages: Firstly, we obtain the highest sensitivity and, secondly, even for a time delay in the loop there is enough tolerance for the feedback loop to react, resulting in a stable measurement. The drawn black point on the electric current characteristics in Figure 4.10 (a) will be called working point in the following.

[2] In the real setup the differential part of the PID was switched off and an RC filter of second order with a cut-off frequency of 23Hz had to be added between the output voltage of the IV-converter and the PID module to enhance the systems stability.

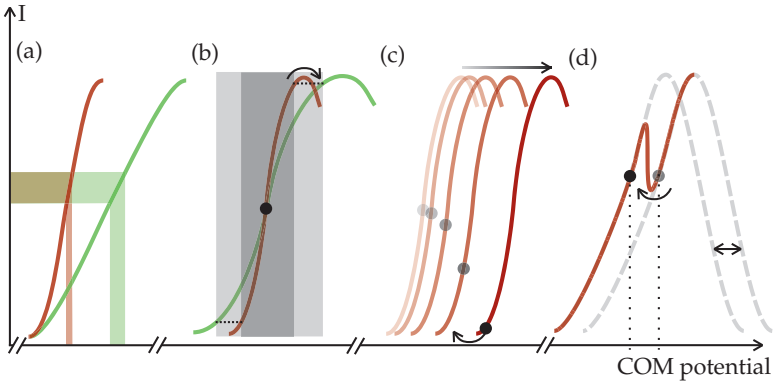

Figure 4.12:
Different situations for the SET current I_D versus COM potential in which the feedback loop becomes instable. (a) Showing the sensitivity difference for high (red) and low (green) capacitive coupling to a sample electrode. The horizontal areas indicate the same electric current range in which the feedback loop can react and the vertical areas the related electrostatic potential change on the island plotted on the COM axis. (b) The gray areas show different levels of fluctuations of the island potential. This can lead to jumps between different charge states of the SET for a small CBO period. (c) Case of a fast change in $Q_{\text{island}}^{ind,vir}$ due to a fast sample potential variation for example. With a too large time delay in the PID, due to RC-filters and the integral part, the feedback loop cannot keep the electric current constant and the working point is shifted towards the next electric current modulation period. As a result the FB signal will jump by e/C_G and retries to fit the measured electric current output voltage of the IV-converter to the reference voltage. (d) The electric current characteristics can have variating slopes due to charging events of particles near the SET island. Therefore, the stability of the feedback loop is reduced.

Nevertheless there are some stability issues for certain cases making the measurement with the FBL method fragile. They are illustrated in the drawings of Figure 4.12. First of all, an enhanced capacitance C_{sample} between sample and island leads to a larger change in the virtual induced charge of the SET island for the same electrostatic potential changes on the sample as (4.1) shows. Therefore, the period of the Coulomb blockade oscillations is decreased and the electric current slope will get steeper as illustrated in Figure 4.12 (a). While the sensitivity of the feedback loop increases it will become less stable for electrostatic potential fluctuations as shown in Figure 4.12 (b). In this case the potential fluctuations on the island can lead to a shifting of the working point to an unstable position on the current-potential characteristic. As a consequence the feedback loop will try to match the reference voltage by fixing the electric current through the SET on the

next Coulomb blockade oscillation peak. In the end the measured signal will jump by the value of e/C_G. Such a jump can also happen if a change of the electrostatic island potential happens too fast and the feedback loop cannot follow[3], which is illustrated in Figure 4.12 (c). Another instability for the feedback loop is coming from particles near the SET island that change their charge state in discrete steps. This sudden change also shifts the electrostatic potential of the SET island and results in a jump in the electric current characteristics of the SET illustrated in Figure 4.12 (d). Therefore, the feedback loop might jump between two stable output values for much smaller fluctuations. The mentioned particles can either sit on the SET itself, on the sample surface, or in the donor layer of the sample. Usually choosing another $Q_{\text{island}}^{ind,vir}$ by applying an additional voltage to the COM signal can solve this problem due to the change of the electrostatic configuration for the particle. The additional COM voltage can be applied by the adder input shown in Figure 4.11.

A surface area scan using the FBL method is displayed in Figure 4.13. This data was intentionally chosen to also illustrate the instabilities of the measurement method. In the setup the value for the reference voltage could have been chosen different

[3]The reaction time of the feedback loop due to all RC-components in the circuit measures around 300 ms.

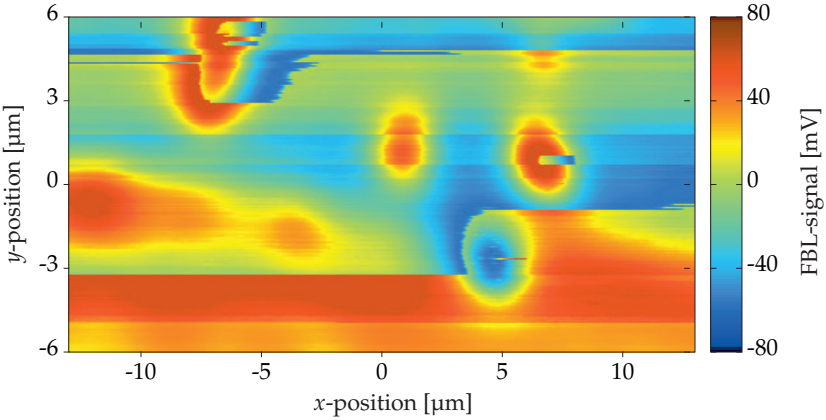

Figure 4.13:
Sample surface area scan executed with the feedback loop method for the same area as for the CBO method area scan in Figure 4.8. In this data the electrostatic potential change of the SET island is shown. In contrast to the CBO method the sign of the charged particles can be measured and the direction in which the sample potential gradient points is measurable.

to get better results. The feedback signal and therefore the shift of the electrostatic potential of the SET island is shown color-coded over the (x, y)-direction. In this measurement as for the CBO method we can see electrostatic potential, capacitive changes and charges located on the surface. As for the measurement with the CBO method we can see the four circular shaped areas and the elongated shape from the left to the right bottom.

The sudden color changes around the dots either result from reset events of the PID module reaching its limits or from a loss of the used charge state of the SET island due to the fast and large electrostatic potential changes of the sample. Another reason for those color changes can be the large COM signal applied slightly asymmetrically to the source and drain contact in the IV-converter module due to the variations of the resistance values around the operation amplifiers[4]. This leads to a changed electric current characteristic in which the old fixed electric current value can be at an instable spot as shown in Figure 4.14 green or red curve.

There are some possibilities to get rid of such jumps. First of all, one has to avoid strong electrostatic potential variations and should seek a nice smooth spot on the relevant sample structure. Secondly, one should extend the COM range and fine tune the added source and drain voltage in the electrical setup. Thirdly, we can

[4]Even that they are as small as 0.01 %.

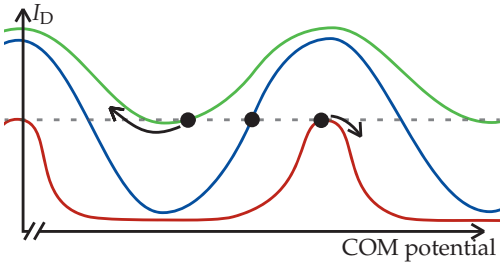

Figure 4.14:
Instable working point configurations resulting from an asymmetrically applied COM voltage which is changing V_{SD}. The blue curve presents the electric current profile for a well adjusted source-drain voltage. The green and red curves show the results of a too large or too small source-drain voltage. In all three cases the electric current through the SET is kept constant in respect to specified reference voltage. For the red and green curves the working point of the feedback loop is at an instable position and can easily jump to the next SET current peak.

reduce the scan speed or fix the source-drain voltage V_{SD} to a more stable working point configuration for this scan area.

In summary, the feedback loop method allows direct access to the electrostatic potential distribution on a surface for fixed partial capacitance between SET and sample. It has some instabilities caused by the delay in the feedback loop or abrupt changes in the SET current characteristics. However the FBL method does not distinguish between a change in partial capacitance, electrostatic potential or a charged particle at the sample surface.

4.4 AC-Feedback Loop Measurement Method

With the microscope setup we want to measure the electrostatic potential distribution of a sample without any part of the signal coming from a change in the capacitive coupling between SET island and sample. Therefore, we have to distinguish in our measurement signal between capacitive changes and potential changes, while scanning the sample surface. In this section an extension of the FBL method will be presented trying to reach this goal.

The capacitance between the island and the sample can be calculated by

$$C_{\text{sample}} = \frac{\partial Q^{ind,vir}_{\text{island}}}{\partial V_{\text{sample}}}, \tag{4.14}$$

sweeping the sample potential up and measuring the amount of charge virtually added to the island. This is done with the CBO method by measuring the electric current through the SET and counting the Coulomb blockade oscillations shifting through. The easiest way to calculate C_{sample} is to change V_{sample} that much that

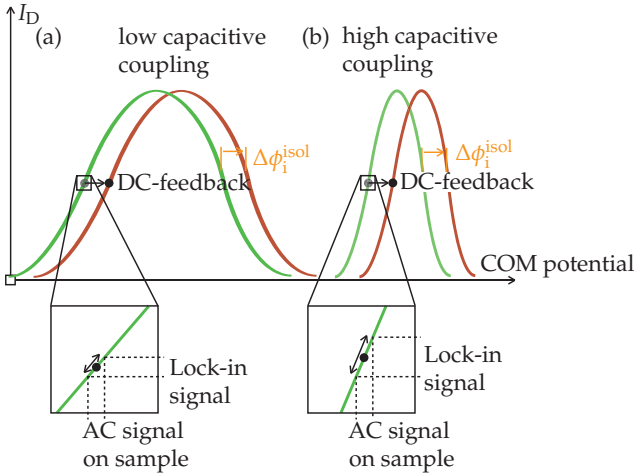

Figure 4.15:
Measurement concept of the AC-FBL method for two different sample-to-SET-island capacitive couplings. (a) Low capacitive coupling between SET island and sample resulting in a large period of the electric current characteristic. (b) High capacitive coupling with a short period in the electric current profile. The zoom-in on the bottom are showing the different slopes, related to the capacitive coupling between SET island and sample, for fixed $Q^{ind,vir}_{\text{island}}$ measured by a lock-in amplifier.

exactly one Coulomb blockade oscillation peak period over sample potential is obtained, therefore, one electron is added to the SET island. However it can be reduced to a fraction of an elementary charge if we can conclude from a part of the electric current modulation to the whole CBO characteristics. Therefore, a larger part of the CBO characteristics has to be measured and fitted by a function in advance. Then we can measure the electric current variation over a small sample potential variation at a known and fixed $Q_{\text{island}}^{ind,vir}$ and interpolate the measurement. For this purpose we can use an AC voltage added to the sample potential producing the mentioned small sweep periodically over time. A lock-in amplifier measures the change in the electric current through the SET with the help of an IV-converter module. In Figure 4.15 (a) the case of a low capacitive coupling between island and gate electrode and in (b) a high capacitive coupling is shown. Due to the higher coupling the CBO peak period over sample potential on the right is shorter and the slope of the flank of the electric current peak steeper.

$Q_{\text{island}}^{ind,vir}$ can be fixed by using the DC feedback loop, which at the same time measures the change of the electrostatic potential for the SET island. With the AC measurement we obtain the partial capacitance between sample and SET island. Knowing about V_{com} and C_{sample} in (4.13) we can calculate V_{sample} by

$$\Delta V_{\text{sample}} \approx \Delta V_{\text{com}} - \frac{const}{C_{\text{sample}}} \tag{4.15}$$

even for changing C_{sample}. This third measurement principle, using an extra AC signal on the sample in the FBL method to gain information about the capacitive coupling, will be called AC-feedback loop (AC-FBL) method.

The electrical setup of the FBL method has to be extended by an AC signal on the sample, by a low-pass filter of higher order in front of the PID module and by a lock-in amplifier as shown in Figure 4.16. The additional AC signal has to be of higher frequency so that the feedback loop cannot follow.[5] The AC filter between IV-converter and PID module helps to reduce the AC signal that the feedback loop can see and therefore should have a cut-off frequency lower than the AC frequency.[6] In this way the alternating signal from the sample is just reaching the lock-in amplifier directly connected to the IV-converter output. The signal of this lock-in amplifier is measuring the capacitive coupling between the SET island and the sample.

[5] With a delay time of 300 ms for the feedback loop, we chose a frequency of around 8.9 Hz to get no crosstalk on the measurement lines.

[6] We chose a cut-off freqeuncy around 6 Hz.

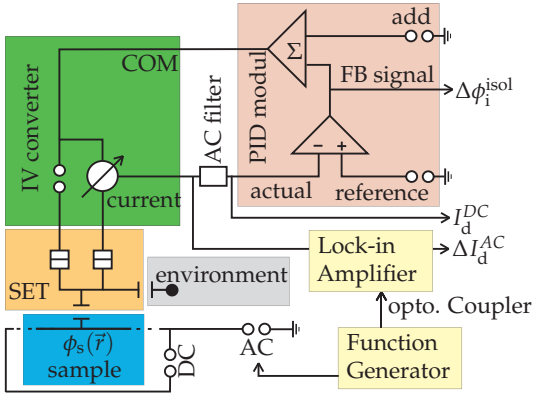

Figure 4.16:
Sketch of the electrical setup necessary to carry out a measurement with the so-called AC feedback method. Compared to the FBL method we have an additional small AC signal on the sample, a low-pass filter between IV-converter and PID module, and a lock-in amplifier. The amplifier is measuring the AC induced electric current oscillation of the SET before the low-pass filter.

Knowing the working principle behind the AC-FBL method we can look at a real measurement, demonstrating the method qualitatively. In Figure 4.17 an approach of the SET tip towards a gold electrode on the sample surface while scanning in y-direction is shown. The line scan was done to get data at different positions to be able to make a comparison or average later on. Figure 4.17 (a) shows the FBL signal and (b) the trans-conductance for the AC signal, both plotted over a y-position range and an z-position with an arbitrary offset. The FBL-signal is showing the electrostatic potential shift of the SET island during this approach. The trans-conductance is displaying the change in the partial capacitance between the SET island and the sample. In the measurement the absolute value of the lock-in signal is showing an increasing capacitance between SET island and surface electrode, as expected for the decreasing tip-sample distance. The SET current and the lock-in phase stayed at a constant value for the whole scan, indicating a correct adjustment of the feedback loop. If this would not be the case $Q_{\text{island}}^{ind,vir}$ could change, causing a change in I_d^{DC} and therefore a different slope would be measured with the AC signal resulting in a changed phase and absolute amplitude value, making the measurement invalid.

The AC-FBL method distinguishes between capacitive and electrostatic potential changes. Nevertheless, the method is quite fragile due to the required small AC signal, compared to the sample potential variations. Another aspect which

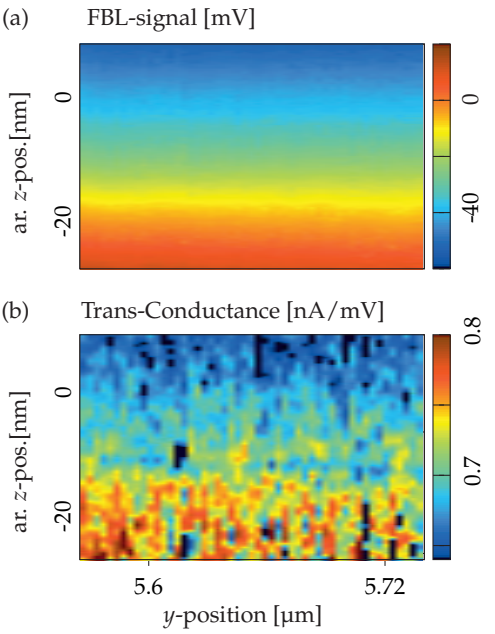

Figure 4.17:
Approach of the SET island to the sample surface for different y-position. The z-position is relative to a freely chosen offset point above the surface. (a) Feedback signal representing the electrostatic potential shift of the isolated SET island. (b) Trans-conductance measured by the lock-in amplifier. It represents the slope $\partial I_D / \partial V_{sample}$ of the current modulation at the working point. The measurement was done with an AC frequency of around 8.9 Hz, an amplitude of 1 mV with a CBO peak period of around 50 mV over sample potential.

was assumed for this measurement method but is not always valid is that there is no local reduction of the AC voltage amplitude for a conductive part of the sample. This could be the case if a conductive area on the sample has a high ohmic connection to the AC voltage contact and the resulting capacitor cannot fully charge and discharge within one period. To reduce the chance of having such a situation on the sample, the AC frequencies have to be kept low.

4.5 Summary and Method Comparison

In this chapter the electrostatic influences on the SET island while scanning a sample surface were explained. Hereby the electrostatic potential ϕ_i of the quasi-isolated SET island can be described by the general equation

$$\phi_\mathrm{i} = \frac{Q_\mathrm{island}^{ind,vir}}{C_\Sigma} - \frac{N \cdot e}{C_\Sigma}. \tag{4.16}$$

In this equation C_Σ is the sum of all partial capacitances between the island and its surroundings. Further, there is the virtual induced charge on the SET island that can either be induced by a variation in the sample potential or capacitance and is calculated by $Q_\mathrm{island}^{ind,vir} = C_\mathrm{sample} \cdot V_\mathrm{sample}$ or by charge located on the sample surface. Due to the quasi-isolated case of the island and the quantization of the electric charge this continuously changing charge cannot be obtained by Gauss's law and therefore is denoted as virtual. N is the number of electrons located on the SET island.

After the theoretical part, three different measurement methods were introduced: the Coulomb blockade oscillation (CBO) method, the feedback loop (FBL) method and the AC extended FBL (AC-FBL) method. The first two allow to obtain different information about the electrostatic situation of the SET island. The third combines those two methods by using an AC and a DC voltage on the sample. All three methods are shown in Figure 4.18 where (a) illustrates the scanned sample structure.

In the case of the CBO method, we measure the electric current variation through the SET for a fixed source-drain voltage. The mentioned influences on the electrostatic potential of the SET island can change this electric current. A change in sample potential can only be measured and mapped to a potential scale if a linear part of the CBO peak is used. Leaving this linear regime or even going to another CBO peak the electric current through the SET repeats its value and becomes equivocal. That means only for very small electrostatic potential changes the CBO method is a good choice due to its simple electrical setup and the resulting low noise level. Further, we can measure the periodicity of the electric current characteristic versus a sample potential sweep. Thereby we know how much the sample potential has to change to get a different charge state on the SET. This information allows to calculate the capacitive coupling of the island to sample electrode and therefore it allows calculations of the distance to the sample. On the other hand the Coulomb blockade oscillation method is good to get a first robust

measurement, for example, a contour map of the electrostatic configuration on the sample surface, see Figure 4.18 (b). In those contour maps the areas of same electric SET current that are connected are equipotential lines in concern of the electrostatic potential of the SET island.

The feedback loop method, as the name tells, uses an analog feedback loop that keeps the electric current through the SET constant, ideally at constant source-drain voltage. The loop varies the COM potential (source plus drain potential) to stay at the same resonance condition

$$\phi_{\mathrm{i}} - V_{\mathrm{com}} = \mathrm{const} \tag{4.17}$$

for the electric current through the SET even that the electrostatic island potential is affected by external influences. Thereby we can keep the SET in a certain charge state and get a direct mapping of the electrostatic potential of the island to the feedback loop signal. For a pure sample potential change with fixed geometry the feedback loop method allows to record this change directly over a large potential range. An example of a surface area scan is presented in Figure 4.18 (c) for the sample structure shown in (a). The FBL method cannot measure the periodicity in the electric current characteristic, therefore, it does not provide information about the capacitive situation towards the sample.

For the third and last measurement method presented, a small and relatively fast AC signal is applied to the sample. This AC signal is measured and filtered out so that the feedback loop can be operated in DC. By this we can fix a working point on an SET current peak and record all changes the electrostatic potential of the SET island sees in DC. With the AC signal we get information on the CBO peak slope at the working point and therefore know simultaneously about changes in sample-island capacitance. A demonstration of this measurement method is displayed in Figure 4.18 (d) scanning over an edge of a sample electrode. If the AC signal is showing no change on a scanned clean sample, the DC signal displays directly the variation in sample potential.

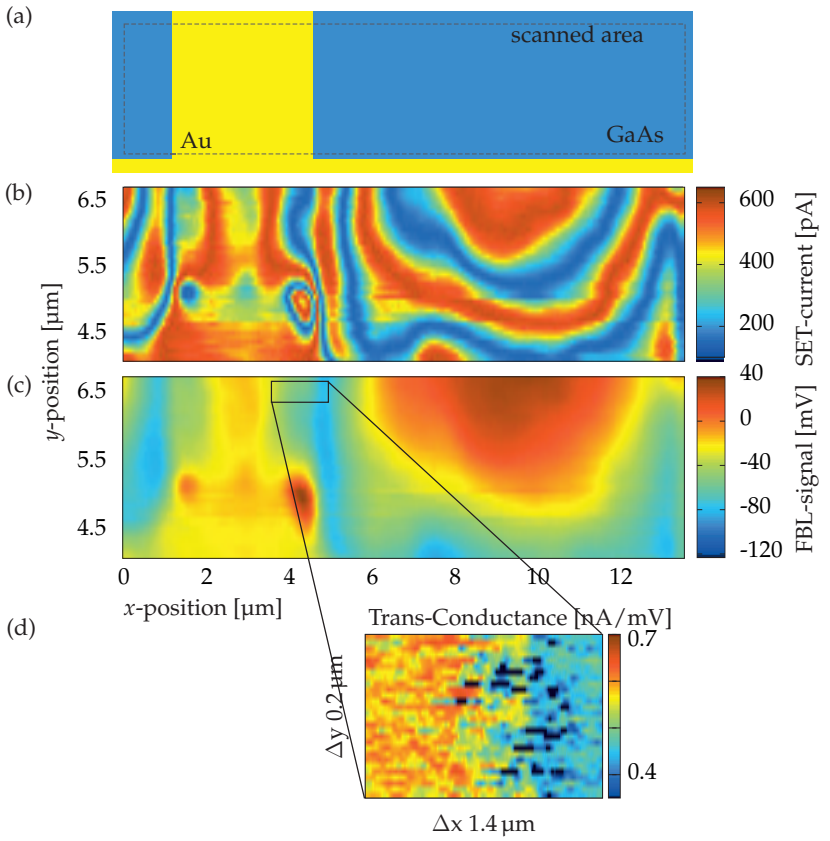

Figure 4.18:
Comparison between CBO, FBL and AC-FBL measurement method for the same scan area on a sample structure. (a) Sketch of the sample structure partly scanned in (b) to (d). The structure includes a gold electrode (yellow) located on top of the GaAs surface (blue) of the sample. The scan range is indicated by the dashed line. (b) Scan done with CBO method showing color-coded the electric current through the SET over the (x, y)-area. The connected areas with the same color present equipotential lines for the electrostatic potential of the SET island. (c) Measurement done with the FBL method displaying color-coded the feedback signal, equal to the electrostatic potential change of the SET island over the sample (x, y)-area. The scan shows similar features as the one recorded with the CBO method. The two dot-like structures are likely to be charged particles on the sample surface. (d) Scan done with the AC-FBL method over a smaller (x, y)-area at the edge of the gold electrode. The AC part of the signal is depicted and indicates a change in the partial capacitance to the sample. This was expected for this area of the scanned structure.

5
Navigation and Sample Design

Atomic force microscopes (AFM) [72] measure the atomic force acting between the tip and the sample surface. Therefore, they allow to record the topology of any sample surface. Scanning tunneling microscopes (STM) [73] need a conductive surface to get a measurement signal showing the topology and are thereby restricted in the choice of samples. In our case of a single-electron transistor as probing tip, our measurement signal is restricted to influences changing the electrostatic potential of the SET island. Thus, we do not have a straight way to scan the sample topology.

Concerning the measurement of potential distribution in a quantum Hall effect sample a further difference to most scanning probe tasks is that we need to navigate the probing tips to a certain structured, electrically active sample part. Consequentially, a sophisticated sample design allowing us to navigate over the sample surface solely by capacitive measurements.

Further, we have to approach the sample to a distance of few tens of nanometer to the surface without touching it. A direct contact would harm the SET tip and make the probe useless. In contrast to an AFM or STM tip they cannot be redefined by any procedure, like applying high voltage pulses between tip and sample.

The navigation and its requirements to the sample design are discussed in this chapter.

5.1 Navigation of the Probing Tip over the Sample Structure

The two changes on the sample surface, we are sensitive on with the SET tip are a change in the partial capacitive coupling and a change in sample potential, see relation (4.4). Therefore, we can proceed in two ways to determine our position on the sample:

- Fix the geometric configuration meaning the partial capacitances of the SET island towards its surroundings and sweep the potentials of different sample electrodes one after another.
- Keep the electrostatic potentials of all sample electrodes constant and scan the sample surface. This means we change the partial capacitances and try to identify different geometric configuration for the SET island with structures on the sample design.

Coarse, large distance navigation
For a coarse, fast and long range navigation with more than 10 µm distance between sample and tip we have to choose the first option[1]. The electronic setup is illustrated schematically in Figure 5.1 (a). In this case the electrostatic potentials of different sample electrodes are swept through one after the other. With the Coulomb blockade oscillation method we can measure the periodicity of the CBO peaks over those potential sweeps, shown in Figure 5.1 (b). The smaller this periodicity $e/C_{\text{sam-i}}$ over an electrostatic potential change is, the larger the partial capacitance and therefore the smaller the distance between selected electrode and SET island measures[2]. This coarse navigation measurement method with a tip-sample distance of more than 10 µm covers distance information to electrodes widely spread over the sample, the area we are sensitive to increasing with tip-sample distance.

Fine, small distance navigation
A continuous scan of the SET with fixed electrode potentials over large sample areas would take hours. At 10 µm tip-sample distance we would only see very weak modulations of our measurement signal that make it hardly possible to map them to the sample design.

[1] The initial state after cooling down the microscope has a tip-sample distance of around 1 mm to avoid contact between probing tips and bond wires of the sample.

[2] SET current modulation measurements for closest proximity between tip and surface electode and the resulting strange behavior is shown in Appendix C.1 on page 193.

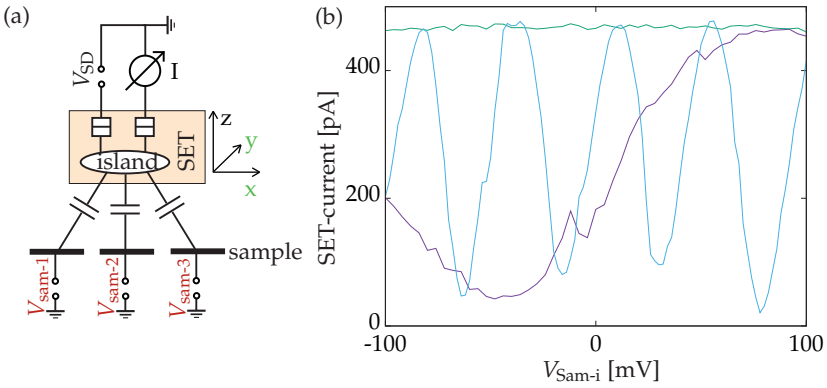

Figure 5.1:
Technique to determine the SET position relatively to several sample electrodes with the CBO method. (a) Sketch of the electronic setup for a coarse navigation measurement with several sample electrodes and their partial capacitances to the SET island. (b) Measurement of the SET current modulation versus applied voltage for three different sample electrodes, located at different distances to the SET island or having different lateral dimensions. Different periodicities of the profiles indicate a smaller distance (blue), a medium distance (violet) and a larger distance (green) between SET island and electrode. A slight variation of the minimum of the SET current value was observed in a large number of measurements but the reason is not clarified up to now.

In the range of less than 10 µm tip-sample distance the coarse measurement technique becomes less useful. This is due to the enhancing partial capacitance to one electrode and its screening of other nearby sample electrodes. Therefore, potential variations of electrodes just several micrometer away can vanish in the measurement signal. In this regime the second way to record sample structures becomes more and more important with decreasing tip-sample distance. While scans with large distances look smeared out, as Figure 5.2 (a) shows, scans with reduced distance become more and more detailed, see Figure 5.2 (b). The amount of features seen in the obtained images can even become confusing and can outbalance the sample structures. For this last case, an example is shown in Figure 5.2 (c). All of those images were taken at the same sample area in which a gold electrode on the sample surface with a rectangular shaped window to the GaAs substrate is present.

The method of moving the SET island over the sample surface with fixed potentials works more or less for all sample parts where a significant change in the geometric situation around the SET island is present. That means this fine navigation

shows sample structures due to material or height changes even without using a particularly designed sample electrode.

Enhanced navigation

To increase even further the certainty about the tip position on the sample design we can combine both techniques. Doing so we get a continuous picture of the sample structures and have the possibility to identify the scanned areas as certain sample electrodes by sweeping their potential.

Tip-to-sample approach

After navigating to a preferably large metal electrode on the sample surface nearby the area of interest, the next step is to approach to the sample surface. This can be done by a similar procedure as for the coarse navigation. We sweep the electrostatic potential of this one sample electrode below the SET island and measure the CBO peak periodicity over sample potential. The electronic setup for this measurement is the same as for the coarse navigation method shown in Figure 5.1 (a).[3] In Figure 5.3 (a) and (b) the periodicity of the electric current through the SET over

[3]The smaller this periodicity gets the smaller the tip-sample distance becomes and it is advisable to reduce the distance step size from an irregular Attocube positioner step to a continuously controlled piezo tube elongation. Due to growth defects in the heterostructure with a height of up to 4 µm the tips should be moved with care in lateral direction after approaching the sample.

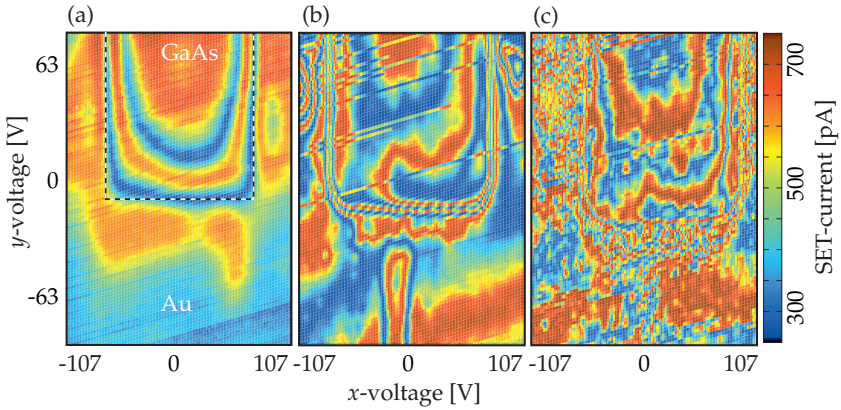

Figure 5.2:
Continuous scans at different heights over a sample area with a framed Au electrode on top of a GaAs substrate. During the scan a constant voltage is applied to the gold electrode. The pictures were taken with the CBO method, therefore, they show the SET current over (x, y)-position given in applied voltage to the piezo tube. The tip-sample distance is reduced from (a) to (c) while the degree of detail in the obtained data increases.

sample potential is shown. This data was simulated with a geometric configuration similar to the real one. The violet curve shows the decrease of the periodicity in SET current by tuning the sample potential with decreasing tip-sample distance. The shape of the curve confirms the measured data from previous measurements done for the diploma thesis [67]. The discrepancy to these previous measurements can be explained due to the following: The SET tips were different and may have therefore different dimensions; The sometimes non-linear resistive positioning system of the positioners was used in the older measurements to determine the z-position.

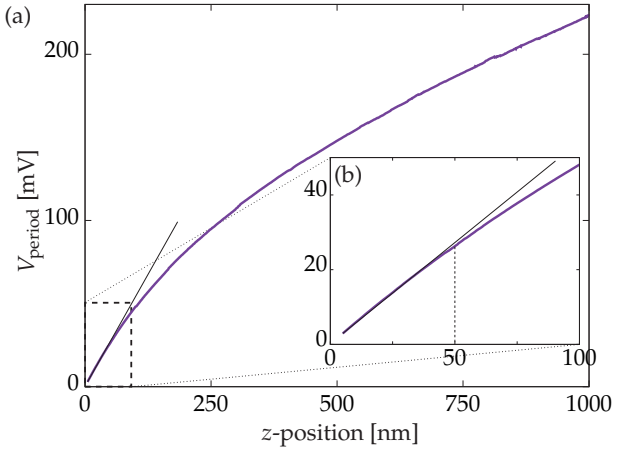

Figure 5.3:
(a) Periodicity of the modulation of the electric current through the SET by tuning the sample potential as a function of the tip-sample distance. (b) Zoom-in. A linear function can be fitted with good agreement for tip-sample distances below 50 nm, indicating a plate-type capacitor-like configuration [27].

5.2 Sample Design

The explained method to execute a coarse navigation measurement promises to be fast in determining the position of the probing tips over the sample. Of course, some rules for the shape and position of the used electrodes have to be obeyed to avoid an ambiguous determination of position, to be able to map the coordinate system of the positioners from Attocube (AP), mentioned in the setup, to the electrode design and not to disturb the area of interest:

- The distance between different electrodes should be decently small, around 5 µm. This value is chosen not to be blind in a large area with the probing tips but also not to risk shortcuts due to the sample fabrication process by optical lithography.
- Some of the electrodes should be sized large enough to easily find them and they should be placed around the sample structures of interest.
- There have to be some borderlines between electrodes going along the x-direction and the y-direction to map the AP coordinate system to the one of the sample. [4]
- The electrodes connected to two different electrical contacts should not be periodic along a spatial direction over a large area, else they are either not resolvable or the borderlines are not distinguishable and the actual position in both cases stays unclear. (An exception is a structure used for calibrating the microscope)
- Small detailed electrodes should be placed in an arrangement around the area of interest to be able to navigate exactly onto the physical relevant structure.
- All electrodes should have enough distance to the area of interest, so they do not disturb the local electrostatic configuration.

Out of those thoughts and requirements the rough outer and the detailed inner sample design shown in Figure 5.4 (a) and (b) was developed. The sample size measures 4.0 mm by 4.5 mm to cover the whole positioning range of the AP within the sample. All positioning electrodes are colored in green. Electrodes shown in yellow are contacts for two six-terminal Hall bar structures. The distance between

[4] The Attocube positioner have a resistive position measurement that has an uncertainty of around 30 µm below 100 mK at 1.4 V excitation.

two neighboring leads or electrode areas measures 6 µm to be on the safe side for the sample fabrication and reduce wastage of the valuable heterostructure material. The electrical connection is done by the bond pads[5] all located on the lower part of the sample to avoid a mechanical contact between bond wires and tips during the cool down procedure. [6] The single small orange colored bonding pad in Figure 5.4 (a) is thought to implement a not yet used back-gate connection.

Looking at the sample overview, we can see five large positioning areas that are designed to easily find out in which quadrant the probing tip is situated initially. Each of those positioning areas has a length of roughly 1 mm in both lateral directions and they have borderlines into x-direction and y-direction of the AP coordinates. The lower left quadrant is divided into two electrodes with the borderline running between calibration structures to characterize the scanning unit and towards the center of the sample. Those two electrodes can be connected and be swept in potential simultaneously for a first coarse navigation of the probing tip to avoid an alternating electrode design in the calibration structure area. Later, after the navigation and approach the periodic design of the calibration structures, their alternating potential can be used to verify the correct piezo tube elongation.

In Figure 5.4 (b) an optical microscope image showing a zoom-in of the structures of (a) around the middle of the sample is presented. Three of the five large positioning electrodes are again colored in green. The two of them featuring the calibration structures with alternating gold fingers are now colored in turquoise and orange.

In dark green the positioning electrodes meant to navigate in the area of the Hall bar structures (blue) are shown. Those small positioning electrodes are arranged in a way that the borderline in the center points towards the middle of the Hall bar structures and the borderlines above and below are pointing to the middle of the lower, respectively upper half of those structures.

The dark green positioning areas have a minimum distance of 30 µm to the physical relevant structures. In true color the contact lines of the Hall bar structures are displayed with the ohmic contacts highlighted in red. The Hall bar structures of 20 µm width are the only areas of the sample possessing a 120 nm deep buried two-dimensional electron system. Those two Hall bar structures are meant to be redundant for the case that one is not working correctly. To make a low resistance

[5] A picture of the wire bonded sample on a flexible circuit board on a sample holder is shown in Appendix D.2 on page 209.

[6] Due to the one-sided direction of the bond wires the sample has to be glued to the sample carrier under the bond pads to avoid mechanical tension and as result broken samples after the cool down.

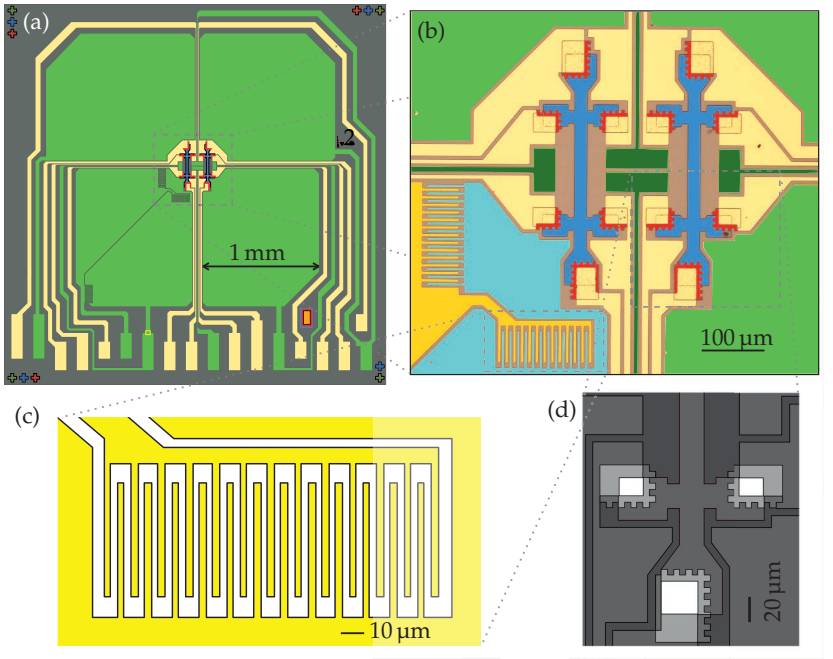

Figure 5.4:
Different zoom-in images showing different aspects of the sample structure. (a) Overview of the sample measuring 4.0 mm by 4.5 mm. The positioning electrodes (green) and the different Hall bar contacts (yellow) are shown. (b) Image taken with an optical microscope showing a zoom-in on the middle of the sample including the two six-terminal Hall bar structures (blue) with ohmic contacts (red). The coarse and fine positioning electrodes (different shades of green) are shown, as well as the calibration structures for the scanning unit (turquoise and orange). (c) Enlargement of the x-direction calibration structure depicting the alternating fingers from two different electrodes. (d) Height map of the lower part of the right Hall bar structure with four different heights, with steps of 100 nm to 150 nm between them. The lighter the gray the further the structure stands out of the sample plane.

contact to this two-dimensional electron system [74,75] the ohmic contacts were designed in a tooth-like shape to have enough borderline in both crystal directions.

A zoom-in of the x-direction calibration structure used for the characterization of the microscope is shown in Figure 5.4 (c). The structure is invariant in y-direction and periodic in x-direction to calibrate the scanning system. By this shape it does not matter where the probing tips are exactly positioned as long as they are located within the structured area of 40 µm by 200 µm.

As a last but very valuable zoom-in, Figure 5.4 (d) shows the lower half of the right Hall bar structure as a height map. The brighter the gray is chosen the further the structure reaches out of the sample surface plane. Between the different heights there are steps of 100 nm to 150 nm in height which can become risky for scans with the probing tips in closest proximity. To avoid damage to the SET tips or even a loss of them, such a height map should be drawn for every new sample structure.

5.3 Summary

In this chapter we saw that the navigation on the sample and the approach rely on the change in capacitance between SET island and sample electrode. Therefore, we need conductive and connected sample areas to sweep their electrostatic potential and conclude from their influence on the SET to the capacitive coupling between them and the SET island. It gives us an idea about the respective distance.

Due to the unreliability of the resistive positioning system of the positioners this is the only way to navigate the probing tips to the right sample spot. For an easy navigation some requirements to the sample design have to be considered:

- A reliable and not repeating arrangement of surface electrodes has to be realized on the sample surface.
- Except the area that has to be investigated the sample surface has to be covered with connected electrodes.
- The electrodes should not interfere with the physically relevant structures.

Based on those general requirements our sample structure was designed.

6
Characterization

The scanning SET array microscope was primarily built to measure the electrostatic potential distribution on samples in the fractional quantum Hall regime. Therefore, the microscope has to reach temperatures in the milli-Kelvin range so that fractional quantum Hall states can be fully evolved [76,77,79]. Due to the low energy scales of the fractional quantum Hall effect, only small voltage excitations on the sample are possible. Thus, a good electrical sensitivity of few 100 µV and a stable measurement signal on the scale of hours is required for the probing tip.

A typical Hall bar structure width, measured by scanning probe microscopes [14,58], lies between 10 µm to 20 µm. Therefore, a scan range of more than 20 µm should be achieved. On the other side, the mechanical stability and the lateral resolution of the microscope have to lie in the few 100 nm range to cover even small features of the electrostatic potential distribution [16].

The fractional quantum Hall effect usually requires high magnetic fields of several Tesla to measure stable states and relieve the demands on operation temperature, electrical sensitivity of the sensor and sample properties. The stainless steel, the microscope consists of, will cause shifts due to the applied magnetic field changes. Hence tip-to-sample position shifts have to be compensated.

All characteristic figures relevant for the mentioned requirements will be presented and specified in this chapter. First, the mechanical properties will be discussed. We start with the adjustment of the different coordinate systems, calibrate the scan range, determine the mechanical stability, figure out the spatial resolution, and finally show how to correct mechanical shifts caused by deformations of the microscope structure due to magnetic field changes. Afterwards, the stability of the measurement signal of our scanning tips and their sensitivity will be determined, leading to the characteristic figures for our microscope. Finally the measurement of the working temperature will be shown and explained.

6.1 Adjustment and Test of the Scanning System

In our case of an one-dimensional tip array scanned over a sample, we get three different coordinate systems we have to adjust to each other. This is necessary to get a geometrically correct area scan of several probing tips at once. The different coordinate systems are illustrated in Figure 6.1 (a). Firstly, there are the three scan axes of the piezo tube $(\vec{x}_t, \vec{y}_t, \vec{z}_t)$ that should be independent and orthogonal to each other. Secondly, there is the coordinate system of the sample $(\vec{x}_s, \vec{y}_s, \vec{z}_s)$ to which the scan axes have to be aligned parallel. Thirdly, there is a line through all SET islands $\vec{a}$ which should be parallel to the sample surface in potential distribution measurements[1].

The goniometer positioner tilting the sample around the $\vec{x}_s$-axis can align the sample surface parallel with the line going through all SET islands of the tip array, see Figuree 6.1 (b). Thereby all SET islands feature the same distance to the sample. We have to keep in mind that after changing the goniometer tilt the coordinate system of the piezo tube has to be readjusted. During the characterization, a tilted array was desired to get simultaneously measurement data of different heights over the sample. In later potential measurements the line defined by the SET islands was adjusted parallel to the sample surface.

[1]The positioning coordinate system is not mentioned here due to its irrelevance during a measurement.

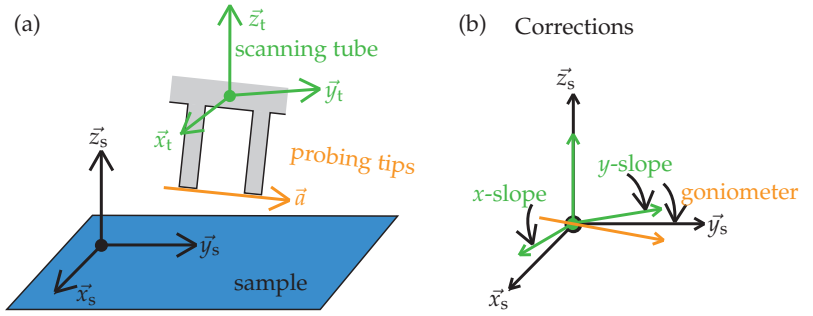

Figure 6.1:
Adjustment of the different coordinate systems. (a) Different coordinate systems for the one-dimensional probing tip array $(\vec{x}_i, \vec{y}_i, \vec{z}_i)$, piezo tube scan system $(\vec{x}_t, \vec{y}_t, \vec{z}_t)$ and sample structure design $(\vec{x}_s, \vec{y}_s, \vec{z}_s)$. (b) Potential corrections to align the different coordinate systems with each other.

For the scanning axes an image of a known sample structure was taken with the microscope and the geometric accuracy of this image was studied. The scanning SET array microscope uses a typical AFM electronic equipment to address the scanning piezo tube with voltages of up to $\pm 215\,\mathrm{V}$. For aligning $(\vec{x}_\mathrm{t}, \vec{y}_\mathrm{t}, \vec{z}_\mathrm{t})$ with $(\vec{x}_\mathrm{s}, \vec{y}_\mathrm{s}, \vec{z}_\mathrm{s})$ the instrument possesses two independent slope correction units for the x- and y-direction. Thus, an increasing tip-sample distance in lateral scanning direction can be compensated by a z-elongation of the piezo tube. A rotation around the z-axis between the two coordinate systems can be compensated by implementing a correlation for $(\vec{x}_t, \vec{y}_t)$ in the measurement routine. By this, the scan coordinate system $(\vec{x}_\mathrm{t}, \vec{y}_\mathrm{t}, \vec{z}_\mathrm{t})$ can be aligned in parallel with the sample axes.

A plot of the electric current through the SET for a not slope corrected (x, y)-direction area scan is shown in Figure 6.2 (a). In the plotted data the areas where the sample surface is made of GaAs are framed in black. The rest of the scanned area consists of a gold layer on top of the GaAs surface. The decrease of the electric current oscillation period over lateral distance along the white arrow indicates a reduced island-sample distance for the negative x-direction. Compensating this slope as plotted in Figure 6.2 (b) we get rid of those oscillations and find an equipotential area in x- and y-direction.

Surprisingly, the sample structures along the dashed line in (a) are tilted in the slope corrected measurement in (b). The reason for this unexpected tilt is a loose contact on the second y-deflection electrode on the piezo tube making an unwanted correlation between the z- and the y-scan direction. As a result the compensation of the island-sample distance by elongating the piezo tube in z-direction influences the y-position. Therefore, a used slope correction in x-direction influences the y-position of the SET on the sample and has to be corrected for every x-position. The same has to be done for the y-position due to the influence of the z-elongation. A corrected scan of a smaller area out of (b) is shown in Figure 6.2 (c). Now it is possible to scan with constant height perpendicularly into both lateral directions $(\vec{x}_\mathrm{s}, \vec{y}_\mathrm{s})$ along the sample structures. As a last step the data set has to be corrected into perpendicular axes as plotted in Figure 6.2 (d). Now $(\vec{x}_\mathrm{t}, \vec{y}_\mathrm{t}, \vec{z}_\mathrm{t})$ is aligned with $(\vec{x}_\mathrm{s}, \vec{y}_\mathrm{s}, \vec{z}_\mathrm{s})$ and the missing y-piezo tube contact is also compensated.

With those adjustments a correct geometry for an area or line scan on a Hall bar structure can be guaranteed.

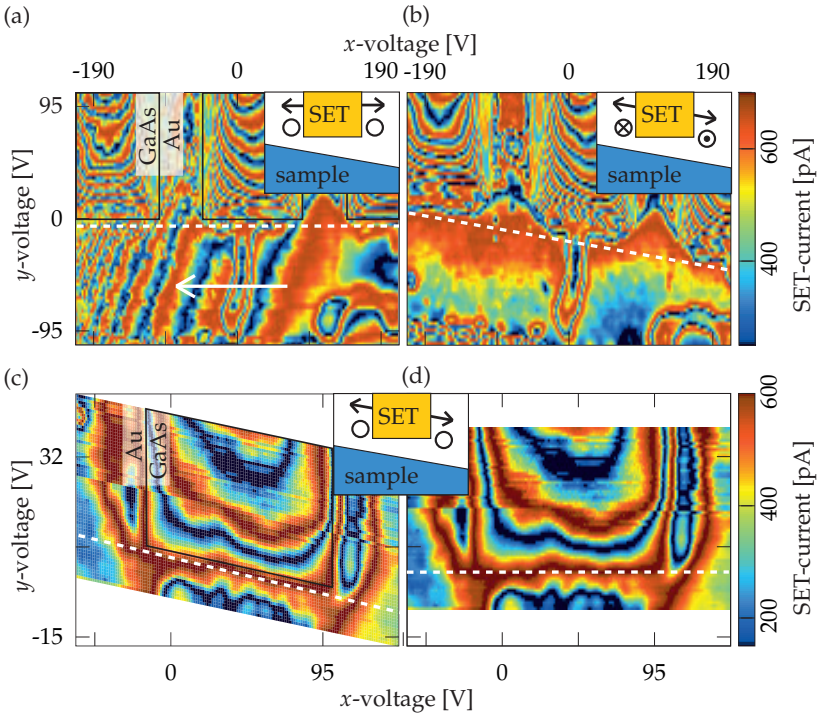

Figure 6.2:
Compensation of a tilted scanning coordinate system relative to the sample surface and correction for the correlation between the different scan directions. All insets depict a cross section of the tip-sample configuration with an illustrated tip movement relative to the sample structure. (a) Color-coded plot of the electric current through the SET over (x, y)-elongation of the piezo tube. A reduced island-sample distance for negative x-direction is depicted by the increased frequency of the electric current modulation along the white arrow. (b) Slope corrected scan with constant island-sample distance. The z-correction influences the y-position indicated by the white dashed line. (c) Area scan of smaller range, for which the slope correction is used and the unwanted y-elongation is corrected. Thereby a scan with independent (x, y)-directions is obtained. (d) Measured data set from (c) corrected by plotting with a perpendicular coordinate system.

6.2 Lateral Scan Range Calibration

After explaining the different coordinate systems present in the microscope and aligning them, we need a length scale before we can specify any other characteristic parameter of the microscope. This means we must correlate the applied voltage to deflect the scanning piezo tube to a scale on the sample surface. There are two possibilities to make this (x, y) scan range calibration:

By a geometrically known sample structure
One is to use the CBO method and simply make a full range area scan over the periodic calibration structure on the sample, the electrical setup is illustrated in Figure 6.3 (a). The scanned structure consists of 100 µm long 3 µm wide electrically connected finger-like structures along the y-direction that have a spacing to each other of 3 µm. They are made of an evaporated gold layer on top of the GaAs surface of the sample. The periodicity of this structure measures 6 µm in x-direction. An excerpt of the structure is shown in Figure 6.3 (b) over the full range scan applying ± 215 V to the scanning piezo tube. We count 4.5 periods in x-direction resulting in a scan range of $27(1)$ µm. Due to the symmetry of the piezo tube and the applied voltage we would expect the same scan range into the y-direction. But as already mentioned, an electrical contact on the scanning tube for the y-deflection was broke and so the scan range in y-direction is halved to 13.5 µm as (x, y)-area scans showed.[2]

By correlating features measured by different SETs with known distances
In Figure 6.3 (c) the simultaneously measured data of two further SETs is plotted. From the design defined for the electron beam lithography of the SET structures we know that the distance between the SET 1 and 2 measures 4.0 µm and between 1 and 3 it measures 8.0 µm. Therefore, we can look at the characteristic features in the different measured images and take the voltage offsets needed to overlay the features in the different images. For SET 1 the black circled feature is found at 75.3 V, for SET 2 at 12.3 V and for SET 3 at -51.5 V. Thus, $63.4(4)$ V applied to the scanning piezo tube in x-direction correlate to 4.0 µm lateral deflection. This gives a scan range of $27.15(15)$ µm for -215 V to 215 V of applied voltage, confirming the result of the measurement of the periodic sample structure. From now on instead of writing the applied voltage we can directly convert an applied voltage change of 15.85 V to 1.00 µm on the length scale in x-direction and 0.5 µm for the y-direction with a negligible error of around 1 %.

[2] The electrical contact is now fixed in the present setup.

The determined scan range covers the width of our Hall bar structures with a structure width of 20 µm. Further, we can now put a length scale on every feature seen in a lateral line or area scan.

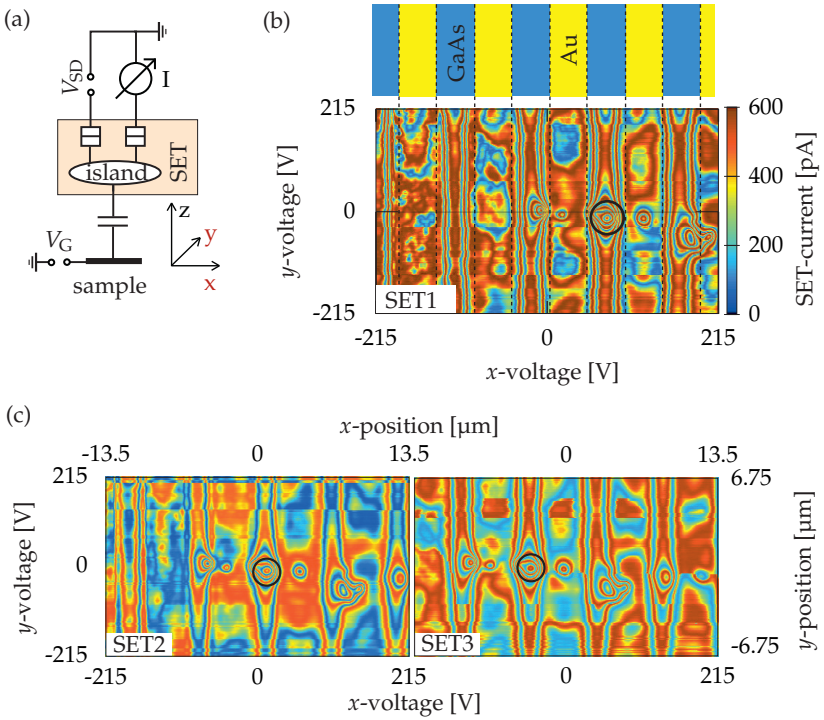

Figure 6.3:
Scan range determination with several probing tips on calibration structures. (a) Sketch of the used electrical setup. (b) Sample structure made up of gold stripes on top of the GaAs substrate, mapped onto the measured data which display the SET current modulation versus the voltages applied to the x- and y-electrodes of the piezo scanning tube. (c) Same measurement as (b) for two neighboring SET that have a distance of 4.0 µm and 8.0 µm from the first one. In all three measurements the same characteristic sample feature is highlighted by the black circle. The periodicity of the sample structure measures 6 µm. The maximum scan range is determined to 27.15(15) µm for ±215 V of applied voltage. Therefore, 15.85 V of applied deflection voltage translate into 1 µm elongation in x-direction and into 0.5 µm elongation in y-direction .

6.3 Vertical Scan Range Calibration

To talk about a tip-sample distance we have to calibrate the z-direction of the scanning tube. Therefore, we have to find a distance range for that we can simulate the situation and map the measurement to the simulation.

The SET island has a surface A of around $0.21(3)\,\mu m$ by $0.15\,\mu m$ parallel to the sample surface. Therefore, we can assume in good agreement the geometric configuration of a plate-type capacitor [27] for a tip-sample distance d of less than $50\,nm$. In this distance range the periodicity of the CBO peaks versus a fixed potential range goes linear with the distance as relation

$$\frac{e}{C_{\text{sample}}} = \frac{e}{\epsilon_0 \epsilon_r A} \cdot d \tag{6.1}$$

shows. In this equation ϵ_0 and ϵ_r are the electric permittivity of free space and the relative permittivity of the medium between electrode and SET islandsss.

The measurement setup and a measurement of an approach of the tips towards the sample are shown in Figure 6.4 (a) and (b). Displayed in color-code is the electric current modulation through the SET versus applied sample voltage for different voltages applied to the piezo tube with an arbitrary offset. The current modulations shift linearly towards a sample potential of $160\,mV$, verifying the linear relation for close proximity of the tips to the sample surface.

To be able to talk about distances in z-direction we simulated with the finite elements method the electrostatic situation of such an approaching tip. The results are presented in Figure 6.4 (c). Calculated was the virtual induced charge $Q^{ind,vir}_{\text{island}}$ on the SET island for an electrode potential variation and distance variation. The CBO profile of an SET as we use it with the CBO method can be described in first approximation by a sine function periodic to one electron charge [27]. Therefore, we can imitate the periodic electric current modulation by a sample potential change at fixed distance reasonably good by using a sine function on the calculated charge obtained by the simulation and then plot it color-coded. When we fit the simulation to the measurement by aligning similar periodicities on the ordinate axis as presented we can take the tip-sample distances from the simulation and map them onto the applied piezo tube voltages. Assuming that the elongation of the piezo ceramic stays linear even for large applied voltages, we can state that $1\,V$ of applied voltage to the tube results in a z-elongation of $1.4(3)\,nm$. The large estimated error of $20\,\%$ comes from the uncertainty of the SET island area. In total we have a reachable z-range of $0.60(12)\,\mu m$ with the piezo tube.

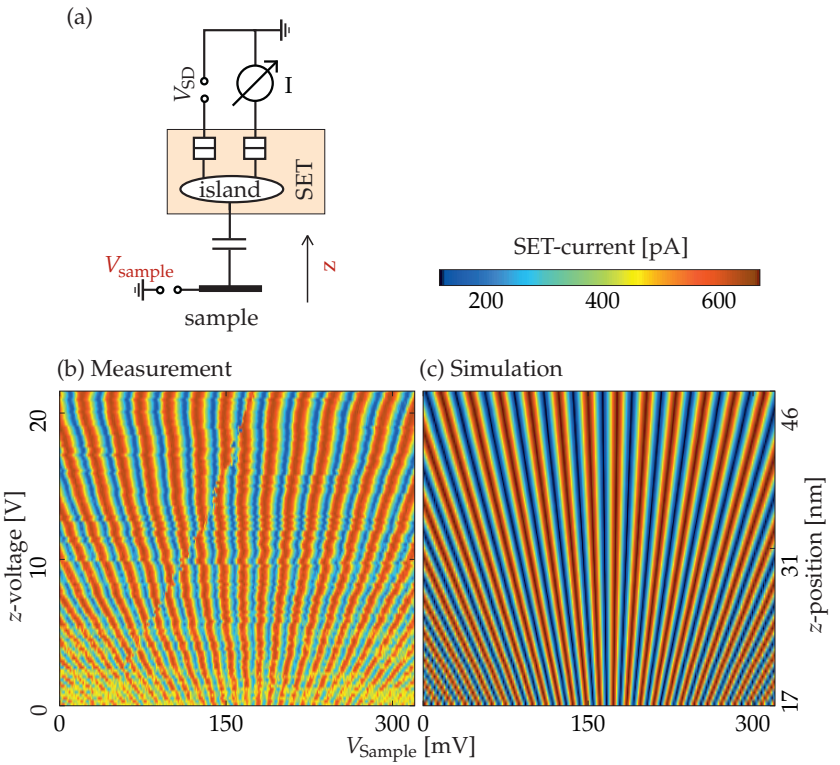

Figure 6.4:
Measurement and simulation of the current modulation through an SET tip versus applied sample voltage for different distances. (a) Sketch of the electrical setup for this kind of approach measurement. (b) Measurement of the electric current through the SET versus applied sample voltage for different applied voltages to the piezo tube for a z-elongation. (c) Simulation of the electric current through the SET versus applied sample voltage for different distances between SET island and sample surface. Furthermore, the simulation was fitted with its ordinate axis to the one of the measurement by comparing the current modulation periodicity versus sample voltage. The simulation reveals that 1 V of applied voltage to the piezo tube results in a distance change of 1.4(3) nm.

6.4 Mechanical Stability

The variations in Hall potential profiles can be of very small scales down to tens of nm [55]. Therefore, the mechanical stability of the microscope is important. Sources for mechanical vibrations can be

- circulation pumps,
- room acoustics,
- thermal relaxation of construction parts,
- boiling of the liquid helium in the cryostat bath,
- hysteresis and fluctuations of the piezo tube.

Thus, it is difficult to separate those sources from each other and we will not be able to investigate them individually. Therefore, we measure the combined result in an experiment-like configuration.

First of all the SET island has to be in very close proximity to the surface to be sensitive in lateral direction and see changes of the electrostatic potential of the island in detail. Secondly, a tip position on the sample has to be found that is significantly changing the electrostatic potential of the SET island within the lateral scale of nanometers. Such a position can usually be found at a material transition, for example, at the GaAs surface near a gold electrode. The change in the partial capacitance between island and sample, the work function difference of the two materials, and charge which accumulate near the edge of a gold electrode produce a strong gradient in electrostatic potential over a lateral position range. To get a simple measurement with high data acquisition rates for the measured signal, the Coulomb blockade oscillation method was used for both directions.

To measure the mechanical stability in x-direction we need a structure with a change along this direction but invariant in y-direction to separate the influences of both directions. The electrical setup for the mechanical stability measurement in x-direction is shown in Figure 6.5 (a). A material changeover going along the y-direction was used, located on the calibration structures of the sample. A sketch and an area scan of the material changeover are shown in Figure 6.5 (b) and (c) for two different SETs, measured simultaneously. To see mechanical jumps and drifts, a line scan (black line in (b) and (c)) was repeated over 15 h. The line length is 135 nm in x-direction with a step size of 0.45 nm. The results for both SETs are shown in Figure 6.5 (d) and (e), in which (d) accords to the structure shown in (b), and (e) to the structure from (c).

In (d) we see sudden jumps in the measurement signal of SET 1, which are not visible in (e), the measurement signal of SET 2. Due to the fixed distance of the two SET in the array structure, the nature of those jumps is not expected to be a mechanical one. Thus, the origin of the fluctuations must come from the electrically detected signal of the individual SETs. Later in the measurement when no jumps are present anymore a drift in positive x-direction illustrated by the black line can be seen. Because both plots show the same slope, this drift has to result from a mechanical drift, probably caused by the piezo tube hysteresis. A

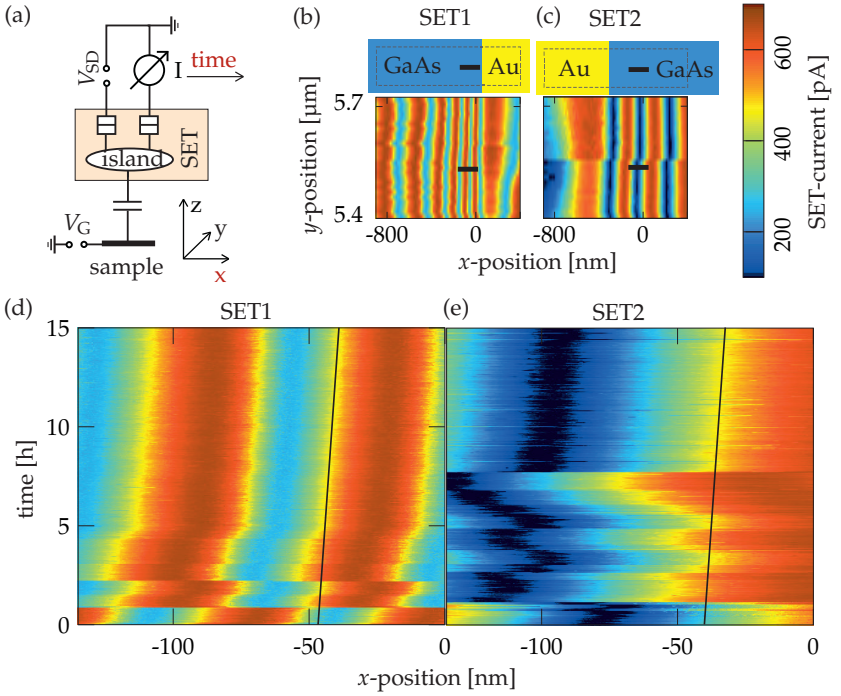

Figure 6.5:
Mechanical stability measurement in x-direction with two different SETs. (a) Sketch of the electrical setup to determine the mechanical stability in x-direction. (b), (c) Sketch of the sample structure around the used scan line position (bold black line) on the GaAs surface near a gold electrode. In the lower half an area scan of the sample surface around the scanned line done with the CBO method is shown. (d) Color-coded SET current over a repeated x-direction line scan during a time span of 15 h. (e) The measurement was done simultaneously for a different SET to compare the measured results. In both plots a black line indicates the drift of the tips into positive x-direction versus time. None of the fluctuations is seen in both measurements simultaneously, therefore, the fluctuations are not of mechanical nature.

reason for the drift can be the conditioning of the scanning piezo tube and thereby the history of the scanned positions, which is well known from AFM and STM setups [80, 81]. Thus, we must have had recently a large relocation of the probing tips relative to the sample done by the scanning tube. The average drift velocity is around $0.5\,\mathrm{nm\,h^{-1}}$. This drift is too small to be relevant during the maximal measurement time of 80 h between two helium filling procedures of the cryostat.

Now repeating the same measurement for the y-direction , again a tip position at a strong gradient for the electrostatic potential of the island near a gold electrode is used. In Figure 6.6 (a) the electrical setup, which just differs by the scanning direction from the previous one, is shown. (b) illustrates the sample structure and the variation of the electrostatic potential of the SET island for an area scan around the scanned line position. This time a line length of 169 nm with a step size of 0.48 nm was scanned over 15 h, shown in Figure 6.6 (c). Due to the unsuitable x-position of the other SET tips over the sample structure, we do not have a second simultaneously measured data set to compare and distinguish between fluctuations and drifts coming from a tip-sample movement or from the electrical signal of the probing tips.

Nevertheless in the measurement we can clearly see that in y-direction we get no persistent drift like for the x-direction. In this case the scanning tube must have been deflected for some time to the later used position.

In Figure 6.6 (d) the data of (c) is plotted with a restricted electric current range between 390 pA to 410 pA and a y-range between -150 nm to -190 nm. In this plot the signal jumps of either mechanical or electrical origin are highlighted and with the two yellow lines their range can be easily estimated to a maximum of ± 11 nm around the mean value. This range, in the worst case of assuming all fluctuations are of mechanical origin, equals the mechanical stability of the microscope. Comparing those fluctuations we are one order of magnitude better in stability than we can expect the resolution to be, due to the tip size of 150 nm by 200 nm.

In summary a drift velocity of $0.5\,\mathrm{nm\,h^{-1}}$ and fluctuations smaller than ± 11 nm can be expect. Position changes of less than ± 20 nm for a 15 h-measurement are a reasonably good result. This should be by far stable enough if we take the tip size of the SET and the Hall bar structure width of 20 µm into account.

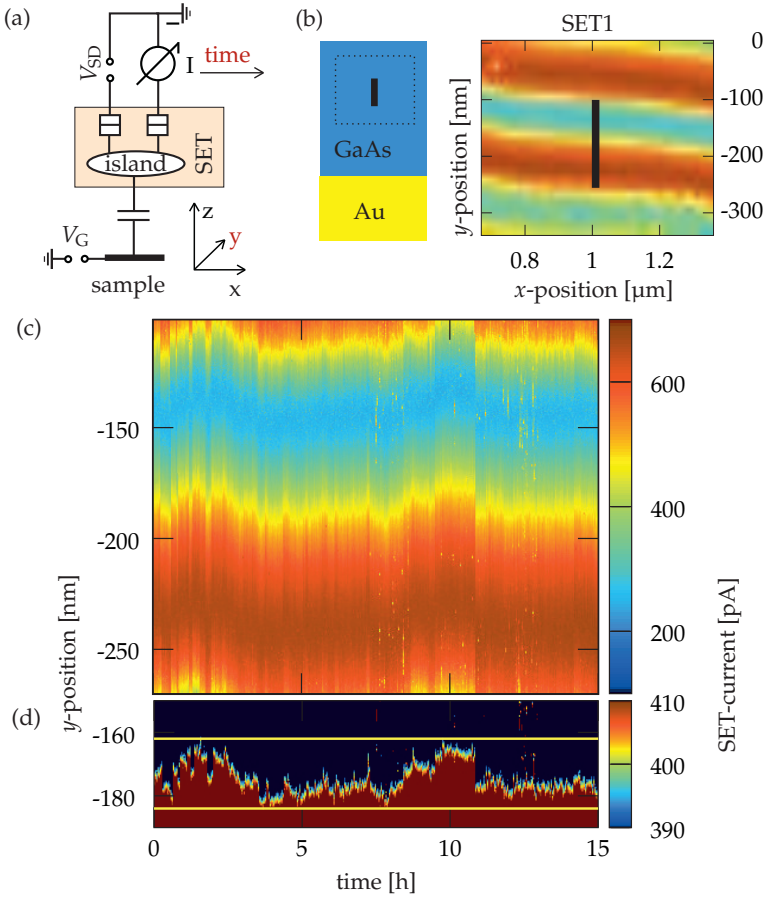

Figure 6.6:
Mechanical stability measurement for the y-direction of the microscope. (a) Sketch of the electrical measurement setup. (b) Position of the line scan (bold black line) relatively to the sample structure. Area scan of the surrounding area, showing a changing electrostatic potential of the island in y-direction measured with the CBO method. (c) SET current modulation for a repeated y-direction line scan over a time span of 15 h. (d) Reduced y-range and electric current range for a part of (c) to enhance the measured fluctuations. The yellow lines mark a range of ± 11 nm in between which all fluctuations lie.

6.5 Spatial Resolution

A scanning tunneling microscope has an atomic resolution with a tip which has in the best case just one atom located at the end and a single orbital reaching out towards the sample [82]. In our case the tip end looks like a flat plate with a size of 200 nm by 150 nm. Thus, the tip size will be a limiting factor for the spatial resolution of the microscope. Analogous to the measurement for determining the scan range the CBO method can be used to determine the lateral resolution. The electrical setup is presented in Figure 6.7 (a). We scan just a very small area of 0.5 µm by 0.25 µm on a gold surface[3]. Fluctuations and drifts of mechanical nature should be less than 11 nm for this measurement. The tip-sample distance was calculated to be less than 25 nm between island and the surface of a gold electrode on the sample. The related measurement is shown in Figure 6.7 (b) as color-coded plot of the SET current over the (x, y)-plane[4]. In the data set there are structures with a diameter size of less than 25 nm. This would be an astonishing result for such a large tip size. Therefore, we have to understand where those structures on a metal surface, where no signal change is expected, come from. Afterwards we have to think about a reason for those small structures.

The electrostatic potential of the SET island can be changed by surface charge, a sample potential change and a variation in the partial capacitance between island and sample. A potential change is not expected over a metal surface, for the surface charge we have to use a scanning electron microscope (short SEM) to see if there are left-over particles of photo-resist or dirt on the structured gold surface. An SEM picture of an evaporated gold surface is shown in Figure 6.7 (c). In this picture, which has the same scale as the scan done with the scanning SET array microscope, we cannot see dirt but we can see a surface structure consisting of gold clusters. Those clusters are typical for evaporated gold surfaces [83, 84]. The size of those clusters is in the range from 10 nm to 50 nm, comparable to the structure sizes measured with the scanning SET array. Thus, we assume that instead of charged particles which cannot be observed in the SEM pictures, variations in the partial capacitance between island and sample are the reason for the observed structures.

[3] Due to the fact that the sample was made by optical lithography, to avoid electron beam induced damage, the smallest structure size possible was 3 µm and thereby far to tall to be used to determine the lateral resolution.

[4] The same measurement was executed with the FBL method and is shown in Appendix C.4 on page 198.

To understand how the structures can be smaller than the SET island size, we look at the case of one cluster reaching out of the sample towards the SET island, as shown in Figure 6.7 (d). As long as the cluster is under the island the capacitive situation does not significantly change. Therefore, the cluster, even that it has smaller spatial dimensions, should result in a structure which has the size of the SET island. Nevertheless we see structures with a size of less than 25 nm in our area scan. This can be explained with Figure 6.7 (e), displaying two clusters reaching out of the sample surface with a lateral distance around the island length. In the shown configuration we have the largest partial capacitance between island and sample for the assumed situation. If the SET is moved into any lateral direction it will lose the partial capacitance towards one of the two clusters. Thus, the

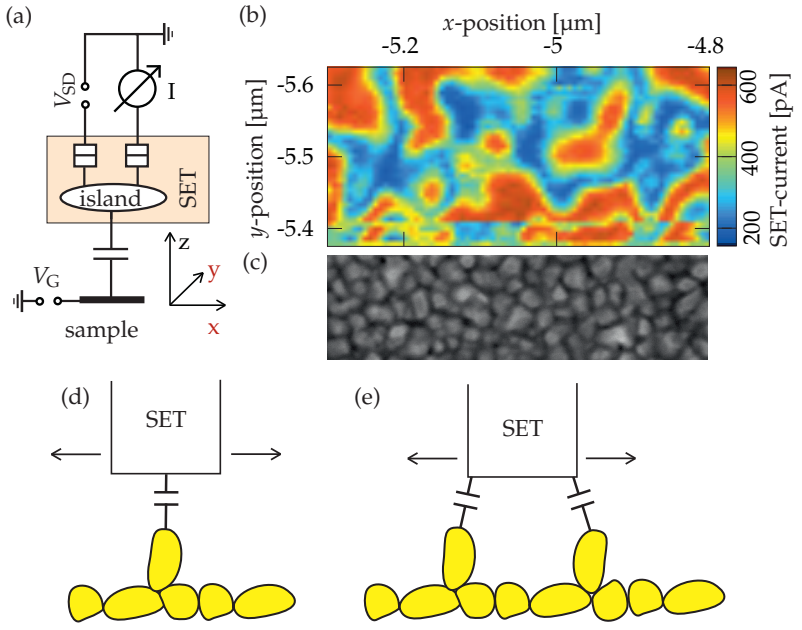

Figure 6.7:
Lateral high-resolution measurement over a gold surface. (a) Sketch of the electrical setup for this measurement using the CBO method. (b) Electric current through the SET, color-coded over the (x, y)-plane. Some measured features have a size of 25 nm or less in diameter. (c) SEM picture of an evaporated gold surface on a (Al,Ga)As heterostructure with similar lateral scale as used in (b). (d) Example for tip-sample configuration in which the microscope would show the measured structure in a broadened way. (e) Sample surface configuration suggesting a better lateral resolution than the SET island size.

capacitive coupling between island and sample will be bisected and therefore the electrostatic potential of the island and respectively the electric current through the SET will change. The example shows that in certain configurations sub-island-sized sample structures can be observed suggesting a better resolution than the microscope can achieve with the given SET island size. In general, if we measure features smaller than the tip size, we can assume that the surface structure is different to the measured data on the scale of less than 100 nm.

Finally we can estimate from the similarity of the cluster sizes and the measured structure sizes that the resolution of the microscope for such small island-sample distances of less than 25 nm is in the range of the island dimensions. Otherwise, the measured structures should all be much taller than the clusters due to their larger lateral influence on the electrostatic potential of the SET island.

The real spatial resolution can only be changed by a complete new SET tip design and fabrication process due to their spatial limitations in the actual process. On the other side the burried two-dimensional electron system of the heterostructure has to be very close to the surface to achieve high spatial resolution.

In the Appendix C.2 on page 195 further high resolution area scans with constant sample potential are shown.

6.6 Compensation of Magnetic-Field-Induced Mechanical Shifts

As a last point for the mechanical characterization of the microscope we need to discuss mechanical deformations that are caused by changes in the applied magnetic field. Those lead to changes in the relative tip-sample position which have to be compensated to get correlated scans of the same sample structure for different magnetic fields. The reason of the mechanical shifts lies in the stainless steel used to build the microscope. Even that it is entitled "non-magnetic" it becomes magnetic for fields higher than 1 T.[5] Therefore, forces act on the microscope construction and will slightly deform it.

As in other characterization measurements we will use the Coulomb blockade oscillation method due to its robustness and sensitivity, the electrical measurement setup is shown in Figure 6.8 (a). For detecting such mechanical shifts again we have to use a position-sensitive tip-sample configuration. This means we need a position for the tip where a shift in the investigated spatial direction changes the electrostatic potential of the SET island. On the other hand, the change should be small enough to recognize the initial position even for large magnetic field changes of several Tesla and the different spatial directions should be distinguishable.

The fastest and simplest way satisfying those requirements is the use of different line scans.[6] First line scans in x- then y-direction over periodic sample structures were executed for high and low magnetic field ranges. Two measurements for the x-direction at different structures for different magnetic field ranges are shown in Figure 6.8 (b). The magnetic shifts in x- and y-direction can both be fitted by a quadratic relation like

$$x_\mathrm{f} - x_\mathrm{i} = f_a \cdot (B_\mathrm{f}^2 - B_\mathrm{i}^2) + f_b \cdot (B_\mathrm{f} - B_\mathrm{i}). \tag{6.2}$$

In this relation B stands for the magnetic field, and x for the position on the lateral axis. The indices i and f stand for initial and final position or magnetic field. f_a, f_b are fit parameters for the quadratic and the linear part of the equation. Values for $f_a = -0.0112\,\mu\mathrm{m/T^2}$ and $f_b = -0.2455\,\mu\mathrm{m/T}$ over a range of more than 10 T for the x-, y-direction were obtained. The fitted curve for the mechanical shift in x-direction is shown in Figure 6.8 (b).

[5] Tested by the use of a neodymium magnet.

[6] Area scans for different fixed magnetic fields were done afterwards to prove the obtained shift correction to be correct.

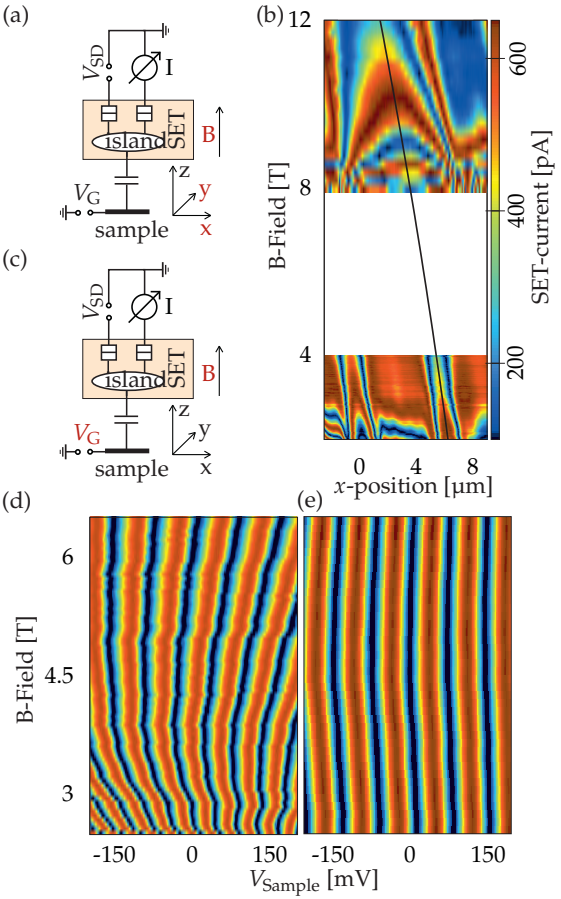

Figure 6.8:
Measurements of the mechanical shift caused by a change in the magnetic field. (a) Sketch of electrical setup using the CBO method to measure different line scans in x- and y-direction over borderlines of electrodes. During those line scans the applied magnetic field is changed. (b) x-direction line scan for a changed magnetic field in the range from 2 T to 4 T and 8 T to 12 T. A guide of the eye for the estimated shift is displayed in black. (c) Sketch of electrical setup using the CBO method to measure the mechanical shift between the SET island and the sample surface caused by magnetic field changes. (d) SET current modulation versus sample potential for different applied magnetic fields to determine the mechanical z-shift. (e) SET current modulation versus sample potential for different applied magnetic field with linear applied z-compensations.

The shift in z-direction was corrected by keeping the capacitive coupling of the sample electrode potential constant versus a variation of magnetic field, see Figure 6.8 (c) for the electrical setup of the measurements in (d) uncompensated case and (e) compensated case. The z-shift is compensated by the linear relation

$$z_\mathrm{f} - z_\mathrm{i} = f_c \cdot (B_\mathrm{f} - B_\mathrm{i}) \tag{6.3}$$

for smaller magnetic field ranges of about a few Tesla. Although the relation might be more complicated, it was not possible to determine the shift value more precisely. f_c stands for the fit parameter in this relation. In the case of a low magnetic field around 1 T to 4 T $f_c = -70\,\mathrm{nm/T}$ is valid, for higher magnetic fields the value has to be changed to $f_c = -80\,\mathrm{nm/T}$.

As a proof of concept we used a line scan with different electrode configuration in one measurement. The line scan we chose is positioned on the sample structure as shown by the black line in Figure 6.9 (a). In this case the different electrode configurations, making the measurement sensitive to the three spatial directions are represented by the invariant borderline of the left electrode and by the spatially limited right one. As a result we get a y-direction sensitivity from the left electrode situation, an x-direction sensitivity by the right electrode as well as a z-direction sensitivity over the whole scan range.

If there is no mechanical shift present while changing the magnetic field we would expect the measured data of the line scan to be invariant over the magnetic field axis. Further, we would expect modulations of the SET current just at the ends of the line scan due to the strong change of the partial capacitance of the SET towards the respective electrode, as shown by the green curve in Figure 6.9 (b). However the measured data without any shift compensation is shown in Figure 6.9 (c). The fully compensated measurement is displayed in Figure 6.9 (d) and shows the expected shape of features in the electric current map and an invariance versus magnetic field.

In summary, we can say that we are able to compensate any mechanical shift caused by a variation in magnetic field. Nevertheless the mentioned corrections are only valid for the used sample holder head[7].

[7] During the writing of this thesis, a new sample holder was designed trying to get more stiffness between tips and sample and eliminating the magnetic shifts. More about this next generation sample holder head, the concepts, advantages and its new kind of realization can be found in the Appendix B on page 189.

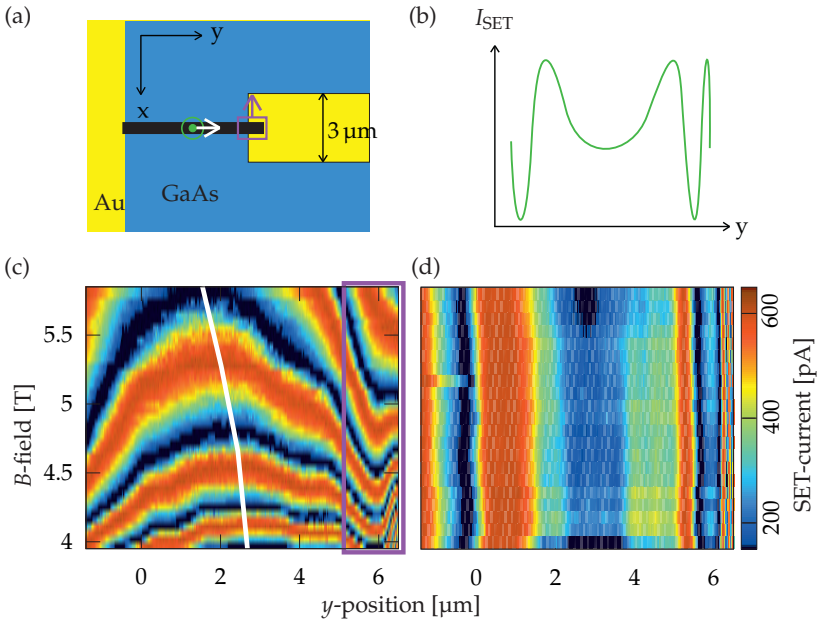

Figure 6.9:
Demonstration of the compensation of mechanical shifts between tip and sample caused by magnetic field changes. (a) Illustration of the used sample surface structure. The thick black line depicts the position of the line scan used in (c) and (d). (b) Guess on the SET current modulation for fixed magnetic field for a line scan as shown in (a). (c) Color-coded plot of the SET current for a line scan in y-direction while the applied magnetic field is changed. (d) Same color-coded plot as shown in (c) with applied shift compensation. The graph indicates no position shift anymore.

6.7 Remarks on the Electrical Characterization

After the mechanical characterization we can now determine the electrical key parameters of the microscope for the Coulomb blockade oscillation and feedback loop method. Before we have to clarify some facts about the following measurements. The calibration of the detected potential change of the sample by the CBO method has to be redone for every new measurement situation. Therefore, we always determine the Coulomb blockade oscillation peak period in the following and map its period onto the potential scale of the sample. The periodicity in the electric current profile tells us the SET-island-to-sample distance and the scaling of the potential variation related to the electric current range. For the feedback loop method we have to ensure that the measured structure is the dominant partial capacitance towards the island compared to the environment. The electrodes of the other SET tips, for close proximity do not produce measurable cross talk. To be sure we always used distances smaller than 100 nm between SET island and sample electrode for all measurements using the FBL method. Further, the range of the feedback loop signal was limited and reset if it exceeded ± 100 mV potential variation on the sample.

6.8 Electrical Signal Stability

The measurement setup is working with a GPIB bus, voltmeters from Keithley and a command line based measurement program called "measkern". In combination, the data acquisition is limited to 4.5 points /s as the fastest achievable rate. Thus, measurements with a variation in two parameters can take hours. For example, a duration of more than 9 h is estimated for a 300 points by 300 points measurement. Therefore, the electrical signal of the SET tips has to be stable on the time scale of several hours. Sources of electrical noise and instabilities within this time span can be

- the electrical setup (IV-converter),
- fluctuations in the sample layers or in the SET tip structures,
- crosstalk between the not individually screened probe and sample wires,
- mechanical vibrations on cables and connectors.

To measure the signal stability, a tip-sample position is needed that is sensitive to the electrostatic potential of the sample but insensitive to small mechanical movements. Hence, we choose a position in close proximity to a connected gold surface on top of the sample and kept the potential of the sample constant during the electrical stability measurement. The sample spot does not change the electrostatic potential of the SET island for slight lateral shifts in the range of 0.3 µm. This lateral invariance was achieved by searching for a very homogeneous area. Further, we keep enough distance to the sample (around 90 nm) so that the previously mentioned gold clusters at the electrode surface are smeared out in the measurement signal. Due to the lateral tolerance (0.3 µm) mechanical shifts (0.01 µm) can be neglected.

Coulomb Blockade Oscillation Method

The electrical setup for the CBO method is shown in Figure 6.10 (a). For the Coulomb blockade oscillation method we wanted to go one step further and see how the SET signal reacts after a large electrostatic potential change. So, we applied a sudden large potential change on the sample electrode and measured the stability to see how the SET island and its surrounding behave. The potential was changed by -400 mV and then kept constant. Several measurements were done until one displayed a sensitive SET current configuration, this one is shown in Figure 6.10 (b). The electric current of the SET lies around 400 pA, in the middle of the full current range of the SET (200 pA to 600 pA). Thus, the slope of the electric current characteristics allows a sensitive measurement.

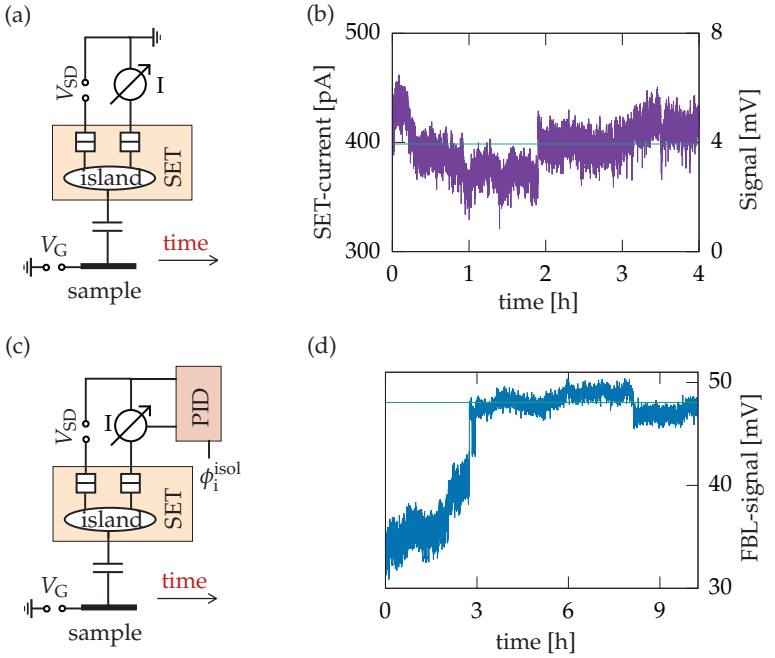

Figure 6.10:
Electrical signal stability measurement for the SET tips executed with the CBO and the FBL method. (a) Sketch of the electrical setup to measure the stability of the CBO method. (b) Stability measurement for the CBO method during a time span of four hours with an acquisition rate of $4.17\,s^{-1}$. The sample voltage was fixed after an initial jump of $-400\,mV$ before the recording was started. The conversion of 1 pA (left ordinate) equals a potential shift of 40 µV (right ordinate) on the sample electrode. Between second hour and fourth hour the standard deviation of the plotted green line is 13.9 pA (557 µV). The running average drifts between 395 pA to 415 pA which corresponds to a potential range of 800 µV. (c) Sketch of the electrical setup to measure the stability of the FBL method. (d) Acquired data for the FBL method with a standard deviation of 0.92 mV between third hour and tenth hour.

The island-sample distance for this measurement was around 90 nm given by a Coulomb blockade oscillation period of ($\Delta V_{sample} = 45\,mV$). Due to the measured SET current slope, a change of 1 pA in the electric current through the SET can be converted to a potential change of 40 µV on the sample, displayed on the second ordinate axis. This conversion compares the measured electrostatic potential fluctuations on the island to an according potential change on the sample for the given CBO peak period. Therefore, potential fluctuations caused by sources near

the SET island are valued much stronger on the sample potential scale. We got a data acquisition rate of 4.17 points /s over a time span of 4 h.

In the first 2 hours the value of the electric current I_{SET} shifts quite a lot and several small jumps can be seen. After that, a big jump of around 40 pA (644 µV) happens and the signal does not indicate fluctuations anymore, just a slow drift of the signal is detected. Thus, waiting some time in a certain measurement configuration will help to stabilize the measurement signal. In the following, we will only calculate the statistic figures for the second half of the measurement. The running average of the data is varying between 395 pA and 415 pA which corresponds to a potential drift of around 800 µV on the sample. The standard deviation measures 13.9 pA, which equals a potential variation on the sample of 557 µV.

A first hint to get a better signal stability is to wait some time before data is recorded so that the SET and its environment can relax and we get a more stable measurement signal.

Finally the limiting factor for this measurement is the noise of the IV converter as we get a standard deviation of around 10 pA for the electric current through the SET. This value was already observed when the IV-converters were characterized on their own. The large distance between sample and island for this measurement results in an increased conversion factor to a comparable sample potential fluctuation. This means a change of the electrostatic potential on the SET island converts to a larger sample potential change for increased tip-sample distance. If the noise is only due to the IV-converter, a reduced distance will systematically decrease the noise of the IV-converter mapped on the sample potential scale.

Feedback Loop Method

In Figure 6.10 (c) the electrical setup for the stability measurement for the FBL method is shown. (d) displays the measured shift of the electrostatic potential of the SET island for a fixed sample potential over a time period of more than ten hours. This time there was no sudden potential shift applied at the start due to the general instability of the feedback loop for such a change. In the first three hours of the measurement we can see again a large noise level and some minor jumps. After a large potential shift of around 8 mV the system stabilizes itself and also the noise is reduced.

The data was fitted with a horizontal line in the time period from hour three until the end. In this fit the standard deviation measures 0.92 mV. The running average for this time span lies between 46.6 mV and 49.4 mV. This results in a total drift of 2.8 mV for the measurement signal.

Finally we can state that the DC measurement signal is stable over hours after waiting some time (two to three hours) in a certain geometric and electrostatic configuration. This was the general observation made during all measurements executed on this microscope.

6.9 Electrical Signal Sensitivity

Another characteristic parameter is the sensitivity of an SET on sample potential changes on a shorter time scale. But first we will discuss how we can improve the measurement data. In Figure 6.11, a rising, noisy signal with a signal jump in the middle as it is usual from time to time for our SET measurements is shown. This jump is an arbitrary measurement artifact and results in an signal offset for the following measurement points. Therefore, we want to get rid of those signal jumps. In Figure 6.11 (a) a time-averaging example is shown, as for example a voltmeter with an increased integration time is doing. As a result the noise is reduced but the arbitrary jump in the measurement signal stays the same. If the measurement is repeated, as shown in Figure 6.11 (b), the jump will occur only in one of the measurement sweeps and will therefore be reduced if we average over a number of measurement sweeps, as the noise reduces. If this jump would be not coincidental it would reappear in every measurement sweep and would not be averaged out.

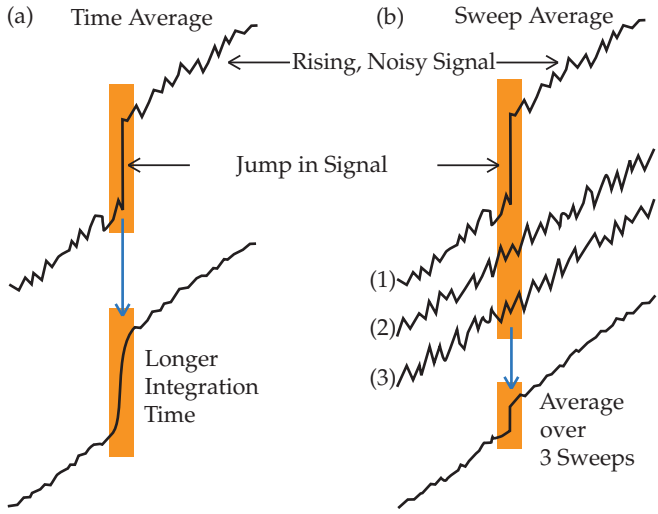

Figure 6.11:
Comparison between (a) time averaging and (b) arithmetic averaging over several independent measurements recorded one after the other. The orange area shows a random signal jump and the averaged result of both techniques. In (b) beside the original measurement (1), two repetitions of the measurement (2) and (3) with same parameters just time delayed are shown that are used to average.

Now we can determine the electrical sensitivity of the microscope for a single and several averaged measurement sweeps. In contrast to the electrical signal stability measurement we used a variation of an electrostatic potential on a sample structure to characterize the probing tips. To reduce the electrical noise coming from the electrical setup, a voltage divider of 1:25 was used, reducing the noise to less than 20 µV on the sample potential.

The sensitivity was enhanced as much as possible by reducing the island-sample distance. We achieved a Coulomb blockade oscillation period of $\Delta V_{\text{sample}} = 12.6\,\text{mV}$, that translates into a distance of $23(3)\,\text{nm}$[8]. Furthermore, the highest sensitivity within this geometric configuration is reached using the steepest slope in the SET current characteristics.

Coulomb Blockade Oscillation Method

The sensitivity measurement was first done for the Coulomb blockade oscillation method, the electrical setup is sketched in Figure 6.12 (a). We varied the electrostatic potential of the gold surface by $1.00(2)\,\text{mV}$ during the measurement. This results in a linear current change through the SET.[9] Therefore, a change in the electric current can be directly converted into a potential variation of the same range as the applied sample potential shift. In this case, a 1 pA current change on the SET corresponds to 16.1 µV potential change on the sample.

Measured data of the Coulomb blockade oscillation method is shown as the green curve in Figure 6.12 (b). The mapping from the values of the abscissa to the ordinate subtracting the potential offset is shown (orange line). Thus, the orange line represents a noiseless measurement. The violet curve shows an arithmetic average over 30 independent measurement sweeps of the same sample potential interval acquired one after another. The standard deviation for each measurement is displayed as dashed lines with a value of 11.15 pA (179.8 µV) for a single DC measurement and with a value of 1.43 pA (23.1 µV) for the averaged one. To get a feeling how many repetitions are roughly necessary for a certain sensitivity, Table 6.1 shows the standard deviations for a different numbers of repetitions.

The standard deviation for the single measurement is quite comparable to the noise level observed on the electric current signal of the IV-converter without using an SET. Hence the IV-converter is likely to be the limiting factor in this sensitivity measurement arrangement.

[8] On the short time scale of the following measurements the mechanical instabilities do not matter.

[9] For the small used potential variation and the assumed linear electric current characteristics we get a negligible deviation of less than 2 % from the real potential change.

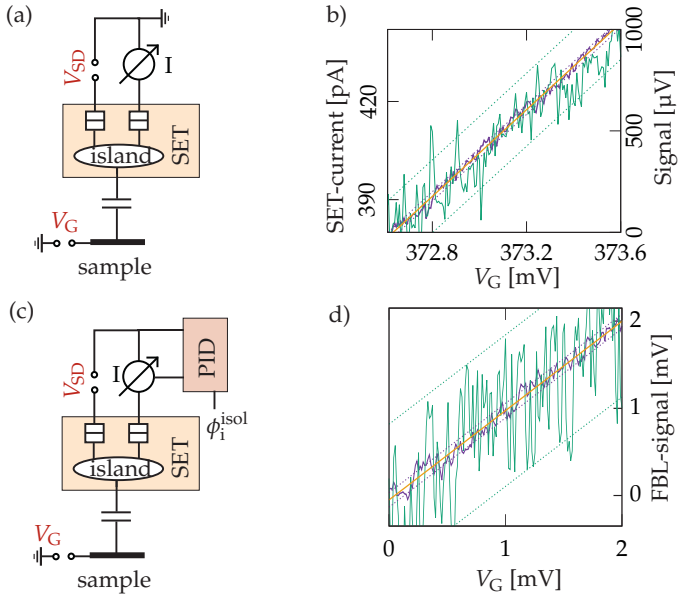

Figure 6.12:
Electrical sensitivity measurement for the SET tips measured with the CBO and the FBL method. (a) Sketch of the electrical setup to measure the sensitivity for the CBO method. (b) Sensitivity measurement (green) and arithmetic average over 30 measurements (violet) plotted versus the applied gate voltage with a conversion of 1 pA (left ordinate) to 16.1 µV (right ordinate). The dashed lines show the standard deviations (179.8 µV and 23.1 µV) for both. In orange the mapping of the gate voltage to an offset subtracted potential scale is shown. (c) Sketch of the electrical setup to measure the sensitivity for the FBL method. (d) Sensitivity measurement for the FBL method with standard deviations of 869 µV, respectively 83.4 µV for an average over 30 measurements.

repetitions	standard deviation
1	179.8 µV
5	53.3 µV
10	35.5 µV
20	27.5 µV
30	23.1 µV

Table 6.1: Number of repetitions of the measurement taken for the arithmetic average on the left and corresponding standard deviation for the CBO method on the right.

Feedback Loop Method

The measurement was repeated for the feedback loop method with a potential sweep of 2 mV. The electrical setup is illustrated in Figure 6.12 (c) and (d) is displaying the measurement results. Again the violet curve shows the averaged measurement and with dashed lines the standard deviations are plotted. In this case the standard deviation values 869 µV for a single DC measurement (green) and 83.4 µV for an arithmetic average of 30 measurements of single potential sweeps. Table 6.2 shows the values for all evaluated repetition numbers:

repetitions	standard deviation
1	869 µV
5	304 µV
10	209 µV
20	109 µV
30	83.4 µV

Table 6.2: Number of repetitions of the measurement taken for the arithmetic average on the left and corresponding standard deviation for the FBL method on the right.

There is a discrepancy between the sensitivity of the Coulomb blockade oscillation and the feedback loop method. The feedback loop method is less sensitive by a factor of around 8 for a single measurement and by a factor of around 6 for the comparison of the averaged measurements. This discrepancy can be explained by the additional electronics of the PID module, the time delay of the loop and its tolerance of comparing the actual output voltage of the electric current value to the reference voltage. Measuring within the linear slope of the electric current characteristics the CBO outmatches the FBL method and it is easy to translate the electric current change into a measured potential change. For larger potential ranges the FBL method is indispensable and will become more accurate than the CBO method with its non-linear SET current to sample potential conversion.

In conclusion, we can say that with the used DC techniques we obtain a sensitivity around 180 µV for the CBO method and around 870 µV for the FBL method with a single measurement. This is already sufficient for measurements on samples with the integer quantum Hall effect, applying up to several mV at the sample structures. The fractional quantum Hall effect (e.g. $\nu = 2/3$) is even more fragile and we expect that the applied voltage should be below 1 mV. In this case we should cycle at least 10 times. Another possibility is to use AC techniques. Nevertheless averaging over several measurements will also be advisable for the use of AC techniques.

6.10 Working Temperature

The determined mechanical and electrical properties of the microscope allow a measurement of the potential distribution over a sample in the integer and fractional quantum Hall regime. A last important specification is the working temperature of the microscope.

In the temperature range below 100 mK the cooling power of the used ^{3}He-^{4}He dilution fridge is below 400 µW, decreasing with temperature. Thus, every input of heat has to be seen critically. Nevertheless we had to install a combination of 96 connected leads into the microscope to cover the positioning, scanning unit and all sample, probing tip connections. This was done without the use of low temperature heat exchangers [85] due to our restrictions in space. Therefore, the achievable electron temperature in sample and probing tips was a crucial point for this microscope setup. The aim was a value of less than 100 mK while the helium mixture achieves 16 mK base temperature.

With the single-electron transistors as probing tips, we have an array of temperature sensors, fitting to the milli-Kelvin range. To get reasonable measurements for the working temperature in the sample we can put the SET in close proximity of the sample surface. The thermal broadening in the conductance G of the SET, while sweeping a gate voltage, tells us with the help of the relation

$$\frac{G}{G_{\max}} \approx \cosh^{-2}\left(\frac{\Delta_{\min}}{2.5 k_B T}\right) \tag{6.4}$$

the electron temperature of the device [86]. The relation is valid for a metallic SET that has a large single-electron charging energy compared to the thermal energy $k_B T$. Fitting this equation to our purpose by a measurement in which we sweep the sample potential, we get

$$G(V_{\text{sample}}) \approx G_{\max} \cdot \cosh^{-2}\left(\frac{\frac{C_{\text{sample}}}{C_\Sigma} \cdot (V_{\text{sample}} - V_{\max}) \cdot e}{2.5 k_B T}\right). \tag{6.5}$$

In this relation $C_\Sigma, C_{\text{sample}}$ are the total capacitances of the SET island and the partial capacitance between island and sample electrode. V_{sample} stands for the voltage applied to the sample electrode, $V_{\max}$ for the position of the conductance maximum $G_{\max}$ on the V_{sample} parameter axis. $G_{\max}$, $V_{\max}$ and the temperature T are the usable fit parameters.

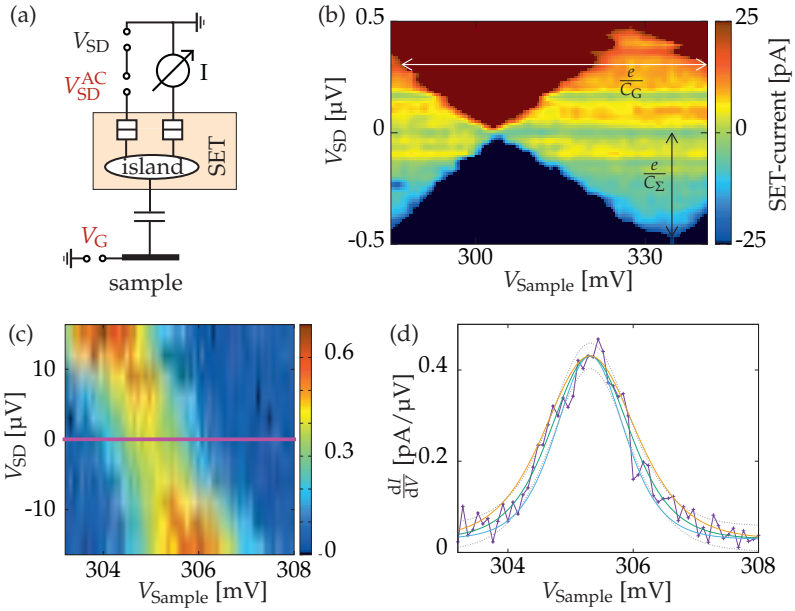

Figure 6.13:
Temperature measurement with a single-electron transistor as sensor. (a) Sketch of the electrical setup to measure the thermal broadening in the SET conductance. (b) SET current plotted versus source-drain and sample voltage cut off at ±25 pA to clarify the Coulomb blockade regime. (c) Color-coded plot of the conductance versus source-drain and gate voltage for a configuration in which two Coulomb blockade regimes meet. The measurement was done with 2.8 µV AC excitation voltage (amplitude) at 1.3 Hz. (d) Cross-section along the violet line in (c) and fits for 30 mK, 34.7 mK and 40 mK (blue, green and orange curve). The standard deviation between fit and measurement is displayed as dashed lines.

For the measurement of the conductance we used the Coulomb blockade oscillation method with an AC voltage smaller than $k_B T/e$ applied to the source contact and swept the sample potential, see Figure 6.13 (a). (b) shows a color-coded plot of the DC SET current over the variated DC source-drain and sample voltage. This plot was cut-off at an SET current of ±25 pA to clarify the range of the Coulomb blockade regime. As a period in the electric current modulation along the sample potential axis we get $e/C_G \approx 51$ mV. Hence the distance between island and sample is estimated to around 100 nm . Half of the span of the Coulomb blockade regime along the source-drain voltage axis gives $e/C_\Sigma \approx 455$ µV. With those values we can calculate C_{sample}/C_Σ needed to fit our measurements with equation (6.5).

In Figure 6.13 (c) the conductance of the SET is plotted color-coded over different DC source-drain voltages and swept sample voltage. The presented measurement was done with an excitation voltage of 2.8 µV (amplitude) at 1.3 Hz in the parameter range where two Coulomb blockade regimes meet. A lower AC excitation voltage does not change the results for the thermal broadening as further measurements in the appendix C.3 on page 197 demonstrate. Therefore, we can assume that the results are not falsified due to additional broadening in the measurement data by the used AC excitation. The cross section of the violet line in Figure 6.13 (c) is plotted in (d). The measured data was fitted resulting in a temperature of 34.7 mK (green curve). For this value the fit curve and the data have a standard deviation of 28 fA μV^{-1} (dashed lines). To get a better comparison the fit curves for 30 mK (blue) and 40 mK (yellow) are plotted too. Due to the small spatial distance of around 100 nm and the same wiring of sample and probing tips we assume the measured temperature also valid for the sample. Therefore, we can state that the microscope has a working temperature of less than 40 mK.

6.11 Summary and Judgment on Use for the Fractional Quantum Hall Effect

Characteristic key figures of the microscope

In this chapter we showed how the three coordinate systems of the SET islands' height, scanning tube and the sample can be adjusted and how they were fixed to work correctly. Further, we determined the scan range in x-direction to $27(1)$ µm by a geometrically known sample structure and to $27.15(15)$ µm by correlated features measured by different SETs with known distance. We measured for all noise sources, acting on the tip-to-sample position, fluctuations of less than ± 11 nm in both lateral directions. A negligible small tip-sample position drift of $0.5\,\mathrm{nm\,h^{-1}}$ has been recorded in x-direction. During high resolution scans with the microscope features with sizes of less than 50 nm were recorded. These feature dimensions and the mechanical stability lie far below the SET island size of 200 nm by 150 nm that should be the limiting factor for the lateral resolution. An explanation for this discrepancy was given. Afterwards the successful compensation of mechanical shifts caused by deformations of the microscope due to an applied magnetic field was demonstrated.

In the second half of the chapter the electrical properties were presented. The electrical signal stability was measured over time periods of 4 h to 10 h with and without initially applied potential variation. In the first 2 h to 3 h sudden shifts in the SET signal were observed. After that instable period of time only small signal variations with a standard deviation of 0.5 mV for the CBO method and 0.9 mV for the FBL method were recorded over hours. The largest signal variations were sudden arbitrary shifts in the measurement signal which were added to the following measurement signal as an constant offset. This is why an averaging over several repetitions of the same measurement is suggested instead of using a larger integration time. For the electrical sensitivity over a shorter period of time we reached a standard deviation of around 180 µV for the CBO method (23 µV for averaging over 30 measurements) and around 870 µV for the FBL method (83 µV for averaging over 30 measurements)

Another characteristic figure was the working temperature of the microscope which was determined with the help of the SET tips. Therefore, the SET islands were positioned 100 nm over the sample surface to get a good estimation of the working temperature for both by measuring only the thermal broadening in the electric current characteristic of the SET. The working temperature was determined to less than 40 mK.

Judgment on use for the fractional quantum Hall effect

The microscope was built to measure primarily the Hall potential profile of Hall samples in the integer and fractional quantum Hall regime. Therefore, we want to discuss now the requirements for those experiments and see whether the characteristic figures of the microscope fulfill them.

The used heterostructure has a two-dimensional electron system buried 120 nm under the surface with a very high charge carrier mobility of $8.9 \times 10^6\,\mathrm{cm}^2/\mathrm{Vs}$ and a charge carrier density of $2.0 \times 10^{11}\,/\mathrm{cm}^2$. This heterostructure was chosen to make the fractional quantum Hall states $\nu = \{\frac{2}{3}; \frac{3}{5}; \frac{4}{3}; \frac{5}{3}\}$ available at magnetic fields from around 4 T to 14 T which the superconducting magnet of the cryostat setup is able to reach. Those large ranges of magnetic field and the resulting mechanical shifts can be almost completely compensated as it was shown. Further, a correct alignment of the probing tip-array with the scanning axes relative to the sample structures is possible. Our sample structure possesses the shape of a standard six-terminal Hall bar structure with a width of 20 µm. Hence the available scan range of the piezo tube of around 27 µm is sufficient for the structure.

The landscape of compressible and incompressible stripes of a two-dimensional electron system in high magnetic field can exhibit a detailed structure at the 2DES edge [55, 57]. Therefore, it would be desirable to achieve a lateral resolution with this microscope of less than 100 nm. Concerning this scale, the mechanical stability (<11 nm) is good enough but the SET island size (200 nm by 150 nm) and the distance between 2DES and SET island are restricting the spatial resolution of the microscope. Both limitations are hard to overcome. To go closer to the surface with the 2DES we would have to significantly sacrifice in the property of mobility of the heterostructure losing perhaps the possibility to measure fractional quantum Hall states. Also a reduction of the SET tip structure would mean to reinvent the whole fabrication process of the SET array. Using a structure and evaporation process similar to the groups of Amir Yacoby [27] and Eli Zeldov [87] we would end up having problems to produce a one-dimensional tip array. Therefore, we can already say that we will be slightly limited by the spatial resolution of the microscope in certain cases of measuring the electrostatic potential distribution of the sample.

As the partly small energy scales of fractional quantum Hall states [76–79] already show, the usable excitation voltage range for the sample will be very limited. Though we will have to apply less than 1 mV to the sample and therefore need a sensitivity of better than 100 µV on the sample potential scale. With the feedback loop method and an averaging over 30 measurements or more we can obtain this

sensitivity level. The sensitivity level can be enhanced by a factor of 4 using the Coulomb blockade oscillation method. Nevertheless with the CBO method we get difficulties to reconstruct the electrostatic potential.

The working temperature of the microscope with less than 40 mK should be sufficient to measure several different fractional quantum Hall states.

To sum up, the microscope has sufficiently good specifications to measure fractional quantum Hall states. The only limitation could be the spatial resolution.

The benefits of an one-dimensional array of probing tips
Firstly, due to the choice between different probing tips we were able to measure with the best suitable probing tip. Secondly, with the SET array slightly tilted we got simultaneous information from probing tips with different sample-island distances. Thirdly, using several SET tips we obtain either simultaneously measurement signals from different sample positions or redundant data on the same sample area. Thereby, the scan range calibration for example was possible at any feature of the sample surface. Also tip or electrically induced systematic errors suggesting an electrostatic potential feature in the measurement can be pointed out by another SET scanning the same area showing a different signal. The separation of mechanical and electrical fluctuations was possible due to the usage of more than one probing tip. Fourthly, the array of SETs saves a lot of time in the event of a single broken tip due to a sample-tip contact.

The disadvantage of the 1D array is small, less than 20 % more fabrication time for an array of eight SETs than for a single one, and some very small and well manageable crosstalk mainly due to the parallel, not single isolated measurement lines in the electrical setup and microscope.

7
Tip-Sample Compensation Voltage

In every scanning probe microscope the probing tip is part of the investigated physical system. Therefore, the tip will influence the sample under investigation resulting in a contribution to its own measurement signal. The same issue is present for the scanning single-electron transistor microscope and has to be minimized to measure the fragile potential distribution in quantum Hall samples.

Due to the electrostatic sensing, for example, a work function difference between sample and probing tip plays a crucial role. The work function as a thermodynamic variable defines the necessary energy to release one electron from the bulk of a material to vacuum. A tip made of a different material than the sample will cause a work function difference resulting in an electrostatic potential difference between them, affected by details of the material's surface.

This difference can produce reversible and even irreversible changes to the sample properties. Our system to be characterized, a two-dimensional electron system (2DES) can be depleted locally or, in the worst case, charge can be deposited on the surface or in the donor layer of the heterostructure embedding the 2DES. The resulting changes of the charge carrier density in the 2DES are unwanted because they change locally the Landau level filling factor and can thereby create measurement artifacts in the recorded Hall potential profiles.

Before using a 2DES as electrode a simple gold electrode was used to get first experience of how to determine a compensation voltage with the microscope and its probing tips. However even on this simple metal surface an unexpected behavior showed up.

The compensation voltage in different configurations with a gold electrode will be discussed and explained in this chapter. This is done with measurements and the help of simulations on the electrostatics in this arrangement carried out by finite element calculations, see Appendix A.1 on page 183.

7.1 Distance Dependence of the Compensation Voltage

Between the used gold[1] electrodes on the sample surface and the sensing single-electron transistor[2] a work function difference is present. During an approach of the single-electron transistor towards a gold electrode the partial capacitance C_{sample} to the sample in equation (4.4) changes. Thereby the electrostatic potential of the SET island varies if an electrostatic potential difference like a work function difference between tip and sample is present. The shifting of the SET current peaks (CBO method) in the parameter space tip-sample distance versus applied sample voltage is shown in the simulation of Figure 7.1 (a), assuming a work function difference of 160 mV. If we apply a voltage to the sample, compensating the work function difference of $V_{\text{WF}} = 160\,\text{mV}$, there would be no change in the electrostatic potential of the SET island while approaching the sample. Therefore, the Coulomb

[1] The work function of gold lies in a range around 4.7 eV to 5.4 eV [88, 89].

[2] The SET is made of Al which usually has a work function around 4.2 eV to 4.4 eV [90], but can differ from those values due to the surface composition.

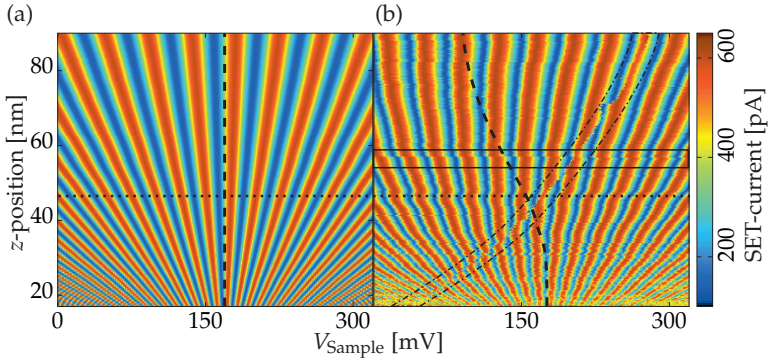

Figure 7.1:
Comparison between a measurement and a simulation of the CBO method for a tip-sample approach. (a) Simulation with the SET current color-coded versus sample potential and tip-sample distance. The data below the dotted line with its linear character was already used to calibrate the z-axis of the scanning piezo tube in Chapter 6.3. The dashed line highlights sample potentials that show an invariant SET current over a small distance change. Therefore, it indicates the compensation voltage over distance. (b) Measurement data corresponding to the simulation in (a). The required electrode voltage for a tip-sample compensation is shown as dashed line. The rectangular framed box highlights a jump in the electric current through the SET. Another jump in the current characteristic is present within the area framed by the dash-dotted line.

blockade peaks in the measurement do not shift for this applied voltage (dashed line), which we will further denote as tip-sample compensation voltage or short compensation voltage. With this compensation voltage the current through the SET stays constant during an approach as shown for 160 mV sample potential in Figure 7.1 (a).

In Figure 7.1 (b) the measurement with the CBO method corresponding to the simulation is shown[3]. Our measurements in concern of the sample-island capacitance as well as for the shift of the compensation voltage for different distances correspond well to the shown data in the publication of M.J.Yoo et al. [27].

If we draw now a curve crossing all points that have an invariance of the SET current for a small tip-sample distance change

$$\frac{\partial I}{\partial z} = 0 \tag{7.1}$$

we end up with the dashed curve. The curve illustrates the tip-sample compensation voltage for different heights[4].

Unexpectedly, the required compensation voltage changes drastically with distance. This means either that we approach an area containing different materials or that influences like surface charge shift the recorded tip-sample compensation voltage besides a static work function difference. It is not mentioned in the publication of Yoo et. al but looking closer at the plotted data in the publication, a shift of the compensation voltage into both sample potential directions over the island-sample distance is visible. To figure out why the compensation voltage is shifting and how to handle it we repeated our approach measurements with swept sample voltage for different sample surface configurations. Those measurements will be shown in the following sections and the origin of such compensation voltage shifts will be explained by simulations.

In the approach measurement in Figure 7.1 (b), there are several further features visible, for example, the one in the framed rectangular box and the one inside the area framed by the dash-dotted line. Those features will be explained at the end of this chapter.

[3] In the Appendix C.7 on page 202 the work function compensation with the use of the feedback loop method is shown and explained.

[4] If we have a very clean sample surface to approach to we can assume that the work function difference will be the strongest influence on the compensation voltage for closest tip-sample proximity. The value of the compensation voltage at closest distance would then be the work function difference between the materials.

7.2 Compensation Voltage Shifts over Different Sample Surface Configurations

Due to the unexpected height dependence of the compensation voltage in the shown approach measurement in Figure 7.1 (b) we investigated the approach measurements further. The approach measurements were repeated over homogeneous and inhomogeneous sample areas. The measured data are shown in Figure 7.2 for the homogeneous case and in Figure 7.3 for the inhomogeneous one.

Firstly, the approach measurements over a homogeneous surface area will be discussed. The area consists of a gold electrode and the result of an area scan executed at 60 nm distance with the use of the CBO method is shown in Figure 7.2 (a). Approach measurements at different sample positions are shown in Figure 7.2 (b). The corresponding compensation voltage curves (dashed lines) in Figure 7.2 (b) are reproducible for each sample position (1 to 4) but differ between the different sample position. All of the compensation voltage curves shift towards positive sample potentials for approaching the sample surface and end up in a range from $-10\,\mathrm{mV}$ to $50\,\mathrm{mV}$. Therefore, we have an uncertainty of around $\pm 30\,\mathrm{mV}$ for the compensation voltage even that we took care to measure on a homogeneous area of the sample surface. Looking at the area scan several roundish shaped features can be seen. Those features lead to the assumption that dielectric particles or even charged particles on the electrode surface could produce those distance dependent compensation voltage shifts. In this case the surface would not be as homogeneous as it seems.

The distance dependence of the compensation voltage becomes even more pronounced looking at Figure 7.3 (b) and (c). The inhomogeneous sample surface configuration for those measurements is shown by the (x, y)-area scan in Figure 7.3 (a), again using the CBO method. This time the surface is only partly covered by gold electrodes and the rest of the surface consists of the underlying GaAs layer. The locations where the tip-sample approach measurements with swept sample potential were taken, are marked by the numbers. All of them are showing strong changes of the compensation voltage value in dependence of the distance between SET island and sample which is a significant aberration from the ideal approach characteristics, obtained in the simulation. Astonishingly the compensation voltage this time shifts towards both sample potential directions, meaning that a tip-sample compensation voltage value can reappear at different distances. This behavior is pointing out a complex sample surface configura-

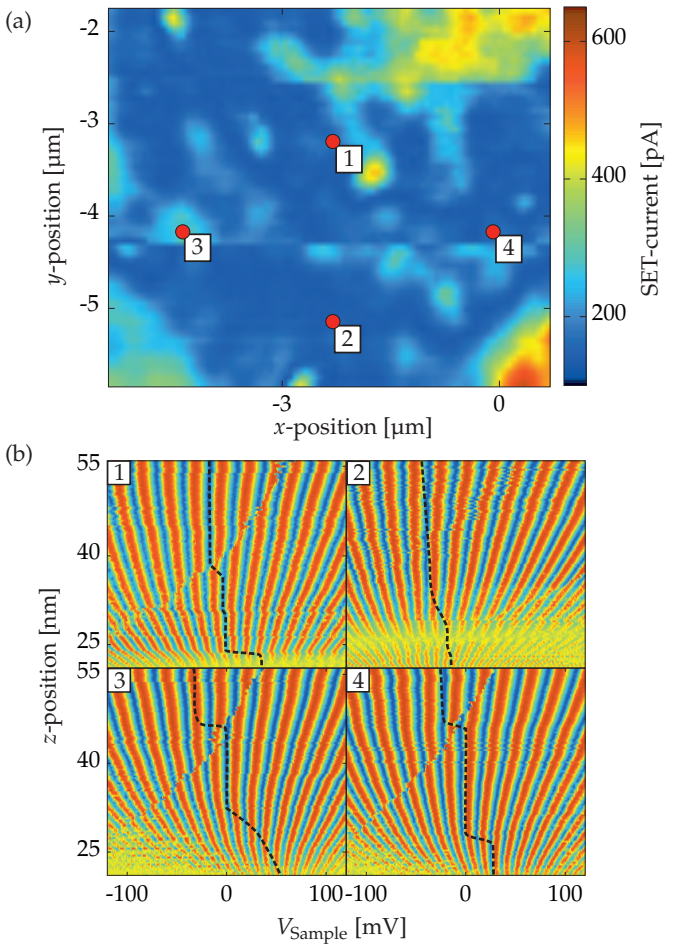

Figure 7.2:
Approach measurements to identify the compensation voltage (dashed line) between tip and sample over different positions on a homogeneous gold electrode surface. (a) Color-coded plot of the current through the SET over (x, y)-position at a distance of 60 nm to the sample surface. The numbers mark the position of the corresponding measurements in (b). Between the different positions the electrostatic potential of the SET island shows only small variations. This indicates a homogeneous sample surface. (b) Color-coded plots of the SET current versus applied sample electrode voltage and relative island-sample distance. The measurements suggest different compensation voltage values at different distance to the surface in the range from -10 mV to 50 mV, applied to the sample.

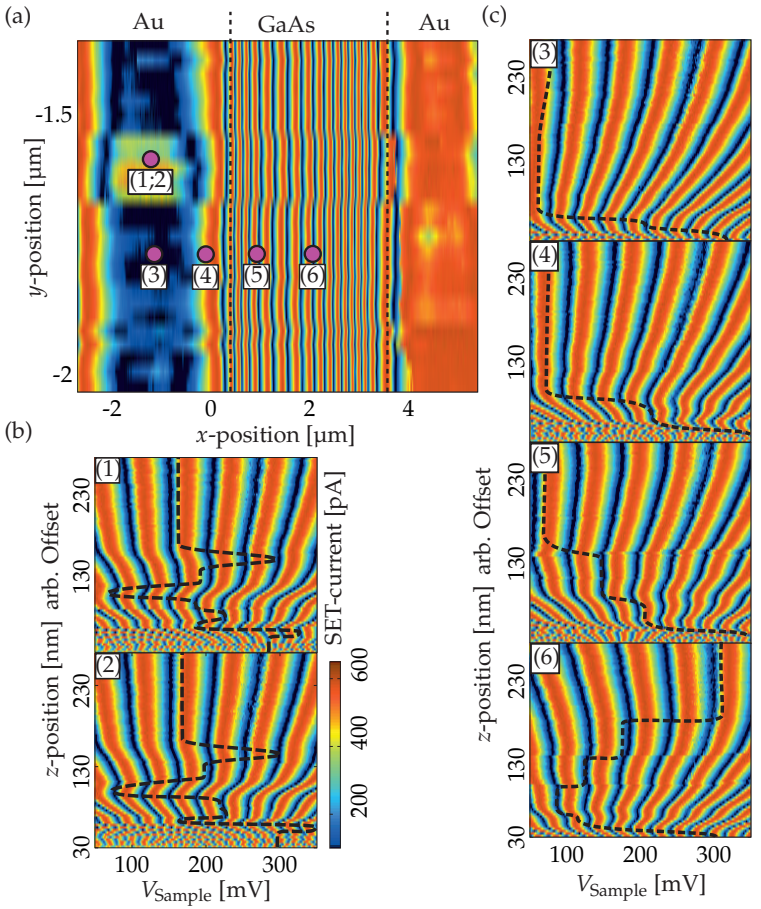

Figure 7.3:
Approach measurements to determine the compensation voltage between tip and sample over different positions and materials. (a) Color-coded map of the current through the SET for an (x, y)-scan. The different surface materials are indicated above the plotted data. The numbers identify the position for the approach measurements shown in (b) and (c). (b) Color-coded plot of the SET current versus sample electrode voltage and relative SET-island-to-sample distance. Measurement (2) is a repetition of (1) for the same (x, y)-position and shows a nearly identical graph. (c) From (3) to (6) the approach measurements where taken over a gold electrode, the border between gold and GaAs surface and over a GaAs surface. The shift of the Coulomb blockade current peaks along the island-sample distance axis indicates an inhomogeneous sample surface.

tion and we will try to explain its origin in the following section by electrostatic simulations on model arrangements.

Also the form of the curve representing the shifts is very different from position to position. Still the compensation voltage shifts are not arbitrary: Figure 7.3 (b) shows two approach measurements (1;2) at the same location before and after all the other measurements were taken and they look nearly identical. For the other measurements (3;4;5;6) the sample surface on which the approach measurement happens changes step by step from a gold electrode over the borderline to a GaAs surface. Due to the work function difference between the materials, a lot of charge is expected to accumulate at the interface between gold and GaAs during the cool down of the sample. The accumulation of charge was measured in several measurements showing rapidly varying SET current modulations at the borderline between gold and GaAs surface. This charge can be the origin for the shifts of the compensation voltage.

Compared to usual work function differences in AFM or STM measurements the achieved variance of $\pm 30\,\mathrm{mV}$ in the compensation voltage over the homogeneous gold electrode surface represents already a very small mismatch. Nevertheless for an ideal measurement with marginal influence of the tips onto an inhomogeneous sample surface we would have to make the applied tip-sample compensation voltage position dependent. Therefore, we would need a preceding measurement figuring out which compensation voltage has to be applied for each sample position. This course of action is very time consuming, instead, we should search for a homogeneous surface area to do potential measurements on.

7.3 Simulation of Distance Dependent Compensation Voltage Shifts

To find out the reason for the shifts of the compensation voltage with distance to the sample mentioned in the previous section, we simulated many different sample surface configurations and different approach scenarios. For instance we tried out a tip approach on a rough metal electrode, a non-perpendicular approach, dielectric particles on the sample electrode, all of them just showed slight deviations from the ideal approach characteristics of Figure 7.1 (a). In those attempts, for example, the period of the SET current peaks versus sample potential changed slightly different for an approach compared to the ideal case. A change in the compensation voltage, versus tip-sample distance was difficult to achieve. Only charged particles on the sample surface were able to shift the compensation voltage significantly. Usually the compensation voltage showed a shift into one sample direction. Solely the case of a charged particle reaching out of the sample surface, as shown in Figure 7.4 (a), was able to shift the compensation voltage value up and down on the sample potential scale while the tip is approaching the sample surface. Until the tip is on the same height as the particle the compensation voltage is shifted towards the electrostatic potential of the particle. While the SET island is beside the particle, the capacitive coupling between island and particle becomes weaker, and the island will be even shielded against the charged particle by the SET source contact. Then the sample surface potential, respectively work function of the surface electrode, dominates the value for the voltage needed to achieve a compensated situation. This behavior is nicely shown by the dashed line of the approach simulation in Figure 7.4 (b). In this simulation the charged particle was around 25 nm tall which is the turning point for the compensation voltage shift.

With a complex configuration of charged particles it becomes possible to model a sample surface with which the measurement results of Figure 7.3 can be simulated.

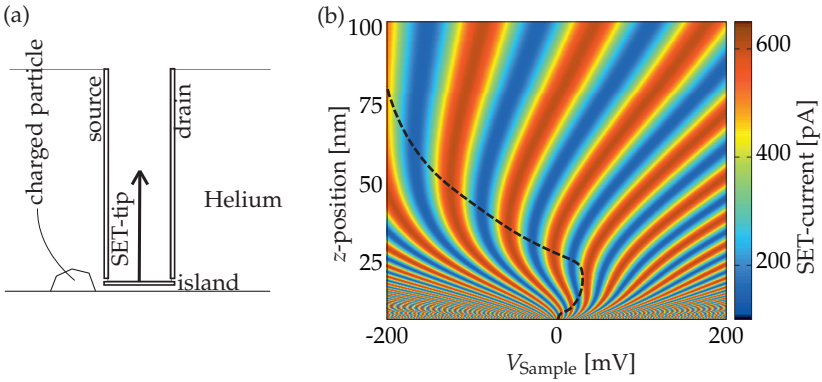

Figure 7.4:
Simulation of an approach measurement with a compensation voltage shifting up and down. (a) Geometric configuration of the SET tip over the sample surface next to a charged particle. (b) Simulation of the electric current through the SET versus applied sample voltage and island-sample distance. The dashed line shows the required compensation voltage. The compensation voltage shifts towards more positive sample voltages until an SET-island-to-sample distance of around 25 nm, equal to the particle size. Then the compensation voltage shifts towards smaller values and instead of the particle potential the sample surface potential dominates the compensation voltage value.

7.4 Simulation of Correlated SET Current Jumps

As a last part of this chapter the two types of features of the measured data mentioned in the context of Figure 7.1 (b) will be discussed. They are shown by jumps in the SET current correlated to the distance between island and sample surface and one of them even to the potential applied to the sample surface electrode.

The horizontal feature in Figure 7.1 (b) (black framed box) measures a jump of around 3.3 mV on the scale of the sample potential. This jump is too large to result from the electrical setup applying the voltage to the sample surface electrode. The largest potential jumps that can be expected by the electrical setup should be smaller than 0.1 mV. Also the IV-converter can be excluded because a change in the measurement electronics would rather result in an increase or decrease of the current measured, than in a shift on the sample potential axis. The feature could be a result of a charged particle on the sample surface or near the SET island arbitrary changing its charge state due to thermal fluctuations or a changed electrostatic configuration. Also the other less pronounced horizontal features suggest such instable particles.

The other measurement feature of Figure 7.1 (b) that is framed by a dash-dotted border is more difficult to be explained. It correlates with the sample potential and SET-island-to-sample distance. Therefore, it has to be influenced by the capacitive coupling towards the sample electrode and by the electrode's electrostatic potential. The appearance of this feature is not arbitrary and it was seen in many different approach measurements over several different sample positions, see Figure 7.2 (b). Hence, it has to be correlated with the environment of the SET tip structure, for example, a charged particle on its surface.

One possibility is to assume a particle changing its charge state or getting polarized over a certain threshold potential value. Concerning the location of such a particle the simulation that was matching the measurement the best had a particle near one tunnel barrier of the SET, the geometric configuration is shown in Figure 7.5. We simulated the usual geometric configuration of the SET tip and sample with an additional squared particle next to one tunnel barrier of the SET. The particle has a metallic surface at the top (green) to calculate the resulting potential for constant charge on the surface. This potential for the upper surface is plotted in color-code as a function of sample electrode potential and island-sample distance in Figure 7.5 (b). As a tricker for a polarization or charging of the particle we assumed an arbitrarily electrostatic potential of 30 mV for the top surface. If we

look at the contour line marking this value in the plot we get a curve with a very similar shape to the feature in the measurements.

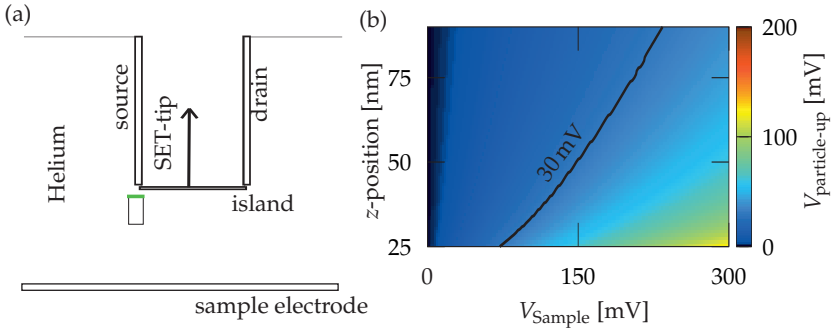

Figure 7.5:
Simulation of the electrostatic potential of a particle near one SET tunnel barrier. (a) Geometric configuration for the particle, SET and sample electrode. The upper surface of the particle (green) is modeled as electrode with fixed charge. (b) Electrostatic potential of the electrode versus sample voltage and distance between SET island and sample surface. The contour line indicates an arbitrarily chosen value of the electrode's electrostatic potential. The contour line symbolize the threshold value for a polarization or change of charge state for the particle.

7.5 Summary

In this chapter we have shown the differences between a simulated ideal approach characteristic of the SET towards a metal surface electrode and real measurements. In both cases we varied the electrostatic sample potential while changing the island-sample distance stepwise. The compensation voltage was determined by an invariance of the current through the SET over a variation of the SET-island-to-sample distance.

A remarkable point was the distance dependence of the required compensation voltage used to minimize the electrostatic potential difference between SET island and sample surface. Over a homogeneous gold surface the compensation voltage value only increased during the approach and ended up in a range from $-10\,\mathrm{mV}$ to $50\,\mathrm{mV}$.

For an inhomogeneous surface area, where gold on bare GaAs is present, we found as expected different compensation voltages at different positions. However in an approach the value for the compensation voltage was shifted up and down by more than $100\,\mathrm{mV}$. To explain the measured compensation voltage behavior we simulated several geometric configurations. Thereby we found out that charged particles reaching out of the sample surface were the only configuration showing such behavior.

Further measurement features like arbitrary jumps in the SET current were explained. A tip-sample distance and sample potential dependent SET current jump was explained by simulations. They result from particles on the sample or tip structure charging either randomly at a threshold value of their electrostatic potential.

In the Appendix C.6 on page 200 a further measurement can be found showing the mechanical induced alteration of a surface gold electrode by a touching SET tip.

8

Potential Probing of a Buried Electrode Structure

In this chapter we want to change from the probing of a surface gold electrode to a two-dimensional electron system (2DES) in an (Al,Ga)As heterostructure. The gold electrodes were used for the microscope characterization and to test the method for the tip-sample compensation. The buried 2DES will be the physical system we want to probe the Hall potential distribution of the integer and fractional quantum Hall effect on.

First, the possible contribution of the different (Al,Ga)As layers of the used heterostructure to the electrostatic potential distribution above the sample surface will be explained. As a next step the electrostatic potential distribution for a probing tip over a surface electrode and over a buried electrode will be compared by highlighting the differences for a broader and a narrower electrode structure. In this comparison we will calculate the partial capacitance between island and sample electrode for different electrode widths to quantitatively verify the differences. Due to the changed electrostatic configuration between SET island and sample electrode a new z-calibration will be simulated and compared to the one of a metal surface electrode.

Another important aspect is the change of the potential distribution due to the dielectric layers between SET island and 2DES. Therefore, a periodic structure of electrodes with alternating electrostatic potential is simulated for both geometric configurations to show similarities and differences between the electrostatic potential profiles possibly seen by the SET. To illustrate the importance of the tip-sample compensation we will give a short estimation of the change of the charge carrier density due to a remaining potential difference between island and 2DES.

As a last part of this chapter the necessary measurement technique to probe Hall potential distributions will be introduced. Step by step we will explain how we

get rid of contributions to our measurement signal that are superposed to the electrostatic potential variations coming from the buried layer structure we are interested in.

Due to the experimental inaccessibility of the situation, the whole chapter relies on electrostatic simulations done with the method of calculating finite elements.

8.1 Complications Probing a Two-Dimensional Electron System in a (Al,Ga)As Heterostructure

Previously, we have used gold electrodes located on top of the heterostructure directly under the probing tip to characterize the microscope. To measure Hall potential profiles in the quantum Hall regime we have to change to a buried two-dimensional electron system (2DES) in an (Al,Ga)As heterostructure due to its well understood and controlled structure and behavior.

Such heterostructures on the other hand have some additional charged layers between the 2DES and the probing tip, shown in Figure 8.1. There is the positively charged donor layer providing electrons to the 2DES and to the sample surface. For simplicity we assume a charge density around $-2.0 \times 10^{11}\,/\mathrm{cm}^2$ for the 2DES and the surface charge layer and $4.0 \times 10^{11}\,/\mathrm{cm}^2$ for the doping layer. Thereby, we obtain an electrical neutral situation but due to the asymmetric position of the doping layer in between the 2DES and surface charge layer we obtain a constant offset in the electrostatic potential above the sample for the simulations.

However, if the charge density in those layers is inhomogeneous, they will create an electrostatic potential gradient along the sample surface on their own. Such an inhomogeneity will make it more difficult to determine the tip-sample compensation, as comparably shown in chapter 7 for an inhomogeneous sample surface.

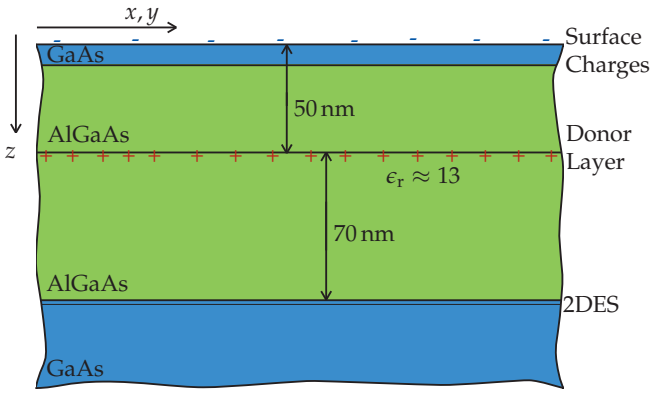

Figure 8.1: Layer composition for a two-dimensional electron system in an (Al,Ga)As heterostructure with charge located in the donor layer and on the surface of the sample. The layers above the 2DES possess a relative dielectric constant of $\epsilon_r \approx 13$.

Another effect on the electrostatic potential distribution above the heterostructure arises due to the difference of the dielectric constant in the layer above the 2DES and the volume above the sample surface. The layers in the heterostructure consist of GaAs and $Al_{\gamma}Ga_{1-\gamma}As$ and thereby have a dielectric constant of roughly $\epsilon_r \approx 13$. The liquid helium above the sample surface, around the SET tip has a dielectric constant of $\epsilon_r \approx 1.06$. We have to expect that the electrostatic potential distribution above the sample surface will not be identical to the one in the 2DES.

8.2 Capacitive Coupling between SET Island and a Buried Electrode Structure

The electrostatic potential distribution for a laterally broad and narrow electrode structure as a comparison between surface electrode and buried electrode are shown in Figure 8.2 (a) and (b)[1].

For a broad conductive structure, Figure 8.2 (a), there is no noticeable difference between the left (surface electrode) and right (buried electrode) configuration. In the case of the buried electrode the dielectric layer brings the electrode structure effectively closer to the sample surface.

In contrast, the situation for a confined conductive structure differs a lot for both cases, see Figure 8.2 (b). The electrostatic potential distribution over a surface electrode shows a gradient at a constant height above the surface. Contrary the electrostatic potential distribution at a constant height above the dielectric layer stays constant for a broad lateral range even away from the underlying electrode edge.

The difference in the electrostatic potential distribution between a surface electrode and a buried one can also be shown by calculating the capacitance between the SET island and the conductive structure. Therefore, we consider several different electrode sizes from 100 nm to 2000 nm for a surface electrode and a buried electrode[2]. A 129 nm distance is chosen between surface electrode and SET island. For the other case with the dielectric medium 120 nm between surface and SET island was chosen with the dielectric medium as described in the layer structures before.

The partial capacitance between SET island and electrode was calculated for different electrode radii and both geometric configurations. The values are displayed in Table 8.1.

With the values given in Table 8.1 we conclude that the smaller the lateral size of the electrode under the dielectric medium is, the larger the difference between the two geometric configurations becomes. For example, a buried electrode structure with a radius of 100 nm has nearly the same partial capacitance to the SET island

[1] To obtain enough details of the electrostatic potential distribution between sample surface and SET tip we have to reduce the electrostatic potential range in Figure 8.2 (a) and (b) due to the charge layers.

[2] To obtain more accurate values for this simulation a rotation symmetry around the z-axis is assumed by making the SET island round with a radius of 100 nm.

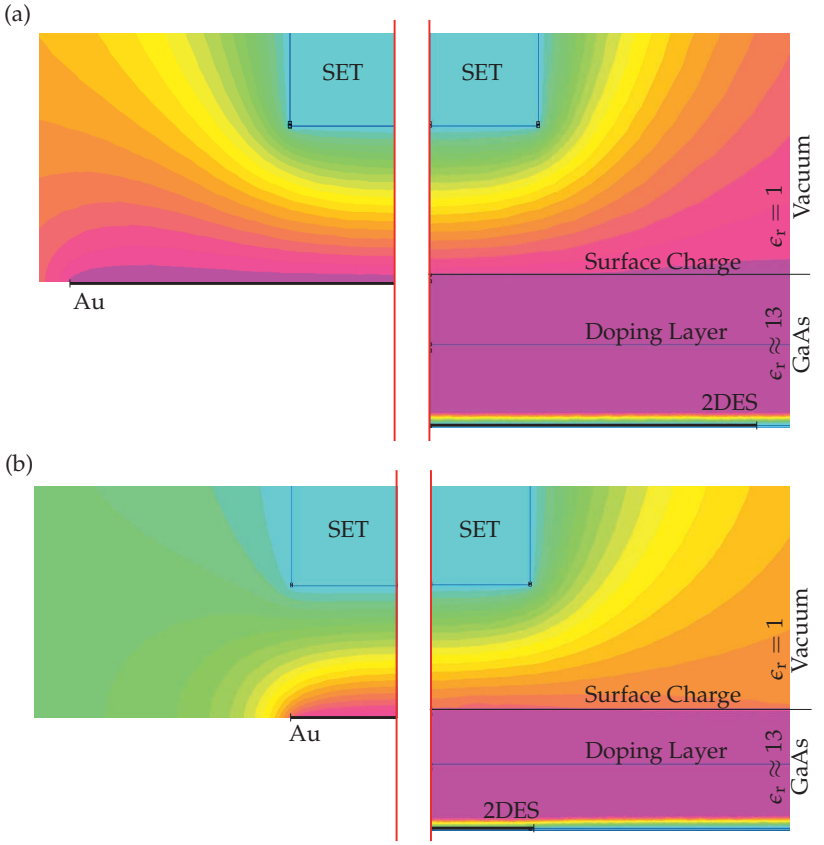

Figure 8.2:
Potential distribution between SET island and sample electrode. Comparison between gold surface electrode with a distance of 129 nm (left sides) and a two-dimensional electron system (here: metal electrode) buried 120 nm below the sample surface. Each of the four simulations is axially symmetric around the vertical red line. For the buried configuration a distance between SET island and sample of 120 nm was chosen (right sides). For the buried metal electrode with the charged layers the electrostatic potential range was reduced to less than 0.1 V to show the interesting parts with enough detail. The colors represent equidistantly the decreasing electrostatic potential starting at 0 mV (turquoise) to 100 mV (pink). (a) Simulation of sample electrodes with a radius of 300 nm. The difference in the electrostatic potential distributions is negligible. (b) Simulation of sample electrodes with a radius of 100 nm. There is a severe difference in the electrostatic potential distribution between the two configurations.

as a surface electrode with twice the radius. The differences become negligible if we have an electrode radius several times larger than the SET island size.

Therefore all measurements depending on the capacitive coupling like navigation, approach and also the probing of the electrostatic potential will show results that can not be transfered that easily to a surface electrode configuration.

electrode radius [nm]	partial capacitance surface electrode config. [aF]	partial capacitance buried electrode config. [aF]
100	2.368	3.781
200	3.760	4.315
300	4.144	4.394
400	4.260	4.421
2000	4.362	4.435

Table 8.1: Values for the partial capacitance between the SET island and sample electrode of different radii. Calculated for the geometric configuration of a surface electrode and a buried electrode.

8.3 z-Calibration over a Buried 2DES

Due to the changed capacitive coupling between the island and the now buried electrode, we have to redo the z-calibration of the microscope, presented in Chapter 6.3. The distance calibration between SET island and sample surface can be done analogous to the simulations for the gold surface and can be compared to those former simulations.

The geometric configurations for the z-calibrations that are used in the simulations are shown in Figure 8.3 (a) and (b). The variable d_1 represents the distance between SET island and a surface electrode and d_2 the distance between SET island and the sample surface 120 nm over the buried electrode. The result of the simulations are shown in (c) which displays a color-coded map of the current modulation through the SET versus sample potential and SET-island-to-sample distance. The left ordinate corresponding to the overall plot represents d_1 (distance in (a)) and the right ordinate which corresponds only to the dashed box represents d_2 (distance in (b)). The framed box was scaled in proportion and with an offset on the distance axis to fit the underlying plot. Special attention for the scaling was paid to the current peaks crossing the frame at the lower left end and at the upper right end.

We can see that d_2 has an offset compared to d_1 of around 9 nm. This fits roughly with the geometric configuration of a plate capacitor (sample and SET island) with a dielectric medium between them of 120 nm height and a dielectric constant $\epsilon_r \approx 13$. For larger island sample distances the vertical scale of d_2 is slightly compressed so that a height of 95 nm in d_1 corresponds very well to a height of 95 nm in d_2. The reason for this compressed scale is simply the finite lateral scales of the executed simulation model and the effect on the electrostatic potential distribution of the dielectric medium at the edges of the electrodes. Nevertheless those finite lateral dimensions are present in the real structures as well and have to be thought of.

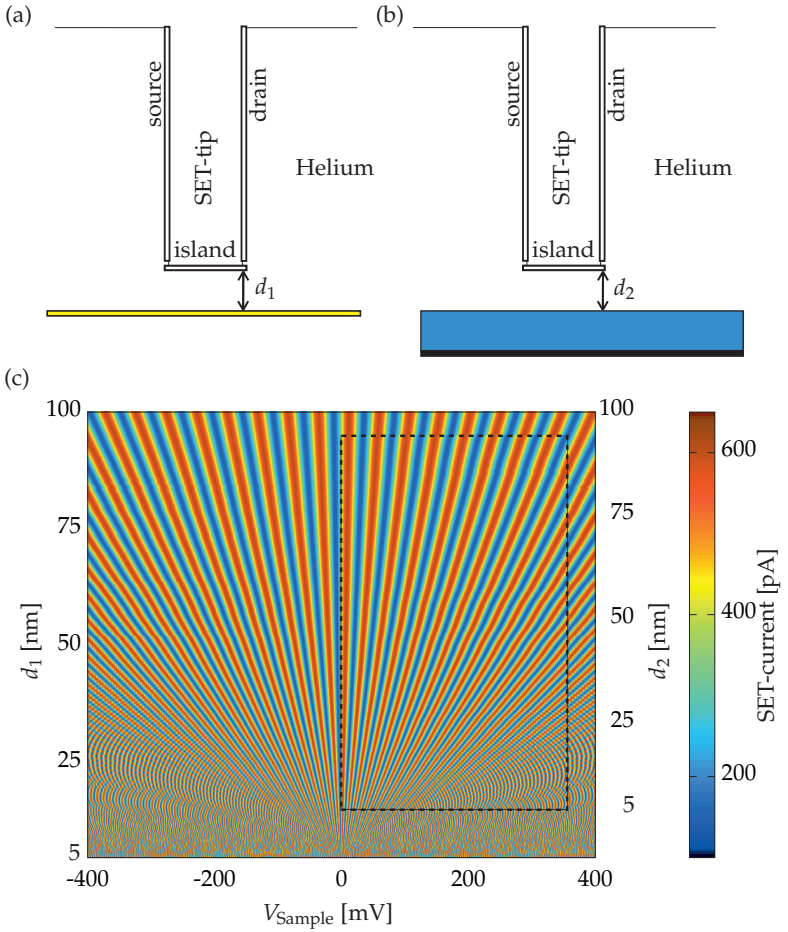

Figure 8.3:
z-calibration by the simulation of the SET current modulation versus applied sample voltage for different distances. (a) Geometric configuration of the SET over surface sample electrode. (b) Geometric configuration of the SET over a buried sample electrode (120 nm deep). (c) Color-coded plot of the simulated current through the SET versus sample potential for different sample-to-SET-island distances. The underlying plot displays the data from configuration (a) and the boxed plot uses the data of the simulation of configuration (b). The boxed area was scaled linearly to fit the underlying plot.

8.4 Potential Distribution over a Buried Periodic Electrode Structure

The decay of the measurement signal strength above the sample surface were simulate for a buried periodic electrode structure (with a period of two times the SET island size) with an alternating applied electrostatic potential[3]. With just 20 nm distance from the sample surface[4] the electrostatic potential modulations already decreased to roughly 60 % of its original value, for a distance of around 110 nm to 30 %. Therefore, we can state that it is important to keep the distance between probing tip and probed system as small as possible even if this means a risk to the probing tips.

Concerning the electrostatic potential distribution over the sample surface, we simulated a periodic electrode configuration with alternating electrode potentials, once without dielectric medium (Figure 8.4 (a)) and once with buried electrode structure (b). The result is shown in (c) where the underlying plot corresponds to (a) and the two rectangular boxes correspond to the geometric configuration of (b). For the left box we tried to fit the plotted structure to the range around $d_1 = 20\,\text{nm}$ and for the right one to the range around $d_1 = 140\,\text{nm}$. In both cases it was not possible to use an offset and linear scaling of the boxed plot so that they fit to all neighboring features. Thereby, we have to assume that a strongly changed electrostatic potential distribution due to the dielectric layer above the buried electrodes is present.

For close proximity of the SET to the sample surface the electrostatic potential of the SET island will stay longer at the same electrostatic potential if moved away from the center line of an electrode. The transition to another electrode of different potential will happen faster over the same position range. For larger SET-island-to-sample-electrode distances the difference between both configurations of periodic electrodes with alternating electrostatic potentials vanishes.

Therefore, we can conclude for measurements on a real 2DES structure that the potential distribution in close proximity will show more details than for larger distances but will exhibit a different distribution due to the dielectric medium between SET island and sample electrode. This means that the evolution of the Fourier components, describing the potential distribution defined at the electrodes, evolves differently versus distance for a space filled with two different dielectric media. With increasing distance the differences between the probed potential

[3] The electrostatic potential distribution can be found in the Appendix C.8 on page 203

[4] Around the smallest sample-island distance achieved with this microscope.

distributions will vanish but so do the details and the signal strength of the investigated electrostatic potential distribution.

Therefore, we can state that for potential distributions varying on small scales it can become difficult to conclude from the measured potential distribution exactly to the potential distribution present under the dielectric layer.

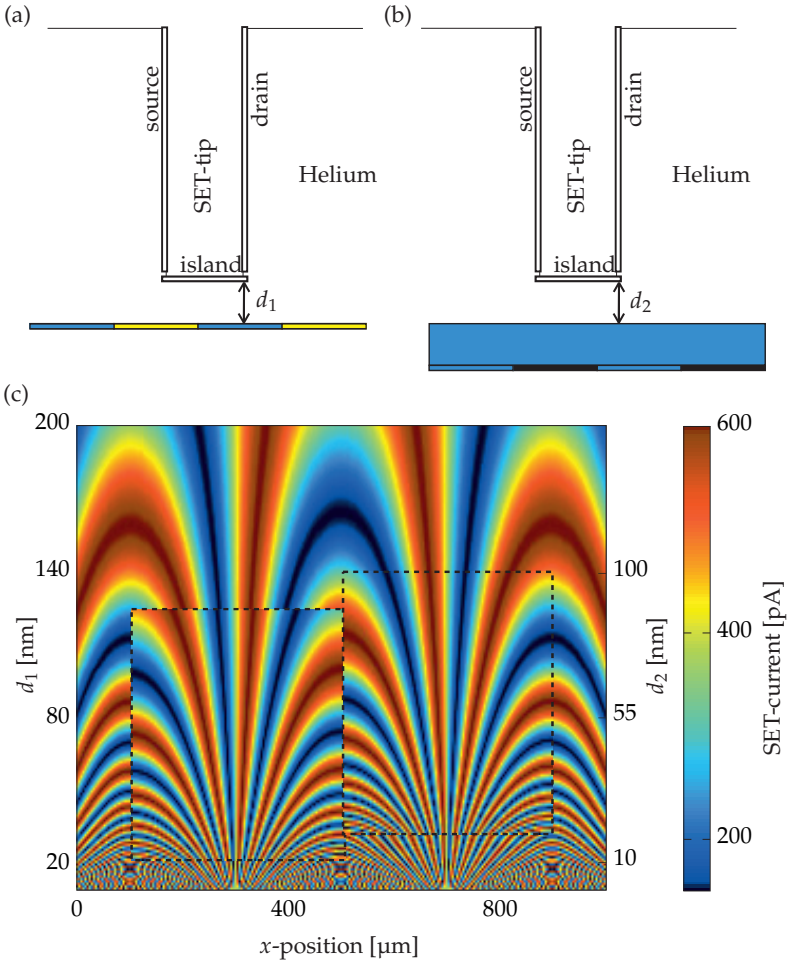

Figure 8.4:
Simulations of a periodic sample electrode configuration with alternating electrostatic potentials. (a) Geometric configuration for the periodic sample electrodes directly at the surface. (b) Geometric configuration of a 120 nm deep buried periodic sample electrode structure. (c) Color-coded plot representing the simulated current modulation of the SET for different x-position and different distances between SET island and sample surface. The underlying graph results from configuration (a) and the boxed one from the geometric configuration of (b). The boxed graph could not be fitted to all neighboring features by an offset and linear scaling. This indicates that a different electrostatic potential distribution is measured by the SET for configuration (b) compared to (a) that is not easy to map linearly.

8.5 Distortion of the 2DES by the Probing Tip

In the previous chapter we discussed the tip-sample compensation voltage and earlier in this chapter we calculated the contribution of the different sample electrode areas to the partial capacitance between SET island and the sample electrode. We will now assume a tip-sample compensation voltage mismatch of 30 mV which was a realistic value for the variation of our tip-sample compensation voltage on a homogeneous gold electrode. For the calculation we assume an SET island to sample surface distance of 25 nm with a two-dimensional electron system 120 nm under the surface. The distance results in a periodicity of around 15 mV for the SET current peaks. This means for a tip-sample compensation voltage mismatch of 30 mV roughly two additional electrons will populate the SET island and will partly deplete the two-dimensional electron system. The area exactly below the SET island (area 1) will see 84 % of this influence and a ring around this area with a width of 100 nm (area 2) will see another 14 %. The rest of 2 % over a large area is negligible. Due to the electron density in the 2DES of 2.0×10^{11} /cm^2 we have approximately 63 electrons in area 1 and 189 electrons in area 2. Our distortion will deplete statistically less than 1.7 electrons in area 1 and 0.3 electrons in area 2. Therefore, we get a change in charge carrier density of 2.7 % in area 1 and less than 0.2 % in area 2. Those values can be scaled linear to higher and lower tip-sample compensation voltage mismatches with roughly 0.1 % change in the charge carrier density for 1 mV mismatch. In this estimation we are not considering the charged layers in the sample structure.

8.6 Probing Technique for Current Induced Electrostatic Potential Distributions

Previously, measurement methods like the Coulomb blockade oscillation method and the feedback loop method were introduced. They exhibit the problem that the measurement signal is affected by the electrostatic potential of the sample and the capacitive coupling between SET island and the sample or the environment. Even local charge on the sample make an influence on the measured signal. To overcome this problem the AC-feedback loop method was introduced. In this case a second signal is obtained by an additional AC modulation only measuring the capacitive coupling. Nevertheless it is difficult to calculate the electrostatic potential distribution within the 2DES by this method. Furthermore, the measurement method is not sufficiently stable and quite large excitation voltages are required, destroying fragile quantum Hall states. Hence, another method had to be found to gain the right information from a scanned sample.

Therefore, we want to have a look at a heterostructure possessing a two-dimensional electron system, as it is displayed in Figure 8.5. If we scan the sample surface with the feedback loop method in DC, the measured signal would roughly look like the color-coded surface of the sample. We can see the following influences as a change in the measurement signal:

- Charges and charged particles located on the surface of the structure, positively charged ions in the donor layer ($\Delta Q^{ind}_{\mathrm{Env}}$),
- conductive layers in the nearby environment ($\Delta C_{\mathrm{Env}} \cdot V_{\mathrm{Env}}$),
- dielectric particles and changes in the capacitive coupling between SET island and 2DES at the borders of the structure ($\Delta C_{\mathrm{sample}}$),
- variations in the electrostatic potential of the two-dimensional electron system ($\Delta V_{\mathrm{sample}}$).

The result is a quite confusing measurement signal giving us no distinct information about what is happening due to an evolving quantum Hall effect state.

To describe this situation mathematically we can use relation (4.11) and add Q^{ind}_{env} as a virtually induced charge on the SET island by real charge located on or in the sample structure. This leads for an isolated island to the constant charge equation

$$\begin{aligned} \mathrm{const} = Q_0 = {} & C_{\mathrm{sample}}(V_{\mathrm{sample}} - \phi_{\mathrm{i}}^{\mathrm{isol}}) + C_{\mathrm{S}}(V_{\mathrm{S}} + V_{\mathrm{com}} - \phi_{\mathrm{i}}^{\mathrm{isol}}) \\ & + C_{\mathrm{D}}(V_{\mathrm{D}} + V_{\mathrm{com}} - \phi_{\mathrm{i}}^{\mathrm{isol}}) + C_{\mathrm{Env}}(V_{\mathrm{Env}} - \phi_{\mathrm{i}}^{\mathrm{isol}}) + Q^{ind}_{\mathrm{env}}. \end{aligned} \tag{8.1}$$

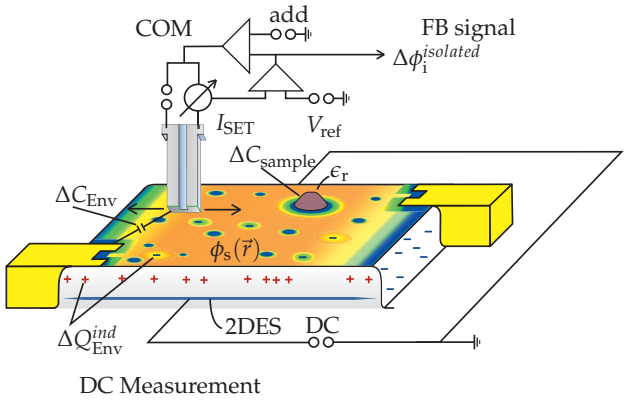

Figure 8.5:
Electrostatic potential distribution near the sample surface over a 2DES buried in a (Al,Ga)As heterostructure. The color-coded surface shows a sketch of the measurement signal of a DC feedback loop measurement. The measurement signal is influenced by surface charge, dielectric particles, the donor layer, as well as the border of the 2DES and other structures.

Rearranging this equation we can mark some parts of it as constant

$$\begin{aligned} \text{const} = Q_0 = C_{\text{sample}} \cdot V_{\text{sample}} + C_{\text{Env}} \cdot V_{\text{Env}} - \phi_i^{\text{isol}}(C_{\text{sample}} + C_{\text{Env}}) \\ + \underbrace{(V_{\text{com}} - \phi_i^{\text{isol}})}_{const.} \underbrace{(C_D + C_S)}_{const.} + \underbrace{C_S \cdot V_S}_{const.} + \underbrace{C_D \cdot V_D}_{const.} + Q_{\text{env}}^{ind}, \end{aligned} \tag{8.2}$$

which we can further sum up to the constant c_1. The corresponding electrostatic potential for the isolated island is given by

$$\phi_i^{\text{isol}} = \frac{C_{\text{sample}} V_{\text{sample}} + C_{\text{Env}} V_{\text{Env}} + Q_{\text{env}}^{ind} + c_1}{C_{\text{sample}} + C_{\text{Env}}}. \tag{8.3}$$

If we apply now a sinusoidal AC signal

$$V_{AC}(t) = \hat{V}_{AC} \cdot \sin(\omega t) \tag{8.4}$$

to drive an alternating current through the sample we get a time dependent sample potential distribution with a position dependent amplitude

$$V_{\text{sample}}(\vec{r}, t) = V_{AC}(\vec{r}) \cdot \sin(\omega t). \tag{8.5}$$

The electrostatic potential of the isolated island now follows the expression

$$\phi_{\mathrm{i}}^{\mathrm{isol}}(\vec{r},t) = \frac{C_{\mathrm{sample}}(\vec{r}) \cdot V_{\mathrm{AC}}(\vec{r}) \sin(\omega t) + C_{\mathrm{Env}}(\vec{r}) V_{\mathrm{Env}}(\vec{r}) + Q_{\mathrm{env}}^{ind}(\vec{r}) + \mathrm{c}_1}{C_{\mathrm{sample}}(\vec{r}) + C_{\mathrm{Env}}(\vec{r})}. \quad (8.6)$$

Neither an electrode nor a charge in the near environment is following this sinusoidal signal, therefore, the lock-in amplifier detects a signal influenced by a position dependent capacitive pre-factor multiplied with the position dependent potential amplitude:

$$V_{\mathrm{FB,AC}} = \phi_{\mathrm{i}}^{\mathrm{isol}}(\vec{r}) = \frac{1}{1 + \frac{C_{\mathrm{Env}}(\vec{r})}{C_{\mathrm{sample}}(\vec{r})}} \cdot V_{\mathrm{AC}}(\vec{r}). \quad \textbf{(}\alpha\textbf{-trace Measurement)} \quad (8.7)$$

This measurement type in which we apply an alternating voltage to drive an alternating current through the sample will further be denoted as α-trace measurement.

The demodulated signal is now free of all static influences of the sample structure and environment that can not follow the sinusoidal signal, as shown in Figure 8.6 (a).

Still the position dependent capacitance factor is part of the measurement signal. Hence, we have to execute a second measurement just sensitive to the capacitive coupling between the SET island and the sample/environment. This can be done by applying an alternating voltage to the entire, investigated sample structure, as shown in Figure 8.6 (b), obtaining a position independent amplitude

$$V_{\mathrm{AC}}(\vec{r}) = V_{\mathrm{AC,COM}}. \quad (8.8)$$

In contrast to the α-trace measurement we are not driving a current through the sample and therefore denote this type as β-trace measurement:

$$V_{\mathrm{FB,AC,COM}} = \phi_{\mathrm{i}}^{\mathrm{isol}}(\vec{r}) = \frac{1}{1 + \frac{C_{\mathrm{Env}}(\vec{r})}{C_{\mathrm{sample}}(\vec{r})}} \cdot V_{\mathrm{AC,COM}}. \quad \textbf{(}\beta\textbf{-trace Measurement)} \quad (8.9)$$

To get rid of the position dependent capacitance factor and to figure out the electrostatic potential distribution caused by the current through the sample we have to divide the data obtained by the α-trace measurement by the data obtained by the β-trace measurement for the same sample position range

$$\phi_{\mathrm{s,cal}}(\vec{r}) = \frac{\phi_{\mathrm{i,source}}^{\mathrm{isol}}}{\phi_{\mathrm{i,COM}}^{\mathrm{isol}}} = \frac{V_{\mathrm{AC}}(\vec{r})}{V_{\mathrm{AC,COM}}}. \quad \textbf{(Calibrated Potential)} \quad (8.10)$$

Further, we will refer to the calculated result as a calibrated potential profile. If the applied excitation voltage amplitudes are the same, the values for the calibrated potential can reach from 0 to 1 due to the division of the two AC amplitudes. The resulting distribution of our example is displayed in Figure 8.6 (c). There is no dielectric particle and no border of the sample present in the resulting measurement signal any more. This calibration technique is from an experimental point of view similar to the one used for previous scanning probe microscopes measuring the electrostatic potential distribution in two-dimensional electron systems under quantum Hall conditions [12, 16, 18, 58, 91]. The theoretical description differs and less aspects have to be considered, as first of all, we do not measure the electrostatic potential variation by the detour over a force measurement and, second, we do not have to consider image charges resulting in higher order terms.

A weakness of this calibration technique is the necessity that the investigated sample area only consists of low-ohmic connected areas. Otherwise it could happen

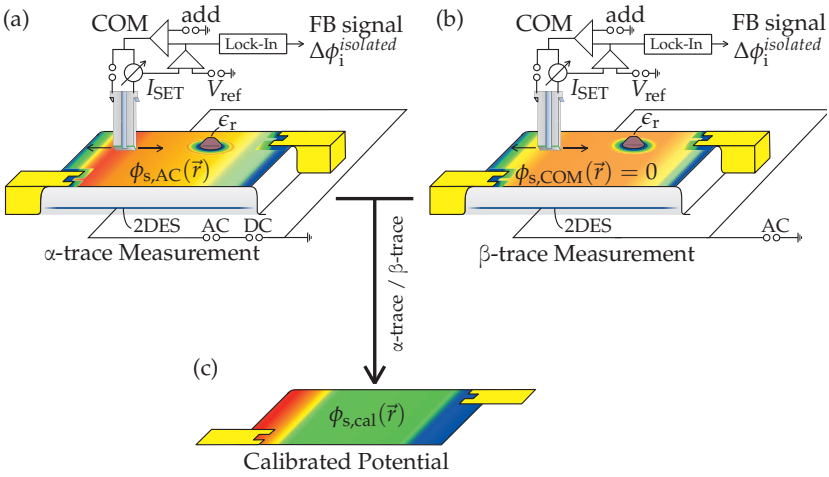

Figure 8.6:
Sketch of the probing technique and the resulting measurement signals. (a) α-trace measurement with an AC current through the sample. The measurement signal represents the demodulated feedback signal for an alternating current driven through the sample. (b) β-trace measurement driving no current through the sample but alternating the whole sample potential. The measurement signal represents the demodulated feedback signal for an applied alternating sample potential with out driven current. (c) Calibrated potential distribution resulting from a division of the α-trace measurement data by the β-trace measurement data for the same scan positions.

that even the AC amplitude of the β-trace measurement $V_{AC,COM}$ could become position dependent and would falsify the resulting calibrated potential distribution. Due to the used AC excitation we have to be aware of this occurrence.[5]

With the described sinusoidal signal we achieve an integration of the measurement signal over a range of driven currents for the α-trace measurement even for both current directions. To avoid this integration over both current directions we can add a DC voltage offset of $V_{DC,Offset} = \hat{V}_{AC}$. Therefore, the alternating voltage is always above zero and we only integrate over one current direction. If we want to avoid now the integration over different current levels at all we have to change from a sinusoidal excitation form to a rectangular one, still with the DC offset voltage as mentioned before. As a result the current switches between a certain value and zero. Compared to the previous scanning probe setups we do not have quadratic or other higher order terms of the local sample potential in equation (8.6). Therefore, we are less limited in the choice of an excitation function.

[5]We want to give an estimation about the required sample resistance. If the whole Hall bar structure is assumed as a capacitor plate with a metal layer covering the surface of the heterostructure as a second plate, it requires an ohmic resistance of more than 23 MΩ that 1.3 Hz would be the cut-off frequency. This estimation represents a worst case scenario with a minimal required resistance value.

8.7 Summary

In this chapter the complications for measuring an electrostatic potential distribution in a two-dimensional electron system in an (Al,Ga)As heterostructure were explained. First we looked at the different layers of the used heterostructure lying above the 2DES and explained their expected influence on the electrostatic potential distribution measured by the SET.

Then a comparison between the SET tip over a surface metal electrode and the SET tip over a two-dimensional electron system treated as a metal electrode buried 120 nm under the sample surface was done. For both configurations we simulated the electrostatic potential distribution between conductive layer and SET island. They displayed that the dielectric medium between electrode and SET island changes significantly the electrostatic potential distribution at the sample surface. Afterwards, we compared the capacitance between SET island and sample electrode for different dimensions of the electrode for both geometric configuration. An enhanced capacitive coupling was found for buried narrow electrodes compared to narrow electrodes on the surface.

Further, we simulated approach measurements for both geometric configurations. Thereby, we got a new z-calibration due to the change to buried electrodes. The dielectric layers above the 2DES vary the capacitive situation and therefore the measurement of the distance between an electrode and the SET island. We obtain an offset of around 9 nm compared to the approach measurements for a metal surface electrode. The offset is explained by the dielectric medium.

Afterwards an electrostatic potential distribution of a periodic structure (with dimensions in the size of the SET island) with alternating electrostatic potential was simulated to obtain information about the possible measurement signal strength. The result was a decrease of the electrostatic potential modulation strength to 60 % from its original value with a 20 nm SET-island-to-sample surface distance and down to 30 % for a distance of 110 nm.

Further we simulated a measurement with the CBO method to see the difference in the electrostatic potential distribution in comparison between a buried and a surface electrode. Therefore, we simulated again a periodic electrode configuration with alternating potentials for both geometric configurations. Fitting the two geometric configurations with and without dielectric layer proved to be impossible with an offset and a linear z-direction scaling. The conclusion is that for larger distances the electrostatic potential distribution of both geometric configurations becomes more similar but a lot of details in the distribution and modulation

strength are lost while measuring with a large island-electrode distance. For close proximity of the probing tip and the sample surface a modified electrostatic potential distributions will be measured.

Afterwards we estimated the influence of a not completely compensated SET tip on the 2DES. For every 1 mV mismatch in the compensation voltage the charge carrier density will be changed around 0.1 % in the area directly under the SET island. Due to such a depletion the local filling factor of the quantum Hall effect can change and thereby falsify a measured Hall potential distribution.

As a last part of this chapter we presented a probing technique to measure current induced electrostatic potential distributions. This was done by taking two scan measurements, one with an AC modulated current through the sample (α-trace measurement) and one alternating the electrostatic potential of the whole sample (β-trace measurement) without a current. If the data of the α-trace measurement is divided by the data obtained by the β-trace measurement for the same sample positions we obtain a calibrated potential distribution. The value of the calibrated potential varies at maximum in the range from 0 to 1 for identical excitation voltages for both measurements and shows the changes of the electrostatic potential distribution caused by a current through the sample. With this probing technique we are able to probe the Hall potential distribution of a quantum Hall sample with a buried two-dimensional electron system even if there are charges, dielectric particles, 2DES edges, etc. present.

9
Hall Potential Profiles

The primary purpose to set up this scanning probe microscope is the measurement of the Hall potential profile for different filling factors in the integer and fractional quantum Hall regime. With the knowledge from the preceding chapters it is possible to probe those current-induced electrostatic potential distributions with the presented setup.

In this chapter, firstly, we characterize the sample itself by measuring its Hall resistance and longitudinal voltage drop. To find a sample area suitable for the potential distribution measurements, areas are scanned to obtain information about the location of particles located on the heterostructure surface. Then the tip-sample compensation voltage for the best suitable area, chosen for later Hall potential profile scans, is determined.

To illustrate how we obtain a calibrated Hall potential profile for a line scan from the α- and β-trace we will show the raw data of the two measurements and the resulting calibrated potential distribution. This will help to understand all following graphs of the Hall potential profiles. The profiles will be presented in two ways, firstly, as an area plot to show the x-direction homogeneity and, secondly, as line scans versus magnetic field to show the evolution of the Hall potential distribution over a whole filling factor range. From these measurements the Hall current distribution over the cross section of the sample in the quantum Hall regime can be determined.

9.1 Hall Bar Characterization

Before the electrostatic potential distribution is measured on the relevant sample area we have to characterize the sample. The easiest way to do so is a standard quantum Hall measurement including the Hall resistance and the longitudinal voltage drop.

The used electrical circuit to characterize the sample is shown in Figure 9.1 (a). A difference to most other measurements is that we apply a constant source-drain voltage V_{SD} to the Hall bar structure and measure the electric current on drain and source side. This course of action protects the sample and all parts of the structure from an exaggerated voltage in the case of a strong change in the sample resistance compared to a constant electric current applied through the sample. In addition this method is necessary for the used calibration technique. For the recorded data we measure with two differential amplifiers between two side contacts located on the same sample side and between two opposing side contacts across the Hall bar. Thereby we measure V_{long} , V_{Hall} and can calculate $R_{\text{Hall}} = {}^{V_{\text{Hall}}}/_{I}$ and $R_{\text{long}} = {}^{V_{\text{long}}}/_{I}$.

The characteristic Hall voltage V_{Hall} (blue), source and drain current $I_S = I_D$ (green), longitudinal voltage drop V_{long} (orange) and the calculated Hall resistance R_{Hall} (black) with some quantized values of $R_{\text{Hall}} = {}^{h}/_{\nu e}$ are plotted in Figure 9.1 (b). The two-dimensional electron system is located 120 nm below the sample surface. It has a charge carrier density of around $2.0(1) \times 10^{11}\,\text{cm}^{-2}$ obtained from the classical Hall resistance curve in the range of $\pm 0.3\,\text{T}$ in our measurement system[1]. Therefore, the integer bulk filling factors $\nu = 1$ and $\nu = 4$ lie at 8.27 T and 2.07 T. The best developed fractional filling factor $\nu = {}^{2}/_{3}$ lies around 12.4 T. For at least all of the mentioned quantum Hall states the longitudinal voltage drops close to zero. Therefore, we assume that they are well developed states. Except for $\nu = 4$, the other mentioned filling factors have not yet been investigated by previous scanning probe measurements of our group with respect to their Hall potential profiles. Nevertheless we decided that measuring around filling factor $\nu = 4$ would be a good first step as the small changes in the magnetic flux density to cover the whole resistance plateau and thus the resulting position corrections are rather small. Further, the Hall potential distributions for $\nu = 4$ can be compared to previous measurements [16] to verify the functionality of the microscope.

[1] For the heterostructure DII0222A, grown and provided by C. Reichl from the W. Wegscheider group at ETH Zurich mediated by W. Dietsche, a charge carrier density is stated at $1.4 \times 10^{11}\,\text{cm}^{-2}$ and the charge carrier mobility lies around $8.9 \times 10^{6}\,\text{cm}^2/\text{Vs}$ for the non-illuminated case.

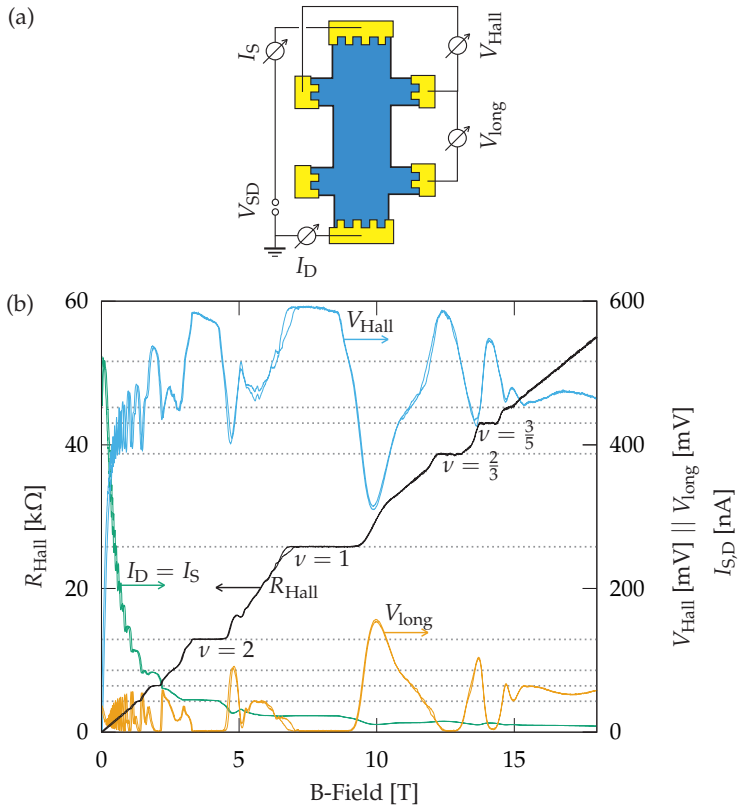

Figure 9.1:
Standard characterization of a two-dimensional electron system in strong magnetic fields. (a) Sketch of the measurement setup for a six-terminal Hall bar structure. In all our measurements we apply a source-drain voltage (here $V_{SD} = 0.59\,\mathrm{mV}$) to the 2DES instead of driving a constant electric current through the device. We measure the sample current on source and drain side. Furthermore, the longitudinal and transversal potential difference are measured by differential amplifiers. (b) Hall resistance curve (black) with partly labeled quantum Hall plateaus, measured Hall voltage (blue) and longitudinal voltage (orange), as well as measured electric current through the sample on source and drain (green) side. The Hall resistance and longitudinal voltage drop show that the quantized states with filling factor $\nu = \{4; 2; 1; 2/3\}$ are fully developed and suitable for Hall potential profile measurements.

9.2 Surface Homogeneity of the Investigated Sample Area

With the longitudinal resistance we can state whether the 2DES between the side contacts (along the sample) is in the quantum Hall regime. A Hall resistance plateau is telling us whether the 2DES in the area between and around the side contact (across the sample) is in the quantum Hall regime. Therefore, we chose the most homogeneous sample area in the vicinity of two side contacts (across the sample) and between the side contacts (along the sample). With those criteria we ended up to probe the area beneath the red colored rectangle illustrated in Figure 9.2 (a).

Further, in Figure 9.2 (b) and (c) surface area scans executed with the CBO and FBL method are presented. In the plot of the SET current obtained by the CBO method we can clearly see roundish features that are probably dielectric or even charged particles. Most likely those particles are remains of the resist used for the optical lithography. Nevertheless this area was one of the most homogeneous areas on the active structure that was found. The area scanned with the CBO method is around 6.5 µm by 22 µm large and is thereby chosen a bit larger than the mesa structure width. Its borders are marked by the dotted line.

For later line scans across the 2DES a x-position around 2 µm is used highlighted by the black line in the CBO method measurement. This position was chosen for its mostly homogeneous potential distribution due to the absence of particles on this line.

The feedback loop method measurement shows the same roundish shapes and a strong electrostatic potential drop for the SET island at the left and right border of the sample structure. All roundish features are shifting the electrostatic potential of the SET island towards the same direction. Therefore, it is likely that at all those positions an enhancement of the capacitive coupling towards the 2DES by dielectric particles is present.

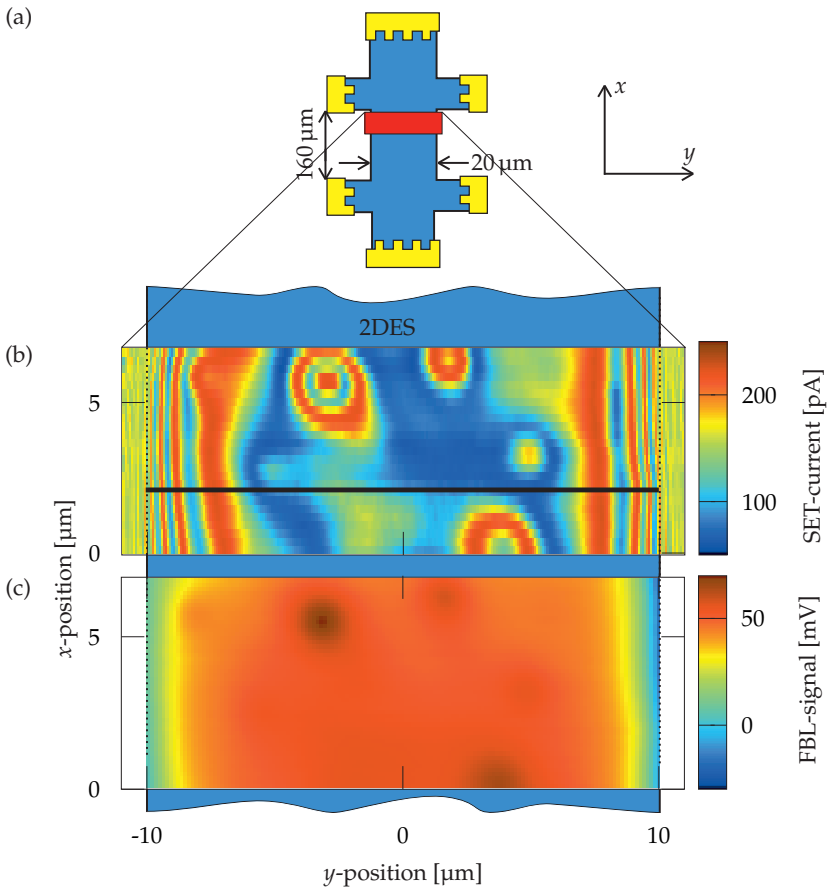

Figure 9.2:
Area chosen to probe the Hall potential profiles. (a) Sketch of the Hall bar structure. The red area is the area used for the area scans. The microscope coordinate system had to be adjusted to fit to the common used coordinated system for Hall measurements. (b) Area scan executed with the CBO method showing the electric current through the SET for different (x, y)-positions. The round shaped features indicate particles on the surface of the structure. Still it is one of the most homogeneous areas found on the sample. The black line over the most homogeneous part of this area indicates the position range for Hall potential line scans. (c) Area scan executed with the FBL method showing the round shaped features at the same position. All particles shift the electrostatic potential of the SET island towards the same direction. Therefore, those features are likely to be dielectric particles changing the capacitive coupling between tip and 2DES.

9.3 Tip-Sample Compensation

As explained in the previous chapter, a wrongly compensated probing tip can, for instance, deplete the two-dimensional electron system. Therefore, the local filling factor around the tip area can differ from the other areas. To reduce the influence on the sample by our probing tip we did twice a tip-sample compensation measurement at different positions on the black colored line in Figure 9.2 (b). The results of those two measurements are shown in Figure 9.3 (a) and (b).

We obtain a necessary compensation voltage of 63 mV in the first measurement and of 57 mV in the other measurement. Without spending more time on further compensation measurements due to their good accordance we can state a tip-sample compensation voltage of 60(3) mV. The mismatch could give us a relative depletion of less than 0.3 % in the area below the SET island. This value is very small compared to previous scanning probe experiments. Therefore, we can assume a well compensated tip-sample configuration that is nearly non-disturbing for the two-dimensional electron system[2].

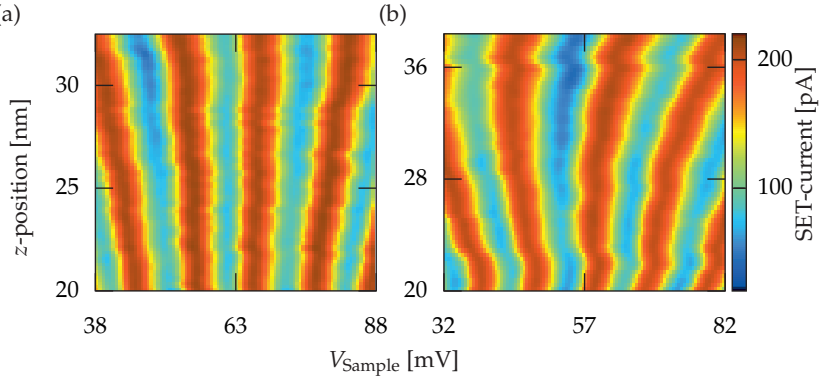

Figure 9.3:
SET current modulation versus applied sample voltages for different tip-sample distances. The measurements help to obtain the tip-sample compensation voltage over a buried 2DES. Measurement (a) indicates a compensation voltage of 63 mV, and measurement (b) indicates a compensation voltage of 57 mV. Therefore, a compensation voltage of 60 mV is applied to the 2DES for the Hall potential profile measurements with a mismatch of around ±3 mV.

[2]The applied voltage to the source contact of the SET lies around 0.5 mV and is therefore smaller than the compensation voltage mismatch.

9.4 Line Scans - Raw Data and Resulting Calibrated Potential

As illustrated in the previous chapter, so-called α- and β-trace measurements are necessary to get rid of static influences and changed capacitive coupling between SET island and 2DES. In Figure 9.4 (a) and (b) α- and β-trace measurements are shown along the mentioned black line in Figure 9.2 (b) for a magnetic field of 1.95 T. In the shown graphs, as in the measurements of the following sections, the line was scanned five times and then we averaged over those data sets as explained in chapter 6. The magnetic field corresponds to a filling factor of $\nu = 4.24$ and the distance between sample surface and SET island measured roughly 20 nm. In (a) we can see the potential distribution multiplied with a pre-factor including the capacitive coupling. The capacitance between island and sample changes at the edges of the scan range, where a clear drop of the signal is visible. The same drop at the edges can be recognized in the β-trace representing the capacitive coupling multiplied with a homogeneous modulation amplitude of electrostatic

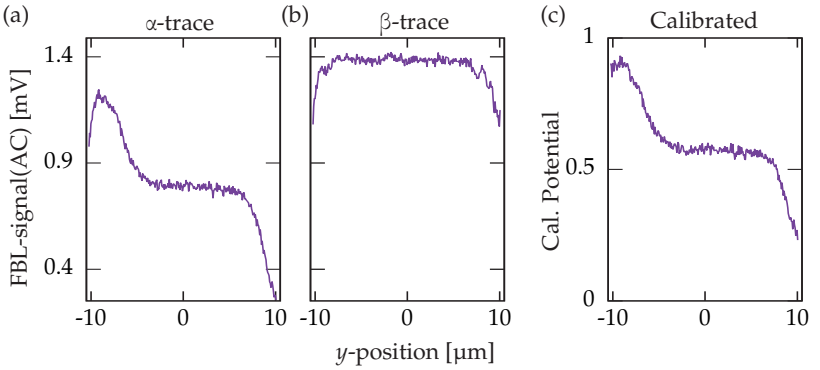

Figure 9.4:
Complete set of raw data as described by the probing technique in Chapter 8.6 to achieve a calibrated Hall potential profile. (a) α-trace measurement showing the demodulated feedback signal over y-position for the case of an alternating current through the sample. (b) β-trace measurement representing the demodulated feedback signal over y-position for the case of an applied alternating voltage without electric current through the sample. (c) Calibrated potential profile resulting from the division of the α-trace measurement data by the β-trace measurement data for the same scan positions. The calibrated potential shows only the position dependent difference between the electrostatic potential distribution of the 2DES with and without driven current. Any static influences or variations in the capacitive coupling between SET and environment/sample are not recorded.

potential over the whole two-dimensional electron system. This drop at the edges of the Hall bar structure arises from the end of the 2DES as sample electrode. The smoothness of the sample surface along the measured line can be seen at the nearly constant middle part of the β-trace.

Dividing the α-trace by the β-trace we get the calibrated potential distribution presented in Figure 9.4 (c). The drop due to the capacitive coupling at the edges is not present anymore.

The calibrated Hall potential curve is neither reaching 0 nor 1 due to series resistances before and after the investigated area. The applied voltage for the α-trace measurement is thereby divided between the different parts in the circuit. Resistive parts of the 2DES, the ohmic contacts and the wiring through the microscope rod can contribute to such series resistances. For the β-trace measurement, due to the currentless situation, the applied voltage from the electrical measurement setup is not divided and completely present in the sample. Therefore, a division of the α- and β-trace data is in the range of $0 < V < 1$.

The measurement was executed with an excitation voltage of $V_{\mathrm{AC,Rms}} = 1.41\,\mathrm{mV}$ as all following Hall potential distribution measurements. If the excitation signal strength is reduced, the recorded data shows more noise and the devision by the β-trace data can create a strong noise in the calibrated potential curve.

In the following sections of this chapter only calibrated potential profiles will be shown.

9.5 Hall Potential Profiles at $\nu = 4$

After characterizing the sample, scouting for a suitable sample area and having the tip-sample configuration compensated, we scan areas for different magnetic fields.

A zoom-in on the Hall and longitudinal resistance of the sample and the filling factor over the magnetic field is shown in Figure 9.5. We have chosen a range of filling factors around $\nu = 4$ to avoid large mechanical shifts between tip and sample position due to the small changes in the applied magnetic field to cover one complete Hall resistance plateau.

The magnetic fields and resulting filling factors used for the area scans in Figure 9.6 are marked by the vertical black lines in Figure 9.5. For the area scans we have chosen different magnetic field values, respectively filling factors, lying slightly before, in or after a Hall resistance plateau.

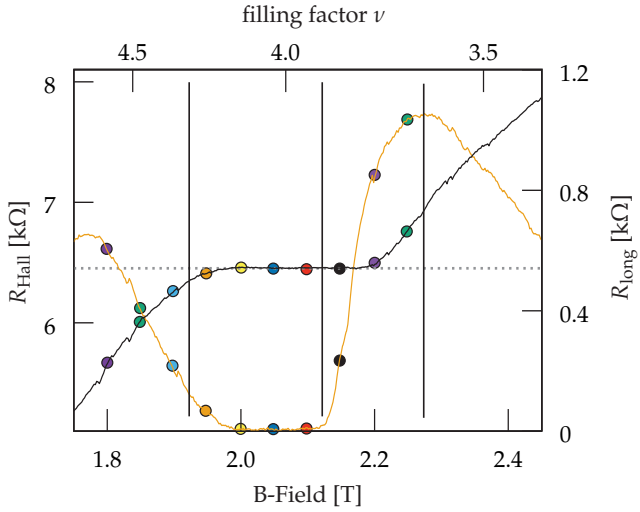

Figure 9.5:
Hall and longitudinal resistance curve over a range of magnetic field with corresponding Landau level filling factors (around $\nu = 4$). The vertical black lines mark the magnetic fields for which the later (x, y)-area scans are executed. The colored dots mark the position on both curves for which the later line scans are executed. The colors of the line scans, shown later, correspond to the colors of the dots.

In Figure 9.6 (a) the Hall potential distribution outside of the quantum Hall regime at filling factor $\nu = 3.64$ is visible as a color-coded plot of the calibrated Hall potential on the left side and as a pseudo 3D representation on the right side. We can see a non-linear potential drop over the whole width of the structure. From previous scanning probe experiments we would expect a linear drop. The reason for this discrepancy has not yet been clarified.

Figure 9.6 (b) shows the bulk dominated regime at filling factor $\nu = 3.89$. The measurement was recorded for an applied magnetic field for which the longitudinal resistance is close to zero and the Hall resistance shows a quantized plateau. Therefore, the quantum Hall effect has to be present in the scanned area. We can clearly see that there is only one large potential drop near the center of the 2DES ($y \approx -3\,\mu m$). This potential drop has a constant y-position over the whole range measured along the sample structure. The electric current through the 2DES flows perpendicular to the potential drop as stated by (2.25). Therefore, the shown potential distribution contradicts the commonly used picture of edge-channels carrying the electric current through the sample in the quantum Hall effect by two points: Firstly, we have only one potential drop over the whole width and, secondly, we have a drop positioned clearly in the bulk of the 2DES.

Figure 9.6 (c) depicts the Hall potential distribution around the edge-dominated regime at filling factor $\nu = 4.30$. Characteristic for this regime are the two potential drops along the edges of the 2DES with a constant Hall potential in between. In our measurement the right potential drop is constantly at the same y-position over different x-positions, however the left potential drop varies slightly its y-position. This can be caused by a raised charge carrier density due to the large feature visible in Figure 9.2 (b).

Figure 9.7 shows the Hall potential profile[3] evolution in a range of applied magnetic fields from 1.80 T to 2.25 T in steps of 50 mT. The corresponding position on the Hall and longitudinal resistance curve for each line scan is indicated by the dots in Figure 9.5 with the same color as the measurement curves.

In those measurement curves the potential drop on the left in between the dashed lines shifts towards the center of the 2DES and becomes larger with increasing magnetic field until it vanishes. The right Hall potential drop in contrast broadens only slightly and vanishes with increased magnetic field. Therefore, we can distinguish between three regimes [16]: outside the quantum Hall effect with a potential drop over the whole 2DES width, the edge-dominated regime with two

[3]The whole set of α-trace , β-trace and calibrated potential are shown in Appendix C.9 on page 204.

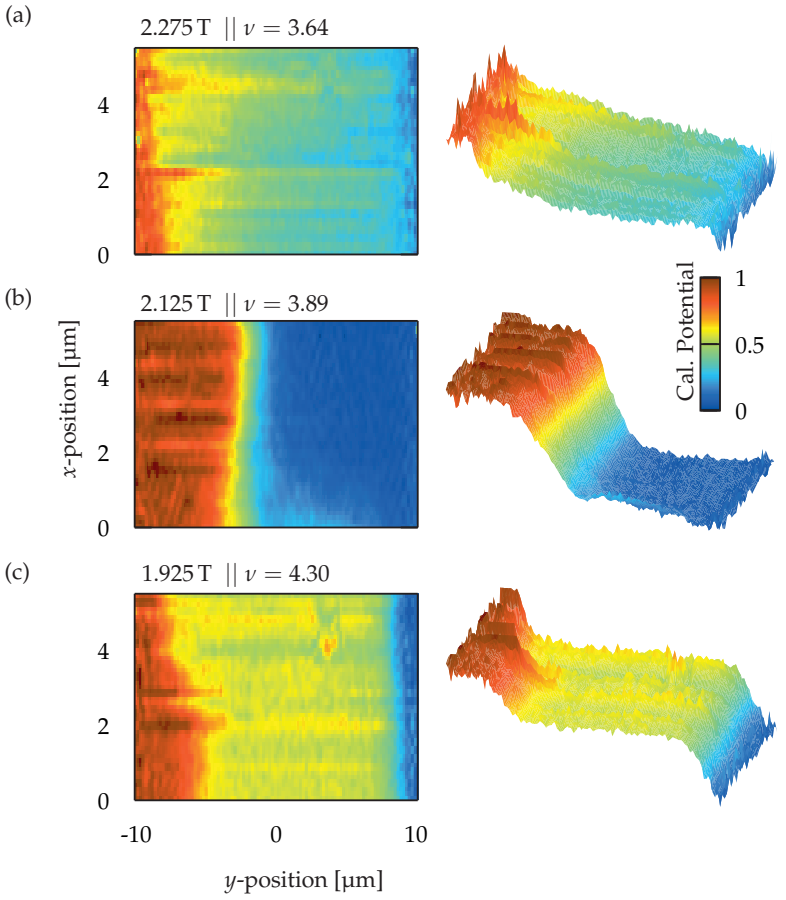

Figure 9.6:
(x, y)-area scans showing the Hall potential distribution for different filling factors. (a) Hall potential distribution between two Hall resistance plateaus for filling factor $\nu = 3.64$. For this filling factor no quantization of the Hall resistance of the 2DES is recorded. The potential drop is spread across the sample width. (b) Hall potential distribution for the bulk-dominated regime on the high magnetic field side of the Hall resistance plateau. The longitudinal resistance along the sample is close to zero. A small position range in y-direction is showing one potential drop around the middle of the sample. (c) Hall potential distribution for the edge-dominated regime on the low magnetic field side of the Hall resistance plateau. Two Hall potential drops are visible, one near each edge of the 2DES. In the middle of the sample a constant Hall potential is present extending over more than 12 µm.

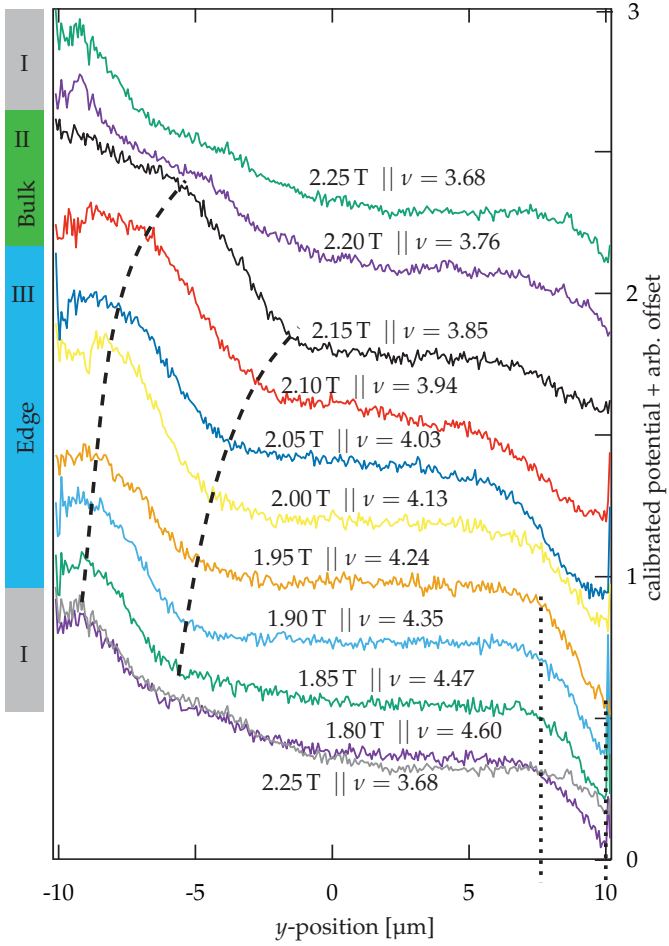

Figure 9.7:
Evolution of the Hall potential profile over a range of applied magnetic fields, on a line scan across the 2DES. Arbitrary offsets are used for each curve to enhance the visibility. The step size in the magnetic field measures 50 mT and the filling factors range from 3.68 to 4.60. On the left side the different regimes are indicated. Gray is indicating the range assumed for the sample to show no quantization in the Hall resistance. Filling factor 3.68 is plotted twice to show the repetition of the Hall potential distribution. The dashed lines follow the left potential drop and highlight its shift towards the middle of the 2DES and its broadening in the y-direction. The dotted lines enclose the narrowest potential drop with around 2.5 µm width.

potential drops, one near each edge of the 2DES, and the bulk dominated regime with just one potential drop around the middle of the 2DES.

An unexpected aspect of the measured Hall potential distribution is the width of the potential drops. The dotted lines mark one of the smallest drop widths of around 2.5 µm. Compared to previous scanning probe experiments [12] the drop width in our measurements is a factor of 2.5 larger. However there are some major differences to previous experiments:

- The 2DES is buried 120 nm below the sample surface which is around 60 nm lower than before,
- the charge carrier density is less than half the value compared to previously investigated heterostructure material,
- the SET tip is larger than the previously used metal coated AFM tip.

Nevertheless with these measurements we are able to show the full functionality of the microscope in concern of probing Hall potential profiles. Further, we can verify previous measurements showing a Hall potential drop in the bulk of the 2DES for the quantum Hall effect. The same Hall potential distribution is obtained by two different kind of probing tips. In our case a direct measurement of the electrostatic potential distribution caused by the electric current is possible without the indirection over a force measurement. Further, we achieve a much higher sensitivity with less excitation voltage, see Appendix C.10 on page 205, therefore even fragile fractional quantum Hall states can be probed with this microscope in future projects.

9.6 Summary

In this chapter we have shown the Hall potential distribution over a homogeneous sample area for filling factors around $\nu = 4$. Therefore, the high mobility sample was characterized showing well developed integer quantum Hall states for $\nu = \{1; 2; 3; 4; ..\}$ and fractional quantum Hall states for $\nu = \{2/3; 3/5\}$. All those quantized states are showing a plateau in the Hall resistance and their longitudinal voltage drop goes close to zero.

For the scan area we chose a position in the vicinity of the side contacts. In this area we found a line across the sample that was homogeneous and clean of particles located on the sample surface. Charged particles or inhomogeneities in the investigated area can cause variations in the 2DES and should therefore be avoided. Further, we executed two approach measurements and determined the required compensation voltage to minimize the electrostatic potential difference between tip and sample. We obtained a compensation voltage of 60 mV with a mismatch of ± 3 mV. This mismatch influences the charge carrier density by less than 0.3 %.

Next we showed exemplary how the raw data of the α- and β-trace looks like from which the calibrated Hall potential is calculated. All measurements were done with a modulation amplitude of $V_{\mathrm{AC,Rms}} = 1.41$ mV and a distance of around 20 nm between SET island and sample surface. Area scans of Hall potential distributions for the edge, bulk dominated regime and outside of the quantum Hall effect were presented to show the homogeneity along the sample structure and to illustrate the significant difference between the three regimes. As a last point the evolution of the Hall potential distribution was shown in a filling factor range from $\nu = 4.60$ to $\nu = 3.68$ in steps of $\Delta\nu \approx 0.1$. Thereby we were able to highlight the shift of one Hall potential drop towards the middle of the sample and the vanishing other Hall potential drop. Further, the resemblance between the Hall potential distributions of $\nu = 3.68$ and $\nu = 4.60$ was shown.

The path of the electric current through the sample and the Hall potential drop measured by the microscope are linked by the relation

$$j_x = \nu \frac{e^2}{h} E_y. \tag{9.1}$$

In this equation j_x stands for the current density in x-direction, E_y for the electric field in y-direction, h for Planck's constant and e for the elementary charge. There-

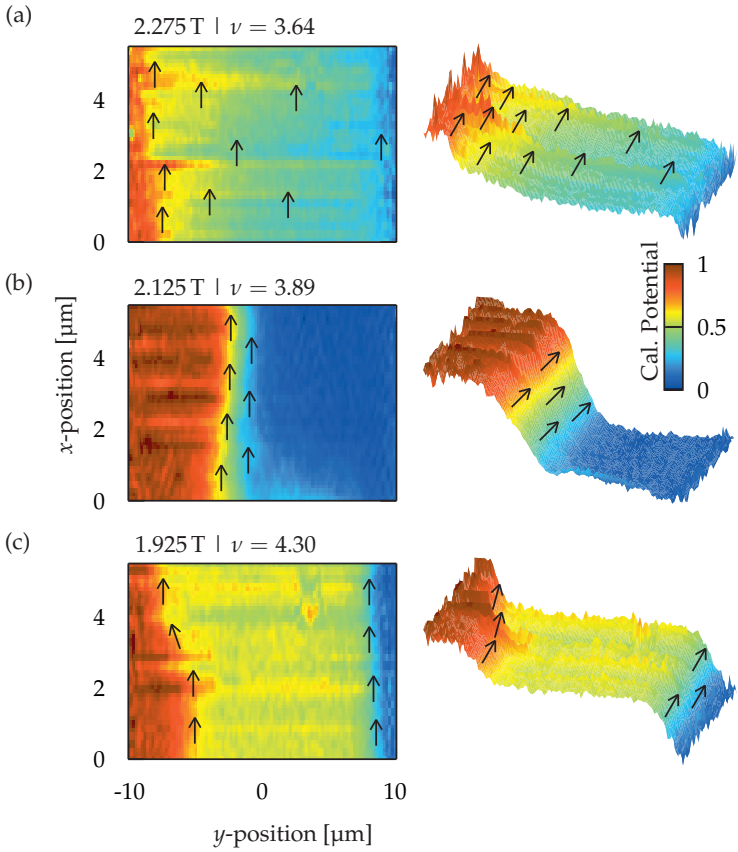

Figure 9.8:
Sample area scan over the whole width of the 2DES showing the Hall potential distribution. The arrows indicate the distribution of the electric current across the sample. The three different regimes: (a) without quantization in the 2DES, (b) bulk-dominated quantum Hall effect and (c) edge-dominated quantum Hall effect. The Hall potential distribution of (b) and the resulting distribution of the electric current contradicts the commonly used edge-channel picture due to its potential drop in the middle of the sample.

fore, the distribution of the electric current according to the Hall potential drop position is shown in Figure 9.8 for the area scans.

The key message of those Hall potential distribution measurements is that the position of the electric current through a 2DES in the quantized state of the quan-

tum Hall effect can change and is not fixed to the so called "one-dimensional edge-channels" at the border of the structure. The model of compressible and incompressible stripes [55, 57] with the electric current through a well developed most inner incompressible stripe [40, 41] explains the measured data and its evolution versus changed magnetic field.

The measurement of the Hall potential distribution can be enhanced in further experiments by switching on and off an electric current using an offset and a rectangular voltage function for the α- and β-trace. Further, the different electric current directions through the sample should be probed to verify the measured data.

10
Summary and Outlook

The task of this PhD thesis was to set up a scanning probe microscope and use it for measuring Hall potential profiles of a two-dimensional electron system under quantum Hall conditions. The microscope was meant to work reliable at temperatures below 0.1 K, magnetic fields up to 18 T and have several highly sensitive probing tips. Furthermore, the presence of the probing tips should not disturb the two-dimensional electron system while probing the potential distribution. Thereby it will become possible to probe even fragile fractional quantum Hall states in future projects.

As probing tips an one-dimensional array of single-electron transistors (SET) was fabricated in the local cleanroom facilities. The fabrication process as it is described in the PhD thesis of Jochen Weber was modified and transfered to new wafer material. This specially fabricated array with eight highly sensitive electrometers provides the opportunity of probing the electrostatic potential distribution at different sample positions at the same time makes this microscope unique. The lateral size of those electronic nano-scale devices is limited by the SET island that measures around 150 nm by 200 nm. The distance between neighboring tip structures measures 4 µm. The single-electron charging energy of some of those SETs was reaching up to 265 µeV. Therefore, a detailed current-voltage characteristic of those SETs could already be obtained at temperatures just below 0.9 K.

To achieve temperatures suitable for the probing tips and fragile quantum Hall states a ^{3}He-^{4}He dilution refrigerator was moved and reinstalled in a new highly vibration isolated laboratory premises. With a sophisticated concept for the pumping lines we were able to reduce the vibration elongation amplitude by around two orders of magnitude. In the frequency range between 3.5 Hz and 1200 Hz the maximum vibration amplitude measured less than 15 nm on the cryostat top plate.

To use the SET as highly sensitive electrometer three different measurement methods were introduced: the Coulomb blockade oscillation (CBO) method, the feedback loop (FBL) method and the AC extended FBL (AC-FBL) method. A demonstration of all three methods is shown in Figure 10.1 with an illustration of the scanned sample structure in (a).

Within the CBO method (see Figure 10.1 (b)) the electric current through the SET is directly recorded. Thereby, any change in the electrostatic potential of the SET island caused by its surrounding can be detected. The CBO method distinguishes itself by a very low noise level, a high sensitivity and a robustness against fast potential variations. A disadvantage of this measurement method is that the measurement signal is periodic over a large potential variation and is therefore equivocal for the reconstructing of the electrostatic potential from the recorded measurement signal. However from the periodicity of the current modulation versus a sample potential sweep we can determine the partial capacitance between SET island and sample electrode.

The FBL method (see Figure 10.1 (c)) uses an analog feedback loop that keeps the electric current through the SET constant. Thereby, a direct mapping of the electrostatic potential variation of the SET island, caused by a scan over a sample area, is possible.

For the newly developed AC-FBL method (see Figure 10.1 (d)) a small alternating voltage is applied to the sample but the feedback loop is kept on the DC signal. In this arrangement the AC signal obtains information about changes in the sample-island capacitance and the DC FBL signal simultaneously maps the electrostatic potential variation of the SET island, shifted by the local sample potential times the capacitive coupling.

Due to the inability to directly scan the sample topology with our probing tips, the navigation and approach of the probing tips towards sample surface rely on the measurement of the partial capacitance between SET island and sample surface electrodes. This measurement is done with the CBO method. To ensure an easy navigation of the probing tips, the sample design has to fulfill specific requirements. Those are for example a clear and easy to identify electrode structure with a high coverage of the samples surface. Based on the requirements for navigation sample structure was designed as it is shown in Figure 5.4.

An extensive characterization of the microscope was done during this PhD work to verify the functionality of the microscope. A calibration structure consisting of an arrangement of periodic gold electrodes on the sample surface was used for these

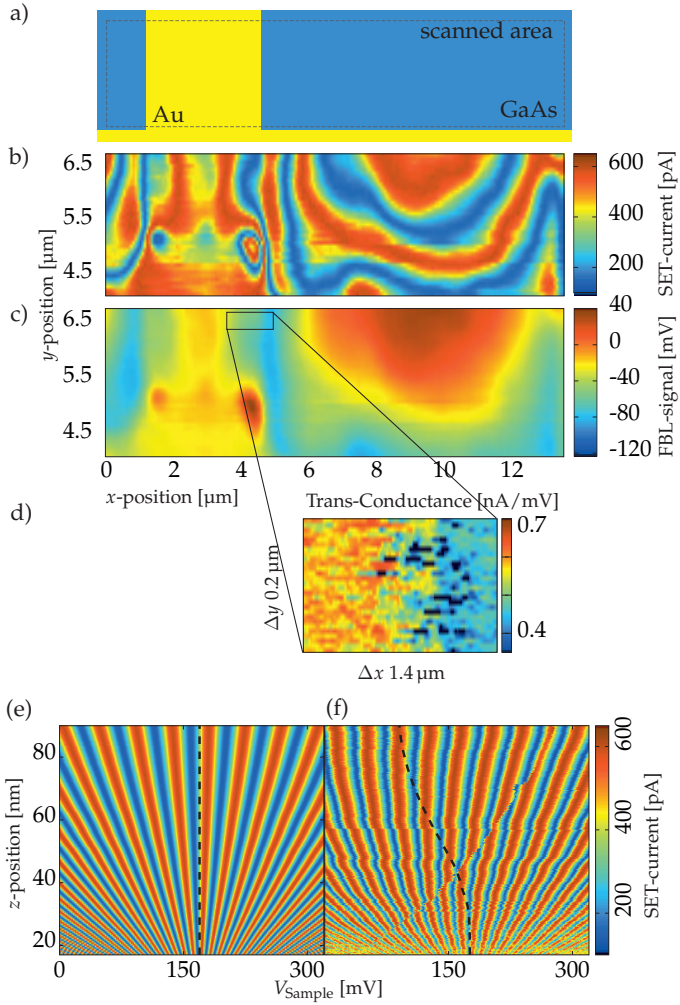

Figure 10.1:
Demonstration of CBO, FBL and AC-FBL method and comparison between the simulated and measured CBO method signal versus applied sample potential for different distances between SET island and sample surface. (a) Scheme of the scanned sample area. Data obtained by (b) CBO, (c) FBL and (d) AC-FBL method for the same scanned sample surface structure. Comparison between (e) simulated and (f) measured electric current modulation versus sample voltage for different tip-sample distances. The required tip-sample compensation voltage is depicted as dashed line.

characterization measurements. The characteristic features listed in Table 10.1 were determined.

The chosen heterostructure is displaying fractional quantum Hall states with Landau level filling factors of $\nu = \{\frac{2}{3}; \frac{3}{5}; \frac{4}{3}; \frac{5}{3}\}$. The microscope's working temperature, sensitivity on electrostatic potential variations and mechanical stability should be sufficient to probe the Hall potential profiles for those fractional quantum Hall states. Nevertheless, one restriction of the microscope is its lateral resolution of more than 0.2 µm. This restriction is caused by the probing tip size and distance between the 2DES and the SET island. However, both are difficult to overcome due to the concept of the probing tips fabrication process and the correlation between high charge carrier mobility and depth of the 2DES in the sample structure

Having an one-dimensional array of probing tips possesses some significant benefits, for example,

- choosing the most suitable sensor out of up to eight available probing tips for the desired measurement,
- the possibility to carry out simultaneous measurements at different sample positions or with different heights over the sample surface can be executed, as shown in Chapter 6.2,
- the identification and elimination of measurement artifacts due to the redundancy of the measurement signals from different probing tips for the same sample area (see Chapter 6.4),
- new calibration possibilities due to the repeated measurement pattern, as shown for the scan range calibration,
- and, last but not least, in the event of a single broken tip other SET tips are still available for continuing the measurements.

To avoid a local variation of the charge carrier density in the 2DES, due to different work function values of the different used materials, a compensation voltage between tip and sample has to be applied. This voltage can be determined with the CBO method by an invariance of the electrostatic potential of the SET island over a variation of the distance between SET island and sample. A surprising discovery was that it even was not easy to find the right compensation voltage over a surface electrode made of gold, see Figure 10.1 (f). A comparison between measured and simulated data showed that charged particles standing out of the sample surface can be the reason for a strong dependence of the compensation voltage on the distance between probing tip and sample.

Feature	Value
positioning range horizontally	3.2 mm by 3.2 mm
positioning range vertically	2.5 mm
sample tilt to match equal probing tips' distance	$\pm 3.5^\circ$
scan range	27 µm by 27 µm
mechanical stability	around ± 10 nm over hours
measured feature size	<50 nm
estimated lateral resolution	>200 nm
magnetic field induced shift	corrected to <0.1 µm over 1.8 T
electrical sensitivity (CBO)	around 35 µV
electrical sensitivity (FBL)	around 200 µV
working temperature	below 40 mK
SNR for Hall potential profiles	33:1 for 1.4 mV excitation voltage

Table 10.1: Characteristic features of the scanning SET microscope.

Further simulations were carried out to investigate the influence of the different dielectric and charged layers between 2DES and SET on the measurements of a potential distribution over the sample surface. The dielectric layers do not only weaken a potential modulation from the 2DES above the sample surface, they also change the profile of the potential distribution seen above the sample surface. Furthermore, the capacitive coupling between 2DES and SET island for buried narrow electrodes compared to narrow electrodes on the sample surface is changed. In this context an estimation of the influence of a compensation voltage mismatch on the charge carrier density was calculated.

To overcome issues with fixed charges and changing capacitive coupling between the 2DES and a scanning SET island we introduced a probing technique. This technique is similar to previous scanning probe experiments and allows to measure current induced variations in electrostatic potential distributions of a sample. This was done by recording two AC measurements, one with an electric current through the sample (α-trace measurement) and one alternating the electrostatic potential of the whole sample (β-trace measurement) without an externally imprinted sample current. If the data of the α-trace measurement is divided by the data obtained by the β-trace measurement for the same sample positions we get a calibrated potential distribution. With this probing technique we were able to probe the Hall potential distribution of a sample with a buried two-dimensional electron system.

By the end of this thesis we were able to demonstrate the functionality of the microscope by measuring Hall potential profiles across a Hall bar containing a 2DES in the quantum Hall regime. This was done over a homogeneous sample surface. The applied magnetic field was chosen in a range that the 2DES showed Landau level filling factors reaching from $\nu = 4.60$ to $\nu = 3.68$ in steps of $\Delta\nu \approx 0.1$ ($\Delta B \approx 50\,\mathrm{mT}$) as shown in Figure 9.7. Thereby, we were able to highlight the shift of the Hall potential drops from the edges of the sample structure towards the middle of the sample within one Hall resistance plateau. Furthermore, the resemblance between the Hall potential distributions of $\nu = 3.68$ and $\nu = 4.60$ was shown. Further area scans of Hall potential distributions for the edge-, bulk-dominated regime and outside of the quantum Hall regime were executed and are shown in Figure 10.2. All those measurements were executed for a tip-sample compensated situation with a very small mismatch of around $\pm 3\,\mathrm{mV}$.

The Hall potential distribution measurements coincide nicely with former Hall potential profile measurements done with an electrical force microscope. However we are able to use much lower AC excitation voltage for the probing technique and still obtain a significantly better signal-to-noise ratio.

Outlook and next steps

In this PhD thesis, current induced Hall potential profiles were measured around filling factor $\nu = 4$. Already during the writing of this thesis, Hall potential profiles around the filling factors $\nu = \{2/3; 1; 2\}$ were measured with the microscope setup built and characterized during this PhD thesis. The Hall potential profiles of the filling factors $\nu = \{3/5; 5/3\}$ will follow soon. Furthermore, the capacitive coupling between SET island and 2DES over a cross section of the Hall bar versus magnetic field was measured. This was done to gain insights about the compressibility of the sample and the electric isolation between edge and bulk of the sample.

In addition, there are new interesting and up to now unique measurement possibilities due to the instrument established within this work. The performance of a sample excitation by one SET tip acting as a disturbing gate and the simultaneous measurement with the neighboring probing tips is just one example. Thereby, connected compressible areas between two or more tips can be identified. For an area scan of this kind even the size of the compressible areas can be determined which would be of interest for the bulk dominated regime. This measurement would be unique due to the array of probing tips and not achievable by other scanning probe microscopes. Furthermore, the measurement would contribute to a better understanding of the experimental data obtained by Jan Hüls [92] and Jochen Weber [66].

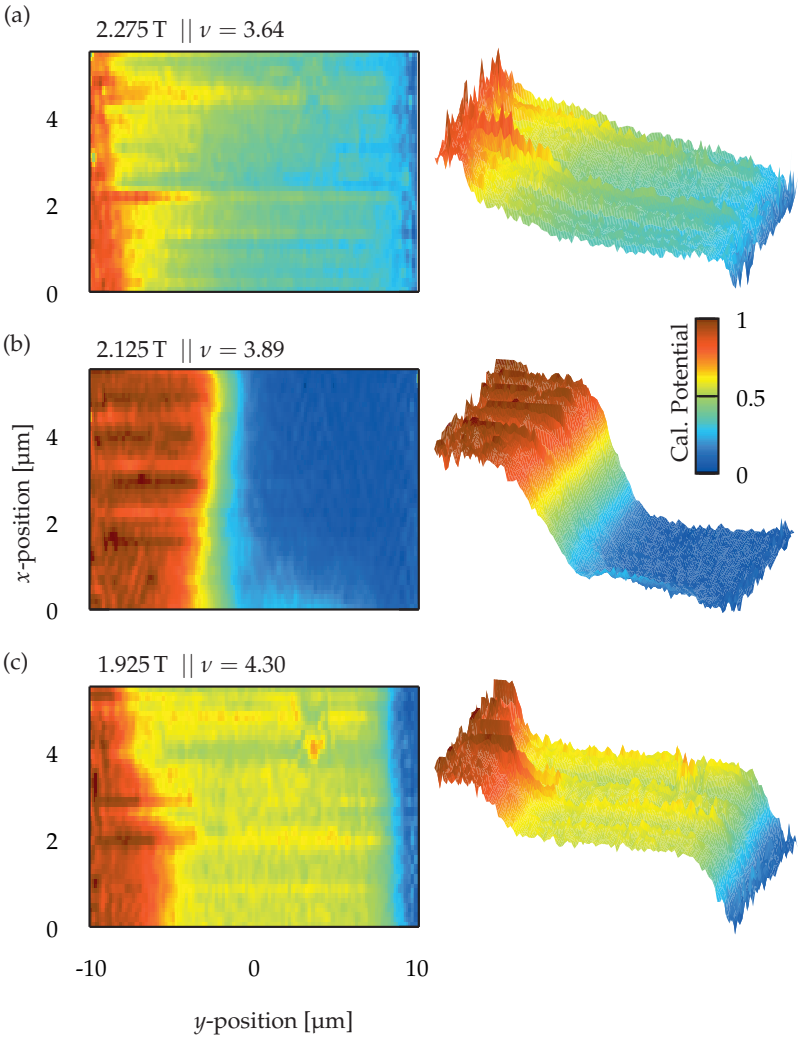

Figure 10.2:
(x, y)-area scans showing the Hall potential profiles for different magnetic fields. (a) Outside the quantum Hall regime at filling factor $\nu = 3.64$. (b) Bulk-dominated regime on the high magnetic field side of the Hall resistance plateau at filling factor $\nu = 3.89$. (c) Edge-dominated regime at filling factor $\nu = 4.30$, slightly below the Hall resistance plateau in concern of the applied magnetic field.

On the other hand, changing the sample to one with gates near the ohmic contacts brings the opportunity to verify the picture behind freshly obtained integral measurement results on the breakdown of the quantum Hall effect [93].

Another major step would be the realization of Hall sensors [69] neighboring the SET tips. Thereby, the microscope would gain another capability to probe the electric current distribution without the detour over the electrostatic potential distribution. With its sensitivity to electrostatic potential variations, charge, capacitance, contact potential, and temperature the instrument might help to understand unsolved issues in other material systems.

11
Zusammenfassung

Das Ziel dieser Doktorarbeit bestand darin, ein Rastersondenmikroskop aufzubauen und die Hall-Potentialprofile eines zweidimensionalen Elektronensystems (2DES) unter Quanten-Hall-Bedingungen zu messen. Das Mikroskop sollte dabei zuverlässig bei Temperaturen unter 0.1 K und Magnetfeldern von bis zu 18 T arbeiten, sowie mehrere hoch empfindliche Sondenspitzen besitzen. Desweiteren sollten die Spitzen das zweidimensionale Elektronensystem durch ihre Anwesenheit nicht stören, so dass auch fragile fraktionale Quanten-Hall-Zustände in zukünftigen Projekten gemessen werden können.

Als Sondenspitzen wurde ein eindimensionales Array aus Einzelelektronentransistoren (SET) in den Reinraumanlagen des MPI hergestellt. Dafür wurde der Fabrikationsprozess, der in der Doktorarbeit von Jochen Weber [66] beschrieben wurde, modifiziert und auf die Begebenheiten von neuem Wafer-Material angepasst. Dieses Array aus hoch empfindlichen Elektrometern, das die Möglichkeit bietet, elektrostatische Potentialverteilungen an verschiedenen Probenpositionen gleichzeitig zu messen, zeichnet die Einzigartigkeit des Mikroskops aus. Der elektrostatisch empfindliche Teil, die Insel des Einzelelektronentransistors, misst etwa 150 nm auf 200 nm und ist 30 nm dick. Zwischen benachbarten Spitzenstrukturen ist ein Abstand von 4 µm vorhanden. Die Einzelelektronenladeenergie einiger dieser SETs erreichte Werte von bis zu 265 µeV. Daher konnte eine detaillierte Strom-Spannungs-Charakteristik dieser SETs schon bei Temperaturen knapp unter 0.9 K gemessen werden.

Um Temperaturen zu gewährleisten, unter denen die Potentialsonden optimal arbeiten und fragile Quanten-Hall-Zustände erreicht werden können, wurde ein ^{3}He-^{4}He Mischkryostat in eine neue, extrem vibrationsisolierte Laborumgebung umgezogen und aufgebaut. Mit einem durchdachten Konzept für die Pumpenleitungen wurde es möglich, die Amplitude der Vibrationen auf dem Kryostaten um zwei Größenordnungen zu reduzieren. In einem Frequenzbereich von 3.5 Hz

bis 1200 Hz war die maximale Schwingungsamplitude kleiner als 15 nm auf der Oberseite des Kryostaten.

Um den Einzelelektronentransistor als hoch empfindliche Potentialsonde einsetzen zu können, wurden drei Messmethoden präsentiert: Die Coulomb-Blockade-Oszillations (CBO) Methode, die Rückkopplungsschleifen (FBL) Methode und die um ein AC-signal erweiterte Rückkopplungsschleifen (AC-FBL) Methode. Eine Demonstration aller drei Methoden ist in Abbildung 11.1 mit einer Illustration der gerasterten Probenstruktur (a) zu sehen.

Für die CBO Methode (siehe Abbildung 11.1 (b)) wird der elektrische Strom, der durch den SET fließt, direkt aufgezeichnet. Jegliche Veränderung des elektrostatischen Potentials der SET-Insel, verursacht durch Einflüsse aus deren Umgebung, kann somit detektiert werden. Insbesondere Potentialvariationen einer Probe werden beim Abrastern sichtbar. Die CBO-Methode zeichnet sich durch ein sehr niedriges Rauschlevel, eine hohe Empfindlichkeit und eine hohe Robustheit gegenüber schnellen Potentialänderungen aus. Das Messignal ist jedoch periodisch für große Potentialänderungen und erlaubt daher keine eindeutige Rekonstruktion des elektrostatischen Potentialverlaufs aus dem Messsignal. Dennoch kann aus der Periodizität der Strommodulation über einem kontinuierlich veränderten Probenpotential die Teilkapazität zwischen SET-Insel und Probenelektrode bestimmt werden.

Die FBL-Methode (siehe Abbildung 11.1 (c)) verwendet eine analoge Rückkoppelschaltung, die den Stromfluss durch den SET konstant hält. Hierdurch ist ein direkter Rückschluss auf Änderungen des elektrostatischen Potentials der SET-Insel, verursacht durch Änderungen im lokalen Probenpotential oder der kapazitiven Kopplung, möglich.

Für die neu entwickelte AC-FBL Methode (siehe Abbildung 11.1 (d)) wird eine kleine Wechselspannung auf die Probe gegeben. Die Rückkoppelschaltung wird jedoch weiterhin auf dem Gleichspannungssignal gehalten. Durch dieses Vorgehen lässt sich aus dem alternierenden Signal die Teilkapazität zwischen SET-Insel und Probenelektrode gewinnen. Die Änderung des elektrostatischen Potential der SET-Insel, durch ein geändertes lokales Probenpotential, kann direkt über die Rückkoppelschleife gemessen werden.

Die Probenoberfläche kann mit unseren Messsonden nicht direkt erfasst werden. Deshalb musste für die Navigation und die Annäherung der Sonden auf eine Probenelektrode die Änderung der Teilkapazität zwischen SET-Insel und Probenelektroden gemessen werden. Diese Messung erfolgt mit der CBO-Methode. Um die Navigation der Messonden möglichst einfach zu gestalten, wurden einige

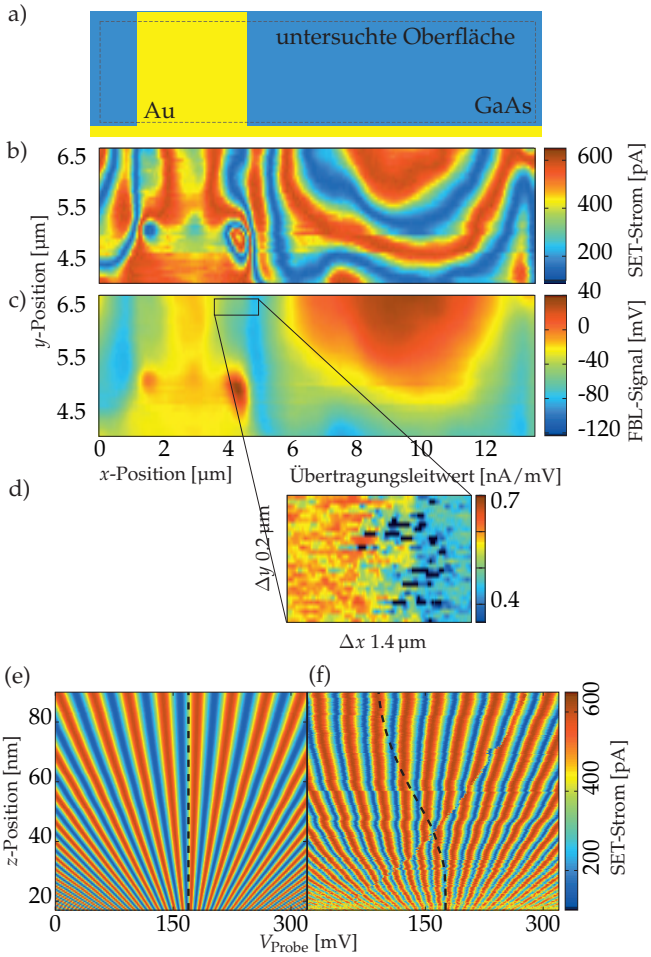

Figure 11.1:
Gegenüberstellung der CBO-, FBL- und AC-FBL-Methode, sowie ein Vergleich zwischen simuliertem und gemessenem Signal der CBO Methode für verschiedene Probenspannungen und unterschiedliche Abstände zwischen SET-Insel und Probenoberfläche. (a) Zeichnung der untersuchten Probenoberfläche. Messignal der (b) CBO-, (c) FBL- und (d) AC-FBL-Methode für dieselbe untersuchte Oberflächenstruktur. Vergleich zwischen (e) simulierter und (f) gemessener Modulation des elektrischen Stroms durch eine Messsonde für verschiedene Probenspannungen und verschiedene Abstände zwischen Messsonde und Probenoberfläche. Die benötigte Ausgleichspannung zwischen Messsonde und Probe ist als gestrichelte Linie eingezeichnet.

Anforderungen an das Probendesign gestellt, wie z.B. eine klare und einfach zu identifizierende Elektrodenstruktur mit einer hohen Abdeckung der Probenoberfläche. Auf Basis der Anforderungen der Navigation wurde unser Probendesign, das in Abbildung 5.4 zu sehen ist, gestaltet.

Während dieser Doktorarbeit wurde eine ausführliche Charakterisierung des Mikroskops durchgeführt, wodurch die Funktionalität des Mikroskops nachgewiesen werden konnte. Für diese Charakterisierung wurde eine Kalibrierungsstruktur bestehend aus periodisch auf der Probenoberfläche angeordneten Goldelektroden verwendet. Hierbei wurden die in Tabelle 11.1 aufgeführten Spezifikationen ermittelt.

Die gewählte Heterostruktur zeigt fraktionale Quanten-Hall-Zustände mit Landau-Level-Füllfaktoren von $\nu = \{\frac{2}{3}; \frac{3}{5}; \frac{4}{3}; \frac{5}{3}\}$. Die Arbeitstemperatur, die elektrische Empfindlichkeit und die mechanische Stabilität des Mikroskops sind ausreichend, um Hall-Potentialprofile für diese fraktionalen Quanten-Hall-Zustände zu messen. Die Einschränkung des Mikroskops wird hierbei die laterale Auflösung von mehr als 0.2 µm sein. Diese Limitierung wird durch die Größe der Messsonden und den Abstand zwischen 2DES und SET-Insel erzeugt. Aufgrund des Konzepts der Messondenherstellung und der Korrelation zwischen hoher Ladungsträgerbeweglichkeit und Tiefe des 2DES in der Probenstruktur sind diese beiden Ursachen jedoch schwer zu überwinden.

Die Verwendung eines eindimensionalen Arrays von Messonden besitzt einige signifikante Vorzüge, wie z.B.

- die geeignetste Messsonde von den bis zu acht zur Verfügung stehenden Messsonden für die gewünschte Messung auszuwählen,
- die zeitgleiche Messung an verschiedenen Probenpositionen oder mit unterschiedlichem Probenabstand, wie in Kapitel 6.2 gezeigt wurde,
- Artefakte in den Messdaten können durch die Redundanz der Messsignale von verschiredenen Messsonden für den selben Probenbereich identifiziert und eliminiert werden (siehe Kapitel 6.4),
- neue Kalibrierungsmöglichkeiten aufgrund des wiederholten Messmusters, wie es für die Kalibrierung des Rasterbereiches verwendet wurde,
- und zu guter Letzt im Falle einer beschädigten Messsonde, sind weitere Messsonden verfügbar um mit den Messungen fortzufahren.

Um eine lokale Variation der Ladungsträgerdichte im 2DES aufgrund von unterschiedlichen Austrittsarbeiten der verwendeten Materialien zu vermeiden, muss eine Kompensationsspannung zwischen Messonde und Probe angelegt werden.

Merkmal	Wert
Horizontaler Positionierungsbereich	3.2 mm auf 3.2 mm
Vertikaler Positionierungsbereich	2.5 mm
Probenneigung zum Angleich an das Messondenarray	$\pm 3.5^\circ$
Rasterbereich	27 µm auf 27 µm
Mechanische Stabilität	ca. ± 10 nm über mehrere Stunden
Gemessene Strukturgröße	<50 nm
Erwartete laterale Auflösung	>200 nm
Magn. erzeugte mech. Verschiebung	korrigiert zu <0.1 µm über 1.8 T
Elektrische Empfindlichkeit (CBO)	ungefähr 35 µV
Elektrische Empfindlichkeit (FBL)	ungefähr 200 µV
Arbeitstemperatur	unter 40 mK
SNR für Hall-Potentialprofile	33:1 für 1.4 mV Anregungsspannung

Table 11.1: Charakteristische Merkmale des Rastersondenmikroskops mit SETs als Messsonden.

Diese Spannung kann mit Hilfe der CBO-Methode und einer Invarianz des elektrostatischen Potentials des SET über dem sich ändernden Abstand zwischen Sonde und Probe bestimmt werden. Eine überraschende Entdeckung hierbei war, dass selbst für eine einfache, aus Gold bestehende Oberflächenelektrode die Bestimmung der richtigen Kompensationsspannung herausfordernd war (siehe Abbildung 11.1 (f)). Ein Vergleich zwischen gemessenen und simulierten Daten zeigte, dass es sich bei starkem Verschieben der Kompensationsspannung mit dem Abstand zwischen Sonde und Probe um geladene Teilchen handelt, die von der Probenoberfläche abstehen.

Weitere Simulationen wurden durchgeführt, um den Einfluss der dielektrischen und geladenen Schichten zwischen 2DES und SET auf Potentialmessungen über der Probenoberfläche zu untersuchen. Die verschiedenen Schichten schwächen nicht nur eine durch das 2DES gegebene Potentialmodulation ab, sondern verändern sogar den Potentialverlauf an der Probenoberfläche. Desweiteren verändert sich die kapazitive Kopplung zwischen 2DES und SET-Insel für eingebettete schmale Elektroden im Vergleichen zu schmalen Elektroden an der Oberfläche. In diesem Zusammenhang wurde der Einfluss einer Abweichung von der Kompensationsspannung auf die Ladungsrägerdichte abgeschätzt.

Um Probleme mit Oberflächenladungen und veränderter kapazitiver Kopplung zwischen 2DES und Messsonde zu überwinden, haben wir eine Messtechnik entwickelt. Diese Messtechnik ist ähnlich zu der in vorangegangenen Rastersondenexperimenten verwendeten und erlaubt es, die durch einen aufgeprägten elektrischen Strom erzeugte Veränderung in der Potentialverteilung einer Probe zu messen. Hierzu werden zwei Messungen durchgeführt. Eine mit einem Wechselstrom durch die Probe ("α-trace " Messung) und eine mit einer Wechselspannung an der gesamten Probe ("β-trace " Messung) ohne einen extern aufgeprägten Probenstrom. Wenn nun die Daten der "α-trace " Messung durch die Daten der "β-trace " Messung der selben Probenpositionen geteilt werden, erhalten wir eine kalibrierte Potentialverteilung. Mit dieser Messtechnik wurde es uns möglich, die Hall-Potentialverteilung einer Probe mit eingebettetem zweidimensionalem Elektronensystem zu vermessen.

Am Ende der Arbeit war es uns möglich, die Funktionalität des Mikroskops durch die Messung von Hall-Potentialverteilungen zu demonstrieren. Dazu wurde eine homogene Probenoberfläche verwendet. Das angelegte magnetische Feld wurde in einem Bereich gewählt, dass das zweidimensionale Elektronensystem Landau-Level-Füllfaktoren von $\nu = 4.60$ bis $\nu = 3.68$ in Schritten von $\Delta\nu \approx 0.1$ ($\Delta B \approx 50\,\mathrm{mT}$) zeigte (siehe Abbildung 9.7). Hierdurch war es uns möglich die Verschiebung der Hall-Potentialabfälle, innerhalb eines Hall-Widerstandplateaus, von den Rändern der Probe hin zur Mitte der Probe zu zeigen. Weiterhin wurde die Ähnlichkeit zwischen der Potentialverteilung bei Füllfaktor $\nu = 3.68$ und $\nu = 4.60$ gezeigt. Es wurden weitere Messungen für Hall-Potentialverteilungen in einem Probenbereich für den Rand-dominierten, den "Bulk"-dominierten Bereich und außerhalb des Quanten-Hall-Plateau-Bereich durchgeführt. Diese sind in Abbildung 11.2 zu sehen. All diese Messungen wurden mit einer angelegten Kompensationsspannung durchgeführt, deren Fehlanpassung nur sehr klein im Bereich von $\pm 3\,\mathrm{mV}$ war.

Die Messungen der Hall-Potentialverteilung zeigen große Übereinstimmung mit Hall-Potentialprofilen aus vorangegangenen Messungen mittels Rasterkraftmikroskopie. Es ist uns jedoch möglich, deutlich kleinere Anregungsspannungen für die Probe zu verwenden und dennoch ein deutlich besseres Signal-zu-Rausch-Verhältnis zu erhalten.

Ausblick und nächste Schritte

In dieser Doktorarbeit wurden Hall-Potentialprofile um den Füllfaktor $\nu = 4$ gemessen, die durch einen elektrischen Strom durch die Probe erzeugt werden. Während des Verfassens dieser Arbeit wurden Hall-Potentialprofile für die Füll-

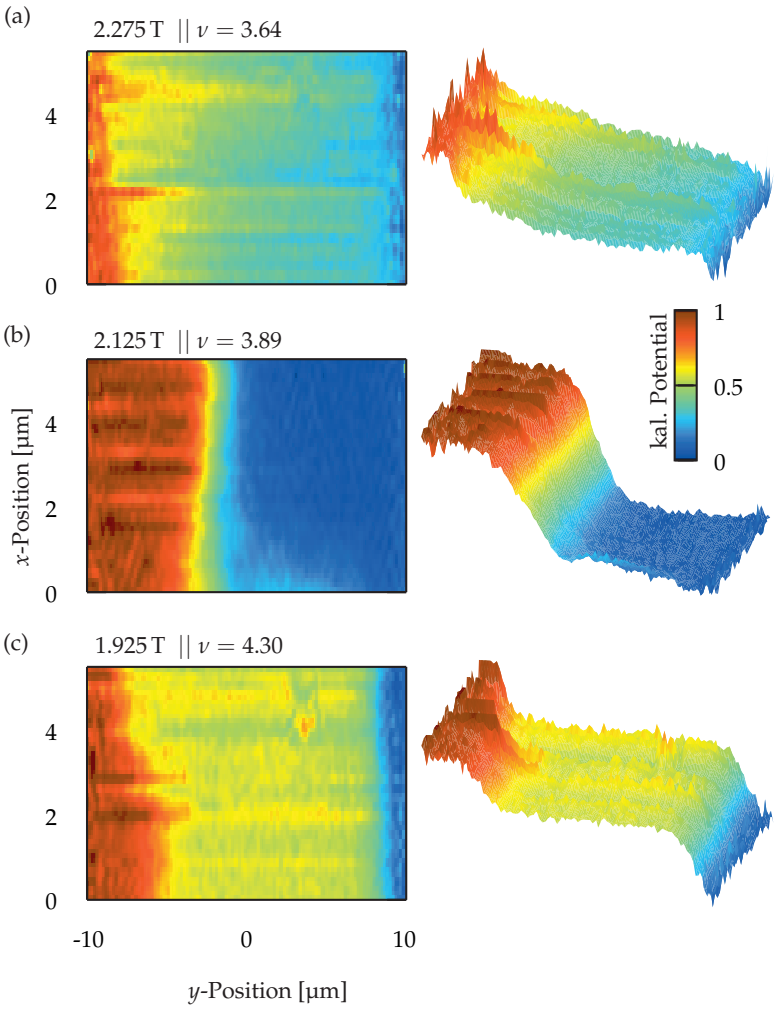

Figure 11.2:
(x, y)-Flächen Abtastung, welche die Hall-Potentialverteilung für verschiedene Hall Potentialregime zeigt. (a) Außerhalb des Quanten-Hall-Regimes mit einen Landau Füllfaktor von $\nu = 3.64$. (b) Bulk-dominiertes Regime mit Füllfaktor $\nu = 3.89$, im oberen Bereich des Hall-Widerstandplateaus in Bezug auf das angelegte Magnetfeld. (c) Edge-dominiertes Regime mit Füllfaktor $\nu = 4.30$, im Bereich leicht unterhalb des Hall Widerstandplateaus in Bezug auf das angelegte Magnetfeld.

faktoren $\nu = \{2/3; 1; 2\}$ mit dem während dieser Doktorarbeit entstandenem und charakterisierten Aufbau vermessen. In naher Zukunft werden die Hall-Potentialprofile für die Füllfaktoren $\nu = \{3/5; 5/3\}$ folgen. Desweiteren wurde das kapazitive Verhalten zwischen 2DES und SET-Insel über einem Probenquerschnitt für verschiedene Magnetfelder gemessen. Hierdurch konnten Informationen über die Kompressibilität des 2DES und die elektrische Isolierung zwischen Rand und Mitte des zweidimensionalen Elektronensystem erhalten werden.

Hieraus ergeben sich neue interessante und bis heute einzigartige Messmöglichkeiten mit diesem Mikroskop. So kann eine SET-Spitze als störende Spitze verwendet werden, um die Reaktion der Probe durch gleichzeitige Messung mit benachbarten Messsonden zu detektieren, um nur ein Beispiel zu nennen. Hiermit können zusammenhängende kompressible Bereiche zwischen zwei oder mehreren Messsonden im 2DES identifiziert werden. Mit einer Oberflächenmessung dieser Art kann sogar die Größe der kompressiblen Bereiche bestimmt werden, welche für den "Bulk"-dominierten Bereich des Quanten-Hall-Effektes von Interesse wäre. Diese Messung wäre einzigartig und nicht durch andere Rastersondenmikroskope erreichbar. Desweiteren würde diese Messung zu einem besseren Verständnis der Messdaten von Jan Hüls [92] und Jochen Weber [66] beitragen.

Durch einen Probenwechsel zu einer Probenstruktur mit Gateelektroden nahe den ohmschen Kontakten bestünde die Möglichkeit, das Bild hinter jüngst gemessenen integralen Messdaten an Hall-Proben zu bekräftigen [93].

Ein weiterer großer Schritt wäre die Realisierung von Hall-Sensoren [69], welche direkt an die SET-Messsonden angrenzen. Hierdurch würde das Mikroskop eine weitere Fähigkeit zur Messung von Stromverteilungen ohne den Umweg über die elektrostatische Potentialverteilung erhalten. Mit seiner Empfindlichkeit gegenüber Veränderung im elektrostatischen Potential, Ladung, Kapazität, Kontaktpotential und Temperatur gibt es eine Vielzahl von Anwendungsmöglichkeiten, auch für andere Materialsysteme, in denen das Mikroskop Antworten liefern kann.

A

Used and Developed Software

A.1 Simulation of Electrostatic Potentials and SET Current

For all simulations in this thesis we use the program *Finite Element Method Magnetics* (FEMM) in version 4.2 from *www.femm.info* which is capable of doing electrostatic potential simulations in two-dimensional space [94]. The calculations are done using the method of finite elements [95, 96]. With a modified version of the multi-paradigm programming language *Lua* [97] we are even able to program dynamic situations like shifting the probing tip geometry over a modeled sample surface and save the data to a file to plot it later on.

At the beginning we experienced small numerical errors for the calculated charge on the SET island when we use the real dimensions of our configuration (nanometer scale) and a solver precision of 1.0×10^{-12}. To get rid of those artifacts in the simulations we enlarged each spatial dimension by a factor of 100 and set the solver precision to 1.0×10^{-16}. This procedure has to be corrected by dividing all calculated capacitance and charge values by a factor of 100 to transfer the values to the real SET dimensions. For our standard configuration we chose a Cartesian coordinate system and a depth of the configuration of 15 µm, 100 times the depth of the SET tip. To simulate the capacitive coupling we chose a radial configuration around the SET axis to avoid large discrepancies due to edges in the geometry that would not be calculated correctly, see Chapter 8.2.

The geometric configuration we use in the simulations is shown in Figure A.1. The probing SET tip consists of a source electrode with a fixed potential of 0.5 mV, a drain electrode with a fixed potential of -0.5 mV and an island electrode with a fixed potential of 0.0 mV. Thereby we can simulate a quite realistic configuration and can easily retrieve the induced charge on the SET island. With this charge

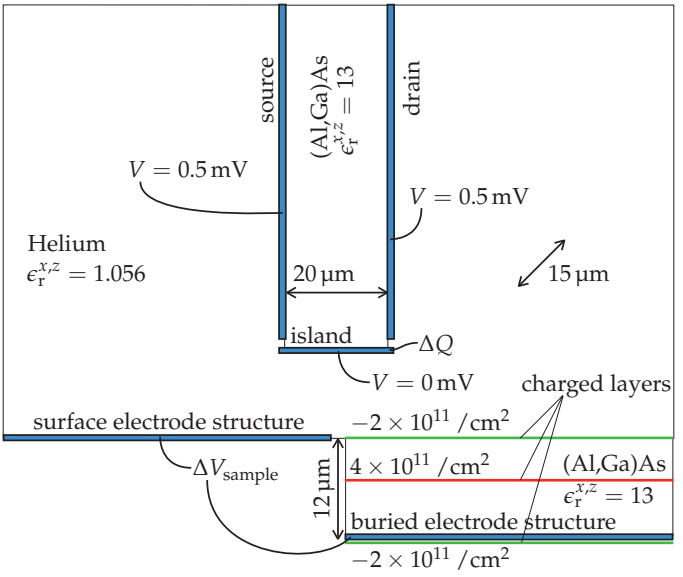

Figure A.1:
Standard geometric configuration for electrostatic potential simulations. In blue all metal electrodes in the configuration are illustrated. The green lines display negatively charge layers and the red line a positively charged layer.

and the applied potential to the sample electrode we can calculate the present partial capacitance between sample and SET island, see Chapter 8.2. Applying an electron-charge-periodic sinusoidal function on the calculated charge value on the island we get a rough estimation of the current through the SET, see Figure 6.4.

For the different media we chose isotropic ϵ_r-values, for example, liquid helium $\epsilon_r = 1.056$, (Al,Ga)As layers and tip structure $\epsilon_r = 13$. For the surface charge layer and 2DES we chose a surface charge density of $-2.0 \times 10^{11}\,/\mathrm{cm}^2$, and to stay electrically neutral, a surface charge density of $4.0 \times 10^{11}\,/\mathrm{cm}^2$ for the doping layer was configured. For simplicity we used metal electrodes for the 2DES areas. We put the charged layer of the 2DES slightly below (2 nm) the buried electrodes. This is valid due to the infinite small z dimension of the electrodes and because they are all located on the same height. Therefore, they are all located on an equipotential line and will not change the electrostatic potential distribution if there is no potential difference present between them.

Example of a Lua code for an tip-sample approach versus sample potential simulation:

```
showconsole()

workfile = "wf"

potMin = -200 -- mV
potMax  = 50 -- mV
potDiff = 5   -- mV

zMin    = 20    -- nm
zMax  = 200 -- nm
zDiff   = 5     -- nm

mydir="B:/git_mpi/simulations/Au-roughDiel-PotZ/"
open(mydir .. "cadSituation.fee")
ei_saveas(mydir .. "temp.fee")
file = openfile(mydir .. workfile .. "_z-" .. zMin .. "-" .. zMax .. "-" .. zDiff .. "_pot-" ..
    potMin .. "-" .. potMax .. "-" .. potDiff .. ".csv", "w")

print("\n #-------------------------")
print(workfile .. "_z-" .. zMin .. "-" .. zMax .. "-" .. zDiff .. "_pot-" .. potMin .. "-" ..
    potMax .. "-" .. potDiff)
print(format("potMin: %5d \t potMax: %5d \t potDiff: %3d", potMin, potMax, potDiff))
print(format("zMin: %5d \t zMax: %5d \t zDiff: %5d", zMin, zMax, zDiff), "\n\n")

write(file, "#",workfile .. "_z-" .. zMin .. "-" .. zMax .. "-" .. zDiff .. "_pot-" .. potMin ..
    "-" .. potMax .. "-" .. potDiff)
write(file, "#",format("potMin: %5d \t potMax: %5d \t potDiff: %3d", potMin, potMax, potDiff), "\n")
write(file, "#",format("zMin: %5d \t zMax: %5d \t zDiff: %5d", zMin, zMax, zDiff), "\n#\n")

for z=zMin,zMax,zDiff do

   for pot=potMin,potMax,potDiff do
      ei_modifyconductorprop('pot', 1, pot/1000)

      ei_analyze()
      ei_loadsolution()

      ei_seteditmode("group")
      eo_groupselectblock(1)

      U,Q = eo_getconductorproperties("i");
      chrg = -Q/1.602*1e17

      print(format("%.2f \t %.2f \t %.3f", pot, z, chrg))
      write(file, format("%.2f \t %.2f \t %.3f", pot, z, chrg), "\n")
   end

   ei_selectgroup(1)
   ei_movetranslate(0, zDiff/10)

   print("\n")
   write(file, "\n")
end

--eo_close()
--ei_close()
closefile(file)
```

A.2 Developed Measurement Software

To communicate with the measurement instruments like the voltmeters, lock-in amplifiers, DA converters and the power supply of the superconducting magnet, a Linux implemented measurement software called *measkern* based on C++, Python and Labview drivers was used. This software provides the user with the possibility to configure and start measurements with the command line. Due to the variety of measurement types (over 130 different types at the end of this PhD thesis) and the repetition rate of some measurements (sometimes more than 200 of the same kind a day) a new interface and content management software called *measpy* was written. This additional software uses measkern as a base component to connect to the instruments and is written in Python 2.68.

Measpy handles the way of starting measurements by a text based user interface (TBUI) and allows to use and embed measurement files and scripts through the TBUI[1]. It stores measurement files in self organized folders correlated to the measurement type. It logs all activities and changes of the measurement settings in a history file. Parameter changes can be applied either dynamically or by a settings file, thereby the amount of work needed to execute a measurement is reduced drastically. Further a queue of tasks can be set for the system to be executed subsequently. This queue as well as the parameters for the different measurements can be changed even during a running measurement. An additional feature is the display of the status of the present measurement with an estimated remaining time as well as the function to already plot the measured data automatically while the measurement is still running and afterwards. Today measpy is used on all three installed measurement systems in the laboratory and was already used efficiently by four users in the last two years.

To give the possibility to exploit the benefits of measpy I want to give a really short introduction into the software with the shortcuts *m-* for measurement- and *v-* for variable.
In the main folder called *measpy* two folders and three files are present:

- *dataPlots* (folder) includes all measured data sorted in folders named after the m-type and a folder called `_HISTORY` including the m-log file `_HISTORY` to be able to restore the used settings for a measurement executed on a certain date,
- *sys* (folder) includes python files necessary for *measpy* ,

[1] Measpy can be linked in Linux that it can be started in the console from any working path.

- *a_settings.ini* (file) has to include all m-parameters as variable definitions in the measkern style,
- *a_setup.ini* (file) has to include all m-instrument definitions in the *measkern* style,
- *feed.ini* (file) represents a task list written in the form "m-type \t v-name1=value1 \t v-name2=value2". Each line represents one measurement instruction. Comments can be set with "#" and further variable changes can be attached by a tab spacing "\t" as shown.

The file *_HISTORY* includes the changed variable definitions in the form of "date || m-type \n SettingsVar: \t v-name1 value-old >>>> v-name1 value-new", where "\n" stands for a line break.

All measurements are stored as zip files and plot file (.png) of the preset parameter space, more about this in *setGnuplot.txt* . In the zip files also the present settings and setup file are stored to be able to reproduce the measurement.

In the folder *sys* besides the necessary Python files you will find four folders:

- *how to* including some files how to do things (not completed),
- *measmoduls* all m-type files have to be placed into this folder to be available and listed in the TBUI of measpy,
- *scriptmoduls* all scripts that shall be available and listed in the TBUI have to be placed in this folder,
- *tmp* while a measurement is running the buffering is done in this folder and all files of this folder are zipped after each measurement and stored in their dataPlots folder

In *measmoduls* the m-files have to be named in a certain way to use automatic routines of measpy an example is given by "m_i+var1+var2-var3-var4...".
The name starts with the letter *m* or *s* that stands for *measurement* files or for files that are just there to *set* voltage values directly to the DACs. The difference is that a measurement file contains variables defined in *a_settings.ini* and a set file asks for variables defined by the console entry. This first letter is followed by an underline and one further letter (here "i") that is used for sorting the m-types and grouping them together in the TBUI to keep the overview. In the following part of the name a "+" can be used for a sweeping parameter ("+var1" and "+var2") and a "-" for a constant parameter ("-var3" and "-var4"). The plotting of the file and the handling of the measured data will depend on the number of "+" in the name the

parameters declared with "-" are just for information. Measpy will either plot in 2D with a line style or with a color coded plot style.

Further there are files in the *measmoduls* folder starting with the letters "set". They are used to set different values in general, i.e. an explanation like for the variables required by the console entry or they are used to set the default plotting parameters. To use them please check already established examples.

To use now *measpy* you can simply type "measpy" into the console. The result will be a listing of all available m-types and set types with an attached number. Now the *a_settings.ini* file has to be edited to chose the right parameter spaces and then the number of the suitable measurement type has to be typed in like "*measpy* 17", for the measurement type correlated with the shown number "17". Measpy will start the measurement display the progress, plot the data if the measurement takes more than a minute and after the execution ask for a comment then it will zip and store the measurement data and plot.

B
New Head for Microscope Rod

At the end of this PhD thesis a new, advanced head for the microscope rod was designed and manufactured by newly available printing technologies. The new design is shown in Figure B.1 and in Figure B.2 from different perspectives. The frame holding all movable and electronic parts consists of an alloy of titanium. This material was chosen because it should not be affected by high magnetic fields. Thereby we can get rid of the mechanical shifts changing the tip and sample position due to changes in the magnetic field.

The used metal printing technology allows a fast production of the microscope frame it only took two weeks including transportation to get a new microscope head (compared to around three to six months for the according complex stainless steel parts). Further the whole head is printed as one part giving the frame an unequaled strength and the opportunity of new filigree construction design options like large windows to exchange and position the tips and sample more easily, a cable guide and more space for the positioning units.

Further the new sample rod head is exchangeable with the old head, thereby new probing tips and a new sample can already be prepared while testing or measuring with the old ones. As another big step the scanning piezo tube was removed completely and replaced by scanners from the company Attocube. The piezo tube was the most trouble shooting part of the present microscope.

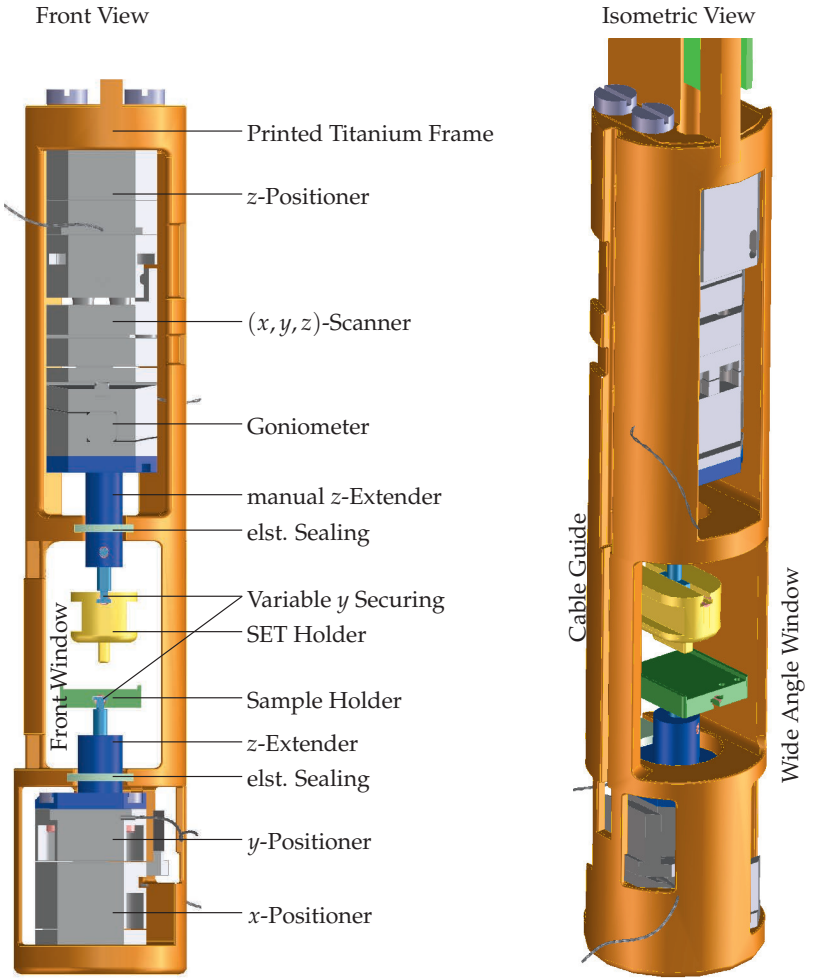

Figure B.1:
Front and isometric view on the new, active part of the microscope rod printed with a titanium alloy.

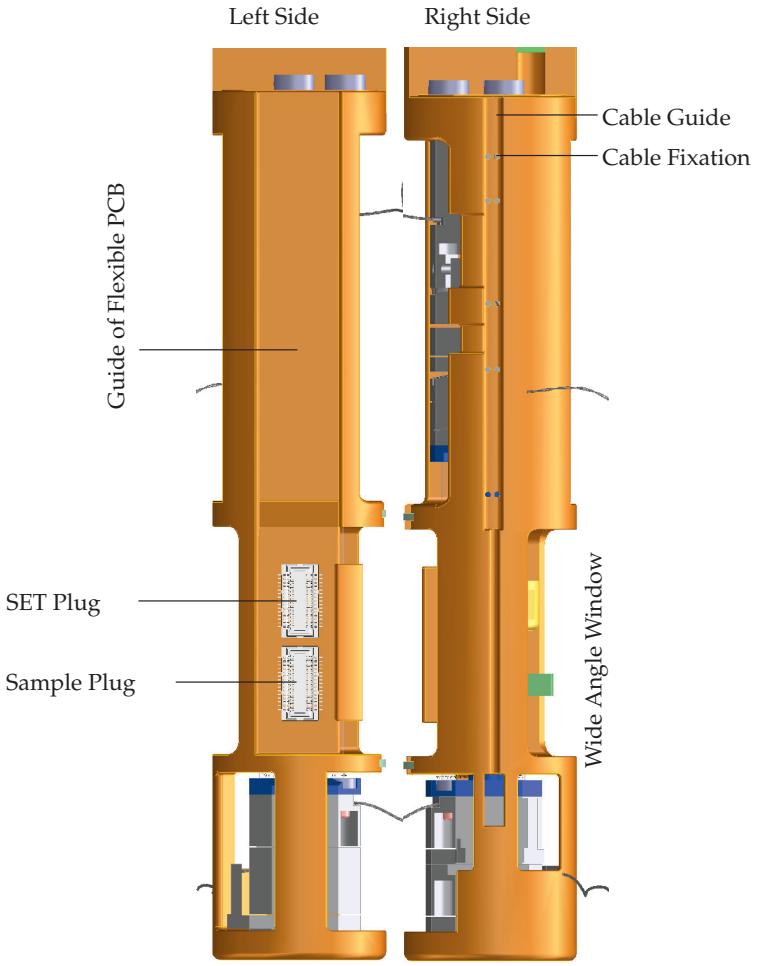

Figure B.2:
Left and right view on the new, active part of the microscope rod printed with a titanium alloy.

C

Further Measurements and Simulation

C.1 Strange SET Current Modulation Behavior

For extremely small SET-island-to-sample distances (sub 20 nm) the modulation amplitude of the SET current as used in the CBO method changed its value for different sample voltages. This behavior was reproducible. It is neither an averaging effect nor has it a time dependence to explain the recorded data by mechanical vibrations. A guess is that the SET island could make an electric contact (tunnel barrier) to the gold surface electrode and a part of the current is flowing through this connection (tunnel barrier). But the oscillatory behavior of the current modulation amplitude points to a more complex situation. It was not possible to additionally measure the source current of the SET with the present electrical setup, to determine a leakage current.

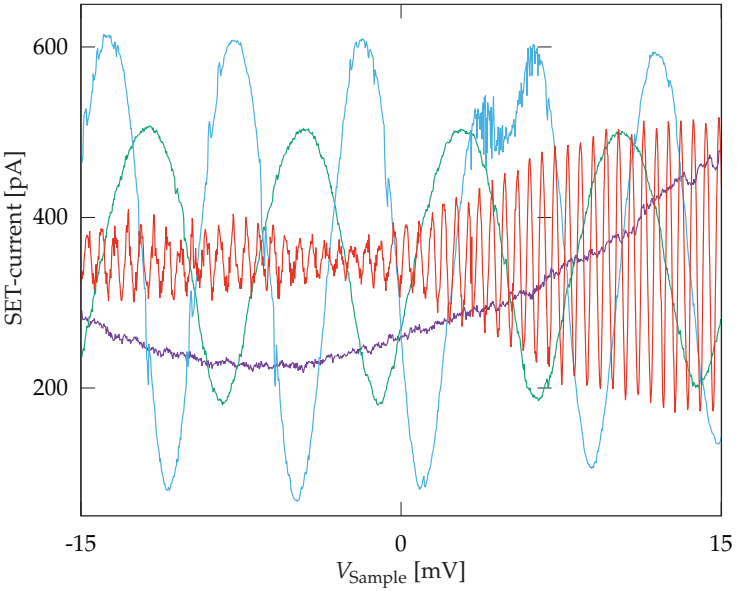

Figure C.1:
Strange current modulation amplitude behavior for very close sample-to-SET-island proximity. (red) drain current of SET 1, (blue) drain current of SET 2, (green) drain current of SET 3, (violet) drain current of SET 8. The distance between surface electrode and SET islands increases from SET 1 to 8. The CBO current modulation period of SET 1 should lie around or slightly below the one of SET 2 (6 mV) but measures less than 1 mV.

C.2 High Resolution Area Scans

In Figure C.2 and Figure C.3 the simultaneous area scans of four SETs are shown. The scans were executed at the lower end of the calibration structures, see Figure 6.2 in Chapter 6.1 without the y-shift corrections. The sample-to-SET-island distance increases from SET 1 to 8 which was on purpose not corrected to have the opportunity of recording simultaneously probing signals at different heights over the sample surface. The scans were done with a very high resolution of 331 pts by 331 pts, requiring more than 12h measurement time.

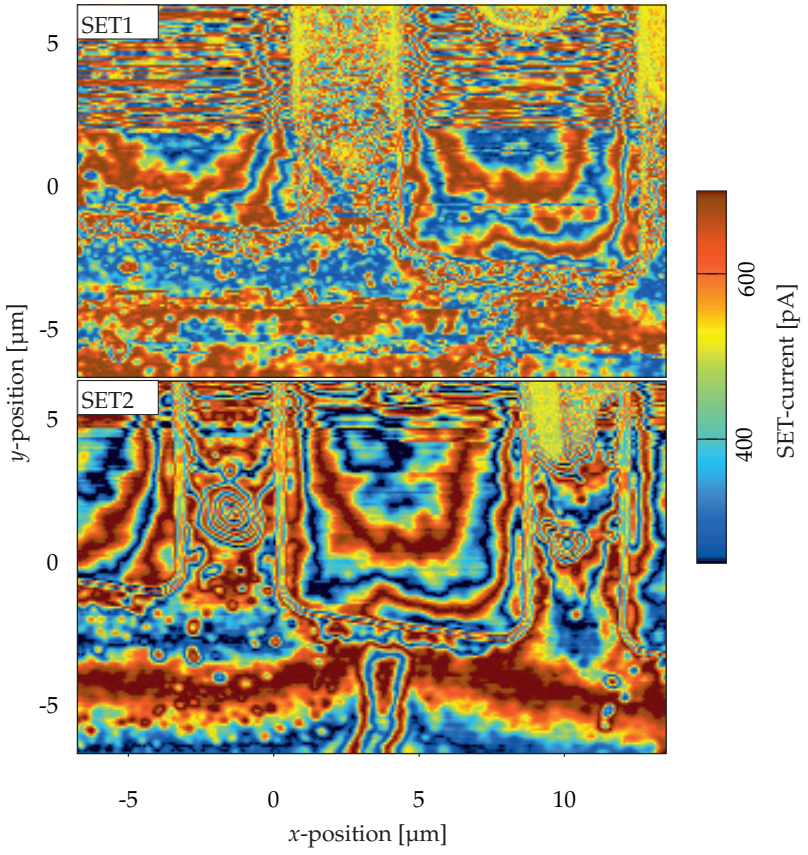

Figure C.2:
Area scan of SET 1,2 over U-shaped gold electrode with high resolution.

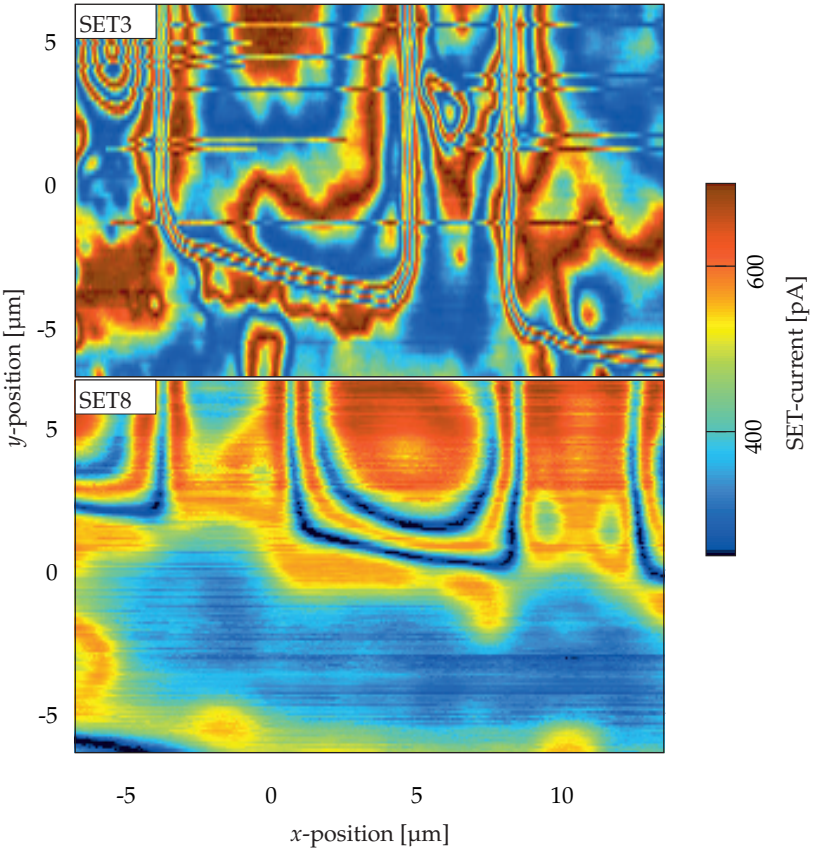

Figure C.3:
Area scan of SET 3,8 over U-shaped gold electrode with high resolution.

C.3 Different Excitation Amplitudes for the Temperature Measurement

In Chapter 6.10 the working temperature of the microscope was determined. Here we show some more measurement data, see Figure C.4.

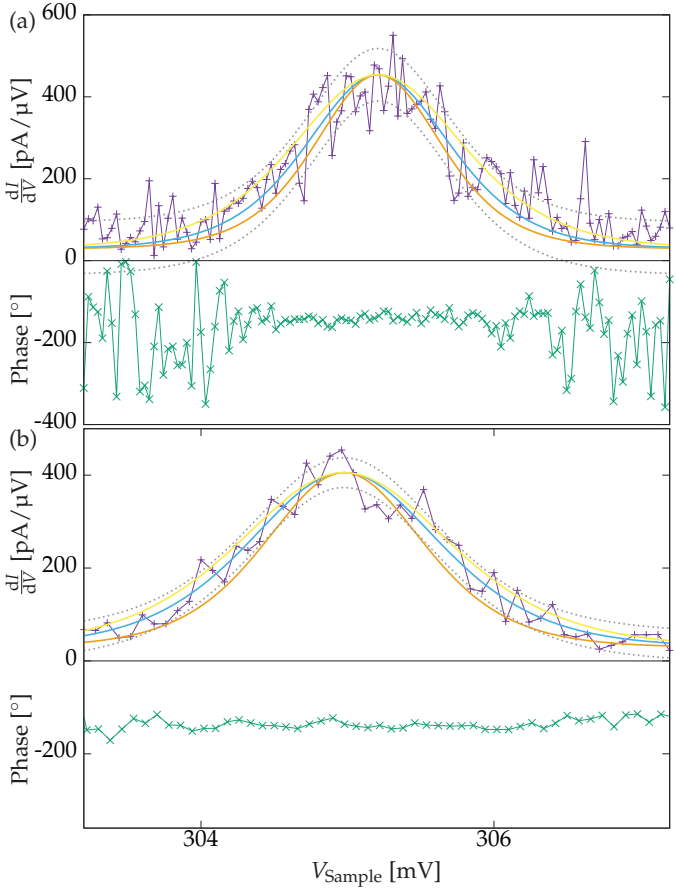

Figure C.4:
Further measurements for the determination of the working temperature with different AC excitation voltage amplitudes. (blue) fit, (brown) 30 mK, (yellow) 40 mK, (dotted) standard deviation from fit. (a) Measurement with 1.4 µV AC amplitude resulting in a fitted temperature of (34.4 mK). (b) Measurement with 2.8 µV AC amplitude resulting in a fitted temperature of 36.4 mK.

C.4 Resolution Comparison Between CBO and FBL Method

To obtain the lateral resolution of the FBL method we repeated the measurement of the CBO method in which we approached the sample surface the closest possible (20 nm) and recorded the measurement signal variations due to capacitive effects. In Figure C.5 the comparison between (a) a measurement executed with the CBO method and (b) the same measurement executed with the FBL method are shown. The lateral resolution is roughly the same but the FBL method shows a lot more instabilities in the FB signal due to fast and strong electrostatic potential changes while scanning the surface.

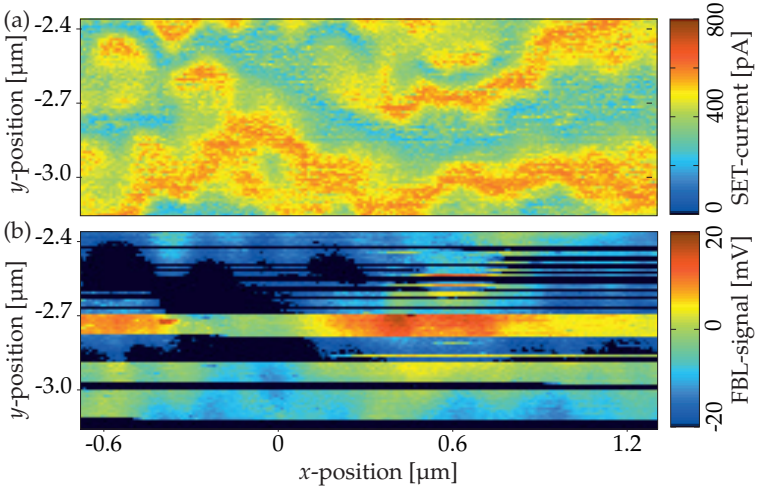

Figure C.5:
Comparison between the lateral resolution of the CBO method and the FBL method. (a) Measurement executed with the use of the CBO method. (b) Measurement executed with the use of the FBL method for the same scan area.

C.5 Electrostatic Potential Area Scan for Different Sample Potential with the CBO Method

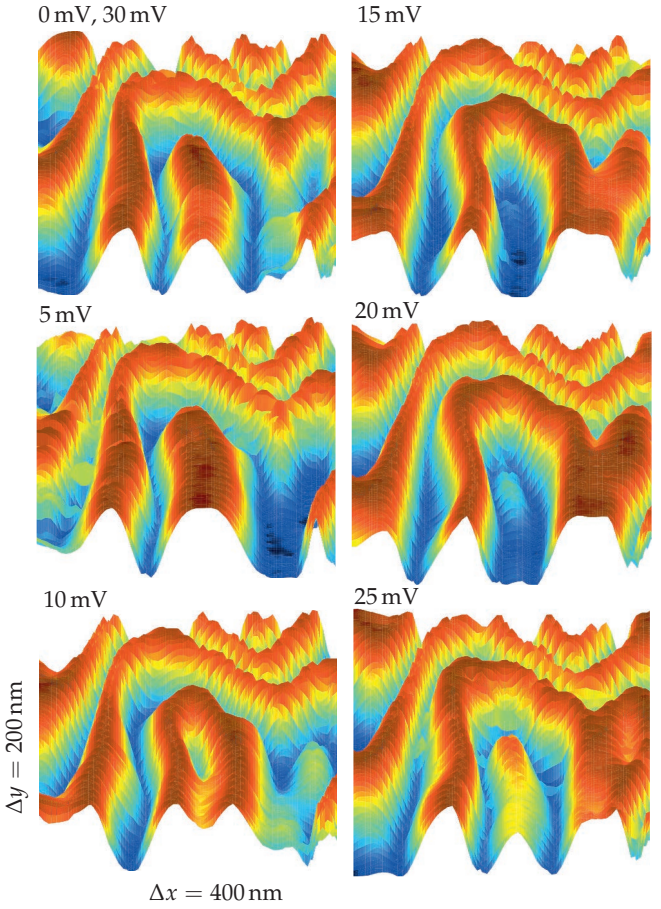

Figure C.6:
Recorded SET current over a scanned rough surface electrode for different electrode potentials. The different area scans, plotted in pseudo three-dimensional representation, show the recorded current through the SET for six different applied sample voltages in steps of 5 mV. Due to an SET current modulation period of 30 mV sample potential difference the first area scan (0 mV) also represents the recorded SET current for 30 mV sample potential. The scanned area measures 400 nm by 200 nm and the SET current modulation amplitude 200 pA.

C.6 Mechanical Induced Alteration of a Metal Electrode

A mechanical contact between the tips and the sample of a scanning probe microscope usually leaves a trace on the sample surface and damages the probing tip. On a thin evaporated gold electrode the SETs can withstand a minor contact with the sample without being destroyed. However by this mechanical contact the grainy surface structure of gold electrodes can be mechanically changed as Figure C.7 shows. The area scan displaying color-coded the current modulation through the SET over position was taken on the stripe-like calibration structures of the sample. In the framed box we can see clearly two areas with different measurement signal than the rest of the metal electrodes. The yellowish area arises from a too fast modulation of the SET current during the scan, resulting in an averaging. This indicates a detailed fast changing partial capacitance between SET and sample over position.

Due to the SET touching the gold surface and dragging some metal clusters along the sample surface a rough surface is the result, showing fast changes in the partial capacitance between tip and sample. The dragging of metal clusters would also

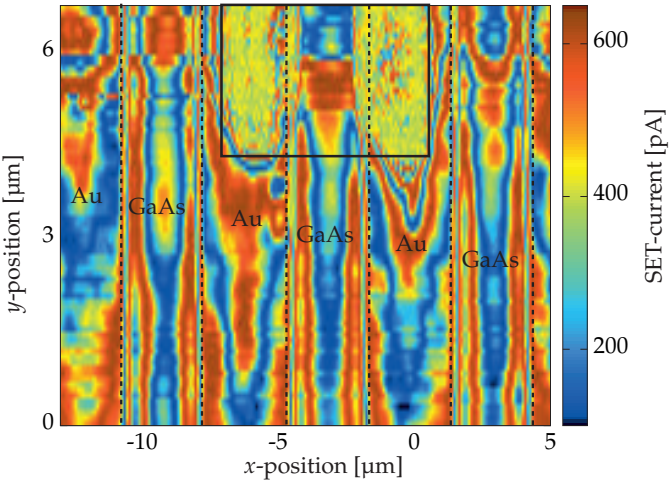

Figure C.7:
Result of a mechanical contact between probing tips and a gold electrode on the sample surface. We see color-coded the SET current modulation over the (x, y)-position. With the black box the two yellow areas on the gold electrodes are framed that are restructured by the mechanical contact with the probing tip.

explain why the fast measurement signal variations can also be seen on the borders of the still smooth GaAs surface.

C.7 Tip-Sample Compensation by FBL Method

Figure C.8 shows approach measurements with the use of the feedback loop for different sample potentials. The jump in the measurement signal every roughly 50 mV results from the reached FB signal limit and the resulting reset. This reset shifts the COM potential to zero and searches for the next available CBO peak to fix the working point to its flank.

As long as the FB signal changes with distance for a certain sample potential the compensation voltage between sample and tip is not reached. In the compensated case the FB signal would not change over tip-sample distance. The black dashed lines show a contour line of the FB signal value over sample potential and tip-sample distance. The larger their slope (in Figure C.8 from right to left) becomes the closer we come to the sample voltage that compensates the tip-sample configuration.

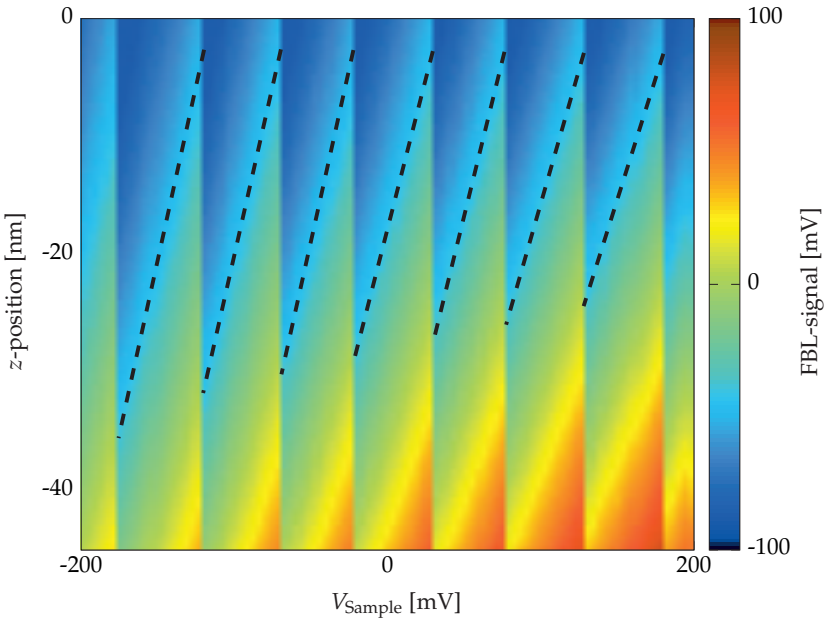

Figure C.8:
Tip-sample compensation with the use of the FBL method. The dashed black lines show contour lines in the FB signal. For a vertical dashed line the compensation between sample and SET island would be obtained.

C.8 Decay of Potential Modulation

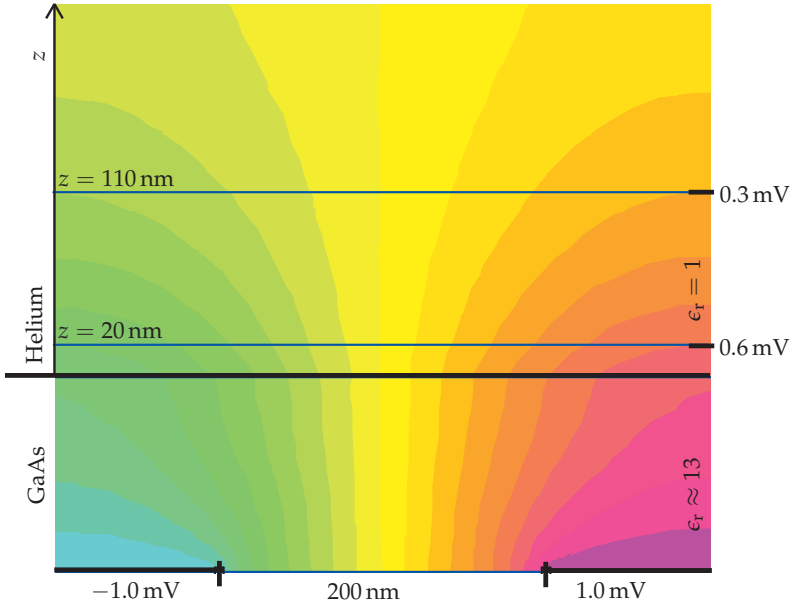

Figure C.9:
Decay of the electrostatic potential modulation over an applied alternating potential distribution mentioned in Chapter 8.4.

C.9 α- and β-Trace of Potential Profile Measurements

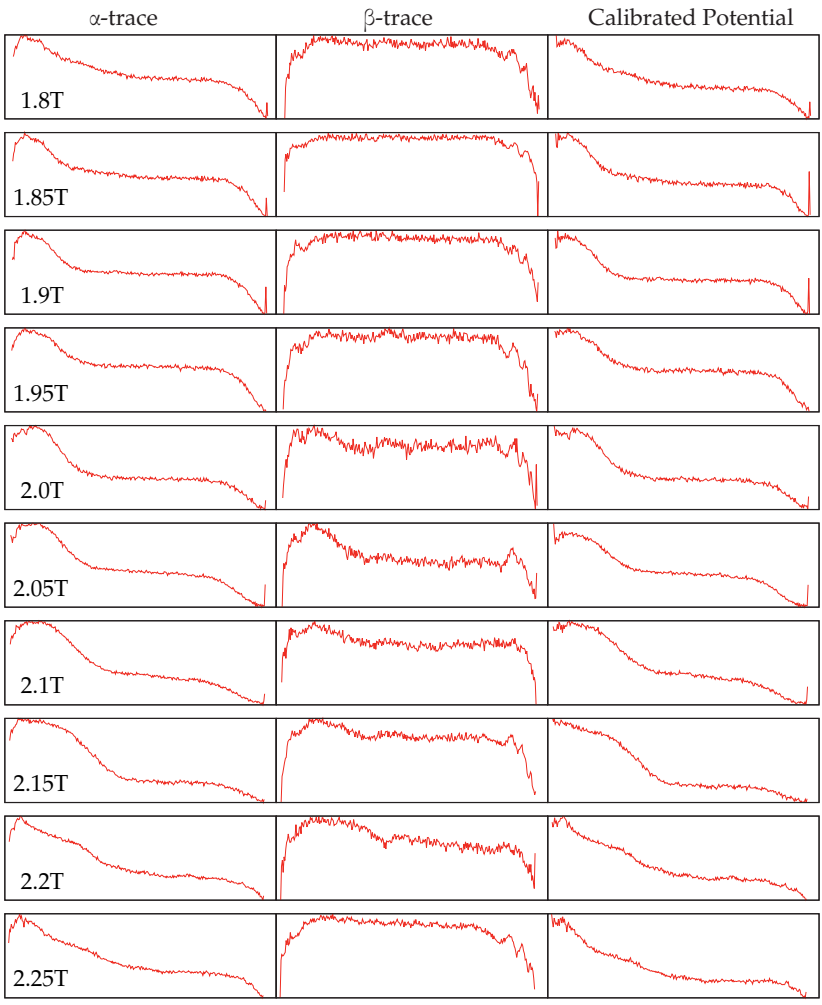

Figure C.10:
Raw data for the Hall potential line scans including the α-trace , β-trace and the resulting calibrated potential used in Chapter 9.5.

C.10 Signal-to-Noise Ratio

The signal-to-noise ratio of the microscope can be determined on the Hall potential plateau of the edge-dominated regime. In Figure C.11 we show an according calibrated potential. The area from $-3\,\mu m$ to $6\,\mu m$ in y-direction is used to fit a horizontal line. In this chosen data set of the calibrated potential we obtain a standard deviation of 0.01. Compared to the whole variation of the calibrated potential for this line scan from 0.267 to 0.927 we get a noise level of less than 3 %. This gives us a signal-to-noise ratio of 33:1. The previously used electrostatic force microscope achieved a signal-to-noise ratio of 5.5:1 for filling factor $\nu = 4$ with a 7.5 times larger excitation voltage ($V_{RMS} = 10.6\,mV$). We enhanced the resolution of the potential probe measurements significantly by a factor of six with a strongly reduced excitation of the sample. Therefore we can resolve now even small electrostatic potential variations with enough significance and are able to probe fragile states like for the fractional quantum Hall effect.

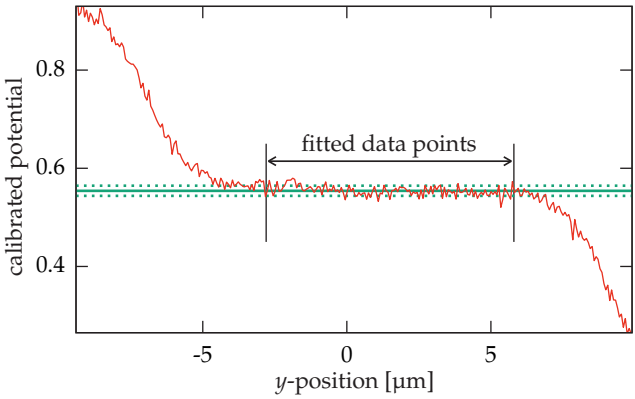

Figure C.11:
Determination of the SNR from a calibrated Hall potential of the edge-dominated quantum Hall regime for filling factor $\nu \approx 4$ over y-position for a line scan across the sample structure. The signal varies from 0.267 to 0.927 and the standard deviation in the marked data range lies around 0.01 (green: linear fit), resulting in a signal-to-noise ratio of 33:1.

D
Laboratory Premises

D.1 Image of the Electrical Setup used for the SPM

The SETs as probing devices require very small applied voltages of less than 2 mV with a step size of around 1 µV and very low input noise. Further the modulation amplitude of the current through an SET usually lies below 200 pA and needs a resolution of less than 10 pA DC. Therefore custom-built electronics in the microscope setup is used separating the voltmeters, lock-in amplifiers and DA-converters from the investigated fragile sample and probing tips. With the electrical setup we achieved the following essential properties:

- applying voltages to the SET with a range limitation of ± 3.96 mV with a step size of 0.12 µV with low output noise of around $60\,\mathrm{nV}/\sqrt{\mathrm{Hz}}$ from the operation amplifiers,
- resolving voltage signals from the sample in the range of ± 10 mV with less than 5 µV resolution in DC ,
- detecting currents through the SET with a range limitation of ± 10 nA with a resolution of less than 10 pA DC,
- simultaneously operating up to four SETs with stable analog PID feedback loops covering a potential range for ± 100 mV of the SET island,
- two Hall bars can be characterized and operated simultaneously,
- signal stability over several months with shifts in the applied parameters and measured signals of less than 1 %.

Figure D.1 shows a picture of the electrical setup of the instrument above the cryogenic system underneath the floor.

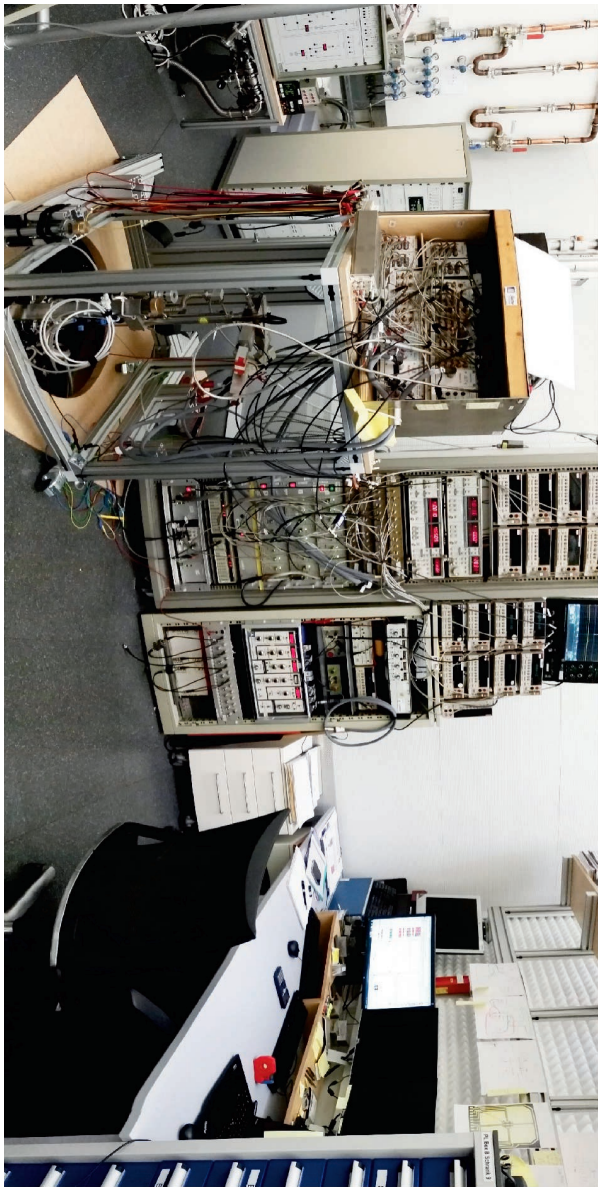

Figure D.1:
Picture of the scanning SET microscope setup located in the highly vibration isolated precision laboratory.

D.2 Image of Investigated Sample

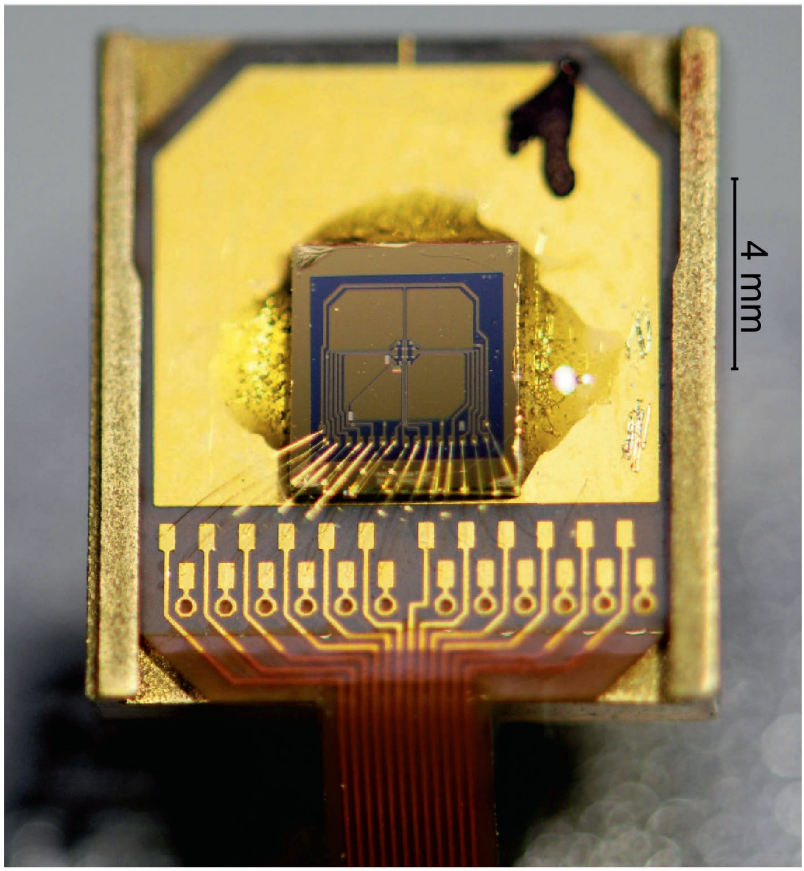

Figure D.2:
Picture of one of the used samples wire bonded and glued on a flexible circuit board on top of a sample holder made of brass.

D.3 Image of Ultra High Vacuum System for SET Fabrication

An ultra high vacuum (UHV) system, to fabricate the SET tips, had to be disassembled, moved and reinstalled. Further it got an enhanced cooling system with a phase separator for liquid nitrogen. A small leakage was detected for the aluminum chamber near the electric connectors to read out the layer growth. Still we reach pressures of less than 9.0×10^{-10} mbar for the evaporation chamber and pressures of less than 8.0×10^{-11} mbar for the transfer chamber. Further the sample is cooled below $-25\,^{\circ}\mathrm{C}$ during evaporation. This is done to obtain a smoother aluminum layer. Figure D.3 shows a picture of the UHV system in the clean room premises.

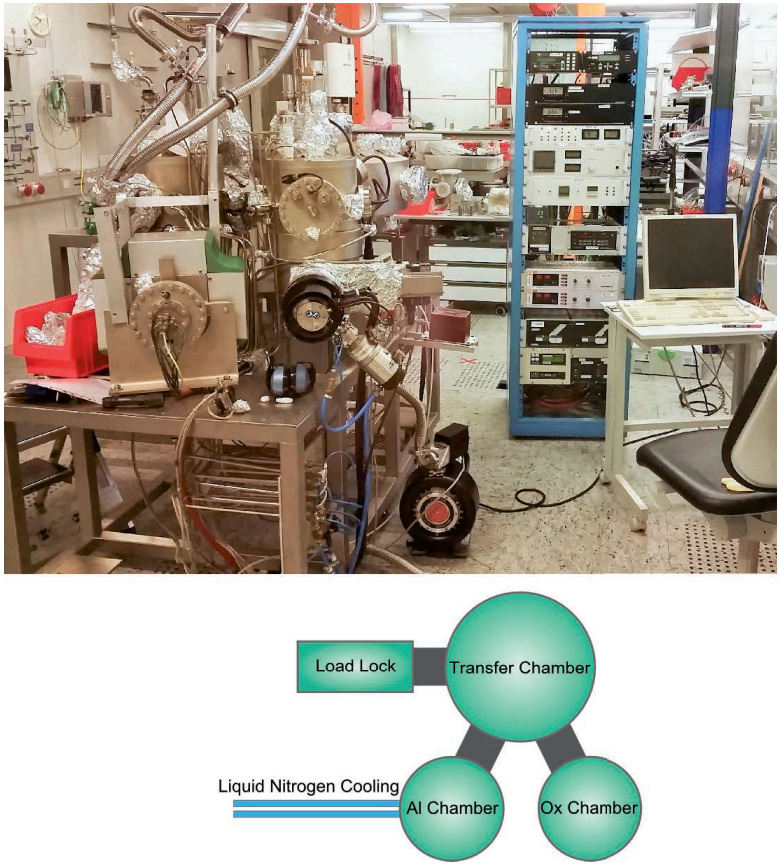

Figure D.3:
Picture of the installed ultra high vacuum chamber cluster for evaporating and oxidizing aluminum onto the cooled tips structures.

Bibliography

[1] E. H. Hall, "On a new action of the magnet on electric currents," *American Journal of Mathematics*, vol. 2, pp. 287–292, September 1879.

[2] K. v. Klitzing, G. Dorda, and M. Pepper, "New method for high-accuracy determination of the fine-structure constant based on quantized Hall resistance," *Phys. Rev. Lett.*, vol. 45, pp. 494–497, Aug 1980.

[3] D. C. Tsui, H. L. Stormer, and A. C. Gossard, "Two-dimensional magnetotransport in the extreme quantum limit," *Phys. Rev. Lett.*, vol. 48, pp. 1559–1562, May 1982.

[4] R. B. Laughlin, "Anomalous quantum Hall effect: An incompressible quantum fluid with fractionally charged excitations," *Phys. Rev. Lett.*, vol. 50, pp. 1395–1398, May 1983.

[5] I. M. Mills, P. J. Mohr, T. J. Quinn, B. N. Taylor, and E. R. Williams, "Adapting the international system of units to the twenty-first century," *Philosophical Transactions of the Royal Society of London A: Mathematical, Physical and Engineering Sciences*, vol. 369, no. 1953, pp. 3907–3924, 2011.

[6] I. M. Mills, P. J. Mohr, T. J. Quinn, B. N. Taylor, and E. R. Williams, "Redefinition of the kilogram: a decision whose time has come," *Metrologia*, vol. 42, no. 2, p. 71, 2005.

[7] R. Steiner, "History and progress on accurate measurements of the Planck constant," *Reports on Progress in Physics*, vol. 76, no. 1, p. 016101, 2013.

[8] A. Eichenberger, G. Genevès, and P. Gournay, "Determination of the Planck constant by means of a Watt balance," *The European Physical Journal Special Topics*, vol. 172, no. 1, pp. 363–383, 2009.

[9] A. Eichenberger, H. Baumann, B. Jeanneret, B. Jeckelmann, P. Richard, and W. Beer, "Determination of the Planck constant with the METAS Watt balance," *Metrologia*, vol. 48, no. 3, p. 133, 2011.

[10] I. A. Robinson, "Towards the redefinition of the kilogram: a measurement of the Planck constant using the NPL Mark II Watt balance," *Metrologia*, vol. 49, no. 1, p. 113, 2012.

[11] K. L. McCormick, M. T. Woodside, M. Huang, M. Wu, P. L. McEuen, C. Duruoz, and J. S. Harris, "Scanned potential microscopy of edge and bulk currents in the quantum Hall regime," *Phys. Rev. B*, vol. 59, pp. 4654–4657, Feb 1999.

[12] K. P. Weitz, *Untersuchungen zum Verlauf der Hall-Spannung in einem zweidimensionalen Elektronensystem unter Bedingungen des Quanten-Hall-Effekts mittels eines Raster-Kraft-Mikroskops*. PhD Thesis, University of Hamburg, 1999.

[13] P. Weitz, E. Ahlswede, J. Weis, K. Klitzing, and K. Eberl, "Hall-potential investigations under quantum Hall conditions using scanning force microscopy," *Physica E: Low-dimensional Systems and Nanostructures*, vol. 6, pp. 247 – 250, 2000.

[14] E. Ahlswede, P. Weitz, J. Weis, K. von Klitzing, and K. Eberl, "Hall potential profiles in the quantum Hall regime measured by a scanning force microscope," *Physica B: Condensed Matter*, vol. 298, no. 1–4, 2001.

[15] E. Ahlswede, J. Weis, K. v. Klitzing, and K. Eberl, "Hall potential distribution in the quantum Hall regime in the vicinity of a potential probe contact," *Physica E: Low-dimensional Systems and Nanostructures*, vol. 12, pp. 165 – 168, 2002. Proceedings of the Fourteenth International Conference on the Ele ctronic Properties of Two-Dimensional Systems.

[16] E. Ahlswede, *Potential- und Stromverteilung beim Quanten-Hall-Effekt bestimmt mittels Rasterkraftmikroskopie*. PhD-Thesis, University of Stuttgart, 2002.

[17] J. Weis, "Hall potential profies in quantum Hall samples measured by a low temperature scanning force microscope," *International Journal of Modern Physics B*, no. 21, pp. 1297–1306, 2007.

[18] F. Dahlem, *Adiabatic transport in the qunatum Hall regime: Comparison between transport and scanning force microscopy investigations*. PhD Thesis, University of Stuttgart, 2008.

[19] F. Dahlem, E. Ahlswede, J. Weis, and K. v. Klitzing, "Cryogenic scanning force microscopy of quantum Hall samples: Adiabatic transport originating in anisotropic depletion at contact interfaces," *Phys. Rev. B*, vol. 82, p. 121305, Sep 2010.

[20] S. H. Tessmer, P. I. Glicofridis, R. C. Ashoori, L. S. Levitov, and M. R. Melloch, "Subsurface charge accumulation imaging of a quantum Hall liquid," *Nature*, vol. 392, pp. 51–54, Mar 1998.

[21] Y. Y. Wei, J. Weis, K. v. Klitzing, and K. Eberl, "Single-electron transistor as an electrometer measuring chemical potential variations," *Applied Physics Letters*, vol. 71, no. 17, pp. 2514–2516, 1997.

[22] Y. Y. Wei, J. Weis, K. v. Klitzing, and K. Eberl, "Edge strips in the quantum Hall regime imaged by a single-electron transistor," *Phys. Rev. Lett.*, vol. 81, pp. 1674–1677, Aug 1998.

[23] J. Weis, Y. Wei, and K. v. Klitzing, "Probing the depletion region of a two-dimensional electron system in high magnetic fields," *Physica B: Condensed Matter*, vol. 256-258, pp. 1 – 7, 1998.

[24] J. Weis, Y. Wei, and K. Klitzing, "Single-electron transistor probes two-dimensional electron system in high magnetic fields," *Physica E: Low-dimensional Systems and Nanostructures*, vol. 3, no. 13, pp. 23 – 29, 1998.

[25] J. Huels, J. Weis, K. von Klitzing, and K. Eberl, "Fine structure in the local chemical potential of a two-dimensional-electron system at filling factor v=2/3," *Physica E: Low-dimensional Systems and Nanostructures*, vol. 6, pp. 64 – 68, 2000.

[26] J. Huels, J. Weis, J. Smet, K. v. Klitzing, and Z. R. Wasilewski, "Long time relaxation phenomena of a two-dimensional electron system within integer quantum Hall plateau regimes after magnetic field sweeps," *Phys. Rev. B*, vol. 69, p. 085319, Feb 2004.

[27] M. J. Yoo, T. A. Fulton, H. F. Hess, R. L. Willett, L. N. Dunkleberger, R. J. Chichester, L. N. Pfeiffer, and K. W. West, "Scanning single-electron transistor microscopy: Imaging individual charges," *Science*, vol. 276, no. 5312, pp. 579–582, 1997.

[28] A. Yacoby, H. Hess, T. Fulton, L. Pfeiffer, and K. West, "Electrical imaging of the quantum Hall state," *Solid State Communications*, vol. 111, no. 1, pp. 1 – 13, 1999.

[29] J. Waissman, M. Honig, S. Pecker, A. Benyamini, A. Hamo, and S. Ilani, "Realization of pristine and locally tunable one-dimensional electron systems in carbon nanotubes," *Nature Nanotechnology*, vol. 8, pp. 569–574, august 2013.

[30] N. Pascher, C. Rössler, T. Ihn, K. Ensslin, C. Reichl, and W. Wegscheider, "Imaging the conductance of integer and fractional quantum Hall edge states," *Phys. Rev. X*, vol. 4, p. 011014, Jan 2014.

[31] M. Pelliccione, A. Sciambi, J. Bartel, A. J. Keller, and D. Goldhaber-Gordon, "Design of a scanning gate microscope for mesoscopic electron systems in a cryogen-free dilution refrigerator," *Review of Scientific Instruments*, vol. 84, no. 3, 2013.

[32] A. E. Gildemeister, T. Ihn, M. Sigrist, K. Ensslin, D. C. Driscoll, and A. C. Gossard, "Measurement of the tip-induced potential in scanning gate experiments," *Phys. Rev. B*, vol. 75, p. 195338, May 2007.

[33] D. V. Averin and K. K. Likharev, "Coulomb blockade of single-electron tunneling, and coherent oscillations in small tunnel junctions," *Journal of Low Temperature Physics*, vol. 62, no. 3, pp. 345–373.

[34] T. A. Fulton and G. J. Dolan, "Observation of single-electron charging effects in small tunnel junctions," *Phys. Rev. Lett.*, vol. 59, pp. 109–112, Jul 1987.

[35] S. Ilani, A. Yacoby, D. Mahalu, and H. Shtrikman, "Unexpected behavior of the local compressibility near the $B = 0$ metal-insulator transition," *Phys. Rev. Lett.*, vol. 84, pp. 3133–3136, Apr 2000.

[36] T. Klaffs, *Experimente zur Potential- und Stromverteilung in Quanten-Hall-Systemen mit Einzelelektron-Transistoren*. PhD thesis, Technische Universität Carolo-Wilhelmina zu Braunschweig, 2004.

[37] J. Weis, *Einzelelektronen Tunneltransistor: Transportspektroskopie der elektronischen Grund- und Anregungszustände in einem GaAs/AlGaAs-Quantentopf*. PhD Thesis, University of Stuttgart, 1994.

[38] J. Weis, *Electrical Transport Through Quantum Dot Systems*. Habilitation Treatise, University of Stuttgart, 2002.

[39] H. Hall, P. Ford, and K. Thompson, "A helium-3 dilution refrigerator," *Cryogenics*, vol. 6, no. 2, pp. 80 – 88, 1966.

[40] J. Weis and K. von Klitzing, "Metrology and microscopic picture of the integer quantum Hall effect," *Philosophical Transactions of the Royal Society of London A: Mathematical, Physical and Engineering Sciences*, vol. 369, no. 1953, pp. 3954–3974, 2011.

[41] K. von Klitzing, R. Gerhardts, and J. Weis, "25 Jahre Quanten-Hall-Effekt," *Physik Journal*, 2005.

[42] H. Stoermer, "Electron mobilities in modulation-doped GaAs-(AlGa)As heterostructures," *Surface Science*, vol. 132, no. 1, pp. 519 – 526, 1983.

[43] L. Pfeiffer, K. W. West, H. L. Stormer, and K. W. Baldwin, "Electron mobilities exceeding 10^7 cm^2/vs in modulation doped GaAs," *Applied Physics Letters*, vol. 55, no. 18, pp. 1888–1890, 1989.

[44] S. Hunklinger, *Festkörperphysik*. Oldenburg Wissenschaftsverlag GmbH, 2009.

[45] F. Stern and S. Das Sarma, "Electron energy levels in GaAs-$ga_{1-x}al_xas$ heterojunctions," *Phys. Rev. B*, vol. 30, pp. 840–848, Jul 1984.

[46] W. Dietsche, "Private communications."

[47] H.Ibach and H.Lueth, *Festkörperphysik*, vol. 3. Springer, Heidelberg, 1999.

[48] P. Drude, "Electron theory of metals.," *Annalen der Physik*, vol. 3, no. 3, pp. 369–402, 1900.

[49] P. Drude, "On the electron theory of metals.," *Annalen der Physik*, vol. 1, no. 3, pp. 566–613, 1900.

[50] Landau and Lifschitz, *Lehrbuch der Theoretischen Physik*, vol. 3. Akademie Verlag, Berlin, 1979.

[51] F. F. Fang and P. J. Stiles, "Effects of a tilted magnetic field on a two-dimensional electron gas," *Phys. Rev.*, vol. 174, pp. 823–828, Oct 1968.

[52] T. Englert, D. Tsui, A. Gossard, and C. Uihlein, "g-factor enhancement in the 2d electron gas in GaAs/AlGaAs heterojunctions," *Surface Science*, vol. 113, no. 1, pp. 295 – 300, 1982.

[53] R. J. Nicholas, R. J. Haug, K. v. Klitzing, and G. Weimann, "Exchange enhancement of the spin splitting in a GaAs-$Ga_xAl_{1-x}As$ heterojunction," *Phys. Rev. B*, vol. 37, pp. 1294–1302, Jan 1988.

[54] P. Weitz, E. Ahlswede, J. Weis, K. Klitzing, and K. Eberl, "A low-temperature scanning force microscope for investigating buried two-dimensional electron systems under quantum Hall conditions," *Applied Surface Science*, vol. 157, no. 4, pp. 349 – 354, 2000.

[55] D. B. Chklovskii, B. I. Shklovskii, and L. I. Glazman, "Electrostatics of edge channels," *Phys. Rev. B*, vol. 46, pp. 4026–4034, Aug 1992.

[56] B. E. Kane, *Ph.D. thesis*. Princeton University, 1988.

[57] K. Lier and R. R. Gerhardts, "Self-consistent calculations of edge channels in laterally confined two-dimensional electron systems," *Phys. Rev. B*, vol. 50, pp. 7757–7767, Sep 1994.

[58] K. Panos, *Current Distribution and Hall Potential Landscape within the Quantum Hall Effect in Graphene and towards the Breakdown in a (Al,Ga)As Heterostructure*. PhD Thesis, University of Stuttgart, 2014.

[59] J. P. Eisenstein, L. N. Pfeiffer, and K. W. West, "Compressibility of the two-dimensional electron gas: Measurements of the zero-field exchange energy and fractional quantum Hall gap," *Phys. Rev. B*, vol. 50, pp. 1760–1778, Jul 1994.

[60] A. Fetter, *Quantum theory of many-particle systems*. Courier Dover Publications, 2003.

[61] A. H. MacDonald, T. M. Rice, and W. F. Brinkman, "Hall voltage and current distributions in an ideal two-dimensional system," *Phys. Rev. B*, vol. 28, pp. 3648–3650, Sep 1983.

[62] U. Klass, W. Dietsche, K. von Klitzing, and K. Ploog, "Imaging of the dissipation in quantum Hall effect experiments," *Zeitschrift für Physik B Condensed Matter*, vol. 82, no. 3, pp. 351–354, 1991.

[63] S. Komiyama, H. Sakuma, K. Ikushima, and K. Hirakawa, "Electron temperature of hot spots in quantum Hall conductors," *Phys. Rev. B*, vol. 73, p. 045333, Jan 2006.

[64] A. Gömmel, S. Appel, K. Beyer, U. Motz, U. Steudel, C. R. Ast, and K. Kern, "Entwicklung von hochgradig erschütterungsarmen Fundamenten für elf Versuchsumgebungen in einem neugebauten Präzisionslabor," *Bauingenieur*, vol. 89, no. 10, pp. 4–12, 2014.

[65] J. Weber, J. Weis, M. Hauser, and K. v Klitzing, "Fabrication of an array of single-electron transistors for a scanning probe microscope sensor," *Nanotechnology*, vol. 19, no. 37, p. 375301, 2008.

[66] J. Weber, *Einzelelektronen Transistor auf Spitzen zur Verwendung in der Rastersondenmikroskopie bei tiefen Temperaturen*. PhD Thesis, University of Ilmenau, 2009.

[67] M. Mausser, *Aufbau eines Milli-Kelvin-Rastersondenmikroskops mit Einzelelektronentransistoren als Sonden*. Diploma Thesis, University of Stuttgart, 2012.

[68] O. V. Lounasmaa, "Dilution refrigeration," *Journal of Physics E: Scientific Instruments*, vol. 12, no. 8, p. 668, 1979.

[69] A. Gauss, *Fabrication and Evaluation of Small Magnetic Field Sensors for Cryogenic Applications*. Master Thesis, University of Stuttgart, 2014.

[70] J. D. Jackson, *Classical Electrodynamics*. Wiley, 1975.

[71] D. Berman, N. B. Zhitenev, R. C. Ashoori, H. I. Smith, and M. R. Melloch, "Single-electron transistor as a charge sensor for semiconductor applications," *Journal of Vacuum Science & Technology B*, vol. 15, no. 6, pp. 2844–2847, 1997.

[72] G. Binnig, C. F. Quate, and C. Gerber, "Atomic force microscope," *Phys. Rev. Lett.*, vol. 56, pp. 930–933, Mar 1986.

[73] G. Binnig, H. Rohrer, C. Gerber, and E. Weibel, "Surface studies by scanning tunneling microscopy," *Phys. Rev. Lett.*, vol. 49, pp. 57–61, Jul 1982.

[74] O. Göktas, J. Weber, J. Weis, and K. von Klitzing, "Alloyed ohmic contacts to two-dimensional electron system in AlGaAs/GaAs heterostructures down to submicron length scale," *Physica E: Low-dimensional Systems and Nanostructures*, vol. 40, no. 5, pp. 1579 – 1581, 2008. 17th International Conference on Electronic Properties of Two-Dimensional Systems.

[75] O. Göktas, *Small alloyed ohmic contacts to 2DES and submicron scale corbino devices in strong magnetic fields : observation of a zero bias anomaly and single electron charging*. PhD Thesis, University of Stuttgart, 2009.

[76] G. S. Boebinger, A. M. Chang, H. L. Stormer, and D. C. Tsui, "Magnetic field dependence of activation energies in the fractional quantum Hall effect," *Phys. Rev. Lett.*, vol. 55, pp. 1606–1609, Oct 1985.

[77] S. Kawaji, J. Wakabayashi, J. Yoshino, and H. Sakaki, "Activation energies of the 1/3 and 2/3 fractional quantum Hall effect in GaAs/AlxGa1-xAs heterostructures," *Journal of the Physical Society of Japan*, vol. 53, no. 6, pp. 1915–1918, 1984.

[78] H. C. Choi, W. Kang, S. Das Sarma, L. N. Pfeiffer, and K. W. West, "Activation gaps of fractional quantum Hall effect in the second Landau level," *Phys. Rev. B*, vol. 77, p. 081301, Feb 2008.

[79] R. L. Willett, H. L. Stormer, D. C. Tsui, A. C. Gossard, and J. H. English, "Quantitative experimental test for the theoretical gap energies in the fractional quantum Hall effect," *Phys. Rev. B*, vol. 37, pp. 8476–8479, May 1988.

[80] S. O. R. Moheimani, "Invited review article: Accurate and fast nanopositioning with piezoelectric tube scanners: Emerging trends and future challenges," *Review of Scientific Instruments*, vol. 79, no. 7, 2008.

[81] N. Tamer and M. Dahleh, "Feedback control of piezoelectric tube scanners," *Proceedings of the 33rd IEEE Conference*, vol. 2, pp. 1826–1831 vol.2, Dec 1994.

[82] F. J. Giessibl, "AFM's path to atomic resolution," *Materials Today*, vol. 8, no. 5, pp. 32 – 41, 2005.

[83] J. Vancea, G. Reiss, F. Schneider, K. Bauer, and H. Hoffmann, "Substrate effects on the surface topography of evaporated gold films by a scanning tunnelling microscopy investigation," *Surface Science*, vol. 218, no. 1, pp. 108 – 126, 1989.

[84] N. Semaltianos and E. Wilson, "Investigation of the surface morphology of thermally evaporated thin gold films on mica, glass, silicon and calcium fluoride substrates by scanning tunneling microscopy," *Thin Solid Films*, vol. 366, no. 2, pp. 111 – 116, 2000.

[85] H. Franco, J. Bossy, and H. Godfrin, "Properties of sintered silver powders and their application in heat exchangers at millikelvin temperatures," *Cryogenics*, vol. 24, no. 9, pp. 477 – 483, 1984.

[86] C. W. J. Beenakker, "Theory of Coulomb-blockade oscillations in the conductance of a quantum dot," *Phys. Rev. B*, vol. 44, pp. 1646–1656, Jul 1991.

[87] A. Finkler, Y. Segev, Y. Myasoedov, M. L. Rappaport, L. Neeman, D. Vasyukov, E. Zeldov, M. E. Huber, J. Martin, and A. Yacoby, "Self-aligned nanoscale SQUID on a tip," *Nano Letters*, vol. 10, no. 3, pp. 1046–1049, 2010. PMID: 20131810.

[88] J. C. Riviere, "The work function of gold," *Applied Physics Letters*, vol. 8, no. 7, pp. 172–172, 1966.

[89] W. Sachtler, G. Dorgelo, and A. Holscher, "The work function of gold," *Surface Science*, vol. 5, no. 2, pp. 221 – 229, 1966.

[90] E. Huber and C. Kirk, "Work function changes due to the chemisorption of water and oxygen on aluminum," *Surface Science*, vol. 5, no. 4, pp. 447 – 465, 1966.

[91] K. Panos, *Aufbau eines Raster-Kraft-Mikroskopes zur Messung von Potentialverteilungen an Quanten-Hall-Proben*. Diploma Thesis, University of Stuttgart, 2009.

[92] J. Huels, *Experimente zur Potentialverteilung zweidimensionaler Eletronensysteme im ganz- und gebrochenzahligen Quanten-Hall-Bereich mit Hilfe eines Einzelelektron-Transistors als Elektronmeter*. PhD Thesis, University of Hamburg, 2001.

[93] P. Haremski, *Electrical Breakdown of the Quantum Hall Effect: Influence of Hall Bar Width and Potential Probing Contacts on the Edge- and the Bulk-Dominated Regime*. Master Thesis, University of Stuttgart, 2015.

[94] D. Meeker, *Finite Element Method Magnetics*. http://www.femm.info/Archives/doc/manual-42.pdf, October 2015.

[95] K.-J. Bathe, *Finite Element Method*. John Wiley & Sons, Inc., 2007.

[96] G. Dhatt, G. Touzot, and E. Lefrancois, *Finite Element Method*. ISTE Ltd. and John Wiley and Sons Inc, 2012.

[97] *Lua 5.3 Reference Manual*. http://www.lua.org/manual/5.3/, 2016.

Acknowledgement

The scanning SET project would not have been possible without the support of other persons either by helping in and around the laboratory (relocation), in the cleanroom facilities, offering space for discussion or just supporting me personally.

I want to thank Prof. Dr. Jürgen Weis for his support in correcting this thesis and for the discussions about physical topics and the freedom to design his new laboratory, the experimental setup and microscope.

I want to thank Prof. Dr. Klaus von Klitzing for the given freedom and financial support to construct and arrange the new laboratory, the cryogenic setup and the measurement equipment in the way I preferred and for the constructive discussions concerning the recorded measurement data.

I also want to thank Prof. Dr. Jochen Mannhart for the constructive discussions, his encouraging enthusiasm in this project and the generosity to use one of his office spaces.

Concerning the samples and wafer materials I needed either for producing samples or fabricating SETs, I want to thank Dr. Werner Dietsche (MPI), Prof. Dr. Werner Wegscheider (ETHZ), Dr. Christian Reichl (ETHZ), Dr. Michael Jetter (Uni. Stgtt.), Prof. Dr. Peter Michler and Dr. Matthias Paul (Uni. Stgtt.). Without the supplied heterostructure material the project would not have been possible.

In regards of clean room related topics like producing SETs or Hall bar samples I am deeply indebted to Achim Güth, Marion Hagel, Bernhard Fenk, Ulrike Weizmann, Maik Hauser and of course Thomas Reindl. You were never hesitating to help me if I had a problem with one of the numerous different fabrication steps or needed something to be done especially at the focused ion beam, electron beam lithography, optical lithography, bonder, or others.

For the construction of the cryogenic setup in the new laboratory I could always rely on the help of the technicians Steffen Wahl and Gunther Euchner. Furthermore I want to thank Manfred Schmid, Ingo Hagel and Peter Specht who helped with designing the new microscope rod, getting parts for a construction in the UHV chamber and amazed me with the sometimes simple and sometimes sophisticated solutions for mechanical constructions. In this subject I also want to thank the whole staff of the mechanical work shop who supported me in any situation. In concerns of setting up the cryogenic cooling system I also want to thank the group of the low temperature service for their support of welding vacuum parts and introducing me into the world of all the different vacuum and high pressure connectors.

I want to thank Stefan Falk for the conceptional ideas and plans for the construction of the used microscope rod which I started to implement during my diploma thesis.

I want to give a special thanks to Dr. Hans Boschker, Dr. Konstantinos Panos, Dr. Maximilian Koepke, Dr. Leonhard Schulz and Stefan Falk for giving me guidance, advice in work related themes and being open for helpful personal discussion.

Johanna Konrad-Mausser, Andreas Gauß, Matthias Münks, Dr. Joe Falson and Dr. Johann Konrad I want to thank for reading this thesis at least partly for corrections and improvements.

Furthermore, I want to thank Matthias Muenks for introducing me to the world of scanning tunneling microscopy and to the theme of simulations done with the method of finite elements which both had a large impact on this work.

Additionally, I want to thank Dr. Daniel Kärcher, Dr. Benjamin Krauss, Dr. Xuting Huang, Matthias Kuehne, Matthias Hepting, Marcus Rommel, Patrick Herlinger, Juliane Mürter and Dr. Benedikt Frieß for the sometimes tough discussions about a big variety of themes and the enjoyable time together.

For the friendly and amusing atmosphere in the institute I want to thank some additional people like for example Rene Berktold, Sibani Bisoy, Bamidele Onipede, Rostyslav Savytskyy, Carsten Woltmann, Iman Rastegar, Ding Zhang, Robin Wanke, Christian Dette, Alexander Hoyer and the unmentioned rest of the von Klitzing, Mannhart and Kern department.

In concern of computer related themes I first want to thank the IT-team for helping me setting up the new laboratory from the perspective of software and hardware. Secondly, I want to thank all the developers of all the software I used to complete this PhD thesis.

In regards of my not work related time I want to thank my dear fellow students and friends for distracting me and cheering me up.

For the support, encouragement I want to thank my whole family in particular my parents G. and W. Mausser, my grandmother R. Neef and in remembrance of K. Neef, my aunt and uncles R. and H. Neef, H. Mausser and my parents-in-law C. and J. Konrad.

I want to thank my successor, reliable colleague and dear friend Andreas Gauß for enduring me, taking over the working microscope, continuing the project and for your encouraging nature.

My beloved wife Johanna Konrad-Mausser, I want to thank you for enduring me while writing this thesis, distracting me at least for some time at the weekends, trying to encourage me after disappointing moments and supplying me with amazing food. Without you my world would be a sadder place.

Curriculum Vitae

Personal Data

Name	Marcel D. Mausser
Date of birth	27.12.1986
Place of birth	Bad Cannstatt (Germany)

Education

1997-2006	Secondary School, Hegel-Gymnasium Stuttgart with general qualification for university entrance
2006-2012	Study of Physics at University of Stuttgart, Department of Prof. Dr. K. von Klitzing, Diploma thesis topic: "Aufbau eines milli-Kelvin Rastersondenmikroskops mit Einzel-elektronentransistoren als Sonden"
2009	Voluntary thermostatic project at University of Stuttgart, Department of Prof. Dr. U. Seifert, topic: "Optimized Protocols in non-Equilibrium Systems"
2009-2010	Research visit to CRANN Institute, Trinity College Dublin, Group of Prof. Dr. G. S. Duesberg
2012-now	PhD study at the Max-Planck-Institute for Solid State Research, Department of Prof. Dr. Klaus von Klitzing